



**HAL**  
open science

# 3D registration of prostate histology slices with MR images

Cécilia Hugues

► **To cite this version:**

Cécilia Hugues. 3D registration of prostate histology slices with MR images. Signal and Image processing. Université Claude Bernard - Lyon I, 2013. English. NNT : 2013LYO10076 . tel-01176310

**HAL Id: tel-01176310**

**<https://theses.hal.science/tel-01176310>**

Submitted on 15 Jul 2015

**HAL** is a multi-disciplinary open access archive for the deposit and dissemination of scientific research documents, whether they are published or not. The documents may come from teaching and research institutions in France or abroad, or from public or private research centers.

L'archive ouverte pluridisciplinaire **HAL**, est destinée au dépôt et à la diffusion de documents scientifiques de niveau recherche, publiés ou non, émanant des établissements d'enseignement et de recherche français ou étrangers, des laboratoires publics ou privés.

THÈSE DE L'UNIVERSITÉ DE LYON

Délivrée par

L'UNIVERSITÉ CLAUDE BERNARD LYON 1

ECOLE DOCTORALE INTERDISCIPLINAIRE SCIENCES-SANTÉ

DIPLÔME DE DOCTORAT

(arrêté du 7 août 2006)

Soutenue publiquement le 27 mai 2013 par

Mlle. Cecilia HUGHES

TITRE :

MÉTHODE DE MISE EN CORRESPONDANCE TRIDIMENSIONNELLE DES  
COUPES IRM DE LA PROSTATE ET DES COUPES HISTOLOGIQUES DES  
PIÈCES DE PROSTATECTOMIE.

Directeur de thèse : M. OLIVIER ROUVIÈRE

Co-directeur de thèse : M. RÉMY PROST

JURY :

Nacim BETROUNI	Chargés de Recherche, INSERM U703, Lille	Rapporteur
Grégoire MALANDAIN	Directeur de Recherche, INRIA, Sophia Antipolis	Rapporteur
Jocelyne TROCCAZ	Directeur de Recherche, CNRS, TIMC-IMG, Grenoble	Rapporteur
Pierre MOZER	Maître de Conférences des Universités Praticien Hospitalier, Hôpital Pitié-Salpêtrière, Paris	Examineur
Gail ter HAAR	Professor of Physics, Institute of Cancer Research, Sutton	Examineur
Olivier ROUVIÈRE	Professeur des Universités Praticien Hospitalier, Hôpital Edouard Herriot, Lyon	Directeur
Rémy PROST	Professeur des Universités, CREATIS, Lyon	Co-directeur



*Aux 3,448,838,611<sup>1</sup> porteurs des prostates dans ce monde.*

---

<sup>1</sup>Le 25 mars 2013 à 18h47

# UNIVERSITE CLAUDE BERNARD - LYON 1

## **Président de l'Université**

Vice-président du Conseil d'Administration

Vice-président du Conseil des Etudes et de la Vie Universitaire

Vice-président du Conseil Scientifique

Directeur Général des Services

**M. F-N. Gilly**

M. le Professeur H. Ben Hadid

M. le Professeur P. Lalle

M. le Professeur G. Gillet

M. A. Helleu

## ***COMPOSANTES SANTE***

Faculté de Médecine Lyon Est - Claude Bernard

Faculté de Médecine et de Maïeutique Lyon Sud - Charles Mérieux

Faculté d'Odontologie

Institut des Sciences Pharmaceutiques et Biologiques

Institut des Sciences et Techniques de la Réadaptation

Département de formation et Centre de Recherche en Biologie Humaine

Directeur : M. le Professeur J. Etienne

Directeur : Mme la Professeure C. Burillon

Directeur : M. le Professeur D. Bourgeois

Directeur : Mme la Professeure C. Vinciguerra

Directeur : M. le Professeur Y. Matillon

Directeur : M. le Professeur P. Farge

## ***COMPOSANTES ET DEPARTEMENTS DE SCIENCES ET TECHNOLOGIE***

Faculté des Sciences et Technologies

Département Biologie

Département Chimie Biochimie

Département GEP

Département Informatique

Département Mathématiques

Département Mécanique

Département Physique

Département Sciences de la Terre

UFR Sciences et Techniques des Activités Physiques et Sportives

Observatoire des Sciences de l'Univers de Lyon

Polytech Lyon

Ecole Supérieure de Chimie Physique Electronique

Institut Universitaire de Technologie de Lyon 1

Institut Universitaire de Formation des Maîtres

Institut de Science Financière et d'Assurances

Directeur : M. le Professeur F. De Marchi

Directeur : M. le Professeur F. Fleury

Directeur : Mme le Professeur H. Parrot

Directeur : M. N. Siauve

Directeur : M. le Professeur S. Akkouche

Directeur : M. le Professeur A. Goldman

Directeur : M. le Professeur H. Ben Hadid

Directeur : Mme S. Fleck

Directeur : Mme la Professeure I. Daniel

Directeur : M. C. Collignon

Directeur : M. B. Guiderdoni

Directeur : M. P. Fournier

Directeur : M. G. Pignault

Directeur : M. C. Viton

Directeur : M. A. Mougniotte

Administrateur provisoire : M. N. Leboisne

# RÉSUMÉ

Le cancer de la prostate est le cancer le plus fréquent et la deuxième cause de mortalité par cancer chez l'homme en Europe [Ferlay *et al.* (2010)a]. La détection, la localisation et l'appréciation de l'agressivité des foyers tumoraux dans la prostate sont un enjeu clinique majeur. Ces étapes diagnostiques sont essentielles pour pouvoir diriger précisément le traitement et diminuer les risques de sur- et de sous-traitement. Bien que des nombreuses techniques d'imagerie soient disponibles (la tomographie par émission de positron (TEP), la tomodensitométrie (CT), l'imagerie ultrasonore (US) ou encore l'imagerie par résonance magnétique (IRM)), il n'existe actuellement pas de technique d'imagerie idéale ni un consensus sur l'utilisation des techniques existantes pour évaluer les cancers de la prostate.

Actuellement, la méthode qui permet la meilleure localisation du cancer dans la prostate est l'IRM multi-paramétrique. Celle-ci consiste à combiner les images IRM d'une séquence pondérée en  $T_2$  ( $T_2$ -W) avec des images obtenues à l'aide de séquences de diffusion (DWI) et de dynamique de prise de contraste (DCE). L'évaluation de la sensibilité et la spécificité de chaque séquence est nécessaire pour pouvoir déterminer la combinaison optimale de celles-ci et donc pour obtenir le diagnostic le plus précis possible du cancer de la prostate.

Les coupes histologiques de la pièce prostatique contiennent la réalité de terrain sur le diagnostic du cancer de la prostate. Actuellement, les coupes histologiques sont la source d'information la plus précise et la plus exhaustive concernant le grade, le stade, l'étendue et les marges positives du cancer. Ainsi, pour pouvoir définir les caractéristiques des signaux IRM issus du tissu cancéreux pour chaque modalité d'imagerie et chaque type de séquence, les coupes histologiques doivent être recalées précisément avec les images acquises. Pour chaque séquence, une analyse quantitative du signal IRM dans les zones qui correspondent exactement aux tumeurs, délimitées par histologie, permettrait la définition du signal caractéristique du tissu cancéreux pour ce type de séquence. Ensuite, la combinaison optimale des séquences pourrait être déterminée.

Le but de cette thèse est le développement d'une méthode de la mise en correspondance tridimensionnelle des coupes histologiques de la prostate et des images IRM. Cette mise en correspondance ne peut pas être considérée comme un problème 2D car cela supposerait qu'à chaque coupe histologique correspond une image IRM, autrement dit, que le plan selon lequel la prostate a été découpée durant la procédure histologique est strictement le même (en terme de hauteur et d'orientation) que le plan dans lequel les images IRM ont été acquises. La mise en correspondance tridimensionnelle est un problème comprenant deux étapes principales : premièrement, il faut s'assurer que les coupes histologiques soient alignées les unes par rapport aux autres et deuxièmement, que cet ensemble de coupes alignées soit correctement orienté par rapport aux images IRM.

Le *premier chapitre* présente une introduction générale du cancer de la prostate. La glande prostatique y est décrite et l'épidémiologie du cancer de la prostate est exposée.

Les systèmes standards utilisés pour la classification du grade et du stade du cancer sont présentés. Le problème du dépistage du cancer de la prostate étant la source de nombreux débats, les arguments «pour» et «contre» sont présentés, ainsi que les tests associés (notamment le test des antigènes spécifiques à la prostate (PSA), le toucher rectal (DRE), les biopsies guidées par ultrasons (TRUS)). Les différentes techniques utilisées pour traiter le cancer de la prostate sont également détaillées, lesquelles incluent la surveillance active, la prostatectomie radicale, la radiothérapie, l'hormonothérapie ou encore la chimiothérapie. Enfin, les modalités d'imagerie disponibles actuellement sont présentées (TEP, CT, US, IRM) ainsi que leurs avantages, désavantages et les indications spécifiques de chacune.

Le *deuxième chapitre* se focalise sur le problème de la mise en correspondance entre l'histologie et l'IRM. Les challenges liés au recalage sont d'abord détaillés, notamment ceux liés aux déformations qui existent entre les deux modalités. Une revue de la littérature concernant les diverses méthodes proposées jusqu'alors pour réaliser la mise en correspondance 2D entre l'histologie et l'IRM est présentée, incluant les divers dispositifs développés pour assurer que le plan de coupe histologique est identique au plan d'imagerie. Ensuite, une revue de la littérature concernant les méthodes proposées pour faire la mise en correspondance 3D entre l'histologie et l'IRM est présentée, tout d'abord dans le cas où le recalage a été considéré comme un problème à deux étapes (i.e. d'abord l'alignement des coupes histologiques puis le recalage de celles-ci avec les images IRM) puis dans celui où le recalage a été considéré comme un problème à une seule étape, combinant l'alignement et le recalage dans le même algorithme.

Des images histologiques, d'IRM *ex vivo* et d'IRM *in vivo* ont été acquises au cours de cette thèse. Le *troisième chapitre* détaille les techniques, routines et protocoles utilisés pour l'acquisition et la préparation des images. Le dispositif développé pour la création de marqueurs internes dans les prostates fraîches est présenté ainsi que le protocole qui y est associé. La procédure de préparation des coupes histologique est également décrite afin de comprendre les déformations et les incertitudes associés aux images histologiques.

Le *quatrième chapitre* porte sur l'alignement des coupes histologiques. L'algorithme développé pour aligner les coupes histologiques marquées y est présenté : celui-ci permet de segmenter en 2D chaque coupe de la prostate, de détecter les marqueurs potentiels dans chaque prostate segmentée, de déterminer lesquels de ces marqueurs potentiels sont des vrais marqueurs et enfin d'identifier par quelle aiguille chaque marqueur a été créé. La méthode utilisée pour l'alignement et la correction du cisaillement de l'ensemble des coupes histologiques est également présentée. Après une initialisation manuelle, l'ensemble de l'algorithme est automatique. Les résultats des tests utilisant des images simulées ainsi que les images acquises pour un échantillon de foie de veau et pour 10 prostates sont présentés.

Le *cinquième chapitre* se focalise sur le recalage 3D des coupes histologiques, une fois alignées, avec les images IRM. L'algorithme développé est basé sur les structures macroscopiques présentes dans le tissu, celles-ci pouvant être soit artificielles, soit naturelles. Le recalage histologie - IRM n'étant pas un recalage rigide, trois phénomènes particuliers, décrit avec cinq paramètres, doivent être pris en compte dans l'algorithme: le rétrécissement, le cisaillement et l'inclinaison. Le rôle de chaque phénomène est expliqué et l'algorithme de recalage développé est décrit. L'algorithme a d'abord été testé en utilisant des marqueurs exogènes (créés par le dispositif présenté précédemment) pour guider

le recalage, puis en utilisant les canaux éjaculateurs comme marqueurs endogènes. Les résultats de ces deux études sont rapportés.

Le *sixième et dernier chapitre* récapitule l'ensemble des résultats obtenus et décrit également les travaux restants pour parvenir à un recalage 3D précis des coupes histologiques avec les images IRM. Il aborde plus particulièrement, le problème du rétrécissement du tissu induit par l'histologie, qui doit être mieux compris et quantifié, ainsi que l'incertitude sur l'espacement et les angles entre les coupes histologiques.

# CONTENTS

INTRODUCTION	1
1 PROSTATE CANCER: AN INTRODUCTION	5
1.1 Introduction	6
1.2 The Prostate Gland	7
1.2.1 Location	7
1.2.2 Anatomy	7
1.2.3 Function	9
1.3 Prostate Cancer Epidemiology	9
1.3.1 Incidence and Mortality	9
1.3.2 Risk Factors	10
1.4 Prostate Cancer Grading and Staging	11
1.4.1 Gleason Grading	11
1.4.2 Cancer Staging	12
1.4.3 Zonal Influence on Cancer Grade and Stage	14
1.5 Prostate Cancer Screening	14
1.5.1 Prostate Specific Antigen (PSA) Test	15
1.5.2 Digital Rectal Examination (DRE)	16
1.5.3 Biopsy	17
1.6 Prostate Cancer Treatment	18
1.6.1 Active Surveillance	18
1.6.2 Radical Prostatectomy	19
1.6.3 Radiotherapy	20
1.6.4 Hormonal Therapy	21
1.6.5 Chemotherapy	21

1.6.6	Alternative Local Treatment Options . . . . .	22
1.7	Prostate Cancer Imaging . . . . .	24
1.7.1	Positron-Emission Tomography (PET) . . . . .	25
1.7.2	Computed Tomography (CT) . . . . .	25
1.7.3	PET/CT . . . . .	25
1.7.4	Ultrasonography . . . . .	26
1.7.5	Magnetic Resonance Imaging (MRI) . . . . .	28
1.7.6	Multimodality Imaging . . . . .	31
1.8	Conclusion . . . . .	32
2	REGISTRATION OF HISTOLOGY AND IMAGED DATA: AN INTRODUCTION	33
2.1	Introduction . . . . .	33
2.2	Registration Challenges . . . . .	34
2.3	2D Registration of Histology and Imaged Data . . . . .	35
2.3.1	Assume that the Histology and Imaging Planes are the Same . . . . .	35
2.3.2	Ensure that the Histology and Imaging Planes are the Same . . . . .	36
2.4	Two-Step 3D Registration of Histology and Imaged Data . . . . .	39
2.4.1	Step 1: Histology Alignment . . . . .	39
2.4.2	Step 2: 3D Registration of Aligned Histology and Imaged Data . . . . .	44
2.5	Combined 3D Registration of Histology and Imaged Data . . . . .	47
2.6	Conclusion . . . . .	48
3	IMAGE ACQUISITION	51
3.1	Introduction . . . . .	52
3.2	MR <i>in vivo</i> Protocol . . . . .	52
3.3	Fiducial Marker Creation . . . . .	52
3.3.1	Apparatus . . . . .	53
3.3.2	Prostate Orientation . . . . .	53
3.3.3	Fiducial Needles . . . . .	54
3.3.4	Needle Insertion Angle . . . . .	55

3.3.5	Model Geometry . . . . .	57
3.3.6	Fiducial Marker Geometry . . . . .	57
3.4	MR <i>ex vivo</i> Protocol . . . . .	58
3.5	Histology Processing . . . . .	59
3.6	Digitisation of the Histology Slices . . . . .	59
3.6.1	JPEG Digitisation . . . . .	59
3.6.2	Histology Slice Inclusion Criteria . . . . .	61
3.7	Conclusion . . . . .	61
4	HISTOLOGY SLICE ALIGNMENT . . . . .	63
4.1	Introduction . . . . .	64
4.2	Glossary . . . . .	64
4.3	Pre-processing . . . . .	64
4.4	Potential Fiducial Marker Detection, Scoring and Classification . . . . .	65
4.4.1	Potential Fiducial Marker Detection . . . . .	66
4.4.2	Potential Fiducial Marker Scoring . . . . .	66
4.4.3	Potential Fiducial Marker Classification . . . . .	67
4.5	True Fiducial Marker Detection and Identification . . . . .	68
4.6	Alignment and Shear Correction of the Histology Slices . . . . .	75
4.6.1	Alignment . . . . .	75
4.6.2	Shear Correction . . . . .	76
4.7	Transformation Summary . . . . .	77
4.8	Validation . . . . .	78
4.8.1	Validation in Simulated Images . . . . .	78
4.8.2	Validation in Beef Liver . . . . .	80
4.8.3	Experimental Validation in 10 Prostate Specimens . . . . .	81
4.9	Results . . . . .	81
4.9.1	Results in Simulated Images . . . . .	81
4.9.2	Results in Beef Liver . . . . .	83

4.9.3	Results in 10 Prostate Specimens . . . . .	85
4.10	Conclusion . . . . .	88
5	HISTOLOGY - MR REGISTRATION . . . . .	93
5.1	Introduction . . . . .	94
5.2	Features Description . . . . .	95
5.2.1	Ejaculatory Ducts . . . . .	95
5.2.2	Urethra . . . . .	97
5.3	3D Parametric Curve Fit . . . . .	98
5.4	Registration Parameters . . . . .	100
5.4.1	Shrinkage ( $s$ ) . . . . .	100
5.4.2	Shear ( $\alpha, \beta$ ) . . . . .	100
5.4.3	Tilt ( $\theta, \phi$ ) . . . . .	100
5.5	3D Histology - MR Registration Algorithm . . . . .	102
5.5.1	Algorithm Overview . . . . .	102
5.5.2	Preliminary Calculations . . . . .	103
5.5.3	Algorithm Pseudo-code . . . . .	104
5.5.4	Calculation of the Points of Rotation for Iteration $i$ . . . . .	105
5.5.5	Calculation of MR Vectors $\mathbf{v}_M(\theta, \phi)$ and Curve Coefficients $\mathbf{c}_M(\theta, \phi)$ . . . . .	107
5.5.6	Calculation of MR Initial Line and Curve Coordinates $\mathbf{p}_M(\mathbf{r}_{i,j}, \theta, \phi)$ . . . . .	108
5.5.7	Calculation of the Optimum Values of $\alpha, \beta$ and $s$ . . . . .	109
5.5.8	Calculation of the Optimum Rotation Point . . . . .	110
5.5.9	Convergence Definition . . . . .	111
5.5.10	Registration Evaluation . . . . .	112
5.6	Registration via Fiducial Needles . . . . .	112
5.6.1	Objectives and Details . . . . .	112
5.6.2	Results and Discussion . . . . .	113
5.7	Registration via Ejaculatory Ducts . . . . .	120
5.7.1	Objectives and Details . . . . .	120

5.7.2	Results and Discussion . . . . .	120
5.8	Conclusion . . . . .	122
6	PERSPECTIVES AND CONCLUSION	125
6.1	Introduction . . . . .	125
6.2	Histology Shrinkage Correction Factor . . . . .	127
6.3	Distances and Angles between Histology Sections and Slices . . . . .	128
6.4	Complete Evaluation . . . . .	129
6.5	Registration Algorithm Extension . . . . .	131
6.6	Virtual Microscopy . . . . .	131
6.7	Conclusion . . . . .	132
A	APPENDIX	135
A.1	Procrustes Analysis . . . . .	135
	REFERENCES	153
	PUBLICATIONS	155
	ABBREVIATIONS	157

# INTRODUCTION

Prostate cancer (PCa) is the most frequently diagnosed cancer of men in Europe and the third leading cause of death from cancer in men [Ferlay *et al.* (2010)a]. The accurate localisation and staging of PCa, enabling low- and high-risk cancers to be distinguished, is a major clinical necessity. It is crucial to enable therapy to be directed more accurately and reduce the risk of over- and under-diagnosis. Though numerous imaging techniques are currently available - positron emission tomography (PET), computed tomography (CT), ultrasonography (US), magnetic resonance imaging (MRI) - to date, no ideal imaging method exists and no consensus exists regarding the use of imaging techniques for evaluating primary prostate cancers.

Currently, the most accurate imaging method for PCa is multi-parametric MRI, that is combining  $T_2$ -weighted ( $T_2$ -W) MR images with diffusion-weighted images (DWI) and dynamic contrast-enhanced (DCE) images. The evaluation of the sensitivity and specificity of each sequence is required in order to determine the optimum combination of sequences to give the most accurate assessment of prostate cancer.

The histology slices of the prostatectomy specimen are the gold standard for prostate cancer diagnosis. To date, they provide the most precise and comprehensive information concerning the cancer grade, stage, tumour extent and margin status. Therefore, in order to define the signal characteristics of prostate cancerous tissue for each imaging modality and sequence, the histology slices must be precisely registered to the imaged data. For each sequence, a quantitative analysis of the signal in the regions corresponding exactly to the histology tumours would enable a definition of the signal characteristics of prostate cancerous tissue for that sequence. The optimum combination of sequences could then be determined.

The aim of this thesis was to develop a method to 3D register the histology slices of radical prostatectomy specimens with MR *in vivo* images. The registration cannot be considered as a 2D problem, as that would assume that every 2D histology slice has a corresponding 2D imaged slice, that is, that the plane along which the prostate specimen was sliced during histology processing is the same (in height and orientation) to the plane along which the imaged data was acquired. The 3D registration is a two-step problem, requiring first the alignment of the stack of histology slices and then the 3D registration of the aligned histology slices with the MR data.

The *first chapter* of this manuscript provides a general introduction to prostate cancer. The prostate gland is described and the epidemiology of prostate cancer is reported. The standardised systems used for grading and staging PCa are presented. PCa screening is a much debated subject, the arguments for and against are presented, as well as the tests involved (the prostate specific antigen (PSA) test, digital rectal examination (DRE), transrectal ultrasound-guided (TRUS) biopsy). The different techniques used to treat PCa are detailed, including active surveillance, radical prostatectomy, radiotherapy, hormonal therapy, chemotherapy. Finally, the different imaging modalities currently available are presented (PET, CT, US, MRI) and the advantages, disadvantages and specific indications of each are considered.

The *second chapter* focuses on the problem of histology - MR registration. First the registration challenges are detailed, in particular due to the various deformations that exist between the two modalities. A literature review is presented of the various methods developed to achieve the 2D histology - MR registration, including various devices that have been created in order to ensure that the histology and imaging planes are the same. Next, a literature review of the developed 3D histology - MR registration techniques is presented, first considering the registration as a two-step problem (i.e. alignment of the histology slices and then registration of the aligned histology slices with the MR images) and then considering the registration as a single-step problem, combining the alignment and registration into one algorithm.

Histology, MR *ex vivo* and MR *in vivo* images were acquired during this thesis. *Chapter three* details each of the different techniques, protocols and routines used to acquire and prepare the images. Internal fiducial markers are created in the fresh prostate specimens, the apparatus and protocol developed to create these markers is presented. The histology processing routine is also described in order to better understand the deformations and uncertainties associated with the histology images.

The *fourth chapter* deals with the alignment of the histology slices. The algorithm developed to segment the 2D prostate in each histology slice, detect the potential fiducial markers within each segmented prostate, detect which of the potential markers are true fiducial markers and to identify by which needle each marker was created, is detailed. The method to align and then shear correct the dataset of images is also presented. The results of tests using simulated images, images acquired from a beef liver sample and 10 prostate specimens are presented.

The *fifth chapter* focuses on the 3D registration of the aligned histology slices with the MR images. The algorithm developed is a feature-based technique, the features employed are detailed. The histology - MR registration is not a rigid registration and three particular phenomena, described using five parameters, need to be included in the registration

algorithm, they are shrinkage, tilt and shear. Each of these phenomena is explained and the developed registration algorithm is described. The algorithm is tested first by using the fiducial needles to guide the registration and then using the ejaculatory ducts to guide the registration. The results of both studies are reported.

The *sixth and final chapter* concludes first with a summary of the results obtained and then more importantly, describes the further work that must be carried out before an accurate 3D histology - MR registration can be achieved. In particular, the histology shrinkage must be better understood and quantified, as well as the spacing and angles between the histology slices.



# 1

## PROSTATE CANCER: AN INTRODUCTION

### CONTENTS

1.1	Introduction . . . . .	6
1.2	The Prostate Gland . . . . .	7
1.2.1	Location . . . . .	7
1.2.2	Anatomy . . . . .	7
1.2.3	Function . . . . .	9
1.3	Prostate Cancer Epidemiology . . . . .	9
1.3.1	Incidence and Mortality . . . . .	9
1.3.2	Risk Factors . . . . .	10
1.4	Prostate Cancer Grading and Staging . . . . .	11
1.4.1	Gleason Grading . . . . .	11
1.4.2	Cancer Staging . . . . .	12
1.4.3	Zonal Influence on Cancer Grade and Stage . . . . .	14
1.5	Prostate Cancer Screening . . . . .	14
1.5.1	Prostate Specific Antigen (PSA) Test . . . . .	15
1.5.2	Digital Rectal Examination (DRE) . . . . .	16
1.5.3	Biopsy . . . . .	17
1.6	Prostate Cancer Treatment . . . . .	18
1.6.1	Active Surveillance . . . . .	18
1.6.2	Radical Prostatectomy . . . . .	19
1.6.3	Radiotherapy . . . . .	20

1.6.4	Hormonal Therapy . . . . .	21
1.6.5	Chemotherapy . . . . .	21
1.6.6	Alternative Local Treatment Options . . . . .	22
1.7	Prostate Cancer Imaging . . . . .	24
1.7.1	Positron-Emission Tomography (PET) . . . . .	25
1.7.2	Computed Tomography (CT) . . . . .	25
1.7.3	PET/CT . . . . .	25
1.7.4	Ultrasonography . . . . .	26
1.7.5	Magnetic Resonance Imaging (MRI) . . . . .	28
1.7.6	Multimodality Imaging . . . . .	31
1.8	Conclusion . . . . .	32

## 1.1 Introduction

This first chapter provides a general introduction to prostate cancer (PCa). The prostate gland itself is first considered, its location, function and anatomy. We then move onto PCa, the most frequently diagnosed cancer of men in Europe. The incidence and mortality rates of the disease are detailed, worldwide and in Europe. We also examine the various risks associated with the disease; not only advancing age but also family history and ethnicity.

A fundamental objective of PCa diagnosis is to distinguish between small, clinically insignificant tumours that present a low risk to the patient and the aggressive tumours with lethal potential, that present a very high risk to the patient. We present the standardised systems used to grade and stage PCa that aim to categorise the risk of the tumours, the amount and location of cancer and the risk of the cancer having spread beyond the prostate.

Whether asymptomatic men benefit from PCa screening is an unresolved question. On the one hand, screening enables cancers to be detected in the early stages. However, some men will be treated unnecessarily, resulting in over-diagnosis and over-treatment. We consider this debate, presenting the results published by various screening programs. We also detail the techniques used to carry out PCa screening, specifically, the prostate specific antigen (PSA) test and the digital rectal examination (DRE). Patients with suspicious PSA and/or DRE results will be further examined by a transrectal ultrasound (TRUS) guided biopsy.

PCa is treated using a variety of different techniques. We present the different treatments, including active surveillance, radical prostatectomy, radiotherapy, hormonal therapy, chemotherapy and also certain alternative local treatment options. Which treatment is chosen to be used is based on the grade and stage of the cancer, as well as the age and general health of the patient.

An imaging technique that could identify tumour stage, volume, and location with high specificity and sensitivity would be invaluable to the diagnosis and treatment of PCa. Low- and high-risk cancers could be distinguished, enabling therapy to be more accurately directed therefore limiting side-effects and reducing over-diagnosis and over-treatment. These advantages and other advantages are further detailed.

To date, no such ideal imaging method exists. We present some of the imaging modalities that are currently available, including positron emission tomography (PET), computed tomography (CT), ultrasonography (US) and magnetic resonance imaging (MRI). Many show considerable clinical value; we consider the advantages, disadvantages and specific indications of each.

## 1.2 The Prostate Gland

The prostate is a gland of the male reproductive system. In this section, we will detail the location, anatomy and function of the gland.

### 1.2.1 Location

The prostate gland is located directly below the bladder and in front of the rectum, see Figure 1.1. The seminal vesicles are located near the base of the prostate. The base refers to the wider part of the anatomy which is located at the bladder neck. The apex is the narrower part, located nearer the perineum, see Figure 1.2(a). The posterior surface of the prostate is adjacent to the rectum, while the anterior surface is located on the opposite side. The prostate surrounds the urethra just below the urinary bladder. It is within the prostate that the urethra merges with the two ejaculatory ducts.

The normal prostate gland is a triangular ellipse that is surrounded by a thin capsule. The normal prostate in adult males measures approximately 4 cm in length, 4 cm in transverse diameter and 3 cm in height [Zagoria (2004)], the volume ranges from 20 to 25 mL, and the weight is approximately  $20 \pm 6$  g [Berry *et al.* (1984)].

### 1.2.2 Anatomy

In the twentieth century, several investigators maintained that the prostate gland was composed of diverse lobes by analogy with laboratory animals [Lowsley (1912), Franks (1954)]. This concept became popular even though no distinct lobes can be seen in the normal adult prostate. McNeal established the current and most widely accepted concept of various zones rather than lobes of the prostate [McNeal (1981)]. In this model, the prostate is divided into four distinct zones, see Figure 1.2.

The **peripheral zone (PZ)** constitutes over 70% of the prostate gland and comprises all the tissue at the apex as well as all of the tissue located posteriorly near the capsule. The **central zone (CZ)** constitutes 25% of the glandular prostate and is a cone-shaped area, with the apex of the cone at the confluence of the ejaculatory ducts and the urethra.

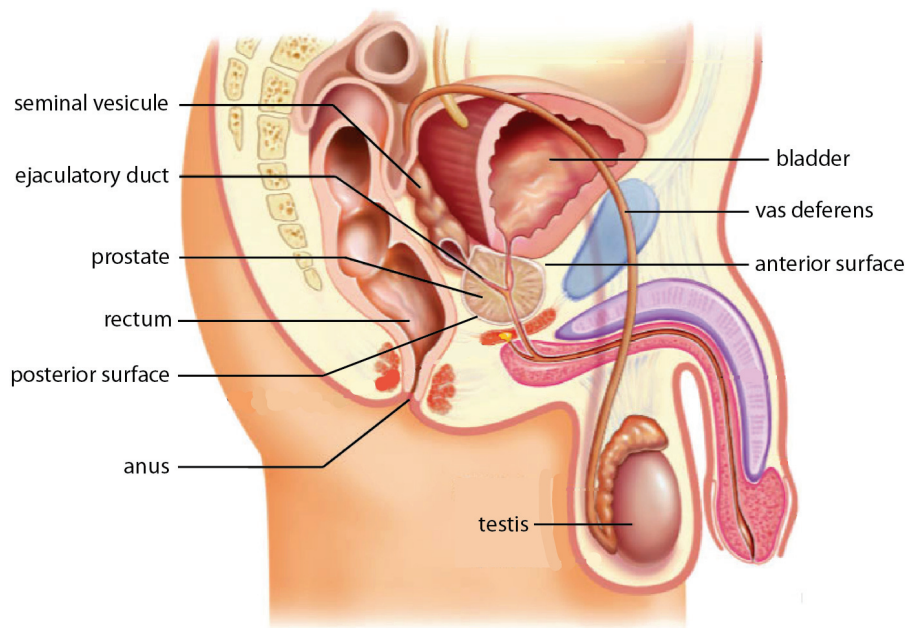


Figure 1.1: *Sagittal view of the male pelvis showing the relative placement of the male reproductive organs. Source: Mosby, Elsevier*

The **transition zone (TZ)** constitutes 5% of the glandular prostate in young adults, increasing with age and with the development of benign prostatic hyperplasia (BPH). The TZ consists of two equal portions of tissue lateral to the urethra in the midgland. The non-glandular **anterior fibromuscular stroma (AFMS)** forms the entire anterior surface of the prostate. It is usually devoid of glandular components and is composed of muscle and fibrous tissue.

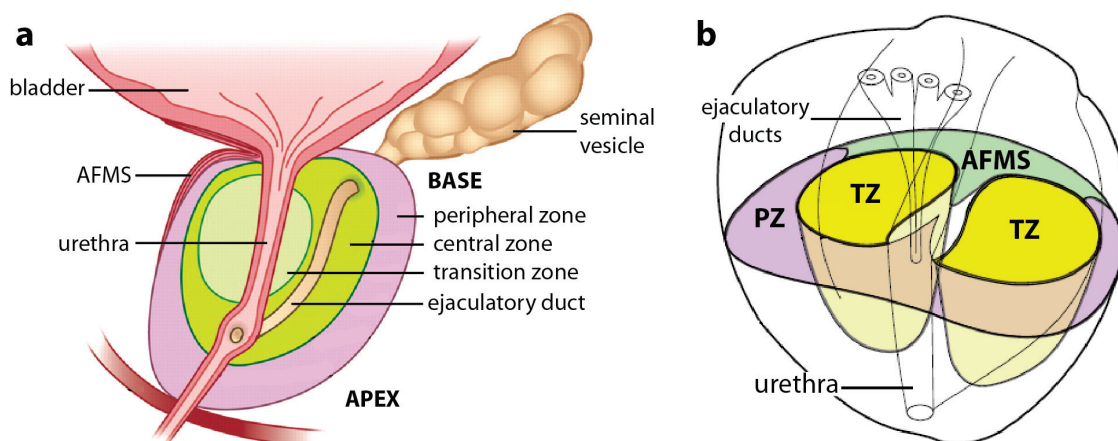


Figure 1.2: (a) *Sagittal view of the prostate gland, illustrating the anatomical features and zonal anatomy. Source: [Verma and Rajesh (2011)].* (b) *Axial image of the prostate illustrating McNeal's zonal anatomy, consisting of the peripheral zone (PZ), transition zone (TZ) and non-glandular anterior fibromuscular stroma (AFMS). Source: [Makni (2010)].*

### 1.2.3 Function

The function of the prostate is to secrete prostatic fluid, that is added to the ejaculatory fluid produced by the seminal vesicles. The prostatic fluid usually constitutes 15 - 30% of the ejaculate volume [Owen and Katz (2005)]. During ejaculation, the sperm produced in the testes is transferred from the vas deferens into the urethra, collecting the secretions from the seminal vesicles and prostate gland, forming the semen. The prostate gland and the surrounding muscles contract and expel the semen out of the body through the urethra. Spermatozoa expelled in prostatic fluid have better motility, longer survival and better protection of the genetic material [Björndahl (2010)].

## 1.3 Prostate Cancer Epidemiology

In this section we consider the epidemiology of PCa. We detail the latest estimates of the incidence and mortality of PCa among men both in Europe and worldwide and we compare these values to those of other prevalent cancers. We detail the identified risk factors associated with PCa, in particular age, but also family history and ethnicity.

### 1.3.1 Incidence and Mortality

#### Europe

PCa is the most frequently diagnosed cancer of men in Europe, estimated to account for 379,000 new cases, that is 20.9% of all new male cancer cases in Europe in 2008. Overall, in both sexes combined, PCa is the fourth most common cancer, accounting for 11.1% of all new cancer cases in 2008 [Ferlay *et al.* (2010)b].

With an estimated 94,000 deaths in 2008, PCa is the third leading cause of death from cancer in men (9.1% of the total). Overall, in both sexes combined, PCa is the sixth leading cause of death from cancer, accounting for 5.1% of all cancer deaths in 2008 [Ferlay *et al.* (2010)b].

The graph in Figure 1.3 shows the relative levels of incidence and mortality of PCa in Europe amongst men compared to the levels of other prevalent forms of cancers.

#### Worldwide

PCa is the second most frequently diagnosed cancer (after lung cancer) of men, estimated to account for 899,000 new cases, that is 13.6% of all new male cancer cases worldwide in 2008. Overall, in both sexes combined, PCa is the fifth most common cancer, accounting for 7.1% of all new cancer cases in 2008 [Ferlay *et al.* (2010)b].

With an estimated 258,000 deaths in 2008, PCa is the sixth leading cause of death from cancer in men (6.1% of the total). Overall, in both sexes combined, PCa is the ninth leading cause of death from cancer, accounting for 3.4% of all cancer deaths in 2008 [Ferlay *et al.* (2010)b].

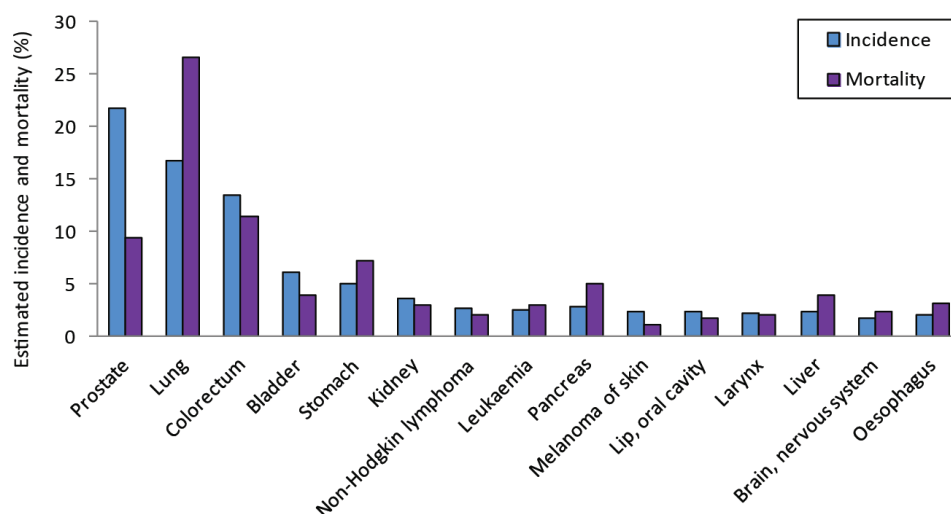


Figure 1.3: *Estimated incidence and mortality (%) of the most prevalent forms of cancer among men in Europe. PCa is the most frequently diagnosed cancer and is the third leading cause of death from cancer in men in Europe. Source: [Ferlay et al. (2010)b]*

### 1.3.2 Risk Factors

#### Age

The strongest known risk factor for PCa is age, with very low risk in men under 50 years old and rising risk with increasing age thereafter, i.e. the older the man, the higher the risk. This is consistent with post-mortem results where approximately 80% of men by age 90 years were shown to have cancer cells in their prostate [Haas et al. (2007)].

#### Family History

A family history of PCa is a strong risk factor. It has been estimated that 5 - 10% of all PCa cases and 30 - 40% of early-onset cases (men diagnosed < 55 years) are caused by inherited susceptibility genes [Johns and Houlston (2003)].

#### Ethnicity

Variation in incidence rates around the world and within countries, suggests that PCa risk is affected by ethnicity. Nearly three-quarters (71.6%, 644,000 cases) of the registered cases occur in developed countries (defined as Northern America, Eastern Asia, Europe, Australia and New Zealand [Ferlay et al. (2010)b]). Incidence rates of PCa vary by more than 25-fold worldwide. The highest rates are in Australia/New Zealand (104.2 per 100,000), Western (94.1 per 100,000) and Northern Europe (86.4 per 100,000) and Northern America (85.6 per 100,000). This is largely because the practice of prostate specific antigen (PSA) testing and subsequent biopsy has become widespread in those regions. The lowest rates are in South-Central Asia (4.1 per 100,000).

There is less variation in mortality rates worldwide (10-fold) than is observed for incidence (25-fold). The highest rates are in the Caribbean (26.3 per 100,000), Southern (19.3 per 100,000) and Western Africa (18.3 per 100,000). The lowest rates are in Eastern Asia (2.5 per 100,000). The number of deaths from PCa is almost the same in developed (136,000) and developing regions (121,000) [Ferlay *et al.* (2010)b]. This is due to the fact that PSA testing has a much greater effect on incidence than on mortality.

Mortality rates are generally high in predominantly black populations (e.g. the Caribbean, 26.3 per 100,000 and sub-Saharan Africa, 18 - 19 per 100,000), very low in Asia (e.g. Eastern Asia, 2.5 per 100,000) and intermediate in Europe (10.5 - 15.7 per 100,000) and Oceania (15.4 per 100,000).

### Other Risks

Other possible risks being investigated include diet, alcohol consumption, smoking, bodyweight, physical activity, medication, medical procedures, infections and diabetes.

## 1.4 Prostate Cancer Grading and Staging

A significant proportion of PCa tumours are small, clinically insignificant and present a low risk to the patient. However, there exist tumours that are extremely aggressive with lethal potential, that present a very high risk to the patient. PCa grading aims to classify the relative risk of tumours based on their histological appearance. Staging is used to categorise the amount and location of cancer and the risk of the cancer having spread beyond the prostate. A standardised system is used for both grading and staging.

### 1.4.1 Gleason Grading

The Gleason system is used to grade PCa in both radical prostatectomy specimens and needle biopsy samples. The tissue is examined and the cancerous cells are classified according to their histologic appearance into different Gleason patterns. The Gleason pattern ranges from 1 to 5, with 5 having the worst prognosis. For example, Gleason pattern 1 is attributed to cancerous tissue that closely resembles normal prostate tissue. The glands are small, well-formed, and closely packed. Gleason pattern 5 is attributed to tissue that does not have recognisable glands. The different histological aspects of the five Gleason patterns are shown in Figure 1.4.

PCa is heterogeneous, therefore Gleason chose to incorporate both a primary and a secondary grade into the system [Gleason (1981)]. The primary grade is the tumour pattern of the majority of the tumour, i.e. the most prevalent pattern in the cancer. The primary grade pattern must be greater than 50% of the total pattern seen. The secondary grade is the next most prevalent tumour pattern in the cancer. The secondary grade pattern must be between 5% and 50% of the total pattern seen. The Gleason score is obtained by adding these two grades.

So if in a specific case the primary tumour pattern is grade 3, and the secondary tumour pattern is grade 4, the Gleason Score is  $3 + 4 = 7$ .

The Gleason grade or pattern ranges from 1 to 5, consequently, the Gleason score ranges from 2 ( $1 + 1$ ) up to 10 ( $5 + 5$ ), with 10 having the worst prognosis. For Gleason Score 7, a Gleason  $4 + 3$  is a more aggressive cancer than a Gleason  $3 + 4$ . A cancer is considered aggressive if the Gleason score is greater than 7.

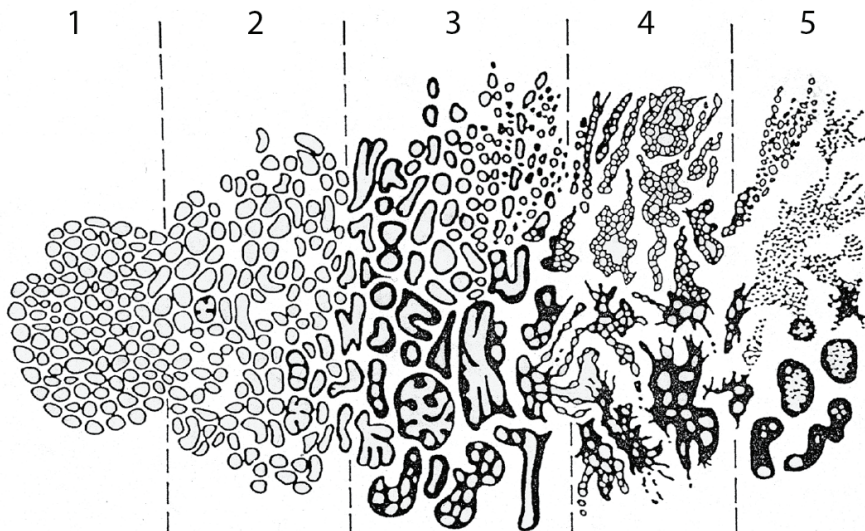


Figure 1.4: *The Gleason system is used to grade PCa by classifying the cancerous cells according to their histologic appearance into different Gleason patterns. The Gleason pattern ranges from 1 to 5, with 5 having the worst prognosis.*

### 1.4.2 Cancer Staging

PCa staging is used to categorise the amount and location of cancer and the risk of the cancer having spread beyond the prostate. The most widely used staging system is the TNM system [Edge *et al.* (2010)] maintained by the American Joint Committee on Cancer (AJCC) and the International Union for Cancer Control (UICC). The TNM staging system is based on the extent of the primary tumour (T), the extent of spread to the lymph nodes (L) and the presence of metastasis (M). The three different categories of the 7th Edition are detailed in Table 1.1. Once the T, N and M values have been determined, they are combined and an overall ‘Stage’ of I, II, III or IV is assigned to the cancer, see Table 1.2.

**Primary Tumour (T)**

TX	Primary tumour cannot be assessed
T0	No evidence of primary tumour
T1	Clinically inapparent tumour neither palpable nor visible by imaging
T1a	Tumour incidental histologic finding in 5% or less of tissue resected
T1b	Tumour incidental histologic finding in more than 5% of tissue resected
T1c	Tumour identified by needle biopsy (for example, because of elevated PSA)
T2	Tumour confined within prostate
T2a	Tumour involves one-half of one lobe or less
T2b	Tumour involves more than one-half of one lobe but not both lobes
T2c	Tumour involves both lobes
T3	Tumour extends through the prostate capsule
T3a	Extracapsular extension (unilateral or bilateral)
T3b	Tumour invades seminal vesicle(s)
T4	Tumour is fixed or invades adjacent structures other than seminal vesicles

**Regional Lymph Nodes (N)**

NX	Regional lymph nodes were not assessed
N0	No regional lymph node metastasis
N1	Metastasis in regional lymph node(s)

**Distant Metastasis (M)**

M0	No distant metastasis
M1	Distant metastasis
M1a	Nonregional lymph node(s)
M1b	Bone(s)
M1c	Other site(s) with or without bone disease

Table 1.1: *The TNM staging system is based on the extent of the primary tumour (T), the extent of spread to the lymph nodes (L) and the presence of metastasis (M).*

Stage	T	N	M	PSA	Gleason
I	T1a-c	N0	M0	PSA < 10	Gleason $\leq 6$
	T2a	N0	M0	PSA < 10	Gleason $\leq 6$
	T1-2a	N0	M0	PSA X	Gleason X
IIA	T1a-c	N0	M0	PSA < 20	Gleason 7
	T1a-c	N0	M0	$10 \leq \text{PSA} < 20$	Gleason $\leq 6$
	T2a	N0	M0	$10 \leq \text{PSA} < 20$	Gleason $\leq 6$
	T2a	N0	M0	PSA < 20	Gleason 7
	T2b	N0	M0	PSA < 20	Gleason $\leq 7$
	T2b	N0	M0	PSA X	Gleason X
IIB	T2c	N0	M0	Any PSA	Any Gleason
	T1-2	N0	M0	PSA $\geq 20$	Any Gleason
	T1-2	N0	M0	Any PSA	Gleason $\geq 8$
III	T3a-b	N0	M0	Any PSA	Any Gleason
IV	T4	N0	M0	Any PSA	Any Gleason
	Any T	N1	M0	Any PSA	Any Gleason
	Any T	Any N	M1	Any PSA	Any Gleason

Table 1.2: *The ‘Stage’ of I, II, III or IV is determined from the T, N and M categories.*

### 1.4.3 Zonal Influence on Cancer Grade and Stage

Peripheral zone tumours account for 75% - 85% of prostate cancers. However, it has been shown that up to 25% of prostate cancers originate in the transition zone [Akin *et al.* (2006)]. Peripheral zone tumours have a preponderance of moderate-grade and high-grade disease and are generally less well differentiated (median Gleason score of 6 - 7) than transition zone tumours (median Gleason score of 5). They are also more likely to extend through the capsule [Greene *et al.* (1991)]. Statistics appear to indicate that tumours that arise in the transition zone have a less malignant potential than those that arise in the peripheral zone [Greene *et al.* (1991)].

## 1.5 Prostate Cancer Screening

Whether asymptomatic men benefit from screening for PCa is an unresolved question. Proponents of screening view it as a means of detecting PCa in the early stages, when it is amenable to local interventions with curative intent. Screening advances the time of diagnosis (lead time) and detects cancers that would not have been diagnosed in the absence of screening (over-detection). Opponents of screening point out that some men will be treated unnecessarily, because they would not have been diagnosed with PCa without screening, and that over-diagnosis results in over-treatment, i.e. the cancer left untreated would not have caused mortality. The key question is whether screening affects the overall and PCa-specific mortality [Postma and Schröder (2005)].

Note that the definition of over-detection varies between different studies; it can be defined as cancer diagnosed that would not have caused symptoms during the patients lifetime [Bangma *et al.* (2007)], cancer diagnosed that would not have caused symptoms or death [Welch and Black (2010)] or the detection of disease that would not have been diagnosed in the patient's lifetime in the absence of screening [Draisma *et al.* (2009), Etzioni *et al.* (2002)]. The lead-time is defined as the time by which screening advances diagnosis.

For a screening program with a 4-year screening interval from the age of 55 to 67, the estimated mean lead time was 11.2 years and the over-detection rate was 48%, [Draisma *et al.* (2003)]. A review of six randomised controlled trials corroborated these results finding that screening was associated with a 46% relative increase in diagnoses of PCa among men being screened compared to men who underwent no screening [Djulbegovic *et al.* (2010)]. Furthermore, it was found that the increase was mainly due to an increase in the number of men diagnosed with stage I PCa. Screening had no significant impact on the diagnosis of stage II, III and IV PCa, suggesting that screening leads to an increase in diagnosis of early stage PCa [Djulbegovic *et al.* (2010)]. However, despite the increased number of diagnoses, PCa screening was found to have no significant impact on overall mortality or death from PCa. This confirms the concerns of over-diagnosis, i.e. the detection of non-fatal cancers.

In summary, screening for PCa aids in earlier diagnosis and helps to detect PCa at an

earlier stage. However, this early detection has not been shown to have a significant impact on mortality and comes at the price of additional testing and the risk of over-treatment with possible adverse effects.

Currently, PCa screening is carried out using the prostate specific antigen (PSA) test and the digital rectal examination (DRE). Patients with suspicious findings on PSA tests and/or DRE are further examined by a transrectal ultrasound-guided (TRUS) biopsy.

### 1.5.1 Prostate Specific Antigen (PSA) Test

Prostate-specific antigen (PSA) is a protein produced by the prostate gland. The PSA test measures the level of PSA in the blood. The level of PSA is often elevated in men with PCa. However, many false positive elevations in PSA (i.e. an elevated PSA level with no PCa) are attributable to benign prostatic hyperplasia (BPH), acute urinary retention and acute prostatitis (inflammation of the prostate gland). A biopsy of the prostate or transurethral prostatectomy can also raise PSA levels. Therefore, although PSA is prostate-specific, it is not a cancer-specific measure.

The sensitivity and specificity of the PSA test and the threshold at which a result should prompt a biopsy are unclear. Traditionally, a PSA value of 4.0 ng/mL has been used as the upper limit of the normal level [Barry (2001)], however this is complicated by the fact that PSA levels tend to increase with age.

Two large randomised clinical trials for PCa have recently published their results, in Europe (The European Randomized Study of Screening for Prostate Cancer, ERSPC trial) and in the USA (The Prostate, Lung, Colorectal and Ovary cancer, PLCO trial).

The ERSPC trial evaluated the effect of PSA testing on PCa mortality. After a median follow-up of 11 years of 162,388 men (55 to 69 years of age), it was estimated that the PCa mortality rate was reduced by 21% in the group that underwent PSA-based screening compared to the control group (absolute reduction in PCa mortality of 1.07 deaths per 1000 men). Therefore concluding that PSA-based screening significantly reduced PCa mortality. However, despite this reduction it was found that screening had no effect on all-cause mortality. The conclusion was that more information on the balance of benefits and adverse effects, as well as the cost-effectiveness of PCa screening is needed before general recommendations can be made [Schröder *et al.* (2012)].

Conversely, the PLCO trial, carried out to evaluate the effect of screening with PSA testing and digital rectal examination on the rate of death from PCa, concluded that screening was associated with no reduction in PCa mortality after 10 trial years, even though at 7 years, screening was associated with a relative increase of 22% in the rate of PCa diagnosis, compared with the control group. The study was carried out on 76,693 men, half of whom received annual screening and the other half, the control group, usual care. Screening included PSA testing for 6 years and DRE for 4 years [Andriole *et al.* (2009)]. They thus advise against screening all men over the age of 75 years.

## 1.5.2 Digital Rectal Examination (DRE)

The digital rectal examination (DRE) involves inserting a gloved and lubricated finger into the rectum to feel the prostate, see Figure 1.5. A suspicious outcome is defined by the presence of significant induration, nodularity, or asymmetry. Note that only tumours in the PZ can be detected.

The diagnostic value of DRE for PCa, estimated by averaging the results of 18 studies, indicate that the DRE appears to be a test of high specificity (0.85) and negative predictive value (0.88), low sensitivity (0.46) and low positive predictive value (0.39) [Tessler *et al.* (2012)].

However the use of DRE as a screening tool is controversial due to its subjective nature with high inter-observer variability. Nevertheless, DRE independently and significantly affects the prediction of PCa risk. An abnormal DRE is a risk factor for high-grade disease.

Furthermore, DRE does detect some prostate cancers that are missed by PSA screening. In one screening study the PSA test detected 45% more cases of cancer than DRE alone, whereas DRE detected 18% more cases of cancer than the PSA test alone; that is, each test detects cancers missed by the other [Richie *et al.* (1993)]. The area under the curve (AUC) of PSA alone to predict PCa at initial screening was estimated to be 0.69. In comparison, the AUC of PSA and DRE was estimated to be 0.73 [Roobol *et al.* (2012)].

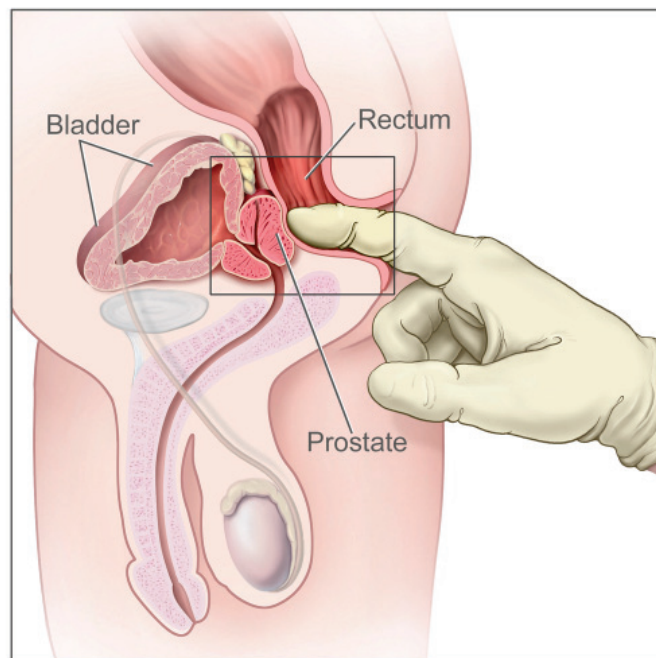


Figure 1.5: *The DRE involves inserting a gloved and lubricated finger into the rectum to feel the prostate. A suspicious outcome is defined by the presence of significant induration, nodularity, or asymmetry. Only tumours in the PZ can be detected. Source: National Cancer Institute.*

### 1.5.3 Biopsy

The standard evaluation for men with suspicious findings on PSA tests and/or DRE is a transrectal ultrasound-guided (TRUS) biopsy [Hara *et al.* (2008)].

The number of biopsies required for the optimal detection of PCa is controversial. The traditional strategy has been to obtain a set of six biopsy specimens in a sextant pattern. However, nearly all studies have shown a higher cancer detection rate with a greater number of biopsies in comparison with the standard sextant technique, a 12-sample procedure improves the cancer detection rate by 22% compared with a 6-sample procedure [Guichard *et al.* (2007)]. Other studies have shown that more than 12 cores are not significantly more conclusive [Eichler *et al.* (2006)].

Prostate saturation biopsy was initially introduced by [Borboroglu *et al.* (2000)], and consisted of at least 20 biopsy cores. Transrectal ultrasound-guided saturation biopsies have a cancer detection rate of 14 - 34% [Merrick *et al.* (2007)]. Transperineal template-guided prostate mapping biopsies (TTMB) are an alternative form of saturation biopsy. As TTMB are conducted under general or regional anesthesia, a large number of cores are typically obtained, enabling access to the entire prostate gland. Using TTMB, [Taira *et al.* (2009)] report a cancer detection rate of 75.9% on initial biopsy, significantly higher than the 40-45% yield expected from standard TRUS biopsy. [Taira *et al.* (2009)] suggest that the improvement is due to the improved sampling in the anterior and apical aspects of the gland, areas that are not consistently sampled through a transrectal approach. The short-comings of the TTMB technique include the need for anesthesia, added cost and the potential for the diagnosis of biologically inconsequential cancer.

The 12-core transrectal prostate biopsy scheme is now the standard. The number of biopsies can be adapted to the prostate volume, for example [Naughton *et al.* (1998)] found that prostates of TRUS volume  $\leq 30$  cc required an average of 8 biopsy cores in order to detect the cancer, compared with an average of 11 biopsy cores required for prostates of TRUS volume  $> 30$  cc.

The prostate is the only organ that is diagnosed by random sampling, meaning that entire tumours can be missed. Therefore a negative biopsy result does not ensure the absence of PCa. If the biopsy results are positive, the volume of the tumour cannot be assessed with certainty. Due to the heterogeneity of Pca, there is significant uncertainty associated with the Gleason score evaluated from a biopsy sample. There is therefore a significant risk of over- and under-estimation of the aggressiveness of the PCa evaluated using biopsies.

The diagnostic accuracy of TRUS biopsy is unknown as men with a negative biopsy result do not undergo radical prostatectomy and there is therefore no confirmation of the biopsy findings. In an attempt to overcome this limitation, a study was carried out in which 18-core needle biopsies were performed on autopsy prostates from 164 men who had no history of PCa. Cancer was detected in 25 of the 47 cancerous prostates (53%), representing 34 of the 87 identified tumour foci (39%) [Haas *et al.* (2007)]. As a negative

biopsy does not ensure the absence of PCa, if the first set of biopsies is negative, repeated biopsies can be recommended, especially in the case of a rising and/or persistent PSA level or a suspicious DRE. In the second set of biopsies, a detection rate of about 10 - 35% has been reported in cases with a negative initial set of biopsies [Heidenreich *et al.* (2008)].

Technical improvements in prostate magnetic resonance imaging (MRI) have resulted in the use of MRI to target prostate biopsies. The benefits of an image-guided approach to prostate biopsy are that fewer men are biopsied overall; men deemed to have a normal MRI are not biopsied. The efficiency of the biopsies are therefore improved, i.e. the number of clinically significant prostate cancers detected per number of men biopsied. [Moore *et al.* (2013)] estimated the efficiency of targeted biopsy sampling to be 70%, compared to the standard TRUS approach at 40%. Furthermore, targeted biopsies reduced the diagnosis of clinically insignificant cancer [Moore *et al.* (2013)].

## 1.6 Prostate Cancer Treatment

Various different modalities of treatment for PCa exist. Factors influencing the choice of treatment involve the grade and stage of the cancer, as well as the age and general health of the patient. The effectiveness of different treatments are often analysed with respect to the associated *overall survival rate* and *PCa-specific survival rate*. In order to clarify the nuance, the overall survival rate is defined as the percentage of people in a study who are still alive for a certain period of time after they were diagnosed with or started treatment for a disease. The PCa-specific survival rate is defined as the percentage of people in a study who have not died from PCa in a defined period of time, i.e. patients who died from causes other than PCa are not counted in the measurement.

### 1.6.1 Active Surveillance

Active surveillance (AS) concerns patients with very low-risk PCa. These patients are initially not treated but are followed and treated with a curative intent if progression or the threat of progression occurs during follow-up.

AS aims to reduce the ratio of over-treatment in patients with clinically confined low-risk PCa. It has been estimated that men with well-differentiated PCa have a 20-year PCa-specific survival rate of 80 - 90% [Heidenreich *et al.* (2011)].

Inclusion criteria for AS vary among studies but include [Dall'Era *et al.* (2012), Heidenreich *et al.* (2011)]

- gland confined PCa (T1 - T2),
- Gleason score  $\leq 6$ ,
- three or fewer biopsies involved with cancer,
- $\leq 50\%$  of each biopsy involved with cancer,
- PSA  $< 10$  ng/mL.

Estimating the percentage of men eligible for surveillance is sensitive to the criteria used. Stringent criteria will limit the number of eligible men and likely exclude some potential candidates. The eligibility has been estimated to be between 4 - 82% [Dall'Era *et al.* (2012)].

Misclassification of insignificant disease based on entry criteria, that is patients included for AS who were found to have high grade cancer, range from 16 - 36% [Iremashvili *et al.* (2012)].

Estimating the number of men on AS who will progress to treatment is highly sensitive to the criteria used to define cancer progression and the criteria used to select AS candidates. Progression is generally defined as changes in PSA over time (PSA >10 ng/mL), the detection of higher-volume or higher-grade cancer on surveillance biopsy (Gleason score progression to  $\geq 7$ ), or concerning changes on physical exam of the prostate. As men are reclassified beyond the initial inclusion criteria of their institution, treatment is often recommended. Approximately 25% (11 - 33%) of patients receive further treatment after a median of about 2.5 years of surveillance (minimum 1.8, maximum 6.8) [Dall'Era *et al.* (2012)]. PCa-specific mortality remains low (0 - 1%) [Dall'Era *et al.* (2012)], however only data from non-mature randomised clinical trials of AS with follow-up <10 years are currently available.

### 1.6.2 Radical Prostatectomy

Prostatectomy is the surgical removal of all (radical prostatectomy, RP) or part of the prostate gland and is commonly used to treat localised PCa. The goals of RP are to remove the cancer completely, minimise complications during the operation and optimise recovery of potency and urinary continence. No surgeon uniformly achieves these results. RP is a complex operation and outcomes are highly sensitive to technique.

A positive surgical margin (PSM) is defined as prostate cancer cells touching the inked surface of the excised prostate gland. A PSM after radical prostatectomy is associated with an increased risk of recurrence and the need for secondary cancer treatment. Positive margins have been reported in 11 - 38% of patients undergoing RP [Yossepowitch *et al.* (2009)]. The success of surgery and the incidence of PSM vary greatly among surgeons, in a particular study of 26 surgeons, the rate of positive surgical margins was 10 - 48% [Eastham *et al.* (2003)].

Compared to AS, RP reduces disease-specific mortality (5.3%), overall mortality (5.0%), and the risks of metastasis (10.2%) and local progression (25.1%), calculated after 10 years [Bill-Axelsson *et al.* (2005)]. The absolute reduction in the risk of death after 10 years is small, but the reductions in the risks of metastasis and local tumour progression are substantial.

Numerous studies have assessed urinary and sexual function one or more years after RP, with rates of incontinence ranging from 4 - 40% and impotence from 29 - 75% [Stanford *et al.* (2000)].

### 1.6.3 Radiotherapy

Radiotherapy uses ionizing radiation to control or kill malignant cells. When absorbed in tissue, ionizing radiation damages the DNA in cells, which increases the probability of cell death. Normal cells are able to repair radiation damage, while cancer cells are not. It can be used to treat all stages of PCa. Two different kinds of radiation therapy are used in PCa treatment: external beam radiation therapy and brachytherapy. The side effects of radiation therapy include diarrhea, mild rectal bleeding, as well as potential urinary incontinence and impotence.

#### External Beam Radiation Therapy (EBRT)

External beam radiation therapy (EBRT) uses a linear accelerator to produce high-energy x-rays that are directed in a beam towards the prostate. CT image data enables the tumour to be localised and therefore the target and non-target tissue structures to be defined. Radiation therapy treatment plans are then generated to control the location and dose of the radiation. External beam radiation therapy is generally given over several weeks, with daily visits to a radiation therapy centre.

Studies have estimated the overall survival and PCa-specific survival outcomes to be similar between RP and EBRT [Kupelian *et al.* (2002)]. The 5-year estimates of overall survival and PCa-specific survival are 85.0% and 95.1% respectively [Shipley *et al.* (1999)]. Patients treated with EBRT have significantly better urinary function, with a lower risk of incontinence than those treated with RP. The difference in sexual function in patients who underwent RP and in those who underwent EBRT is not statistically significant [Frank *et al.* (2007)].

#### Brachytherapy

Brachytherapy is a proven treatment for early, localised PCa. It involves the placement of about 100 small ‘seeds’ containing radioactive material (such as iodine-125 or palladium-103) directly into the tumour. The seeds emit low-energy X-rays, capable of travelling only a short distance. Although the seeds eventually become inert, they remain in the prostate permanently.

Brachytherapy offers several advantages over EBRT in selected patients. Firstly, due to the physics of radiation emanation from the implanted radioisotope, there is dose escalation within the prostate, with rapid dose fall in surrounding normal tissues. Target motion, set-up variation and localisation errors are not of major concern as they are with EBRT.

Brachytherapy is a simple, out-patient procedure that avoids hospitalisation and allows the patient an early recovery. The 10-year estimates of overall survival and PCa-specific survival are 74% and 96% respectively [Stock *et al.* (2006)]. There is no significant difference in urinary function between patients treated with brachytherapy and those treated with RP or EBRT, however there is a significantly lower risk of incontinence than those

treated with RP. Patients treated with brachytherapy had significantly better sexual function than patients treated with EBRT or RP [Frank *et al.* (2007)].

#### 1.6.4 Hormonal Therapy

Both normal and cancerous cells in the prostate gland, as well as cancerous cells that have migrated to other sites in the body, are dependent on androgens to stimulate growth, function and proliferation. Hormonal therapy (HT), also known as androgen deprivation therapy (ADT), inhibits the cancerous cells by reducing the levels of male hormones in the body. Androgen deprivation can be achieved either by suppressing the secretion of testicular androgens by means of surgical or medical castration, or by inhibiting the action of the androgens by using competing compounds known as anti-androgens. Common side effects of hormone therapy include loss of libido and impotence.

HT prior to RP has been investigated in several trials, one study showed that patients who received three months of HT before RP had a significantly lower PSM rate at the time of surgery than those who had no HT before RP. However, there was no difference between the two groups in the biochemical recurrence rate (defined as PSA greater than 0.4 ng/mL) at five years [Soloway *et al.* (2002)]. Another study evaluated HT after RP and reported a 10% clinical recurrence rate at four years in the HT-treated patients compared with a rate of 31% for those receiving placebo [Hellerstedt and Pienta (2008)].

The therapy outcome depends on the stage and grade of disease at diagnosis. In patients with advanced PCa, remission occurs in 80 - 90% of men with a median progression-free survival of 12 to 33 months. At that time, an androgen-independent phenotype usually emerges, leading to a median overall survival of 23 to 37 months from the time of initiation of HT [Hellerstedt and Pienta (2008)]. Only 7% of patients are reported to live 10 years or more [Aus *et al.* (2005)].

In conclusion, HT delays progression in advanced PCa cases and effectively palliates symptoms. Furthermore, it has been reported to shrink the prostate volume by up to 30% [Asha *et al.* (2005)], and is therefore often used to shrink tumours before radiotherapy. Unfortunately the response to hormonal treatment lasts for a median duration of 18 - 24 months. Most men eventually become resistant to therapy and develop hormone refractory prostate cancer (HRPC) [Calabrò and Sternberg (2007)].

#### 1.6.5 Chemotherapy

Chemotherapy remains the only treatment option for HRPC, providing modest survival and palliative benefits. The most commonly used chemotherapy drug to treat PCa is docetaxel, but only half of all patients will respond to docetaxel. Mitoxantrone is less toxic but delivers only palliative benefits. Inevitably, resistance to chemotherapy will develop and the disease then becomes difficult to control.

TAX327, a large randomized study, compared docetaxel-based chemotherapy to mitoxantrone-based therapy. The data demonstrated that treatment with docetaxel can prolong life in

a statistically significant way in patients with HRPC, the median overall survival rates for patients treated with docetaxel was 18.9 months, compared with 16.5 months for the patients treated with mitoxantrone-based therapy [Tannock *et al.* (2004)].

The optimal timing of docetaxel-based chemotherapy is still unknown because there are no prospective clinical trials indicating whether earlier treatment is more effective than delayed treatment.

### 1.6.6 Alternative Local Treatment Options

Focal therapy is an emerging alternative treatment option; the aim is to treat only localised tumours, sparing the rest of the prostate, especially near the neurovascular bundles and the urethral sphincter. Two significant difficulties exist; the first is the precise localisation, visualisation, and characterisation of the cancer foci to be treated. The second difficulty concerns the accurate guidance of the ablative energy to the area to be targeted [Bozzini *et al.* (2012)].

Several of the most commonly used focal therapy techniques are presented below: cryotherapy, high intensity focused ultrasound (HIFU), focal photodynamic therapy (PDT) and focal laser ablation (FLA). Other focal therapy modalities include: interstitial microwave thermal therapy, radiofrequency interstitial tumour ablation (RITA), electroporation and nanoparticle thermotherapy.

#### Cryotherapy

Cryotherapy is an alternative treatment for locally confined and locally advanced PCa. It involves exposing the prostate gland to freezing temperatures by inserting 6 - 8 metal rods transperineally into the prostate under TRUS guidance. Highly purified argon gas is used to cool the rods, freezing the surrounding tissue at  $-40\text{ }^{\circ}\text{C}$ . As the water within the prostate cells freezes, the cells die. The urethra is protected from freezing by a catheter filled with warm liquid.

The procedure is less invasive than RP with a lower risk of incontinence, of patients who are continent before surgery, on average 84.1% regain continence after surgery with an average recovery time of 6.1 months [Bahn *et al.* (2002)]. However, on average, of patients who are potent before surgery, 94.9% are impotent after surgery, though 5.1% recovered their potency with an average recovery time of 16.4 months [Bahn *et al.* (2002)].

The definition given by the American Society for Therapeutic Radiology and Oncology (ASTRO) for biochemical failure is three successive increases of PSA level. Using this definition, the biochemical disease-free survival probabilities after 7 years for cryotherapy (90%) has been shown to surpass the result for EBRT (48 - 69%) and brachytherapy (89%) [Bahn *et al.* (2002)].

### High Intensity Focused Ultrasound (HIFU)

High intensity focused ultrasound (HIFU) is a minimally invasive, non-surgical treatment for localised PCa. HIFU consists of focusing ultrasound waves emitted from a transducer inducing tissue damage by mechanical and thermal effects as well as by cavitation. The goal of HIFU is to heat malignant tissues above 65°C to destroy these tissues by coagulative necrosis. The HIFU treatment is performed under real-time monitoring with ultrasound (US) or magnetic resonance imaging (MRI), enabling the temperature and ablated area to be followed. An advantage of HIFU versus radiotherapy is that it can be repeated if there is a proven local recurrence.

Post-HIFU, approximately 85% of control biopsies were negative at a mean of 3.5 - 6.4 years. The overall survival rate at 5 and 8 years has been estimated at 90% and 83 - 89% respectively, and the PCa-specific survival rate at 5 and 8 years has been estimated at 100% and 98 - 99% respectively. In addition, 62 - 83% of the patients were biochemically disease free at 7 years [Blana *et al.* (2008), Crouzet *et al.* (2010)].

Common side-effects (with complications rates) after HIFU include infravesical obstruction (19.7%), stress incontinence (7.6%) and impotence (49 - 70%) [Blana *et al.* (2006), Aus *et al.* (2005)].

### Focal Photodynamic Therapy (PDT)

Photodynamic Therapy (PDT) is based on the interaction between light supplied by a laser fibre, a photosensitive agent (PS) and the oxygen present in tissue. The photosensitive agent (PS) is administrated topically, orally or intravenously. In its basic state, the PS is pharmacologically inactive and stable. When light is delivered at an appropriate wavelength (specific to each PS), the drug goes into an excited phase, causing a chain reaction inducing the release of singlet oxygen and antioxidant enzymes. The singlet oxygen can directly kill tumour cells by the induction of necrosis and/or apoptosis [Bozzini *et al.* (2012)].

PDT requires the placement of intraprostatic laser fibres, achieved through a transperineal approach using a brachytherapy template under TRUS-guidance. Transperineal needle insertion makes access to anterior tumours difficult. Advantages of PDT include limited morbidity and in the case of primary failure, the possibility of repeated treatment or secondary radical treatment. However, as PDT alters the prostate morphology, follow-up may be more challenging than usual. Limited clinical experience of PDT currently exists [Bozzini *et al.* (2012)].

### Focal Laser Ablation (FLA)

Focal laser ablation (FLA) involves delivering energy to the prostate using laser fibres. The thermal effects produced by the laser energy spread from the absorption zone and cause an increase in the temperature of surrounding tissues. Penetration of the laser

beam varies according to optical and thermal properties of the target tissues. As the laser fibres are MR-compatible, the treatment can be monitored using MR-thermometry, or alternatively using fluoroptic thermometry [Bozzini *et al.* (2012)].

As for PDT, the laser fibres are inserted using a transperineal approach through needles, meaning that access to anterior tumours is difficult. FLA is one of the most recent focal therapy techniques developed and limited data is available regarding oncologic and functional outcome or reliable treatment planning [Bozzini *et al.* (2012)].

## 1.7 Prostate Cancer Imaging

Today, cancers are detected at smaller, lower stages and lower grades than ever before. The challenge is to distinguish between the significant portion of tumours that are small and clinically insignificant and those that are extremely aggressive and lethal. The risk is between overdiagnosis and over-treatment versus the under-detection of cancers with lethal biologic potential.

If imaging could provide an accurate localisation and staging of PCa, low- and high-risk cancers could be distinguished. This would enable PCa cases to be classified into risk groups (low, intermediate, or high), directing therapy more accurately thus improving patient outcome and prognosis, without the cost of over-treatment.

Accurate localisation and staging of the cancer and its margins would enable therapy to be targeted to the cancer, sparing unaffected neurovascular bundles and limiting side effects such as incontinence or impotence. For example, radiation therapy usually treats the whole prostate gland, accurate localisation and staging enable the adjustment of the dose to focus on the tumour and minimise exposure to periprostatic tissues, thus reducing side effects.

Accurate localisation of PCa will pave the way for innovative, minimally invasive therapies and it may be possible to reduce the number of men undergoing biopsy or to improve the diagnostic yield of prostate biopsies by including an imaging method in the diagnostic workup.

Furthermore, an accurate imaging technique would enable the effects of therapy to be better evaluated, allowing earlier cessation of ineffective therapies, shorter duration of phase 2 trials to evaluate new drugs and accelerated approval in phase 3 trials.

The ideal imaging technique should be affordable and minimally invasive, with little inter-observer variability in interpretation. In addition, the test should be able to predict tumour stage, volume, and location with high specificity and sensitivity. To date, no such ideal imaging method exists and no consensus exists regarding the use of imaging techniques for evaluating primary prostate cancers. Many imaging modalities currently available show considerable clinical value, each with its own advantages, disadvantages, and specific indications.

### 1.7.1 Positron-Emission Tomography (PET)

Positron-emission tomography (PET) is a noninvasive imaging technique that computes the three-dimensional distribution of radioactivity based on the detection of photons resulting from annihilation of positrons that are emitted by positron emitter-labelled radiotracers.

The fundamental difference between PET and the various other imaging techniques is that PET assesses functional or metabolic characteristics of the tumour, whereas the other techniques predominantly assess the tumour's anatomical or morphologic features (e.g. density, size, shape).

Currently, the most commonly used PET radiotracer in oncologic clinical studies is  $^{18}\text{F}$ -fluorodeoxyglucose (FDG). However  $^{18}\text{F}$ -FDG has low sensitivity for the detection of cancer in the prostate gland and is not very effective for the diagnosis or assessment of local organ-confined cancer or extracapsular extension [Bouchelouche *et al.* (2010)]. Furthermore, similarities in the  $^{18}\text{F}$ -FDG uptake in prostate tumours and benign prostatic hyperplasia have been demonstrated [Turkbey *et al.* (2009)]. Molecular PET tracers with higher sensitivity and specificity are being investigated as alternatives to  $^{18}\text{F}$ -FDG, in particular  $^{11}\text{C}$ -acetate,  $^{11}\text{C}$ -choline, and  $^{18}\text{F}$ -fluorocholine have shown promising results [Bouchelouche and Oehr (2008)].

### 1.7.2 Computed Tomography (CT)

In contrast to PET, computed tomography (CT) uses an external X-ray beam to generate tomographic images. CT allows the visualisation of morphological and anatomic structures with a high anatomical resolution.

CT is not used in the detection or local staging of PCa as the resolution is insufficient to accurately evaluate the margins of the prostate and the presence of focal intraprostatic lesions [Nicolau *et al.* (2010)]. The major role of CT is in the nodal staging of PCa, for which it is limited.

### 1.7.3 PET/CT

Integrated PET/CT combines PET and CT in a single imaging device and allows morphological and functional imaging to be carried out in a single imaging procedure. Anatomical and morphological information derived from CT can be used to increase the precision of localisation, assessment of extent, and characterisation of lesions detected by PET. Figure 1.6 shows PET/CT images of two different patients in which a tumour is visible, the tumour existence and location is confirmed using MR images.

PET/CT has a potential value in the detection of bone metastases from PCa, the sensitivity, specificity, and accuracy were 81%, 93%, and 86% for  $^{18}\text{F}$ -fluoride and 74%, 99%, and 85% for  $^{18}\text{F}$ -choline, respectively [Beheshti *et al.* (2008)].

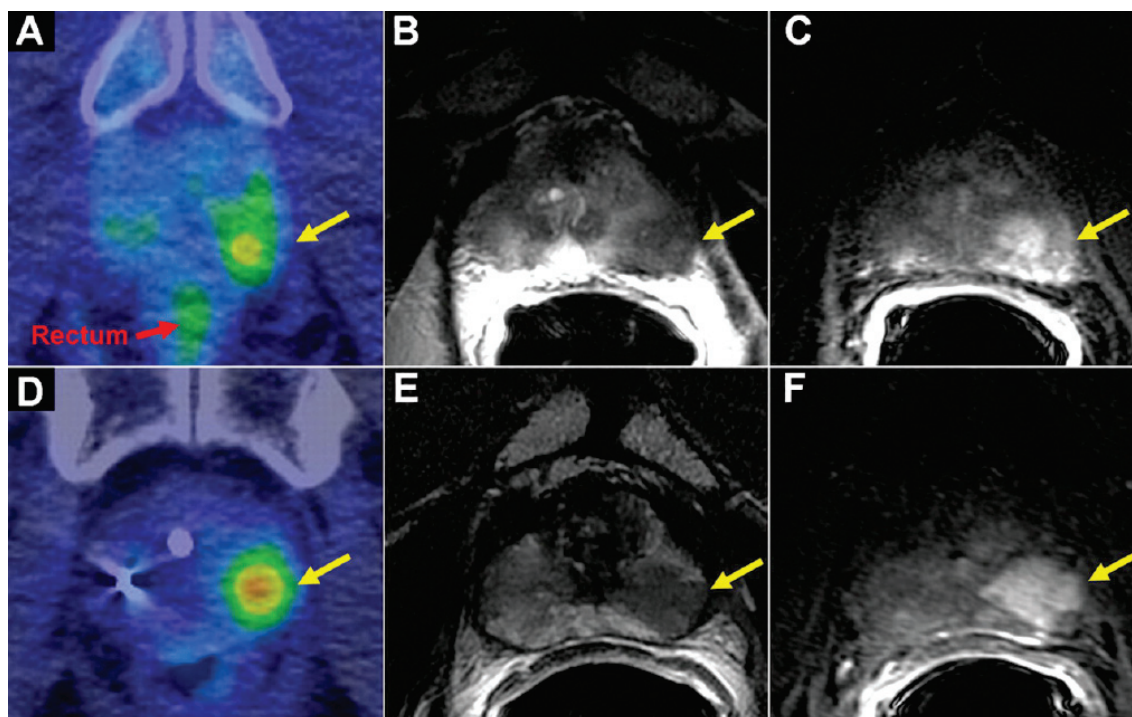


Figure 1.6: (A-C) 73 year old man with biopsy-proven PCa, Gleason 4 + 5. (A)  $^{11}\text{C}$ -choline PET/CT image, the focal radiotracer uptake (yellow arrow) indicates the tumour, the low-level nonfocal activity in the rest of the gland indicates normal prostate tissue, BPH, or prostatic inflammation. Normal activity is noted in the rectum (red arrow). (B)  $T_2$ -W and (C)  $T_1$ -W MR images confirm the tumour. (D-F) 78 year old man with biopsy-proven recurrent PCa, Gleason 4 + 4. The tumour is visible in the (D) PET/CT image, (E)  $T_2$ -W and (F)  $T_1$ -W MR image. Source: [Murphy et al. (2011)]

#### 1.7.4 Ultrasonography

The classic gray scale ultrasound (US) description for PCa is a hypoechoic lesion, however, PCa may also appear echogenic or isoechoic [Halpern (2006)]. Furthermore, prostatitis and benign prostatic hyperplasia mimic the gray scale appearance of PCa [Halpern (2006)]. Given the diverse appearance of PCa and the potential for benign processes to mimic the gray scale appearance of PCa, conventional prostate US has little advantage over DRE for detecting malignant areas [Aarnink et al. (1998)]. Various developments to conventional prostate US are presented below, a visual comparison is presented in Figure 1.7.

##### Transrectal Ultrasound (TRUS)

Transrectal ultrasound (TRUS) provides real-time imaging of the prostate gland at a relatively low cost and is thus a standard imaging tool in PCa. However it has limited accuracy in identifying and localising PCa. A study aimed at estimating the accuracy of TRUS found that only 18% of sonographically suspicious quadrants were cancerous while 65% of quadrants containing cancer were not sonographically suspicious [Flanigan

*et al.* (1994)]. TRUS is thus generally considered to be insufficient for the local staging of the tumour and for the identification of local recurrences. It is primarily used for biopsy guidance and to estimate the volume of the prostate.

### Colour Doppler Ultrasound

Ultrasound Doppler techniques demonstrate the presence of blood flow by detecting a frequency/phase shift in the ultrasound radiofrequency signal reflected from moving blood. Since PCa is associated with increased perfusion, the sensitivity of US PCa detection can be increased with colour Doppler imaging of blood flow within the prostate. The results of one particular study showed that colour Doppler US depicted 15.8% more of the cancers present than gray-scale US [Kuligowska *et al.* (2001)]. However, the study concluded that gray-scale TRUS, even coupled with colour Doppler US, remains inadequate for PCa screening [Kuligowska *et al.* (2001)].

### Contrast-Enhanced Ultrasound

PCa tissue is associated with increased microvessel density. Microvessels in malignant tissue are smaller than those of benign prostate tissue [Halpern (2006)]. However the microvessels in PCa are below the resolution of conventional Doppler imaging. Microbubble contrast agents have enhanced acoustic reflectivity, enabling the microvessels to be visualised by the intense reflected signal from microbubbles within the vessels. It has been demonstrated that the use of microbubble contrast agents can significantly improve the Doppler detection of PCa; the sensitivity of contrast-enhanced colour Doppler was measured to be 93% compared to that of un-enhanced colour Doppler at 54% [Roy *et al.* (2003)].

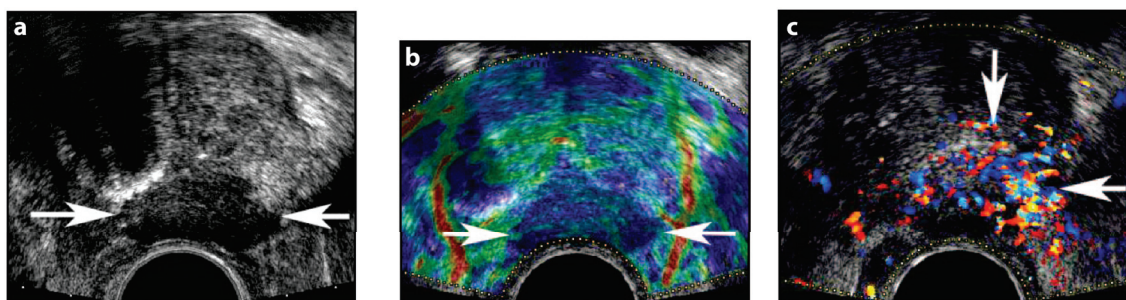


Figure 1.7: An 80 year old man with biopsy cores demonstrating Gleason 9 and Gleason 10 cancer. (a) Conventional gray scale image shows a hypoechoic (the classic description for PCa) mass extending from the prostate (arrows). (b) Real-time elastography shows reduced tissue elasticity (darker blue color) in the region of the mass (arrows). (c) Colour Doppler shows increased flow within and around the mass (arrows). Source: [Halpern (2006)]

## Elastography

Elastography is an alternative ultrasound-based imaging technique that evaluates the elasticity of the tissue. PCa is characterised by a partly limited elasticity or compressibility. In a study including 107 patients, transrectal real-time elastography had a sensitivity evaluated as 68% compared to TRUS whose sensitivity was evaluated as 50% [Kamoi *et al.* (2008)].

### 1.7.5 Magnetic Resonance Imaging (MRI)

Magnetic resonance imaging (MRI) provides the best 3D anatomic imaging of the prostate among all of the imaging modalities because of its high spatial resolution, multiplanar capabilities, and excellent soft tissue contrast, making it an attractive imaging modality for the prostate gland. The majority of the experience with prostate MRI was obtained at 1.5 Tesla (T) with the combined use of a phased array surface coil and an endorectal coil. Higher field strength magnets (e.g. 3 T), with the same combination of coils or with only the phased array surface coil, improve the signal-to-noise ratio (SNR), resulting in higher resolution images with better spatial and spectral differentiation. Various MRI sequences are presented below, a visual comparison is presented in Figure 1.8.

#### $T_1$ -Weighted Imaging ( $T_1$ -W)

On  $T_1$ -weighted ( $T_1$ -W) MRI, the prostate gland usually demonstrates diffuse intermediate signal intensity, hence zonal anatomy and tumours cannot be delineated.  $T_1$ -W MRI is mainly used to detect the presence of biopsy-related residual hemorrhage, which appears as a hyperintense focus relative to normal prostate peripheral zone.

#### $T_2$ -Weighted Imaging ( $T_2$ -W)

$T_2$ -weighted ( $T_2$ -W) MRI is an essential sequence as it provides an excellent display of the zonal anatomy of the prostate. Normally, the peripheral zone (PZ) is high in signal on  $T_2$ -W images, whereas the transition zone (TZ) is generally lower in signal with considerable heterogeneity. The surgical capsule appears as a distinct hypointense rim surrounding the PZ.

PZ cancers are usually rounded or ill-defined, low signal intensity foci surrounded by the high signal of the normal PZ. However, this pattern can be mimicked by various conditions such as prostatitis, benign prostatic hyperplasia, post-biopsy hemorrhage, biopsy-related scars and the effects of radiation treatment.

$T_2$ -W MRI is not sensitive in detecting cancer in regions other than the peripheral zone of the prostate. In the TZ, the signal characteristics of cancerous tissue overlap with those of normal TZ tissue.

$T_2$ -W alone does not achieve adequate sensitivity and specificity for PCa. Sensitivity values have been reported in the range of 27 - 100% and specificity in the range of 32 -

99%. The wide range of sensitivities and specificities is due to the significant variability of the patient populations, as well as differences in the gold standard (biopsy versus surgery) and the level of diagnostic and technical expertise in different studies [Bouchelouche *et al.* (2010)].

Functional MRI imaging techniques, such as MR spectroscopy, diffusion-weighted MRI and dynamic contrast-enhanced MRI, have been investigated for their potential to complement  $T_2$ -W MRI in improving PCa localisation.

### Diffusion-Weighted Imaging (DWI)

Diffusion-weighted imaging (DWI) measures the water diffusion within tissue. Normal glandular prostate tissue tends to allow diffusion of free water molecules, whereas tumours, with their densely packed cells, tend to have restricted water diffusion, which results in preserved signal within tumours compared with normal tissue on diffusion-weighted images. DWI sequences are acquired using a selection of different b values, ranging from 0 - 2000 s/mm<sup>2</sup>, enabling apparent diffusion coefficient (ADC) maps to be generated. Tumours show a lower ADC value than benign regions. DWI acquisition times are short, making it a time efficient sequence.

A wide range of sensitivities and specificities for prostate tumour detection have been reported for DWI (57 - 93.3% and 57 - 100%, respectively), depending on the technology used, field strength, imaging parameters, patient selection, and validation method [Bouchelouche *et al.* (2010)].

The addition of an ADC map to  $T_2$ -W images can improve the diagnostic performance of MR imaging in PCa detection. In a particular study, using only  $T_2$ -W images to detect for PCa, the sensitivity, specificity and accuracy values were evaluated as 73%, 54% and 64% respectively. When  $T_2$ -W and DWI images were combined, the values rose to 84%, 85% and 84% respectively [Tanimoto *et al.* (2006)].

Studies have shown that there exists a significant difference between mean ADCs of low, intermediate, and high clinical risk tumours [Turkbey *et al.* (2011)]. This could enable the non-invasive assessment of the aggressiveness of prostate cancers that are visible on MR images, aiding the selection of patients who are most appropriate for active surveillance.

### Dynamic Contrast-Enhanced Imaging (DCE)

Dynamic contrast-enhanced (DCE) MRI provides quantitative kinetic parameters reflecting the permeability and flow characteristics of the vessels within a lesion. DCE-MRI is performed with fast MR imaging sequences before, during, and after the rapid administration of a low-molecular weight contrast agent (e.g. gadolinium).

The following parameters are usually selected for processing:  $K^{trans}$  (contrast agent transfer rate between blood and tissue),  $k_{ep}$  (contrast agent backflux rate), maximum slope for wash-in and wash-out,  $V_e$  (extravascular-extracellular fractional volume). These

processed data can be analysed either visually (by generating colour maps) or quantitatively through straight values. The raw DCE images can also be visually analysed.

Tumours are expected to show early and increased enhancement compared with normal tissue and more rapidly washout than normal tissue. However abnormal enhancement patterns are seen in both tumour foci and BPH nodules [Rouvière *et al.* (2003)]. Furthermore, smaller and low-grade tumours often do not demonstrate abnormal enhancement on DCE MRI.

For the detection of tumours, DCE MRI alone has a sensitivity and specificity range of 46 - 96% and 74 - 96%, respectively, however these ranges are highly dependent on patient selection, technique, and diagnostic criteria [Bouchelouche *et al.* (2010)].

The combination of DCE with DWI and  $T_2$ -W images for the detection of PCa gave values of 95%, 74% and 86% for the sensitivity, specificity and accuracy respectively, compared to values of 84%, 85% and 84% for the combination of DWI and  $T_2$ -W [Tanimoto *et al.* (2006)].

[Girouin *et al.* (2007)] found that for the localisation of PCa, raw DCE images are more sensitive than  $T_2$ -W images; 50 - 60% and 78 - 81% of tumours (volume > 0.3 cc) were correctly depicted with  $T_2$ -W and raw DCE images, respectively.

## MR Spectroscopy (MRS)

MR spectroscopy (MRS) is a technique that generates metabolite spectra based on the differing proton resonance frequencies of a limited number of metabolites such as choline, creatine and citrate. Normal prostate tissue is rich in citrate and has relatively low choline and creatine levels while this pattern is reversed in cancers.

It has been shown that the (Cho + Cr)/Cit value in a lesion increases with increasing Gleason score. This implies that the sensitivity of MRS for cancer detection depends on the grade. In cancer with a Gleason score of 3 + 3, MRS tumour detection sensitivity was 44.4%, and sensitivity increased to 89.5% in cancers with a Gleason score of more than 8. A large proportion of tumours with a Gleason score of 6 did not generate abnormal voxel metabolite ratios [Zakian *et al.* (2005)].

It has been shown that the addition of 3D MRS to MR imaging provides better detection and localisation of PCa in a sextant of the prostate, with sensitivity and specificity higher than those with MR imaging alone. A combined MR imaging and 3D MRS indicated the presence of tumour with high probability (positive predictive value 89 - 92%), whereas a negative result excluded the presence of cancer with high probability (negative predictive value 74 - 82%) [Scheidler *et al.* (1999)].

However other studies have shown that the sensitivity of MRS is low [Vargas *et al.* (2012)] and that the accuracy of PCa localisation for combined MRS - MR imaging (0.54 - 0.61) is similar to MR imaging alone (0.57 - 0.63) [Weinreb *et al.* (2009)]. In conclusion, MRS is a time-consuming sequence and in practice, it is often not used.

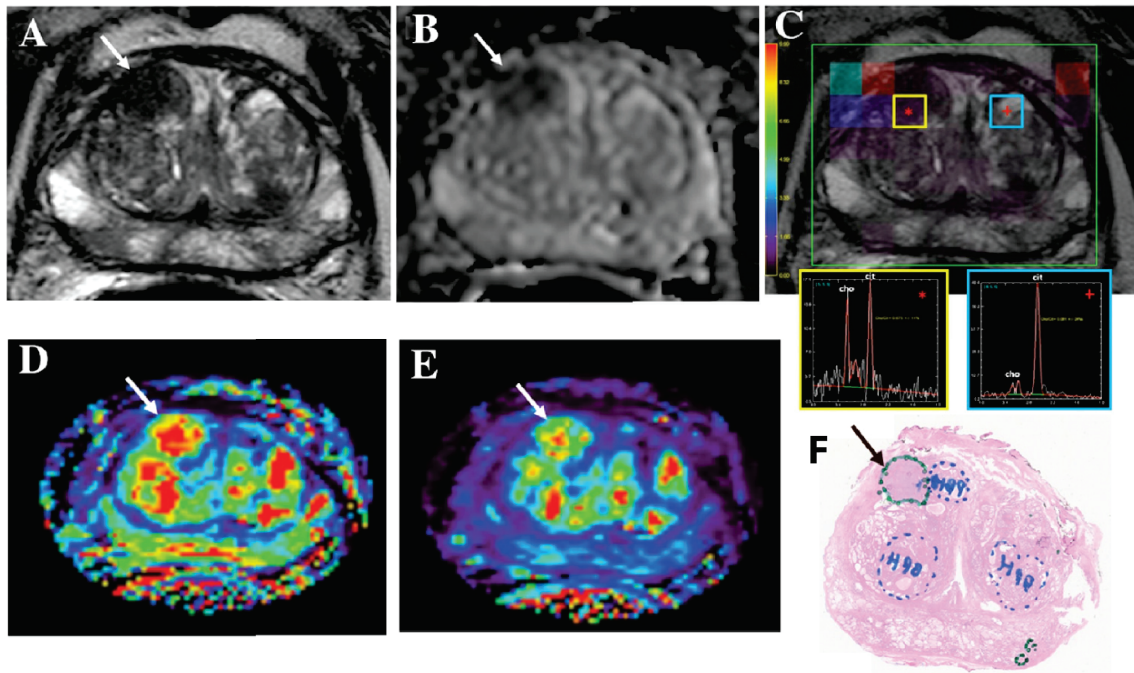


Figure 1.8: *Multi-parametric MRI: the (A) axial  $T_2$ -W and (B) ADC map of diffusion-weighted MRI scans, show a hypointense lesion (arrow), (C) the MRS results show an increased choline/citrate ratio in that region (yellow box) compared to normal adjacent tissue (blue box). (D) Forward contrast rate,  $K^{trans}$  and (E) reverse contrast rate  $k_{ep}$  maps of DCE MRI also indicated the presence of a tumour (arrow). The tumour existence and position is confirmed in the histological whole mount slide (arrow, outlined in green), Gleason score  $3 + 3 = 6$ . The areas outlined in blue represent BPH. Source: [Trivedi et al. (2012)]*

### 1.7.6 Multimodality Imaging

No current imaging technique is capable of detecting PCa stage, volume and location with sufficient specificity and sensitivity and no consensus exists regarding the use of imaging for evaluating primary prostate cancers. The combination and fusion of different imaging modalities has therefore become an important research area, as each modality can provide complementary information.

Significant research has been undertaken to register real-time transrectal ultrasound images with previously acquired MRI images of the prostate in order to target biopsies to regions identified as suspicious in MR images [Singh et al. (2008), Xu et al. (2008), Pinto et al. (2011), Kaplan et al. (2002)]. The technique allows for navigation within dynamic contrast-enhanced maps,  $T_2$ -W or MR spectroscopy images. Furthermore the technique is a rapid way to facilitate MRI-guided prostate therapies such as external beam radiation therapy, brachytherapy, cryoablation, high-intensity focused ultrasound ablation, or direct injection of agents, without the cost, throughput, or equipment compatibility issues that might arise with MRI-guided interventions inside the MRI suite [Singh et al. (2008)].

Research has also been concentrated on evaluating multi-parametric MRI, that is

the combination of multiple MRI techniques, including  $T_2$ -weighted imaging, dynamic contrast-enhanced imaging and diffusion-weighted imaging, for the detection and localisation of prostate cancer [Haider *et al.* (2007), Delongchamps *et al.* (2011), Langer *et al.* (2009), Kurhanewicz *et al.* (2008)].

However, the integration of morphological and functional imaging sequences is challenging for radiologists in routine practice, especially for those not specialised in prostate cancer imaging. Moreover, examination performance is highly reader-dependant due to the subjective nature of the findings [Puech *et al.* (2009)]. Computer-aided diagnosis (CAD) has therefore become a major research subject in medical imaging and diagnostic radiology. With CAD, radiologists use the computer output as a ‘second opinion’ and make the final decisions, meaning that the performance by computers does not have to be comparable to or better than that by physicians, but needs to be complementary to that by physicians [Doi (2007)].

## 1.8 Conclusion

The accurate localisation and staging of PCa, enabling low- and high-risk cancers to be distinguished, is a major clinical necessity. It is crucial to enable therapy to be directed more accurately, to target therapy and reduce the risk of over- and under-diagnosis.

To date, no reliable imaging method exists. Currently, the most accurate imaging method for PCa is multi-parametric MRI, that is combining  $T_2$ -W MR images with DWI and DCE. A challenge to the clinical utility of such a multi-parametric exam is how to optimally combine the data to give the most accurate assessment of prostate cancer in each patient.

Each MRI sequence modality must be evaluated. The images of each sequence must be precisely registered to the ground-truth information, the histology slices of the prostatectomy specimen. For each sequence, a quantitative analysis of the signal in the zones corresponding exactly to the histology tumours would enable a definition of the signal characteristics of prostate cancerous tissue for that sequence. The optimum combination of sequences could then be determined.

The next chapter will present a review of the latest advances in histology - MR and also histology - US registration.

# 2

## REGISTRATION OF HISTOLOGY AND IMAGED DATA: AN INTRODUCTION

### CONTENTS

2.1	Introduction . . . . .	33
2.2	Registration Challenges . . . . .	34
2.3	2D Registration of Histology and Imaged Data . . . . .	35
2.3.1	Assume that the Histology and Imaging Planes are the Same . . . . .	35
2.3.2	Ensure that the Histology and Imaging Planes are the Same . . . . .	36
2.4	Two-Step 3D Registration of Histology and Imaged Data . . . . .	39
2.4.1	Step 1: Histology Alignment . . . . .	39
2.4.2	Step 2: 3D Registration of Aligned Histology and Imaged Data . . . . .	44
2.5	Combined 3D Registration of Histology and Imaged Data . . . . .	47
2.6	Conclusion . . . . .	48

### 2.1 Introduction

Multi-parametric MRI (combining  $T_2$ -W images with DWI and DCE images) is currently the most accurate imaging method for characterising PCa in individual patients. The evaluation of the sensitivity and specificity of each sequence is required in order to determine the optimum combination of sequences. The histology slices of the prostatectomy

specimen remain the gold standard for prostate cancer diagnosis. To date, they provide the most precise and comprehensive information concerning the cancer grade, stage, tumour extent and margin status. Therefore, in order to define the signal characteristics of prostate cancerous tissue for each imaging modality and sequence, the histology slices must be precisely registered to the imaged data, enabling a quantitative analysis of the signal in the zones corresponding exactly to the histology tumours.

There are significant challenges associated with registering the histology slices to the imaged data, due in particular to the many deformations that exist between the two modalities. The difficulties to be considered are discussed in Section 2.2. There are two general approaches to register the histology to the imaged data; the registration is either considered as a 2D problem (Section 2.3) or as a 3D problem (Section 2.4 and Section 2.5).

Considering the registration as a 2D problem, that is, the registration of each histology slice to its corresponding imaged slice, makes the significant assumption that every 2D histology slice has a corresponding 2D imaged slice. The existence of corresponding slices implies that the plane along which the prostate specimen was sliced during histology processing is the same (in terms of the orientation and height) as the plane along which the imaged data was acquired. That the histology and imaging planes are at the same orientation and height is either assumed or ensured. We consider each of these situations in Section 2.3.1 and Section 2.3.2 respectively.

There are two main techniques to registering the histology and imaged data when considering the registration as a 3D problem. The first technique is a two-step method; step 1 involves aligning the histology slices in order to reconstruct a 3D histology volume and step 2 then consists of 3D registering the histology volume with the imaged volume. This technique is detailed in Section 2.4; first the difficulties that need to be considered when aligning histology slices are explored, then the various methods developed to align histology slices are presented and finally the existing 3D methods to register the aligned histology slices to the imaged volume are detailed. The second 3D technique combines the alignment of the histology slices and their registration with the imaged data into one algorithm, the existing methods are detailed in Section 2.5.

Though our particular interest is the registration of histology slices to MR images, the bibliography has been extended to include techniques developed using other image modalities that could be adapted to the histology - MR registration problem. For example, the aligning of histology slices could be considered more generally as the alignment of a set of contiguous thin 2D sections. Techniques developed using autoradiography images are thus included in the bibliography. Similarly, the ‘imaged data’ includes images acquired using MR, ultrasound and CT imaging, both *in vivo* and *ex vivo*.

## 2.2 Registration Challenges

The registration of histology slices and imaged data is challenging. This is due in particular to numerous deformations that exist between the two modalities. If MR *in*

*in vivo* pre-operative images of the prostate are being considered, it should be noted that the acquisition is often performed using an endorectal coil (ERC) in order to improve image quality. The ERC significantly changes the prostate shape and volume; [Heijmink *et al.* (2009)] estimated that the mean total prostate, peripheral zone, and central gland volume decreased by 17.9%, 21.6% and 14.2% respectively after ERC introduction. The prostatectomy operation itself causes a deformation of the specimen.

Once the prostate has been removed, the position of the seminal vesicles, vas deferens and the contour of the prostate can be used as landmarks for quick identification of the base, apex, posterior and anterior surface of the specimen. However, the landmarks available are insufficient for precise orientation of the specimen. Therefore, once the anatomic orientation in the body is lost, it is difficult to section the prostate in the same plane as the images were obtained.

The histology processing induces further significant deformations; the fixation causes a shrinkage and deformation, the consistency of the prostate makes it difficult to slice evenly, the paraffin-embedding and microtome slicing causes tissue loss and further deformation. These difficulties are detailed in Section 2.4.1.

The significant difference in resolution and inter-slice spacing between the histology slices and imaged data further challenge the registration. In general, histology images have a much higher spatial resolution than typical MR images (by several orders of magnitude), meaning that certain structures easily visible in histology, may not be identifiable in MR images.

## 2.3 2D Registration of Histology and Imaged Data

The 2D registration of histology slices with *in vivo* or *ex vivo* imaged data assumes that the histology slicing plane is at the same orientation and height as the imaging plane. This is either assumed (Section 2.3.1) or it is ensured that the histology plane is defined such as to be the same as the imaging plane (Section 2.3.2).

### 2.3.1 Assume that the Histology and Imaging Planes are the Same

[Mazaheri *et al.* (2010)] registers MR *in vivo* images of the prostate to whole mount histology slices. The digitised images of the histology slices are first matched with the corresponding axial MR images by a radiologist. The matching is done on the basis of anatomical landmarks, progressive changes in the diameter of the prostate, the thickness of the peripheral zone, the position of the pseudocapsule, and the presence, size, and shape of the transition zone. The image pair is then registered using a non-rigid method based on B-splines.

The manual matching of the MR images to the histological slices not only assumes that the image acquisition plane is the same as the histology slicing plane, but also lengthens the processing time, introduces inter-user variability and reduces the overall robustness of

the method.

[Kozlowski *et al.* (2006)] aimed to determine whether the combination of DWI and DCE MR images provided higher diagnostic sensitivity for prostate cancer than each technique alone. This was estimated by mapping both the histology and MR results to a standard octant biopsy map (left and right base, lateral mid-gland, medial mid-gland and apex).

In order to identify the MRI parameters that best indicate aggressive cancer, therefore improving the accuracy of MR tumour localisation and evaluation of aggressiveness, [Fan *et al.* (2011)] registered high-resolution (9.4 T) MR *ex vivo* images with histology slices of the prostate. The MR *ex vivo* images and histology slices were 2D registered by visual inspection.

[Patel *et al.* (2011)] aimed to register histology slices of the prostate with MR *in vivo*  $T_2$ -W and DCE images in order to define quantitative MR prostate cancer signatures. The histology slice is elastically registered to the corresponding MR  $T_2$ -W image using a method based on mutual information.

### 2.3.2 Ensure that the Histology and Imaging Planes are the Same

A number of methods have been reported that aim to ensure that the same plane is used for imaging and slicing. [Chen *et al.* (2010)] provides a comprehensive overview and comparison of methods and apparatus developed to optimally slice the prostate specimen to enable correlation of the histology slices with imaged data. Methods of particular interest are detailed below, in addition to other methods that were not included in the literature review of [Chen *et al.* (2010)].

[Jhavar *et al.* (2005)] developed an approach whereby the prostate gland is held in a cradle and the tissue is sliced using a series of evenly spaced blades that can be moved through the slits, see Figure 2.1. The cradle enables the prostate to be held firmly during the dissection permitting even sectioning. However, it is not adaptable for any size of prostate specimen and the gripping force may distort the specimen. Furthermore, the orientation of the prostate within the cradle is achieved manually.

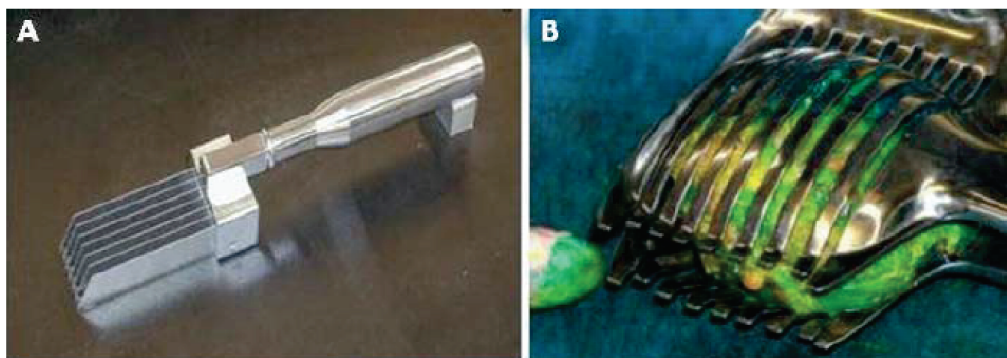


Figure 2.1: Approach developed whereby the prostate gland is held in a cradle (b) and the tissue is sliced using a series of evenly spaced blades (a). Source: [Jhavar *et al.* (2005)]

Similar to this method, [Drew *et al.* (2010)] designed and constructed an adjustable box that holds the fresh prostate specimen fixed during the sectioning process by applying a slight pressure on the specimen from every direction. The walls of the device include 4 mm spaced vertical slots that allow the blades of a knife to pass through the specimen. Though this method is adaptable for any size of prostate specimen, the positioning of the orientation of the prostate remains inaccurate. The device was used by [Moradi *et al.* (2012)] to generate histology slices that were used as a second validation dataset for generated multi-parametric MRI maps.

Another method, developed by [Shah *et al.* (2009)], involved generating a 3D model of the prostate from segmentations in three orthogonal planes of MR *in vivo* images. Patient specific moulds are then fabricated using 3D printing. The prostate specimen, after fixation, is held in the mould and equally spaced slots allow the specimen to be sectioned, see Figure 2.2. The accuracy of the fit of the mould depends on the accuracy of the MR *in vivo* segmentations, the change in the gland size between the image acquisition and surgery and tissue deformation and shrinkage that occurred after surgery and tissue fixation. Inaccuracy in the fit will introduce a difference between the orientation of the MR and histology slices.

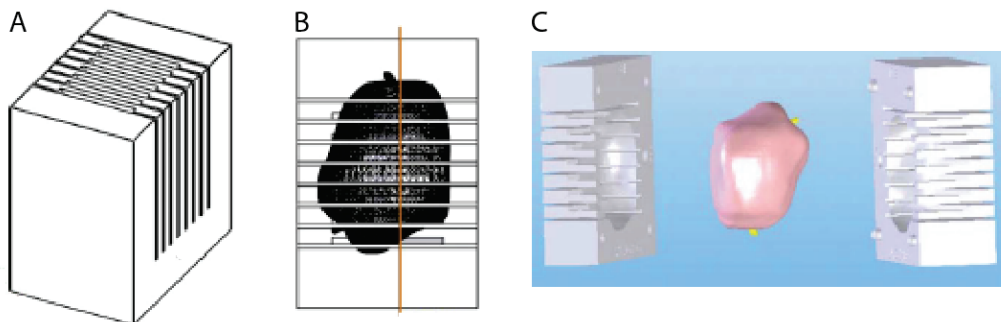


Figure 2.2: (a) The individualised mould has parallel cutting slots, (b) fabricated to be patient specific using a 3D prostate model generated from MR *in vivo* images, (c) the mould is split in two halves to enable the insertion of the prostate specimen (3D model of the prostate with the urethra in yellow). Source: [Shah *et al.* (2009)]

[Madabhushi *et al.* (2005), Chappelow *et al.* (2007), Zhan *et al.* (2007), Ou *et al.* (2009)] developed a technique whereby the fresh prostate specimen is embedded in 2% agar at 50°C in a small plastic box and then cooled to 4°C to solidify the agar. The embedded prostate gland is then MR imaged and parallel histology sections of the embedded gland are cut using a rotary knife, starting at its square face.

[Rouviere *et al.* (2006)] proposed a method to enable histology specimens to be cut along the MR imaging plane. First, three fiducial markers that are visible in both MR and macroscopy are injected into the *ex vivo* tissue to define the imaging plane. The ‘PlaneFinder device’ (PFD) is then used to rotate the specimen in three dimensions under MR guidance to find the predefined imaging plane for dissection. The MR images are acquired parallel to the defined plane. After formalin fixation, the specimen is placed

again in the PFD and MR scanning is used to identify the same orientation for sectioning. Once the predefined plane is horizontal, the specimen is embedded in wax such that the top surface is horizontal. The specimen is then sectioned parallel to the top surface, see Figure 2.3.

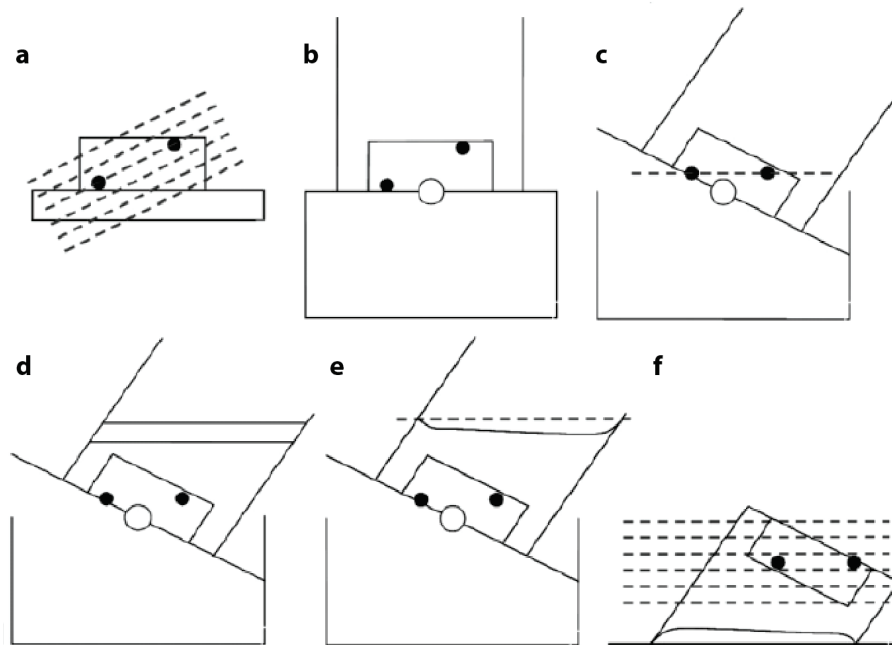


Figure 2.3: Fiducial markers are injected in the tissue to define the imaging plane (a), the tissue is placed in the PFD (b), which is used to rotate the specimen under MR guidance to find the predefined plane (c). The MR images are acquired parallel to the defined plane. After fixation, the specimen is again placed in the PFD, the predefined plane is made horizontal and the specimen is embedded in wax (d). The specimen is sectioned parallel to the top wax surface (f). Source: [Rouviere et al. (2006)]

The method was applied by [Kimm et al. (2012)] to correlate MR *ex vivo* images of the prostate with histology slices. The first limitation of this method involves the fiducial markers that are needed to define the imaging plane. The application of the markers *in vivo* is invasive and technically demanding, furthermore their safety for use *in vivo* is unclear. Without a suitable marker, the application of the method *in vivo* is limited.

[Ward et al. (2010), Ward et al. (2012)] developed a method to orient the prostate specimen such that it is sliced along a plane parallel to the *in vivo* imaging plane. The imaging plane of the MR *in vivo* images defines the desired cutting plane. The 3D MR *in vivo* images are registered to the 3D MR *ex vivo* images using a manual technique followed by a refinement, therefore transposing the desired cutting plane into the *ex vivo* coordinate system. Prior to *ex vivo* imaging, internal and surface-mounted strand-shaped fiducial markers, visible in MR and histology, had been attached to the prostate specimen. The fiducial markers visible in the *ex vivo* images enable a rigid, landmark-based transformation of the desired cutting plane into a magnetic tracker space, where three points on the specimen surface lying within the desired cutting plane are located and physically defined

by inserting three pins. The specimen is then oriented for slicing along the desired plane. The most significant drawback of this method is the 11 hour processing time required.

Similarly, [Langer *et al.* (2009)] used MR *ex vivo* images of the fixed prostate specimen to transpose the desired cutting plane (defined as the *in vivo* imaging plane) into the *ex vivo* coordinate system. This was achieved by acquiring *ex vivo* images of the gel-embedded prostate specimen at regular angle intervals and determining by visual inspection the angle corresponding to the best *in vivo* agreement. The gel-embedded specimen was sectioned using a rotary blade, using a wedge to duplicate the angle determined during *ex vivo* MRI.

[Humm *et al.* (2003)] developed a method of inserting small (0.71 mm diameter) hollow Teflon rods into tissue samples. The rods can be visualised by MRI and PET as well as in histology and autoradiography tissue sections. The template used to insert the rods remains in place during the MR acquisition, enabling the imaging plane to be aligned parallel. During histology processing, the template can be mounted in the microtome, establishing a cutting plane parallel to the template.

[Varghese *et al.* (2003)] registered elastography images with digitised photographs of gross pathology liver specimens in order to evaluate the reliability of elastography for delineating thermal lesion boundaries resulting from radiofrequency tumour ablation. Pathology photographs were obtained in the same image plane used for elastography by slicing through the specimen using external markers.

## 2.4 Two-Step 3D Registration of Histology and Imaged Data

No consensus exists as to an optimum slicing technique [Chen *et al.* (2010)]. Thus, in general, it cannot be assumed that the histology slices are cut along the same plane as the imaged data was acquired and so the registration must often be considered as a 3D problem. There are two main approaches for achieving the 3D registration of histology slices with imaged data. We consider in this section the first approach, which is a two-step method. Step 1 involves aligning the histology slices in order to reconstruct a 3D histology volume and step 2 then consists of 3D registering the histology volume with the imaged volume.

### 2.4.1 Step 1: Histology Alignment

Aligning a set of histology slices can more generally be considered as aligning a set of contiguous thin 2D sections (e.g. histology slices, autoradiography images). The alignment involves reconstructing a 3D volume from a stack of 2D images by registering every pair of consecutive images in the stack to recover their geometrically coherent 3D alignment. Significant difficulties exist and must be considered when aligning histology slices. These difficulties are first detailed before a bibliography of the existing histology alignment techniques is presented.

### Difficulties associated with Aligning Histology Slices

There are numerous difficulties associated with the alignment of histology slices, foremost is that the alignment cannot be considered as a classical image matching problem because the slices to be aligned are obtained from different horizontal planes of the organ, meaning that though the slices present similar s, no two slices are identical.

Other difficulties to be considered are the non-linear 3D deformation as the prostate is extracted from the body, the non homogeneous 3D shrinkage and distortion introduced by the fixation, the slice dependent tissue loss and 2D distortion of tissue due to sectioning (tear, shear, fold, stretch). The staining of the slices can cause a significant difference in intensity from one slice to another.

When placing the histology slice on the glass slide, the boundary of the tissue may overlap the edge of the glass slide or the slide label may cover some of the tissue. Also, when laying the cover-glass over the histology slice, air bubbles can be created, causing spots to appear and creating artifacts in the slices. Examples of some of these difficulties are shown in Figure 2.4.

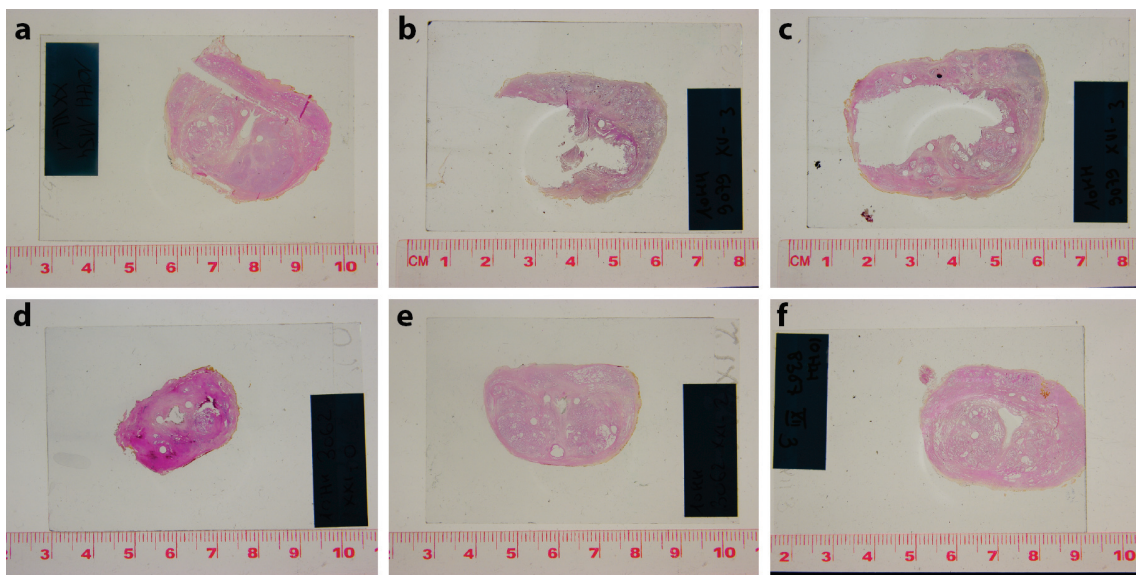


Figure 2.4: *There are numerous difficulties associated with the alignment of histology slices, including tearing of the histology slices (a), tissue loss at the exterior (b), or interior of the histology slice (c), intensity difference between slices, (d) and (e) are two consecutive slices from the same patient separated by 2 mm, and overlap of the histology slice with the label or edge of the glass slide (f).*

Histology slice preparation is a skilled, laborious and time-consuming procedure. In standard clinical practice, the routine must be performed in a reasonable time frame. Therefore, though it is possible to have histology slices cut with a regular  $\mu\text{m}$  inter-slice spacing, in reality it is not feasible outside of an academic environment. Histology slices obtained in standard clinical practice have an uneven inter-slice spacing and the spacing can be significant.

Also to be considered is the ‘shear effect’, that a 3D curved object cannot be reconstructed from 2D cross-sections without additional information. The effect, referred to as the ‘banana problem’, is well illustrated by [Malandain *et al.* (2004)], see Figure 2.5. It is also referred to as the ‘z-shift effect’ [Yushkevich *et al.* (2006)] and is further detailed in [Cifor *et al.* (2011)].

Furthermore, an interesting study by [Gibson *et al.* (2012)b] quantitatively evaluated the assumption that adjacent histology slices are parallel by measuring the average depth and orientation of histology slices relative to the front face of the paraffin-embedded tissue blocks of prostate specimens. They estimated the mean depth of the slices to be  $1.0 \pm 0.5$  mm and the mean orientation of the slices to be  $1.7^\circ \pm 1.1^\circ$ .

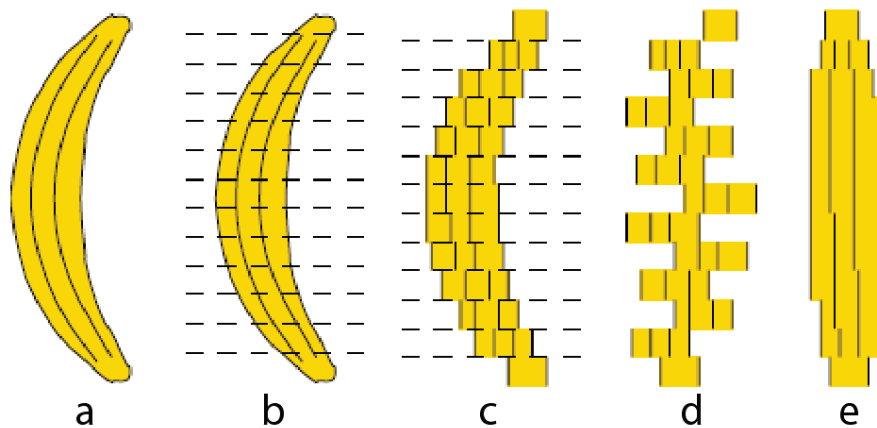


Figure 2.5: *The ‘banana problem’ refers to the difficulty of reconstructing a 3D curved object from 2D cross-sections. If a 3D curved object, e.g. a banana (a), is cut into slices (b), the slices are digitised (c), and then mixed (d), the 3D reconstruction results in a cylindrical banana (e). Source [Malandain *et al.* (2004)]*

### Methods of Aligning Histology Slices

Various methods have been proposed in the literature to align histology slices, a review of the methods is presented in this section. A summary of the different histology alignment techniques can be found in Table 2.1, with the main advantages and disadvantages of each technique listed, as well as the associated references.

The most common method is **manual registration** using interactive operator alignment. It is a laborious and time-consuming method which is subject to inter- and intra-operator variability. [Bauer *et al.* (1999), Loughlin *et al.* (1998)] both used manual registration to align prostate histology slices.

Other methods use an **intermediate modality** as a reference-volume to guide the alignment. Each 2D histology slice is registered to the corresponding 2D intermediate modality image. Generally, the 2D images of the intermediate modality are either already aligned or can be easily aligned.

Block-face images are often used as the intermediate modality. During the histology process, the tissue to be examined is generally sectioned into parallel blocks, which are then embedded in paraffin. These paraffin blocks are then finely sliced using a microtome (see Chapter 3 for a detailed description of the histology process). Block-face images are photographs or scans of the paraffin-embedded tissue. The use of block-face images is attractive for several reasons; as the histology slices are prepared from the paraffin-embedded tissue, there exist many common features between the two modalities to guide the registration. Furthermore the 2D slice-independent deformations associated with the microtome slicing are not present in the block-face photos, the 2D elastic registration of each histology slice to its corresponding block-face photo removes these artifacts from each slice.

[Kim *et al.* (1995)] aligned autoradiography images of a rat brain by 2D registering each image to block-face photos. [Samavati *et al.* (2011), Park *et al.* (2008)] both used block-face photos to align prostate histology slices, guiding the 2D registration by manually identified control points. [Bardinet *et al.* (2002)] aligned histology slices of the human brain by 2D registering each slice to the corresponding block-face photo. The registration was achieved using an intensity based method, using the correlation coefficient as the similarity measure. [Shojaii *et al.* (2011)] aligned histology slices of a mouse tumour by 2D registering each slice to the corresponding block-face photo. The registration was achieved using an edge-based registration technique. Holes were drilled into the corners of the paraffin blocks enabling the block-face images to be easily aligned. Block-face photos were also used by [Gibb *et al.* (2012)] to align histology slices, tested on animal heart specimens. Block-face photos were also used by [van Engelen *et al.* (2011)] to align histology slices of carotid plaque specimens. Each histology slice was registered to the corresponding block-face image using manually annotated landmarks. [Seise *et al.* (2011)] used micro CT images as the intermediate modality to align histology slices of the liver.

The disadvantage of using an intermediate modality to align the histology slices is that it requires the acquisition of the intermediate modality images. Block-face images are acquired during the histology processing, lengthening the processing time of the clinical routine. This supplemental processing time required may not be possible during standard clinical routines.

**Intensity based methods** involve calculating the transformation that maximises the similarity in intensity between corresponding pixels, the similarity can be measured using mutual information or the correlation coefficient. These methods are attractive in that they are non-invasive. However the crucial limitation to intensity based methods is that there must be information redundancy between slices, i.e. local similarities from one slice to another. This information redundancy is dependent on both the underlying morphology of the tissue and the inter-slice spacing between the slices.

Many intensity based methods have been published for the alignment of histology slices of the brain. Intensity based methods are particularly appropriate for this organ as

it has rich structural detail, generating significant information redundancy between slices. Ourselin developed a method using the correlation coefficient to quantify the similarity, tested on histology slices of a human brain (inter-slice spacing 0.7 mm) [Ourselin *et al.* (2001)a] and histology slices of a rat brain (inter-slice spacing 0.4 mm) and a monkey brain (inter-slice spacing 0.1 mm) [Ourselin *et al.* (2001)b]. The method developed by [Yushkevich *et al.* (2006)] used mutual information as the similarity measure, it was tested on histology slices of a mouse brain, though the inter-slice spacing was not stated, it is assumed to be very small as there were 525 histology slices.

[Kiessling *et al.* (2005)] aligned histology slices of mouse and rat tumours using an intensity based registration, the inter-slice spacing was 50  $\mu\text{m}$ . [Mathew *et al.* (2012)] aligned histology slices of mouse lungs using the correlation coefficient to quantify the similarity between images, the inter-slice spacing was 10  $\mu\text{m}$ . The similarity measure was defined as a combination of mutual information and morphological gradient information by [Tang (2011)] to guide the alignment of histology slices of a gekko spinal chord.

Prostate tissue does not have rich structural detail. Furthermore histology slices obtained in standard clinical routine have in general an inter-slice spacing of 3 - 5 mm. In a university hospital, prostate histology slices can be prepared with an inter-slice spacing of 1 mm, however spacings of the order of 3 mm or more will still occur (see Section 3.6.2).

**Feature-based methods** of alignment have the same advantages and disadvantages as intensity based methods, in that they are also non invasive but limited by information redundancy. A variety of features can be used to guide the alignment, including points, contours, anatomical or structural features.

Points were used to guide the alignment of histology slices by both [Park *et al.* (2008)] and [Guest *et al.* (2001)]; [Park *et al.* (2008)] used manually placed control points to align prostate histology slices, [Guest *et al.* (2001)] used automatically generated corresponding points to align mouse embryo histology slices.

[Cohen *et al.* (1998), Cifor *et al.* (2011), Zhao *et al.* (1993)] used contours to guide the alignment; [Cohen *et al.* (1998)] developed a method in which the external contour of the tissue is modelled using a B-spline, the histology slices of the rat brains are then aligned by registering the B-splines of consecutive slices, [Zhao *et al.* (1993)] also used the external contour of the boundary, aligning autoradiographic images of a rat brain, [Cifor *et al.* (2011)] aligned the histology slices of a mouse and rat brain using the contours of curved anatomical structures that could be extracted.

Though certain structures are visible in prostate histology slices, e.g. the urethra and ejaculatory ducts, these structures are not visible in all the slices of the prostate specimen and thus the ensemble of the slices of the specimen could not be registered using this method. The contour of the prostate, though visible in each slice, is not considered to be a reliable feature due to the various deformations and tissue losses that occur, both of which are exacerbated at the edges of the tissue.

[Kay *et al.* (1998)] automatically segmented micro-vessels in prostate histology slices

and registered consecutive slices by matching the detected vessels between slices. The pixel resolution of the slices was  $1.37 \mu\text{m}$  and though the inter-slice spacing is not stated, it is assumed to be small as there were 87 histology slices obtained from the specimen.

Techniques based on the use of **fiducial markers** involve inserting needles into the tissue before slicing to create fiducial markers that are detectable in the histology slices. The slices can then be aligned by overlying the corresponding markers. Quite simply, fiducial markers generate information redundancy between the slices.

[Egevad *et al.* (1998)] developed an apparatus consisting of four parallel needles (diameter 3 mm) attached to a base in a square pattern. The needles are inserted into the fresh prostate specimen. After fixation, the needles are removed, leaving small round holes visible in the histology slices. The device has been used by [Taylor *et al.* (2004), Bart *et al.* (2005)], manually aligning the histology slices by visually aligning the created markers.

[Humm *et al.* (2003)] developed a similar apparatus that guides the insertion of three hollow Teflon rods (diameter 0.71 mm), creating fiducial markers visible in histology and autoradiography slices. The created markers are manually identified enabling the transformation to be calculated that minimises the root mean square Euclidean distance between the respective markers of two images. The method was tested on histology and autoradiography slices of mouse tumours.

### 2.4.2 Step 2: 3D Registration of Aligned Histology and Imaged Data

Once the histology slices have been aligned, the histology volume can be 3D registered to the imaged volume. Various methods have been proposed in the literature to achieve this registration.

Often the **3D external surface boundary** of the tissue is used to guide the registration. [Kiessling *et al.* (2005)] reconstructed the 3D surface volume of mouse and rat tumours from the aligned histology slices and MR *in vivo* images and then registered the two volumes by manually orienting one of the volumes with respect to the other. [Taylor *et al.* (2004)] 3D registered prostate histology and *ex vivo* ultrasound images by calculating the transformation that maximised the surface voxel overlap of the two reconstructed surface volumes. [Bart *et al.* (2005), Reynier *et al.* (2004)] represented the segmented boundary in each modality as a 3D point cloud. The two modalities were then registered by calculating the transformation that minimised the distance between the point clouds. [Reynier *et al.* (2004)] registered prostate MR images with ultrasound images using this method and [Bart *et al.* (2005)] registered prostate histology with MR images.

Registration Technique	Advantages	Disadvantages	References
Manual	Direct implementation Non invasive	Time-consuming Laborious Inter- and intra-operator variability	[Bauer <i>et al.</i> (1999)] [Loughlin <i>et al.</i> (1998)]
Intermediate modality	Overall registration divided into more manageable intermediate registrations Deformations caused by the microtome slicing can be quantified Non invasive	Supplemental time required for image acquisition, lengthening the histology routine	[Kim <i>et al.</i> (1995)] [Samavati <i>et al.</i> (2011)] [Park <i>et al.</i> (2008)] [Bardinet <i>et al.</i> (2002)] [Shojaii <i>et al.</i> (2011)] [Gibb <i>et al.</i> (2012)] [van Engelen <i>et al.</i> (2011)] [Seise <i>et al.</i> (2011)]
Intensity-based	Non invasive	Information redundancy between slices required	[Ourselin <i>et al.</i> (2001)a] [Yushkevich <i>et al.</i> (2006)] [Kiessling <i>et al.</i> (2005)] [Mathew <i>et al.</i> (2012)] [Tang (2011)]
Feature-based	Non invasive	Information redundancy between slices required	[Park <i>et al.</i> (2008)] [Guest <i>et al.</i> (2001)] [Cohen <i>et al.</i> (1998)] [Zhao <i>et al.</i> (1993)] [Cifor <i>et al.</i> (2011)] [Kay <i>et al.</i> (1998)]
Fiducial markers	Information redundancy between slices created	Invasive	[Egevad <i>et al.</i> (1998)] [Taylor <i>et al.</i> (2004)] [Bart <i>et al.</i> (2005)] [Humm <i>et al.</i> (2003)]

Table 2.1: Summary of the different registration techniques proposed in the literature to align histology slices. The main advantages and disadvantages of each technique are listed, as well as the associated references.

The registration can also be achieved using **features** that are common to the two modalities. [Porter *et al.* (2001)] registered ultrasound and MR images of the liver by segmenting vessels visible in the two modalities. The vessels are 3D reconstructed and the transform that maximises the surface voxel overlap of the vessels is calculated. [Kim *et al.* (1995)] registered MR and autoradiography images of a rat brain by calculating the transformation that minimised the distance between control point pairs that has been manually identified in each modality.

One or more **intermediate imaging modalities** can also be used to guide the registration. In order to achieve the 3D registration of prostate histology slices with MR *in vivo* images, [Park *et al.* (2008)] first aligned the histology slices by registering each slice to its corresponding block-face photo. The block-face photos were then stacked and 3D registered to MR *ex vivo* images. The MR *ex vivo* images were 3D registered to MR *in vivo* images. Each intermediate registration step was achieved by calculating the transformation that minimised the distance between manually identified control point pairs. Similarly [Samavati *et al.* (2011)] registered prostate histology slices with MR *in vivo* images by first registering the histology slices to block-face photos. The block-face photos were registered to MR *ex vivo* images of the fixed prostate, which were in turn registered to MR *ex vivo* images of the fresh prostate. Finally the MR *ex vivo* images of the fresh prostate were registered to the MR *in vivo* images.

In order to investigate the lesion induced by radio frequency ablation, [Seise *et al.* (2011)] registered liver histology slices to *in vivo* CT images. The registration was achieved by first registering the histology slices to *ex vivo* micro CT images. The *ex vivo* CT images were then registered to the *in vivo* CT images using segmented vessels visible in both modalities.

[van Engelen *et al.* (2011)] registered histology and MR *ex vivo* images of carotid plaque specimens using block-face images as an intermediate modality, the intermediate registrations were achieved using manually annotated landmarks. [Bardinet *et al.* (2002), Dauguet *et al.* (2007)] also used block-face images as an intermediate modality to register histology slices to MR images of the brain, with the intermediate registrations achieved using intensity based methods. [Bardinet *et al.* (2002)] validated his method on a human brain, with MR *ex vivo* images and the correlation coefficient as the similarity measure. [Dauguet *et al.* (2007)] validated his method on baboon brains, with MR *in vivo* images and used mutual information as the similarity measure. [Gibb *et al.* (2012)] used block-face images as an intermediate modality to register histology to MR *ex vivo* images of animal heart specimens.

**Intensity-based methods** can be used to guide the registration. [Ourselin *et al.* (2001)a] registered the histology slices of a human brain with MR images using an intensity based method. The correlation coefficient was used as the similarity measure. Note that the histology inter-slice spacing was 0.7 mm and the MR pixel resolution was 0.9375 mm.

To investigate the ability of MR imaging to monitor radio-frequency ablation treatments, [Breen *et al.* (2003), Breen *et al.* (2005)] registered MR images and histology slices in order to compare the thermal lesions, tested on rabbit thigh muscle. The registration was achieved using **fiducial markers**. MR compatible needles were inserted into the tissue, creating fiducial markers visible in histology, block-face and MR *in vivo* images. The created fiducial markers were manually identified, enabling the histology and MR images to be registered, using the block-face images as an intermediate modality. The method was first validated by [Lazebnik *et al.* (2003)] using digital phantoms and sheep brain tissue.

## 2.5 Combined 3D Registration of Histology and Imaged Data

The second approach for achieving the 3D registration of histology slices with imaged data is a single-step method that combines the alignment of the histology slices and the subsequent 3D registration of the histology volume with the imaged volume into one algorithm. In this section a bibliography of the methods that have been developed using this approach are presented.

[Malandain *et al.* (2004)] developed a method whereby first an initial alignment of the autoradiograph slices is achieved, generating a 3D autoradiograph volume. The autoradiograph volume is then 3D registered to the MR volume. The MR volume can then be resampled such that each 2D MR slice corresponds to a 2D autoradiograph slice. Each autoradiograph slice is 2D registered to the re-sampled MR slice. The autoradiograph volume is re-generated and the process is iterated to convergence. The method was tested using a monkey brain specimen. The registrations were achieved by calculating the transformation that maximised the intensity similarity between pixels, with the correlation coefficient being used as the similarity measure. The histology inter-slice spacing is not stated, but it is assumed to be small considering that there were 818 slices available.

The same methodology was used by [Goubran *et al.* (2012), Plank *et al.* (2009), Mansoori *et al.* (2007)]. [Goubran *et al.* (2012)] used the iterative technique to register histology slices to MR *ex vivo* images of a human brain sample, similarly using intensity-based methods with the correlation coefficient to guide the registrations. [Plank *et al.* (2009), Mansoori *et al.* (2007)] used the method to register histology slices and MR *ex vivo* images of rabbit heart specimens. Each of the 2D and 3D registrations in the iterative loop were rigid registrations, calculated using an intensity-based method with mutual information as the metric. When the system reached convergence, a final non-rigid transform was calculated to 2D register the histology slices with the last re-sampled MR slices. A non-rigid transform is able to register any pair of histology-MR slices, even if they do not correspond to the same anatomical locations. Therefore, the optimal combination of rigid transforms is first calculated and the non-rigid deformation is placed outside of the iterative loop and is performed only as a last step.

[Xiao *et al.* (2011)] proposed a similar method to register histology slices and MR

*in vivo* images of the prostate. First, the 2D histology - MR slice correspondances are estimated and each histology slice is 2D registered to the corresponding MR slice. The registration is achieved using an intensity-based method, with mutual information being used as the similarity measure. With each histology slice mapped into the MR coordinate space, a 3D histology pseudo-volume is reconstructed using zero-padding. The histology pseudo-volume is 3D registered to the MR volume, again using a mutual information, intensity-based method. The 2D MR slices are updated by slicing the MR volume along the new plane resulting from the 3D registration. The process is iterated to convergence. The authors noted that the 3D registration caused only a moderate change in the slice correspondances.

[Gibson *et al.* (2012)a] registered prostate histology slices with MR *ex vivo* images by attaching ten strand-shaped fiducial markers (three internal and seven surface-mounted) to fixed prostate specimens, visible in both histology and MR *ex vivo*. The markers form a unique cross-section configuration on each histology slice which enables the plane from which the slice was cut in the MR *ex vivo* 3D volume to be identified for each slice. The registration is then calculated that minimises the distance between the respective fiducial markers.

## 2.6 Conclusion

The aim of this thesis is to precisely register the histology slices of prostatectomy specimens with MR *in vivo* pre-operative images. The histology slices and MR images are acquired from standard clinical routines.

During histology processing, the landmarks available on the prostate gland are insufficient for precise orientation of the specimen. Therefore, it cannot be assumed that the prostate can be manually orientated such that the histology slicing plane is the same as the imaging plane. Furthermore, though numerous techniques and apparatus have been developed in order to ensure the histology slicing plane is oriented parallel to the imaging plane, no consensus exists as to an optimum slicing technique. In general, it cannot be assumed that the histology slices are cut along the same plane as the imaged data was acquired. Therefore, for precise prostate histology - MR *in vivo* registration, a 2D technique is not considered to be sufficiently accurate.

Considering therefore the registration as a 3D problem; manual registration is dismissed as an option due its laborious and time-consuming nature, which is subject to inter- and intra-operator variability. The use of one or more intermediate imaging modalities to guide the registration is a popular choice, however it requires the acquisition of the intermediate modality images. Block-face images are the most commonly used intermediate modality. These images are acquired during the histology processing routine, lengthening the duration of the routine. Our aim is to develop a protocol that can be included into standard clinical routine, the supplemental processing time required for the acquisition of the block-face images means that this technique is not a feasible option.

Several intensity and feature-based registration techniques have been presented in the bibliography. The crucial limitation to both of these methods is information redundancy, i.e. there must exist local similarities or features between the slices (either between histology slices or between histology and MR images). Information redundancy is dependent on both the underlying morphology of the tissue and the inter-slice spacing. The methods presented in the bibliography were developed for tissue with rich structural detail (e.g. the brain or heart [Ourselin *et al.* (2001)a, Ourselin *et al.* (2001)b, Yushkevich *et al.* (2006), Malandain *et al.* (2004), Goubran *et al.* (2012), Plank *et al.* (2009), Mansoori *et al.* (2007), Cifor *et al.* (2011), Kim *et al.* (1995)]) and/or images with very small and regular inter-slice spacing (e.g. 10  $\mu\text{m}$  [Mathew *et al.* (2012)], 50  $\mu\text{m}$  [Kiessling *et al.* (2005)], 100  $\mu\text{m}$  [Ourselin *et al.* (2001)b]).

Prostate histology slices present few landmarks. Though certain features exist, e.g. the urethra and the ejaculatory ducts, these structures are not visible in all the slices of the prostate specimen and thus the entire specimen could not be registered using this method. The contour of the prostate, though visible in each slice and image, is not considered to be a reliable feature due to the deformation and tissue loss caused by the prostatectomy and histology processing, which is exacerbated at the edges of the tissue. Prostate histology slices obtained in standard clinical routine have in general an inter-slice spacing of 3 - 5 mm. Though the inter-slice spacing is reduced to 1 mm in a university hospital, the spacing is irregular and spacings of the order of 3 mm or more regularly occur.

For these reasons, a two-step alignment and registration approach was chosen. The histology slice alignment is achieved using a fiducial marker based method and the subsequent 3D registration between the histology and MR is achieved using a feature-based method.

In order to create the internal fiducial markers in the histology slices, an apparatus was developed that inserts three fiducial needles at three unique angles into the fresh prostate specimen. The technique enables the markers to be created in a standardised manner and has been designed to be applicable to standard clinical routine, in terms of time, cost and material.

Once the histology slices are aligned, the histology and MR volumes are 3D registered using the ejaculatory ducts. The ejaculatory ducts are paired structures which begin at the seminal vesicles, pass through the prostate gland along a curved path and enter into the urethra. They are an anatomical landmark present in every prostate and are visible in both histology and MR images at standard clinical routine resolution.

The fiducial needles are MR compatible, enabling MR *ex vivo* images to be acquired of the specimen after insertion of the needles. Applying the developed 3D registration technique to register the aligned histology slices to the MR *ex vivo* volume enables an operator-independent quantification of the accuracy of the technique via the needles which are visible in both histology and MR *ex vivo*.



# 3

## IMAGE ACQUISITION

### CONTENTS

3.1	Introduction . . . . .	52
3.2	MR <i>in vivo</i> Protocol . . . . .	52
3.3	Fiducial Marker Creation . . . . .	52
3.3.1	Apparatus . . . . .	53
3.3.2	Prostate Orientation . . . . .	53
3.3.3	Fiducial Needles . . . . .	54
3.3.4	Needle Insertion Angle . . . . .	55
3.3.5	Model Geometry . . . . .	57
3.3.6	Fiducial Marker Geometry . . . . .	57
3.4	MR <i>ex vivo</i> Protocol . . . . .	58
3.5	Histology Processing . . . . .	59
3.6	Digitisation of the Histology Slices . . . . .	59
3.6.1	JPEG Digitisation . . . . .	59
3.6.2	Histology Slice Inclusion Criteria . . . . .	61
3.7	Conclusion . . . . .	61

### 3.1 Introduction

Patients that had undergone a MR *in vivo* prostate examination and for whom a radical prostatectomy was planned were eligible to be included in our database. Following the prostatectomy, fiducial markers are created in the fresh prostate specimen. A MR *ex vivo* acquisition of the specimen is then performed. The prostate is subsequently histology processed according to standard clinical routine and the resulting histology slices are digitised. This chapter details each of the various different techniques, protocols and routines involved in the overall image acquisition process.

### 3.2 MR *in vivo* Protocol

Each patient included in our database had undergone an MR *in vivo* prostate examination using a 3T clinical MR scanner (Discovery MR750, GE Healthcare, USA) with a 32-channel pelvic phased array (PPA) coil.  $T_2$ -W, DWI and DCE images were acquired for each patient. The MR image acquisition parameters are detailed in Table 3.1. DWI and DCE images were acquired in the axial plane and  $T_2$ -W images were acquired in both the axial and sagittal planes. The axial images were oriented such as to be perpendicular to the rectal surface of the prostate. For DCE imaging, an intravenous injection of 0.2 mL/kg of gadoterate meglumine (Dotarem<sup>TM</sup>, Guerbet, Roissy, France) was performed at 3 mL/sec. The axial  $T_2$ -W, DWI and DCE images were acquired with the same slice thickness and position to enable a direct comparison between the modalities.

Sequence	$T_2$ -W	DWI	DCE
Repetition time (TR) (ms)	5000	5000	3.9
Echo time (TE) (ms)	104	90	1.7
Field of view (FOV) (mm <sup>2</sup> )	220x220	380x380	240x192
Acquisition matrix	384x256	128x128	180x160
Flip angle (degrees)	90/180	90	12
b values (s/mm <sup>2</sup> )	-	0-2000	-
Slice thickness (mm)	3	3	3
Number of temporal acquisitions	-	-	32
Temporal resolution (s)	-	-	7

Table 3.1: MR *in vivo* image acquisition parameters for the  $T_2$ -W, DWI and DCE sequences.

### 3.3 Fiducial Marker Creation

The 3D histology - MR *in vivo* registration requires the prior alignment of the histology slices. The method we have developed to achieve the histology slice alignment is based on the use of fiducial markers. In this section, we detail the apparatus that was developed to

create the fiducial markers and explain the reasoning behind the design choices that were made. We describe the protocol for creating the fiducial markers using the apparatus and the characteristics of the created markers.

### 3.3.1 Apparatus

The objective was to design and fabricate an apparatus that would enable fiducial needles to be inserted, in a standardised manner, into fresh prostate specimens following a radical prostatectomy, such that internal fiducial markers are created and visible in each histology slice. The protocol for creating the fiducial markers was developed such that the following criteria were respected,

- the histological examination and diagnosis of the histology slices would not be impaired,
- the protocol could be easily integrated into the existing histology processing routine,
- the supplemental time required for the fiducial marker creation would be minimised,
- one apparatus could be used for all prostate specimens.

The apparatus developed, see Figure 3.1a, consists of a support that holds horizontal and rigid, a guide to insert three fiducial needles at three distinct angles into the prostate. The guide is made of plexi-glass and is of dimension 50x50x20 mm. The support enables the vertical position of the guide to be adjusted (5 - 70 mm) so that the guide is positioned exactly at the height of each prostate specimen.

### 3.3.2 Prostate Orientation

The orientation of the prostate in the apparatus is standardised; the apex on the top, the base on the bottom with the seminal vesicles behind. During the subsequent histology processing routine (see Section 3.5) the specimen will be sectioned along a plane approximately perpendicular to the rectal surface of the prostate (imitating the MR *in vivo* imaging plane), the fiducial needles must therefore be inserted perpendicular to that sectioning plane.

The needles are inserted from the apex to the base of the prostate because the apex is of a smaller dimension than the base (see Figure 1.2), meaning that,

- (i) positioned on the base, the prostate is in a more stable position and
- (ii) by progressing from the ‘smaller end’ to the ‘larger end’, we minimise the risk that a needle exits the prostate before passing through the entire length of the prostate, which would result in the absence of fiducial markers in histology slices cut from after the needle has exited the tissue.

To ensure that the needles completely exit the prostate, thus ensuring the proper creation of the fiducial markers at the base, the prostate is placed on a layer of polystyrene when

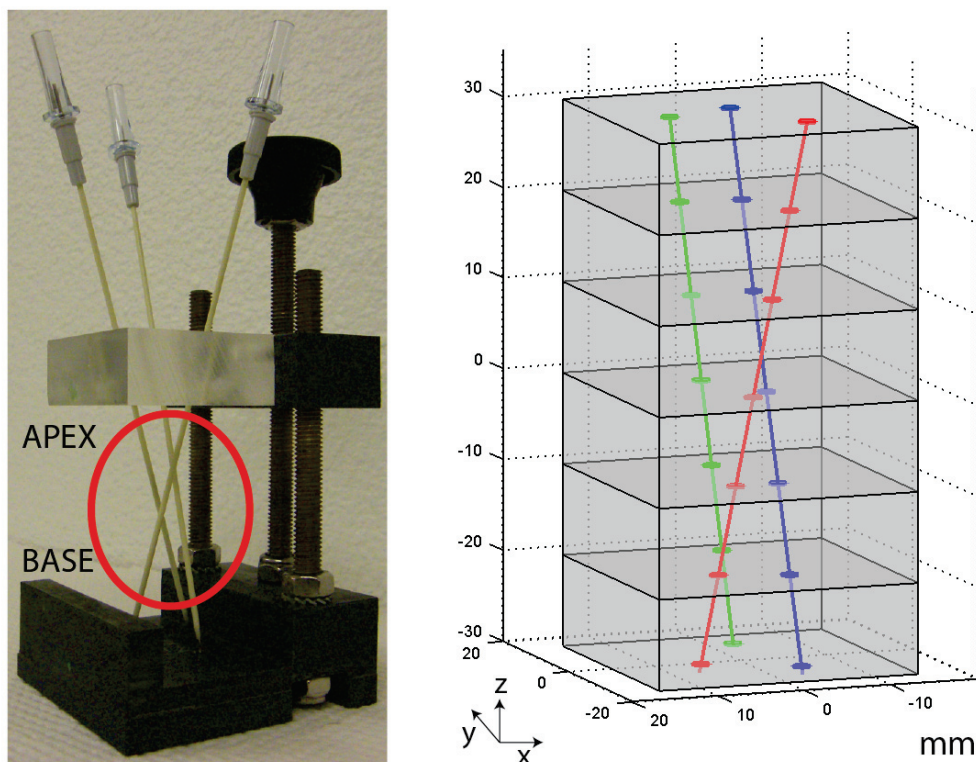


Figure 3.1: (a) Apparatus designed to create fiducial markers in the histology slices, the guide enables three fiducial needles to be inserted at three distinct angles from the apex to the base of the prostate, (b) as the needles are inserted at three different angles, a different triangle is formed by the three created fiducial markers at each horizontal plane a distance  $h$  from the guide.

positioned in the apparatus. The needles are then inserted until they have entered the polystyrene.

### 3.3.3 Fiducial Needles

The needles used are 16 G IV catheters (BD Angiocath), of radius 0.82 mm. They were chosen as they have a rigid plastic sheath. Once the three catheters have been inserted into the prostate, the needles are removed, leaving the sheaths in place within the prostate. The guide can then be slightly raised, the sheaths cut with a scissors and the prostate (with the inserted sheaths within) can be removed from the apparatus, see Figure 3.2. It is necessary that the plastic sheaths remain within the prostate to ensure that the fiducial markers created are maintained, in particular during the fixation step of the histology processing routine, see Section 3.5, as the fixation induces a shrinkage of the prostate tissue which, if the sheaths were not present, would cause the created markers to close.

It was decided to insert three fiducial needles into the prostate as a compromise between minimising the perturbation to the histology examination and the fact that a minimum of two fiducial markers are required in order to align a slice. Three needles would create

enough markers to align the slices, while allowing for some to be lost, either because the tissue was torn during the histology processing routine or the marker falls within, for example, the urethra.

The creation of the fiducial markers is an invasive technique. The primary design constraint was that the histological examination and diagnosis of the specimen would not be impaired by the creation of the markers. Upon examination of the histology slices of a specimen in which fiducial markers had been created, the anatomo-pathologists judged that the insertion of three needles of radius 0.82 mm did not compromise the histology examination.

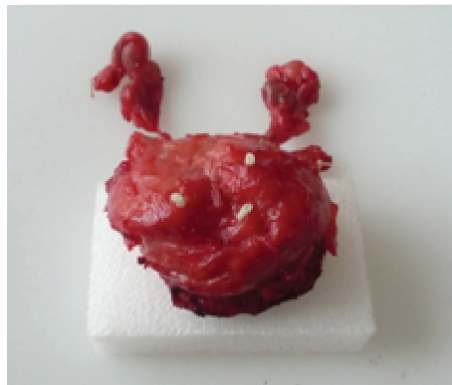


Figure 3.2: *Sample prostate specimen after removal from the apparatus, the plastic sheaths remain within the prostate to ensure that the fiducial markers created are maintained, in particular during the fixation of the specimen.*

### 3.3.4 Needle Insertion Angle

The needles are inserted at three distinct angles and in a *twist* style such that the needles do not intersect. This means that at each horizontal plane a distance  $h$  from the needle insertion guide (i.e. the apex of the prostate), a different triangle is formed by the three created fiducial markers, see Figure 3.1b. We denote the three fiducial markers created at any height  $h$ , i.e. the vertices of the triangle formed, as  $n_1$ ,  $n_2$  and  $n_3$ . If a circumcircle is fitted to the formed triangle, see Figure 3.3, the clockwise order of the fiducial markers around the circumcircle is constant for each histology slice obtained from the specimen. That is, if the clockwise order at the apex is  $(n_1, n_2, n_3)$ , then for every other histology slice, if a circumcircle is fitted to the triangle formed in that slice, the clockwise order of the markers will be  $(n_1, n_2, n_3)$ , see Figure 3.3.

That the clockwise order of the markers is the same for each histology slice is particularly interesting for the later classification of the fiducial markers. If care is taken to orient the histology slices before digitisation, the permutations that result in the markers being in a non clockwise order can be eliminated, as they correspond to a flip orientation, see Figure 4.8.

The fact that a different triangle is formed by the three fiducial markers in each histol-

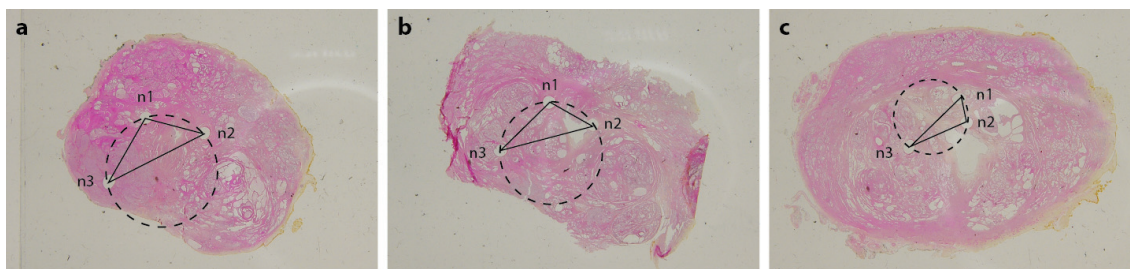


Figure 3.3: If a circumcircle is fitted to the triangle formed by the three fiducial markers, denoted  $n_1$ ,  $n_2$  and  $n_3$ , the clockwise order of the markers (following a path around the circumcircle) is constant for each histology slice obtained from the specimen. The inter-slice spacing between: image (a) and (b) is 4 cm, and between image (b) and (c) is 14 cm.

ogy slice means that the label attached to each histology slice by the anatomo-pathologists, detailing the distance of each slice from the apex, can be verified and, if necessary, corrected. For example, if during the histology processing routine, a 6 mm section was embedded in the paraffin facing the wrong direction (see Section 3.5), the slices obtained from that specific section would be in the reverse order and a discontinuity in the progressively changing shape of the triangle would appear. Inserting the needles each at a different angle enables the detection and correction of such an error.

A further advantage concerns the histology - MR *ex vivo* registration. The fiducial needles are used to quantify the accuracy of the registration technique, the fact that the needles are inserted at angles enables the registration quality along the z-axis to be evaluated.

Another advantage of inserting the needles at an angle, is that if a needle falls within, for example, the urethra, the needle will exit the urethra after a few slices because the needle progression is at an angle, meaning that the fiducial markers of that needle are lost for only a few slices. If the needles were inserted vertically, and a needle falls within the urethra, the fiducial markers of that needle would be lost for the majority of the histology slices of the specimen.

In conclusion, the main advantages of inserting the needles at an angle rather than vertically are that,

- (i) the relative order of the histology slices from the apex can be verified and, if necessary, corrected,
- (ii) the accuracy of the histology - MR *ex vivo* registration can be quantified along the z-axis and
- (iii) if one of the needles falls within, for example, the urethra, the fiducial markers will be lost in a fewer number of histology slices.

### 3.3.5 Model Geometry

We define the model geometry as the three theoretical polar angles with respect to the vertical axis at which the apparatus guides the insertion of the fiducial needles. In order to measure the model geometry, a rectangular sample of 3% agar was prepared and three fiducial needles were inserted using the apparatus. MR axial images of the agar were acquired, with the axial image plane oriented parallel to the surface of the agar which had been positioned beneath the guide of the apparatus. Images were acquired with an inter-slice spacing of 1 mm. The polar angles were measured as:  $\theta_{n1} = 12.8^\circ$ ,  $\theta_{n2} = 13.8^\circ$  and  $\theta_{n3} = 16.6^\circ$ .

Ideally, the polar angles of the fiducial needles created in each prostate specimen would be equal to this model geometry. However, unlike the agar, into which the needles are easily inserted, for a fresh prostate, due to its semi-solid consistency, a certain force is required to puncture the surface. Once punctured, the tissue expands due to the high pressure of any hypertrophic nodules. This causes a slight yet unavoidable displacement of the prostate, repeated by the insertion of each proceeding needle. The result is that the angle geometry created in each prostate specimen is slightly different.

We assume that the insertion of the needles creates fiducial markers in straight 3D lines, though we cannot assume the exact polar angle at which the line is positioned. In order to quantify this assumption, MR *ex vivo* axial images were acquired of 7 fresh prostate specimens after insertion of the fiducial needles, see Section 3.4. A point was placed at the location of each fiducial marker visible in the axial images, and 3D least-squares lines passing through the points were calculated. The average distance of each point from the line was  $0.15 \pm 0.11$  mm. As the radius of the fiducial needle is 0.82 mm, we consider the assumption that the needles create fiducial markers in straight 3D lines to be justified.

### 3.3.6 Fiducial Marker Geometry

The internal fiducial markers created and visible in the histology slices are approximately circular holes, see Figure 3.4 for a sample histology slice, with the created fiducial markers indicated with arrows. However, as the fiducial needles are not inserted vertically, the fiducial markers created are not exactly circles but ellipses. If we quantify the difference of the ellipses created from circles of radius  $r$  in terms of area  $a$  and circular quality  $c$  defined as

$$c = \frac{4\pi a}{p^2} \quad (3.1)$$

where  $p$  is the perimeter, with the ideal values for a circle of radius  $r$  being  $\pi r^2$  and 1 respectively, the percentage difference of the area  $\Delta a$  and circular quality  $\Delta c$  for the three needles is thus

- $\theta_{n1} = 12.8^\circ$  :  $\Delta a = +2.55\%$ ,  $\Delta c = -0.02\%$ ,
- $\theta_{n2} = 13.8^\circ$  :  $\Delta a = +2.97\%$ ,  $\Delta c = -0.03\%$ ,
- $\theta_{n3} = 16.6^\circ$  :  $\Delta a = +4.35\%$ ,  $\Delta c = -0.07\%$ .



Figure 3.4: *Sample histology slice; the created fiducial markers are approximately circular holes, and are indicated with arrows.*

### 3.4 MR *ex vivo* Protocol

The aim of this thesis is to precisely register prostate histology slices with MR *in vivo* pre-operative images. MR *ex vivo* images of the fresh prostate specimen are acquired following the creation of the fiducial markers. Before applying the developed 3D registration technique to register the histology and MR *in vivo* images, the registration technique is applied to register the histology and MR *ex vivo* images. As the needles used to create the fiducial markers are MR compatible and visible in MR *ex vivo* images, they enable an operator-independent quantification of the accuracy of the registration technique to be achieved, before applying the technique to register histology and MR *in vivo* images. The MR *ex vivo* acquisition of the prostate specimen is therefore a step that is only included in the ‘development phase’, in order to quantify and evaluate the accuracy of the developed algorithm before it is applied to register histology and MR *in vivo* images.

Concerning the MR *ex vivo* protocol, the MR *ex vivo* images of the prostate specimen are acquired following the creation of the fiducial markers (the evening of the day on which the radical prostatectomy occurred). The fresh prostate is placed in a plastic box, dimension 10x10x7 cm, which is then filled with saline solution, see Figure 3.5. The polystyrene block, to which the prostate is attached by the plastic sheaths, causes the prostate to float. This enables the MR *ex vivo* axial imaging plane to be oriented parallel to the polystyrene block, i.e. parallel to the needle insertion guide of the apparatus.

The MR images were acquired using the same 3T clinical MR scanner as previously described. For each prostate, axial  $T_1$ -W and  $T_2$ -W images were acquired. The  $T_1$ -W images enable the fiducial markers to be visualised and the anatomical detail of the specimen can be seen in the  $T_2$ -W images. The acquisition parameters were for  $T_1$ -W: TE/TR = 7.1 ms/2197 ms, and for  $T_2$ -W: TE/TR = 120 ms/4158 ms, for both  $T_1$ -W and  $T_2$ -W: FOV 50x50 mm<sup>2</sup>, acquisition matrix 320x320, flip angle 90°, slice thickness 2 mm.

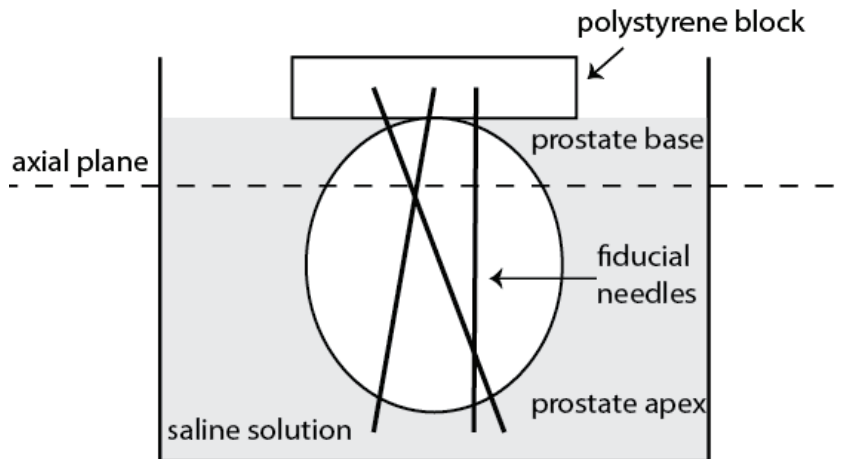


Figure 3.5: *Set-up for the MR ex vivo image acquisition: the prostate, after creation of the fiducial markers, is placed in a plastic box filled with saline solution. The polystyrene block causes the prostate to float, enabling the axial imaging plane to be oriented parallel to the polystyrene block, i.e. parallel to the apparatus needle insertion guide.*

## 3.5 Histology Processing

The morning following the day on which the radical prostatectomy occurred, the polystyrene block is removed and the prostate specimen is fixed in 10% formaldehyde for a minimum of 24 hours. After fixation, the sheaths are removed and the prostate is dissected following the Stanford method [Bostwick and Cheng (2008)]; the seminal vesicles, the bladder neck and a 3 - 5 mm portion of the apex are removed and studied apart. The remainder of the prostate is sectioned, from the apex to the base, into 6 mm sections, see Figure 3.6. The sections are cut such as to be perpendicular to the rectal surface of the prostate, i.e. along the same plane as the MR *in vivo* axial imaging plane.

The 6 mm sections are re-fixed for at least 48 hours, then de-hydrated in formaldehyde and methyl and embedded in paraffin. The paraffin blocks are sliced using a microtome. The first few slices of the microtome cut away the block until a complete slice of the prostate is achieved. Slices are then cut every 500 - 1000  $\mu\text{m}$ , thickness 4  $\mu\text{m}$ . The whole-mount slices (50 x 75 mm) are stained using hematoxylin eosin safran (HES) and sealed. A paper label is attached to each slice, detailing the patient reference and the relative position of the slice from the apex.

## 3.6 Digitisation of the Histology Slices

### 3.6.1 JPEG Digitisation

The histology slices of each prostate specimen are colour digitised using an illuminated workbench, equipped with a support that enables the camera (FujiFilm finePix S8000 fd) to be fixed at a certain height. This ensures a constant pixel resolution for each histology slice of the prostate specimen. A ruler is included in each image to enable the resolution to

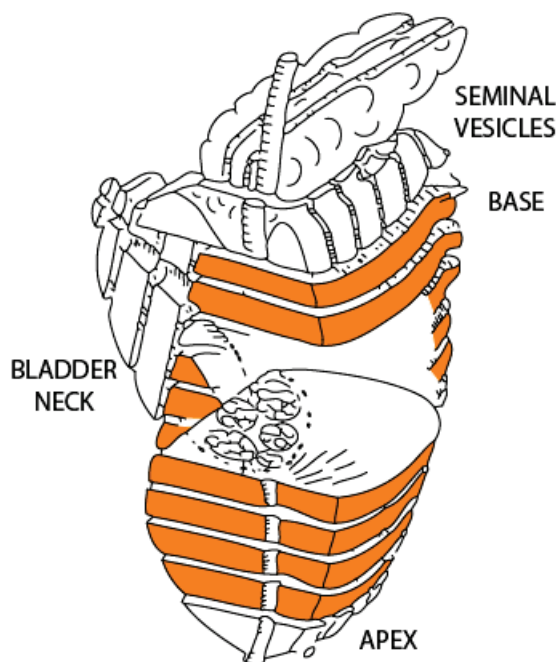


Figure 3.6: *The prostate is dissected following the Stanford method; the seminal vesicles, bladder neck and a portion of the apex are removed and studied apart, the remainder of the prostate is sectioned into 6 mm sections. Figure adapted from [Vieillefond et al. (2004)].*

be later calculated. The histology slices are positioned such that the normal vector of each slice is oriented in the same direction (see Figure 3.7), i.e. that no ‘flip orientation’ need be subsequently taken into account. In order to have a constant illumination intensity for each histology slice, inter- and intra- prostate specimen, the shutter speed must be defined such that the exposure duration is a multiple of the light source period. As this results in a long exposure duration (100 ms), filters are placed between the light source and the slices to avoid over-exposure. The digitised images are of dimension 3264x2448 pixels, pixel resolution 0.03 mm. See Figure 3.8 for a sample digitised histology slice. The file name of each digitised histology slice is the patient reference followed by the relative position of the slice from the apex, this information is detailed on the paper label attached to each histology slice by the anatomo-pathologists.

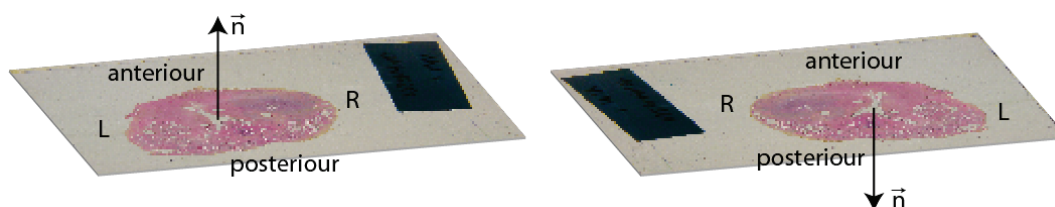


Figure 3.7: *The histology slices are positioned such that the normal vector  $\vec{n}$  of each slice is oriented in the same direction. This ensures that no ‘flip orientation’ need be subsequently taken into account.*

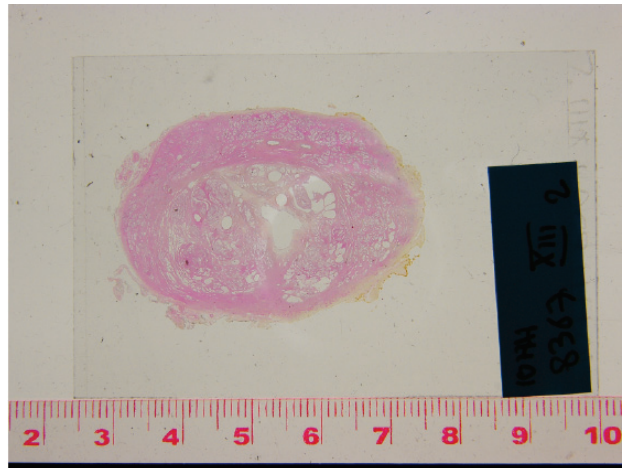


Figure 3.8: *Sample digitised histology slice. A ruler is included in each image to enable the pixel resolution to be later calculated. The paper label attached to each slice by the anatomo-pathologists, detailing the patient reference and the relative position of the slice from the apex, can be seen on the right-hand side of the histology slice.*

### 3.6.2 Histology Slice Inclusion Criteria

Not every histology slice is digitised. Even though the 6 mm sections are sliced every 0.5 - 1.0 mm, on average 3 - 4 slices per section are digitised and included for further study. This creates a certain clustering of the slices, evident in Figure 3.9, which shows the stack of digitised histology slices for a particular prostate specimen with the relative inter-slice spacing indicated on the z-axis. There are a few different reasons for this,

- (i) though the sections were cut 6 mm thick, the following fixation and dehydration steps cause a volume reduction of the section, such that when included in the paraffin, the section is less than 6 mm thick,
- (ii) if the section was embedded in the paraffin at an angle to the horizontal, when sliced with the microtome, the first and last few slices will not contain a full cross-section of the specimen and will be discarded, reducing the number of complete slices achieved for that section,
- (iii) as a minimum of two fiducial markers is necessary to align a slice, slices with significant tissue loss such that less than two markers remain, are not digitised.

## 3.7 Conclusion

MR *in vivo*, MR *ex vivo* and histology images have been acquired during this thesis. This chapter first detailed the MR *in vivo* protocol and acquisition parameters. Following radical prostatectomy, internal fiducial markers are created in the fresh prostate specimen. The apparatus that was designed to create the fiducial markers, as well as the reasoning

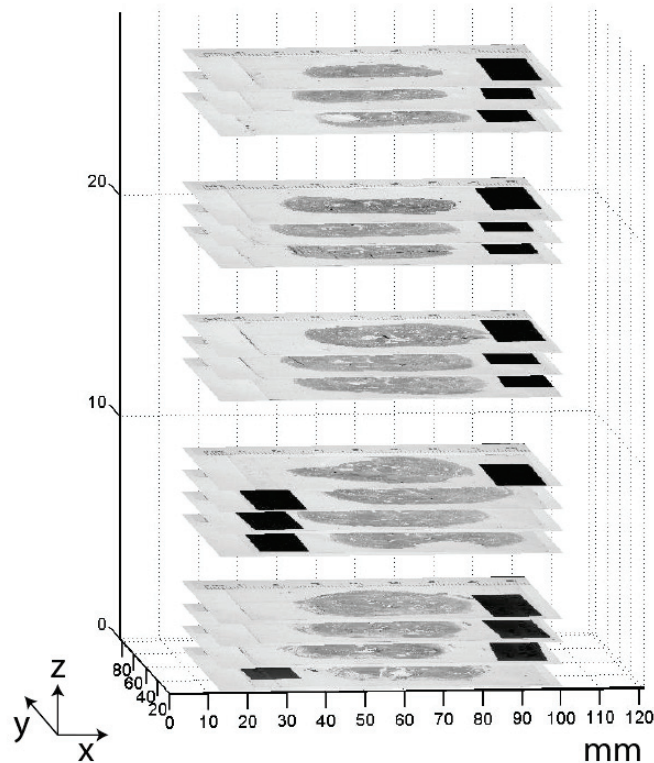


Figure 3.9: Stack of digitised histology slices of a prostate specimen, the relative inter-slice spacing is indicated on the z-axis. On average 3-4 slices per section are included for further study, creating a clustering effect of the slices.

behind the various design choices made, have been explained. The fiducial marker creation protocol is detailed and the characteristics of the created markers are described.

Once the fiducial markers have been created, MR *ex vivo* images of the prostate specimen are acquired. The MR *ex vivo* protocol and acquisition parameters are detailed. As it was not an initial design criterion to fabricate the apparatus to be MR compatible, the prostate is removed from the apparatus before the MR *ex vivo* acquisition. The polystyrene block, attached to the prostate by the plastic sheaths, causes the prostate to float, therefore enabling the imaging plane to be oriented parallel to the needle insertion guide of the apparatus. A future perspective is to fabricate the apparatus such that it is MR compatible so that MR *ex vivo* images could be acquired of the prostate within the guide. This would ensure that the imaging plane is oriented parallel to the needle insertion guide and furthermore that the prostate remains absolutely stationary during the MR acquisition.

The histology processing routine is then described in order to better understand the deformations and uncertainties associated with the histology images. Finally, which histology slices are included for further study and how they are digitised was discussed. The following chapter will detail the method developed to achieve the alignment of the digitised histology slices using the created fiducial markers.

# 4

## HISTOLOGY SLICE ALIGNMENT

### CONTENTS

4.1	Introduction . . . . .	64
4.2	Glossary . . . . .	64
4.3	Pre-processing . . . . .	64
4.4	Potential Fiducial Marker Detection, Scoring and Classification . . . . .	65
4.4.1	Potential Fiducial Marker Detection . . . . .	66
4.4.2	Potential Fiducial Marker Scoring . . . . .	66
4.4.3	Potential Fiducial Marker Classification . . . . .	67
4.5	True Fiducial Marker Detection and Identification . . . . .	68
4.6	Alignment and Shear Correction of the Histology Slices . . . . .	75
4.6.1	Alignment . . . . .	75
4.6.2	Shear Correction . . . . .	76
4.7	Transformation Summary . . . . .	77
4.8	Validation . . . . .	78
4.8.1	Validation in Simulated Images . . . . .	78
4.8.2	Validation in Beef Liver . . . . .	80
4.8.3	Experimental Validation in 10 Prostate Specimens . . . . .	81
4.9	Results . . . . .	81
4.9.1	Results in Simulated Images . . . . .	81
4.9.2	Results in Beef Liver . . . . .	83
4.9.3	Results in 10 Prostate Specimens . . . . .	85
4.10	Conclusion . . . . .	88

## 4.1 Introduction

The creation of the internal fiducial markers in the histology slices creates information redundancy between the slices, enabling each 2D prostate slice to be aligned in order to recreate the 3D prostate volume. This chapter details the method employed to segment the 2D prostate slice in each histology slice, the method that has been developed to detect the potential fiducial markers within each segmented prostate. The algorithm that has been developed to detect which of the potential markers are true fiducial markers and to identify by which needle each marker was created is also detailed. Once the true fiducial markers have been detected and it has been identified by which needle each marker was created, three ‘synthetic needles’, 3D least-squares lines passing through the detected markers for each needle, can be calculated, enabling a 2D transform to be calculated for each image that aligns the dataset of images. The images are then shear corrected.

The proposed method has been tested using simulated images (Section 4.8.1), images acquired from a beef liver sample (Section 4.8.2) and experimentally using 10 prostate specimens (Section 4.8.3). The results are presented in Section 4.9.

## 4.2 Glossary

The digitised histology slices are referred to as images. The set of images of a prostate specimen is called a dataset, with  $N$  the number of images in the dataset. Objects in the image that could be fiducial markers are referred to as potential fiducial markers and as true fiducial markers when it has been established that they are fiducial markers. The three needles are referred to as needle 1 ( $n_1$ ), needle 2 ( $n_2$ ) and needle 3 ( $n_3$ ).

## 4.3 Pre-processing

The file name of each digitised histology slice includes the relative position of the slice from the apex. This enables the images of the dataset to be automatically ordered with respect to their relative position from the apex and the inter-slice spacing between each image to be calculated.

The user is asked to manually identify on the first image of the dataset: two graduations on the ruler (enabling the pixel resolution to be calculated), a sample region of the background, a sample region of the prostate and the location of the three fiducial markers (in any order), see Figure 4.1.

The manually detected markers are identified as having been created by the three needles and labelled as  $n_1$ ,  $n_2$ ,  $n_3$  in any order provided that if a circumcircle is fitted to the triangle formed by the three markers, the sequence of the markers ( $n_1$ ,  $n_2$ ,  $n_3$ ) is in a clockwise order. As previously explained in Section 3.3.4 ‘Needle Insertion Angle’, as the needles are inserted in a *twist* style, a different triangle is formed by the three fiducial markers in each histology slice. If a circumcircle is fitted to the formed triangle, see

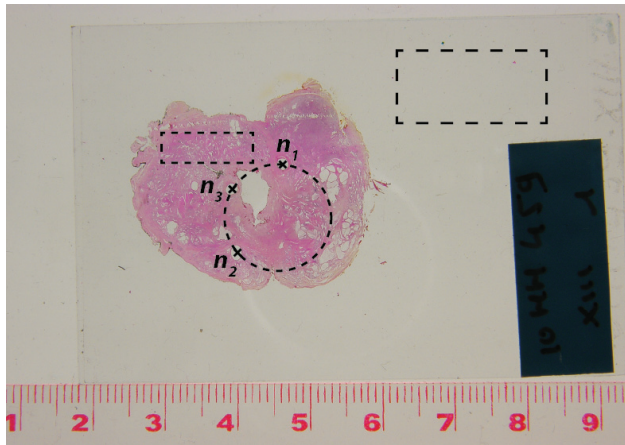


Figure 4.1: *The first image of a patient dataset, the user is asked to manually identify a sample region of the background and prostate (dashed rectangles) and the location of the three fiducial markers (marked with a x). The markers are labelled such that, if a circumcircle (dashed circle) is fitted to the three markers, the sequence  $(n_1, n_2, n_3)$  is in a clockwise order.*

Figure 3.3, the clockwise order of the fiducial markers around the circumcircle is constant for each histology slice obtained from the specimen.

The mean values of the RGB component intensities, for the background and prostate, are calculated from the defined sample regions. For each image, each pixel is classified as background or prostate according to the sum of the least-squares difference of its RGB component intensity from that of the mean values, see Figure 4.2(b). The noise (objects of less than 100 pixels) is removed from the image and closed boundary objects are filled. The objects are then eroded (disk-shaped structuring element of radius 3 pixels), see Figure 4.2(c). The three objects with the largest areas are detected. For the first image of each dataset, the user manually identifies which of the three largest objects is the prostate. For each other image in the dataset, the prostate is detected by comparing the overlap of each of the three objects with the first prostate segmented and the previously segmented prostate. The resultant segmentation is shown for a sample image in Figure 4.2(d).

Each image in the dataset is translated such that the centre of gravity of each segmented prostate is at the centre of each image. The images are then cropped about the segmented prostate and padded such that each image in the dataset is the same size, see Figure 4.3(a). An ellipse is least-squares fitted [Fitzgibbon *et al.* (1996)] to each detected prostate contour, the orientation of which is defined as the angle between the horizontal axis and the major axis of the ellipse, Figure 4.3(b). Each image is rotated such that the orientation of the dataset is uniform, Figure 4.3(c). This first coarse alignment of the images (2D translation and rotation,  $T_{\text{init}}$ ) enables the regions of interest (ROI), in which the fiducial markers will be searched, to be reduced thus reducing the risk of erroneously detecting markers.

#### 4.4 Potential Fiducial Marker Detection, Scoring and Classification

For each dataset of images, the potential fiducial markers in the images are detected. For each potential fiducial marker detected, a geometric score is calculated which quantifies

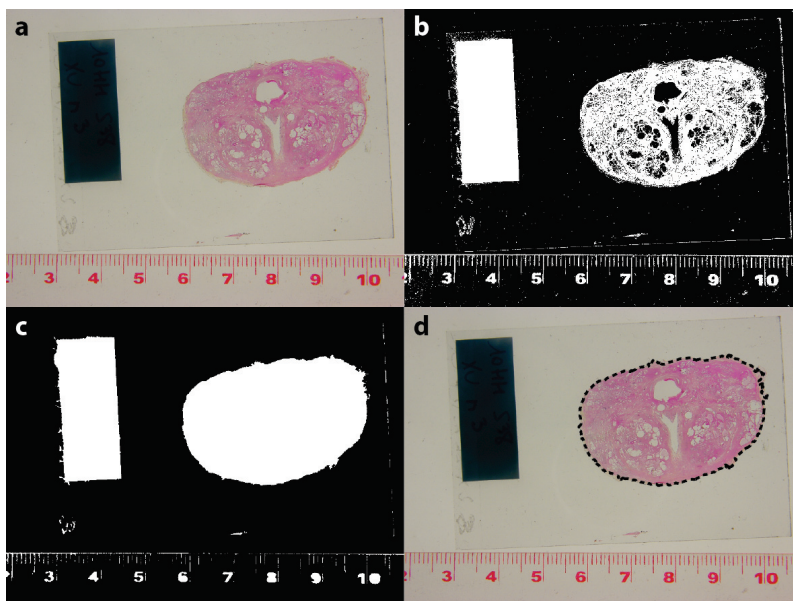


Figure 4.2: *The prostate in each image is segmented by classifying each pixel as background or prostate by comparing to the defined sample regions (b), the noise is removed and closed boundary objects are filled and eroded (c). The resultant segmentation is shown in (d).*

the similarity of the potential marker to the ideal shape, i.e. the cross section of the needle used to create the markers. The potential markers are classified according to their relative geometric score, into high, medium or low probability of being true markers.

#### 4.4.1 Potential Fiducial Marker Detection

The fiducial markers are (approximately circular) holes in the prostate tissue; their pixel intensity is thus that of the background. Potential fiducial markers are defined as objects of background intensity, positioned within the segmented prostate contour, whose area,  $a$  respects  $0.5\pi r^2 < a < 1.5\pi r^2$  (heuristic choice), where  $r$  is the radius of the needle used to create the fiducial markers. For each image, a binary mask is calculated, referred to as the fiducial mask of the image, where the pixels of potential fiducial markers have a value of 1 and all other pixels have a value of 0.

In order to calculate the fiducial mask, each pixel in the RGB image is classified as background or prostate according to the sum of the least-squares difference of its RGB component intensity from that of the mean values. The closed boundary objects are then filled, Figure 4.4(b), and a morphological open is applied using a disk-shaped structuring element of radius 10 pixels, Figure 4.4(c). Objects of area  $a < 0.5\pi r^2$  and objects of area  $a > 1.5\pi r^2$  are removed, Figure 4.4(d).

#### 4.4.2 Potential Fiducial Marker Scoring

For each object  $i$  returned in the  $N$  fiducial masks of the dataset, a geometric score  $s_i$ ,  $0 \leq s_i \leq 1$ , is calculated in order to quantify its similarity to a circle of radius  $r$ ,



Figure 4.3: *The images are translated such that the centre of the segmented prostate is at the centre of each image, cropped about the segmented prostate and padded such that each image in the dataset is the same size (a). An ellipse is then fitted to each detected prostate contour (b) in order to estimate the orientation of the image. Each image is then rotated (c) such that the orientation of the dataset is uniform.*

$s_i = 1$  indicates a perfect geometrical match. For each object  $i$ , the circular quality  $c_i$  (defined as  $c_i = 4\pi a_i/p_i^2$ , with  $p_i$  the perimeter) and area  $a_i$  is calculated, compared to the ideal values for a circle of radius  $r$  (1 and  $\pi r^2$  respectively) and divided by the maximum difference values measured across all the objects under test in that dataset (respectively  $\max |c_i - 1| \forall i$  and  $\max |a_i - \pi r^2| \forall i$ ) in order to calibrate each parameter between 0 and 1.

$$s_i = 1 - \left( w \frac{|c_i - 1|}{\max |c_i - 1| \forall i} + (1 - w) \frac{|a_i - \pi r^2|}{\max |a_i - \pi r^2| \forall i} \right) \quad (4.1)$$

$w$  is a weight coefficient,  $0 \leq w \leq 1$ , of practical value set to  $2/3$ . The geometric score is weighted in favour of the circular quality as we have observed that there are more non marker objects that approach the ideal area than non marker objects that approach a circular form. Figure 4.5 indicates the geometric score calculated for each object returned in the fiducial mask of a particular image.

It has been previously discussed in Section 3.3.6 ‘Fiducial Marker Geometry’, that as the needles are not inserted vertically, the fiducial markers created are not in fact circles but ellipses. However due to the small angles at which the needles are inserted ( $\theta_{n1} = 12.8^\circ$ ,  $\theta_{n2} = 13.8^\circ$ ,  $\theta_{n3} = 16.6^\circ$ ), the difference of the ellipses from circles (quantified in terms of the percentage difference of the area  $\Delta a$  and circular quality  $\Delta c$ ) is considered negligible,  $\theta_{n1}$ :  $\Delta a = +2.55\%$ ,  $\Delta c = -0.02\%$ ;  $\theta_{n2}$ :  $\Delta a = +2.97\%$ ,  $\Delta c = -0.03\%$ ;  $\theta_{n3}$ :  $\Delta a = +4.35\%$ ,  $\Delta c = -0.07\%$ . The markers are thus considered to be circles.

#### 4.4.3 Potential Fiducial Marker Classification

For a dataset of  $N$  images, there are theoretically  $3N$  fiducial markers to detect in the dataset (three markers per image). The potential fiducial markers detected across the  $N$  fiducial masks of the dataset are ordered from the highest to the lowest geometric score, i.e. from the highest to the lowest relative probability of being true markers. The potential markers are then classified into 3 sets: the first set  $S1$ , includes the potential markers with the top  $3N$  scores in the dataset, the second set  $S2$ , includes the potential markers with

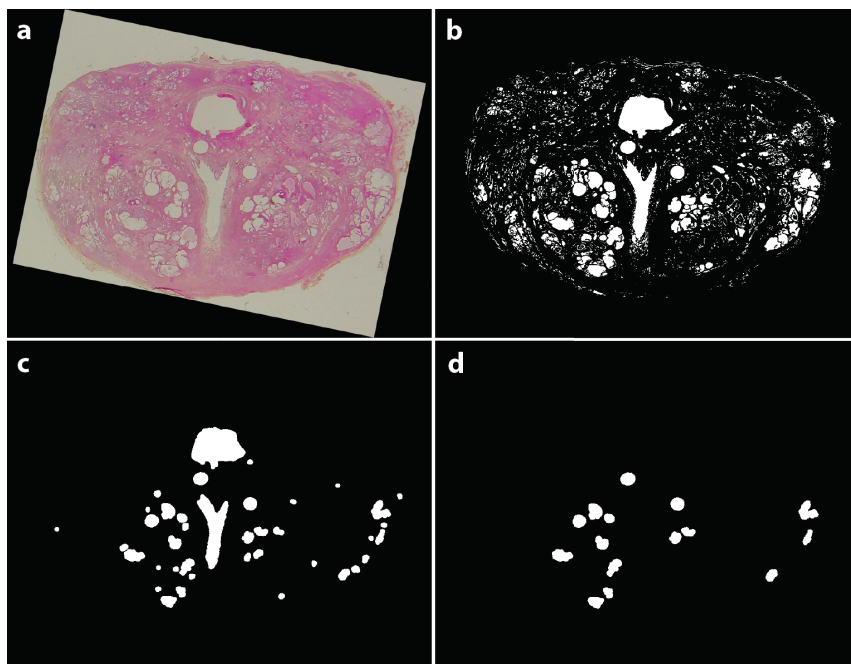


Figure 4.4: For each image (a), the potential fiducial markers are detected by first classifying each pixel as background or prostate (b), then following a morphological open (c), objects of area  $a < 0.5\pi r^2$  and objects of area  $a > 1.5\pi r^2$  are removed (d) resulting in the fiducial mask for the image.

the next best  $N$  scores. The third set, containing the remaining potential markers, is discarded. Figure 4.6 shows the classification of the potential fiducial markers detected for that particular image into  $S1$  (pink) and  $S2$  (blue) according to their relative geometric score with respect to all the other potential markers detected in the  $N$  fiducial masks. The fiducial markers that are not included in either  $S1$  or  $S2$  are no longer considered.

We define as  $N_E^{S1}$  and  $N_E^{S2}$  the number of potential markers in an image classified in, respectively,  $S1$  and  $S2$ , with  $N_E$  the total number of potential markers, i.e.  $N_E = N_E^{S1} + N_E^{S2}$ . Only the five potential markers with the highest scores are retained per image, i.e.  $N_E \leq 5$ .

At the end of the classification, there is for each image in the dataset, a list of the coordinates of the centre of each potential fiducial marker in that image, as well as whether each marker was classified in  $S1$  or  $S2$ .

## 4.5 True Fiducial Marker Detection and Identification

The insertion of the three fiducial needles into the prostate specimen creates three fiducial markers in each histology slice. As discussed in Section 3.3.5 ‘Model Geometry’, due to the semi-solid consistency of the fresh prostate, the needle angle geometry created in each specimen is slightly different and cannot be assumed to be that of the model geometry measured from the agar sample. However we do assume that each needle creates

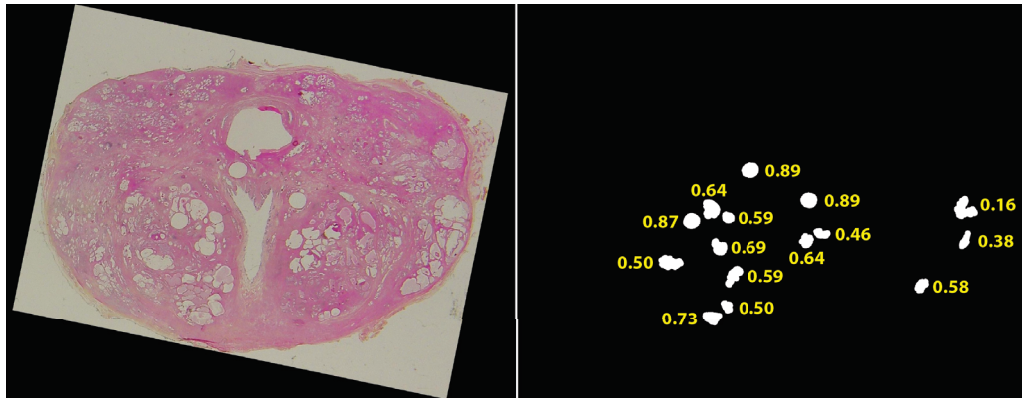


Figure 4.5: For each object returned in the fiducial mask, a geometric score  $s_i$ ,  $0 \leq s_i \leq 1$ , is calculated in order to quantify its similarity to a circle of radius  $r$ .

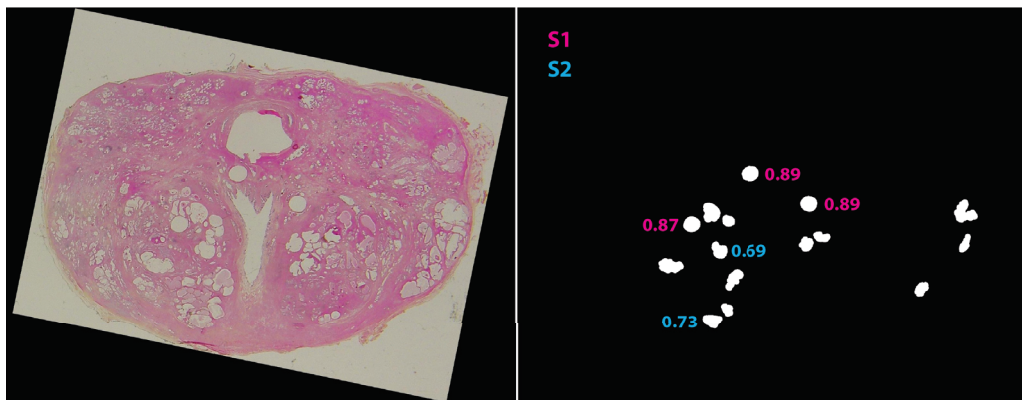


Figure 4.6: The potential fiducial markers are classified into 3 sets;  $S1$  (pink) includes the potential markers with the top  $3N$  scores in the dataset,  $S2$  (blue) includes the next best  $N$  scores, the remaining markers are discarded. Only the five potential markers with the highest scores are retained per image.

fiducial markers in a straight 3D line.

The insertion of the three needles, at three different angles in a *twist* style, creates a different triangle, formed by the three created fiducial markers, in each histology slice. The shape of the created triangle progressively changes from the apex to the base. Furthermore, if a circumcircle is fitted to the formed triangle, the clockwise order of the fiducial markers around the circumcircle is constant for each histology slice in the dataset. Figure 4.7 shows the three needles inserted, from the apex to the base using the developed apparatus, into a rectangular sample of agar. Circles denote the fiducial markers created at sequential axial planes. These axial planes are displayed on the right, in which the different and progressively changing shape of the triangle formed in each image can be visually appreciated. It can also be noted that the clockwise order of the markers on each slice remains constant for each axial plane.

The shape of the triangle at the apex is initialised by the manually identified markers in the first image, Section 4.3 ‘Pre-processing’. Using this initialisation, we study the

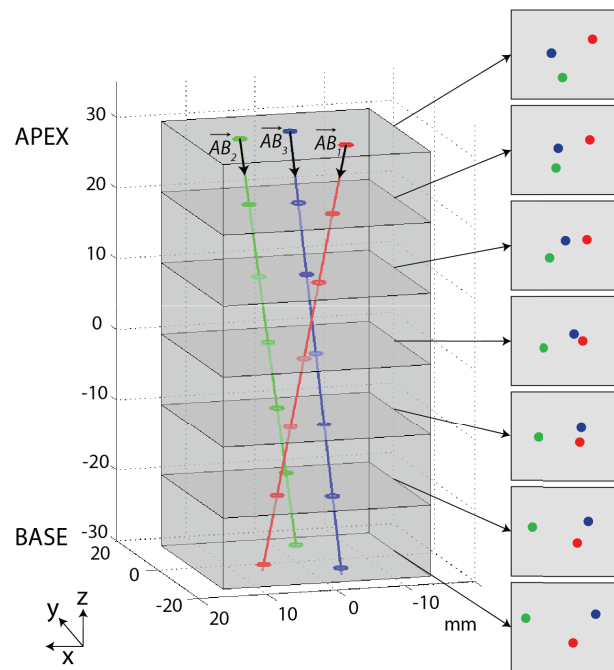


Figure 4.7: *The three needles inserted, from the apex to the base using the developed apparatus, create fiducial markers (denoted by circles) in each axial plane. The different and progressively changing shape of the triangle formed in each plane can be visually appreciated in the axial planes on the right. It can also be noted that the clockwise order of the markers remains constant for each axial plane.*

images, iterating from the apex to the base and then re-looping through the images, searching the gradually changing shape of the triangle amongst the detected potential fiducial markers. We search first amongst the potential markers classified as having a high probability of being true markers (set  $S1$ ), and then amongst those classified as having a medium probability of being true markers (set  $S2$ ). Each time true fiducial markers are detected amongst the potential fiducial markers, the shape of the triangle we are searching in that locality is further defined.

The algorithm developed to detect the true markers from the potential markers classified in  $S1$  and  $S2$  and to identify by which needle each marker was created, consists of four sequential steps. The pseudocode of the overall algorithm is shown in Algorithm 1, with each of the four processing steps detailed in the sections below.

---

Algorithm 1: *Detection and identification of the true fiducial markers from the potential markers.*

---

```

for step  $i = 1$  to 4 do
  while # markers detected  $> 0$  do
    # markers detected = 0;
    for image 2 to  $N$  do
      if # true markers detected for image  $< 3$  then
        Processing step  $i$ ;
        Update # markers detected;
      end
    end
  end
end

```

---

### Processing step 1

Step 1 only considers potential fiducial markers classified in  $S1$ , those with the highest probability of being true markers. This enables the algorithm to initialise with a minimal risk of an error being included.

We consider an image if three true markers have not yet been detected for the image and if there are at least three potential fiducial markers classified in  $S1$  for that image, i.e.  $N_E^{S1} \geq 3$ . Each possible fiducial marker (combinatoric) arrangement of the  $N_E^{S1}$  potential markers is generated,  $A_3^{N_E^{S1}} = C_3^{N_E^{S1}} \times P_3^3$ . For each arrangement, the first position in the arrangement corresponds to needle 1, the second position to needle 2 and the third position to needle 3, that is, each arrangement is of the form  $(n_1, n_2, n_3)$ .

The permutations of each combination that correspond to a flip orientation are eliminated as when the histology slices were digitised, they were positioned such that the normal vector of each slice is oriented in the same direction, see Section 3.6 ‘Digitisation of the Histology Slices’. The permutations that correspond to a flip orientation are those that when a circumcircle is fitted to the potential markers in the arrangement, the sequence  $(n_1, n_2, n_3)$  is no longer in a clockwise order.

Figure 4.8 shows an example of an image  $i$  in which four potential fiducial markers classified in  $S1$  have been detected. The four possible combinations of these potential markers are detailed. Studying the permutations of one of these possible combinations, by referring to the clockwise order defined by the fiducial markers in the first image, the permutations that correspond to a flip orientation can be eliminated.

Each possible arrangement is tested by calculating the 2D least-squares rigid affine transform [Arun *et al.* (1987)] that best registers the arrangement under test to a target set defined for that image. The target set is defined as the 2D coordinates of the closest

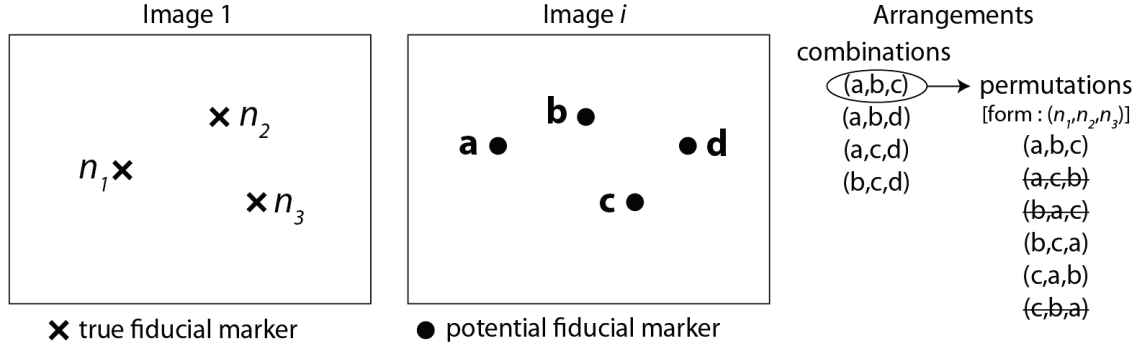


Figure 4.8: Sample image *i* in which four potential fiducial markers classified in *S1* have been detected. For each combination, the permutations that correspond to a flip orientation can be eliminated by referring to the clockwise order defined by the fiducial markers in the first image.

(in terms of inter-slice spacing) previously detected set of true fiducial markers. If, for example, we were considering image *i* in Figure 4.8 and we were testing the arrangement **(a,b,d)** and the closest previously detected set of true markers were those detected in image 1, the transform is calculated to best register **a** to  $n_1$ , **b** to  $n_2$  and **d** to  $n_3$ , that is we calculate the 2D rotation matrix  $R$  and the translation vector  $T$  to minimise

$$\Sigma^2 = \| n_1 - (R\mathbf{a} + T) \|^2 + \| n_2 - (R\mathbf{b} + T) \|^2 + \| n_3 - (R\mathbf{d} + T) \|^2 \quad (4.2)$$

The error of each arrangement is defined as the maximum 2D distance (in mm) between the respective elements of the transformed arrangement under test and the target set, normalised with respect to the number of elements in the arrangement. That is, for the previous example,

$$e = \frac{\max(\| n_1 - (R\mathbf{a} + T) \|, \| n_2 - (R\mathbf{b} + T) \|, \| n_3 - (R\mathbf{d} + T) \|)}{3} \quad (4.3)$$

The arrangement with the minimum error,  $e_{min}$ , is compared to an error limit defined for step 1, denoted  $L_1$ , see Section 4.9.3 for the numerical value. If  $e_{min} \leq L_1$ , the potential markers in the arrangement under test are considered the true markers for that image and identified as having been created by needle 1, 2 or 3 according to their position in the arrangement.

If  $e_{min} > L_1$  the potential markers in the arrangement are temporarily considered the true markers and confirmed if in two following images, arrangements with errors  $e_{min} \leq L_1$  are detected. The temporarily considered arrangement will be used as the target set (closest previously detected set of true fiducial markers) for the following images. As the location of non true markers is considered to be random, an arrangement of non true markers will probably not be reproduced in the following images. So if the temporarily considered arrangement contains non true markers, arrangements with errors  $e_{min} \leq L_1$  will not be found in the following images.

Each image in the patient dataset is considered, from image 2 to  $N$ , in this manner. We then reiterate through the images until no further markers are detected, see Algorithm 1. Images for which three fiducial markers have been detected are not re-studied.

### Processing step 2

The centres of the detected fiducial markers are 2D coordinates. However, as it is known from which image each marker was detected, and the height of each image from the apex is known, the detected fiducial markers can be represented in a 3D-space. From the detected fiducial markers, three ‘synthetic needles’ can be calculated. The synthetic needles are 3D least-squares lines passing through the previously detected fiducial markers. For any image, a distance  $z$  from the apex, the points of intersection of the three synthetic needles with the image plane can be calculated. The points of intersection indicate the expected locations of the markers and thus the expected shape of the triangle formed by the three markers. The three points of intersection thus define the centres of three circular regions of interest (ROIs), radius  $r_{ROI}$ , for that image, see Figure 4.9. The synthetic needles (and thus the positions of the ROIs) are updated each time a new marker is detected.

As in step 1, step 2 only considers potential fiducial markers classified in  $S1$ . Furthermore, if a potential marker is to be considered, it must be positioned within one of the three ROIs. Therefore, an image is considered if three true markers have not yet been detected for the image and if, for that image, there are at least two potential fiducial markers classified in  $S1$  ( $N_E^{S1} \geq 2$ ) and they are positioned within at least two different ROIs.

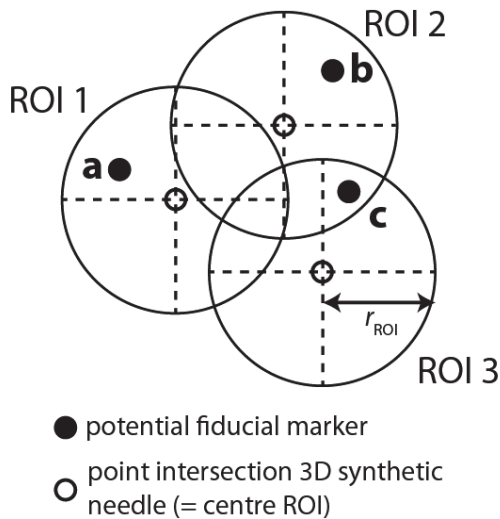


Figure 4.9: *The points at which the synthetic needles intersect an image define the centres of the three ROIs (radius  $r_{ROI}$ ) for that image. Step 2 and 3 only consider elements positioned within the ROIs. When defining the possible arrangements, potential markers are placed in arrangement positions according to the ROI(s) in which they are located.*

Each possible fiducial marker arrangement of the potential markers is generated. As before, each arrangement is of the form  $(n_1, n_2, n_3)$ . The ROIs in which the potential markers are positioned are taken into account when defining the arrangements, that is, if a potential marker is positioned within ROI 1, it can only be placed in the  $n_1$  position of arrangements. However ROIs may overlap and so a potential marker may be placed in

more than one arrangement position. For example, in Figure 4.9, the potential marker  $\mathbf{c}$  could be identified as having been created by needle 2 or 3 and thus can be placed in either the second or third position of arrangements. On the other hand, the potential marker  $\mathbf{a}$  could only be placed in the first position of any arrangement.

Arrangements formed by ‘leaving out’ one of the elements are also generated. However each arrangement must contain a minimum of two potential markers. As in step 1, arrangements that correspond to a flip orientation are eliminated. Considering again the example in Figure 4.9, the possible arrangements for the potential markers (created by needle 1, 2, 3 respectively) are  $(\mathbf{a}, \mathbf{b}, \mathbf{c})$ ,  $(\mathbf{a}, -, \mathbf{c})$ ,  $(\mathbf{a}, \mathbf{b}, -)$ ,  $(\mathbf{a}, \mathbf{c}, -)$ ,  $(-, \mathbf{b}, \mathbf{c})$ , where the symbol  $-$  denotes that no element is tested for that position.

Each possible arrangement is tested by calculating the 2D least-squares rigid affine transform that best registers the arrangement under test to a target set defined for that image. The target set is defined as the 2D coordinates of the centres of the three ROIs of that image. The error, defined as in step 1, is the maximum 2D distance (in mm) between the respective elements of the transformed arrangement under test and the target set, normalised with respect to the number of elements in the arrangement. The potential markers in the arrangement are considered to be the true markers for that image if  $e_{min} \leq L_2$ .

Each image in the patient dataset is considered, from image 2 to  $N$ , in this manner. We then reiterate through the images until no further markers are detected. Images for which three fiducial markers have been detected are not re-studied, however if only two markers have been detected for an image, the image is re-studied to see if there exists an arrangement with a lower associated error than that already detected, in which case the detected fiducial markers for that image are updated.

### Processing step 3

Step 3 considers potential fiducial markers classified in both  $S1$  and  $S2$ , provided that they are positioned within one of the three circular ROIs. Therefore, an image is considered if three true markers have not yet been detected for the image and if, for that image, there are at least two potential fiducial markers classified in  $S1$  or  $S2$  ( $N_E \geq 2$ ) and they are positioned within at least two different ROIs.

The possible fiducial maker arrangements of the potential markers are generated and tested as in step 2, with the target set defined as the 2D coordinates of the centres of the three ROIs of that image. The error of each arrangement under test is as previously defined in step 1 and 2. The potential markers in the arrangement are considered to be the true markers for that image if  $e_{min} \leq L_3$ .

Each image in the patient dataset is considered, from image 2 to  $N$ , in this manner. We then reiterate through the images until no further markers are detected. Images for which three fiducial markers have been detected are not re-studied, however if only two markers have been detected for an image, the image is re-studied to see if there exists an

arrangement with a lower associated error than that already detected, in which case the detected fiducial markers for that image are updated.

#### Processing step 4

For step 4, no ROIs are taken into account. This enables markers to be detected in images where the pre-processing coarse alignment (Section 4.3 ‘Pre-processing’) was insufficient and the potential markers thus do not fall within the ROIs.

Step 4 considers potential fiducial markers classified in both  $S1$  and  $S2$ . An image is considered if three true markers have not yet been detected for the image and if, for that image, there are at least two potential fiducial markers classified in  $S1$  or  $S2$  ( $N_E \geq 2$ ).

The possible fiducial marker arrangements of the potential markers are generated (minimum two potential markers per arrangement) and tested, with the target set defined as the 2D coordinates of the closest (in terms of inter-slice spacing) previously detected set of fiducial markers. The error of each arrangement under test is as previously defined in step 1-3. The potential markers in the arrangement are considered to be the true markers for that image if  $e_{min} \leq L_4$ .

Each image in the patient dataset is considered, from image 2 to  $N$ , in this manner. We then reiterate through the images until no further markers are detected. Images for which three fiducial markers have been detected are not re-studied. Images for which two fiducial markers have been detected are not changed but potential markers that could complete the arrangement are considered.

## 4.6 Alignment and Shear Correction of the Histology Slices

### 4.6.1 Alignment

The fiducial marker detection and identification process completed, we proceed to aligning the histology slices using the detected markers. First, images for which less than two fiducial markers have been detected are discarded as the alignment cannot be calculated. The three synthetic needles, 3D least-squares lines passing through the detected markers, are calculated. For each image a distance  $z$  from the apex, the points at which the synthetic needles intersect the image plane are calculated, the 2D coordinates are denoted as  $s_1$ ,  $s_2$  and  $s_3$ . For each image, a 2D least-squares rigid affine transform is calculated that best registers the detected fiducial markers for that image (denoted as  $n_1$ ,  $n_2$  and  $n_3$ ) to the points at which the synthetic needles intersect the image. That is, for each image, we re-calculate  $R$  and  $T$  such as to minimise

$$\Sigma^2 = \|s_1 - (Rn_1 + T)\|^2 + \|s_2 - (Rn_2 + T)\|^2 + \|s_3 - (Rn_3 + T)\|^2 \quad (4.4)$$

The transformation is applied to the image for which it was calculated. A transformation is calculated for, and applied to, each image in the patient dataset, from image 1 to  $N$ .

Once each image in the dataset has been individually 2D transformed, the sum of the 2D distances of each detected marker from its respective synthetic needle is calculated,

$$d = \sum_{image=1}^N (\|s_1 - (Rn_1 + T)\| + \|s_2 - (Rn_2 + T)\| + \|s_3 - (Rn_3 + T)\|) \quad (4.5)$$

The synthetic needles are then re-calculated and the 2D transformation for each image is re-calculated and re-applied. The process is iterated until the difference of sums between two iterations is less than 0.001 mm, that is  $d_i - d_{i+1} < 0.001$  mm.

#### 4.6.2 Shear Correction

Two final parameters to fix arises from the ‘shear effect’ phenomenon, that the distance between any two points on a horizontal plane is unchanged by the application of a shear matrix,  $T_{\text{shear}}$ ,

$$T_{\text{shear}} = \begin{bmatrix} 1 & 0 & \lambda_1 \\ 0 & 1 & \lambda_2 \\ 0 & 0 & 1 \end{bmatrix} \quad (4.6)$$

where  $\lambda_1$  and  $\lambda_2$  are the shear parameters. The effect can be visually appreciated in Figure 5.5. The shear effect means that, though the histology slices were aligned by registering the detected markers for each slice to the synthetic needles, the ensemble of slices may need to be ‘un-sheared’.

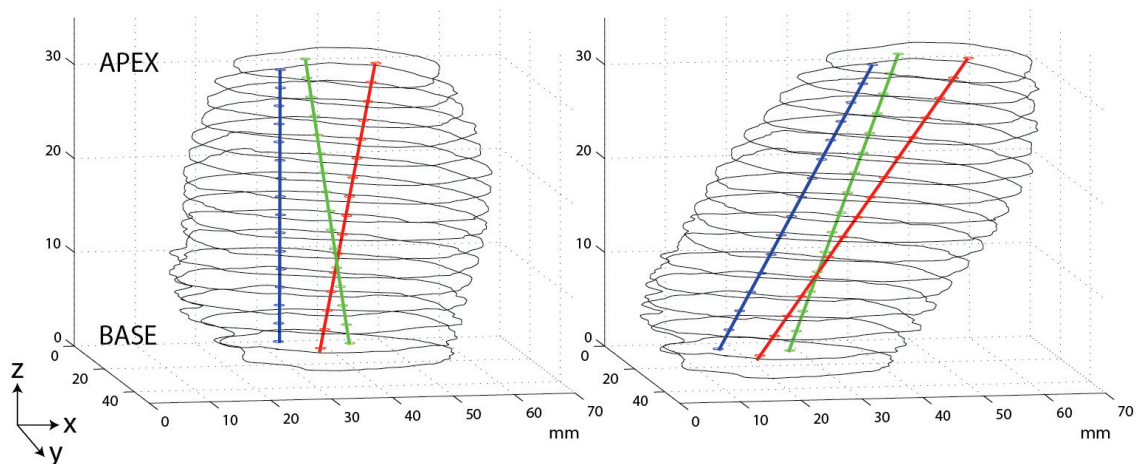


Figure 4.10: The ‘shear effect’ is due to the fact that the distance between any two points on a horizontal plane is unchanged by the application of a shear matrix,  $T_{\text{shear}}$ .

From the model geometry, the direction vectors, from the apex to the base, of the three needles were measured, denoted  $\vec{AB}_1$ ,  $\vec{AB}_2$  and  $\vec{AB}_3$ , describing the direction at which the apparatus guides the insertion of each needle, see Figure 4.7. The three model needles were arbitrarily labelled as needle 1, 2 and 3.

It is undetermined at this point the correspondence between the three synthetic needles

in the patient dataset and the three model needles. Though care was taken when the histology slices were digitised that the normal vector of each slice was oriented in the same direction, that is, that no ‘flip orientation’ exists *between* the slices, the ensemble of histology slices in the dataset may need to be flipped.

In order to determine the correspondence between the three needles in the patient dataset and the three model needles, the  $3!$  possible permutations are generated and each is tested with and without a flip applied to all the slices in the patient dataset, thus a total of 12 permutations,  $p \in \{1, 2, \dots, 12\}$ .

To test each permutation, the synthetic needles in the patient dataset are labelled (as needle 1, 2 and 3) according to the permutation under test and the least-squares rigid affine transform (rotation  $R$  and translation  $T$ ) is calculated in order to align the three markers at the apex of the patient dataset with the three markers at the apex of the model. The transformation is applied to all the slices in the patient dataset. The error of the alignment,  $E_1(p)$ , is defined as the mean distance between the corresponding markers at the apex of the model and the apex of the patient dataset after the transformation has been applied.

The direction vector of each of the three needles in the transformed patient dataset is calculated, denoted as  $\vec{AB}_{p,1}$ ,  $\vec{AB}_{p,2}$  and  $\vec{AB}_{p,3}$ , and the parameters  $\lambda_1$  and  $\lambda_2$  of the shear matrix are calculated such as to minimise the angular difference between the corresponding direction vectors of the model and the transformed patient dataset. That is, we minimise the function  $E_2(p)$ ,

$$E_2(p) = \cos^{-1} \left( \frac{\vec{AB}_1 \cdot \vec{AB}_{p,1}}{\|\vec{AB}_1\| \|\vec{AB}_{p,1}\|} \right) + \cos^{-1} \left( \frac{\vec{AB}_2 \cdot \vec{AB}_{p,2}}{\|\vec{AB}_2\| \|\vec{AB}_{p,2}\|} \right) + \cos^{-1} \left( \frac{\vec{AB}_3 \cdot \vec{AB}_{p,3}}{\|\vec{AB}_3\| \|\vec{AB}_{p,3}\|} \right) \quad (4.7)$$

where  $f \cdot g$  indicates the dot product of vector  $f$  and  $g$ .

The error of each permutation is defined as the average of  $E_1(p)$  and  $E_2(p)$ . The permutation with the minimum error indicates if the ensemble of patient histology slices need to be flipped and the parameters  $\lambda_1$  and  $\lambda_2$  of the optimal shear matrix  $T_{\text{shear}}$  to be applied to the histology slices of the patient dataset to correct for the shear effect.

This shear correction method assumes that the plane along which the histology slices were cut was exactly parallel to the needle insertion guide of the apparatus. It can be noted that, though the histology slices have undergone a shrinkage with respect to the model geometry, as the shear effect is corrected for using angles, it is not necessary to take the shrinkage into account.

## 4.7 Transformation Summary

In summary, the following geometric transformations are calculated for each image:

- (i) a coarse alignment which consists of a 2D rotation and translation,  $T_{\text{init}}$ ,

- (ii) a 2D rotation and translation to align the fiducial markers detected for the image with the three points at which the synthetic needles intersect the image, recalculated and applied each iteration until convergence,  $T_k, k = (1, 2, \dots, K)$ , with  $K$  the number of iterations to convergence and
- (iii) a 3D shear to correct for the shear effect,  $T_{\text{shear}}$ .

Thus for each slice, the total matrix transformation is  $T_{\text{shear}} \times T_K \times \dots \times T_2 \times T_1 \times T_{\text{init}}$ .

## 4.8 Validation

The accuracy of the alignment achieved with the proposed protocol and algorithm was quantified in simulated images (Section 4.8.1), in a beef liver sample (Section 4.8.2) and in 10 prostate specimens (Section 4.8.3). The quality of the shear correction was estimated using the simulated images and the beef liver sample.

### 4.8.1 Validation in Simulated Images

A dataset of simulated images was created for each prostate specimen studied. The parameters of the simulated images were set identical to those of the prostate specimen dataset, i.e. the same number of images  $N$  with the same inter-slice spacing, the same pixel resolution and the same number and distribution of fiducial markers detected. The difference between the datasets is thus the absence of tissue deformation in the simulated images. A comparison of the accuracy of the alignment achieved with the histology images and that achieved with the simulated images of each specimen will thus indicate if there is a residual error associated with the algorithm.

The simulated images are binary images, background = 0, markers = 1, see Figure 4.12. The position of the fiducial markers in each of the  $N$  images is defined by intersecting the model geometry with an axial plane at an appropriate height  $h$  from the apex, as illustrated in Figure 4.7.

A ‘validation marker’ is also included in each simulated image. The validation marker is a pentagon, formed from a symmetric hexagon, side length  $l = 4.62$  mm, of which one point had been shaved flat, see Figure 4.11, the removed point is represented by the dashed lines. We define the direction vector of the validation marker as the vector from the centre of the base of the pentagon to the tip of the pentagon, indicated by an arrow in Figure 4.11. The validation marker is included at the same position in each image.

Once each of the  $N$  images of the simulated dataset has been defined, a random rigid transformation is applied to each image in the dataset, see Figure 4.12. The transformation consists of a random rotation  $R(\varphi)$ ,  $-45^\circ \leq \varphi \leq 45^\circ$ , and a random translation  $T(\gamma)$ ,  $|T(\gamma)| \leq 12$  mm, in any direction.

The fiducial markers were detected in each image and the images were aligned and shear corrected using the method described in Section 4.6. The accuracy of the alignment was quantified at the fiducial markers by calculating the minimum, mean, maximum and

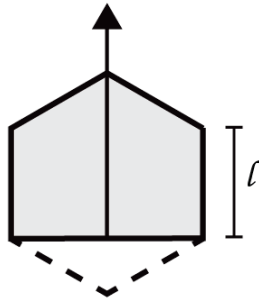


Figure 4.11: The validation marker is formed from a symmetric hexagon, side length  $l = 4.62$  mm, of which one point had been shaved flat (dashed section), resulting in a pentagon. The direction vector of the validation marker, indicated by the arrow, is defined as the vector from the centre of the base of the pentagon to the tip of the pentagon.

standard deviation of the distances of each fiducial marker from its respective synthetic needle after alignment of the slices. The accuracy of the alignment was also quantified at the validation markers; a 3D least-squares line passing through the centres of the validation markers after alignment of the slices was calculated. The minimum, mean, maximum and standard deviation of the distances from the centre of each validation marker to the least-squares line was calculated.

The validation markers were, before application of the random rotation and translation, each located at the same position of the simulated images and each at the same orientation (defined by the direction vector of the validation marker). Therefore, after alignment of the images, the validation markers should each be at the same position and orientation, and a line passing through the centres of the validation markers should be vertical. The angular precision of the alignment was quantified by calculating the standard deviation of the orientations of the direction vectors after the alignment of the images. The quality of the shear correction was measured by calculating the angular difference from the vertical of the 3D least-squares line passing through the centres of the validation markers after alignment of the images.

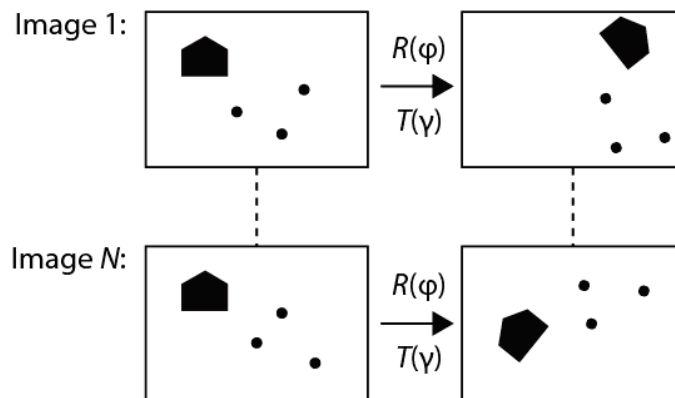


Figure 4.12: For each prostate specimen studied, a dataset of simulated images was created with a validation marker included at the same position before a random rotation  $R(\varphi)$  and translation  $T(\gamma)$  is applied to each image.

Note that the validation marker was situated approximately 20 mm from the fiducial markers. It can be seen from the prostate dimensions in Figure 3.4 that 20 mm represents a position at the periphery of the prostate. Therefore, the quantification of the accuracy

of the alignment at the validation markers enables an estimation of how well a peripheral cyst or tumour would be aligned after alignment of prostate histology slices using the method described in Section 4.6.

### 4.8.2 Validation in Beef Liver

A dataset of validation images was prepared using a sample of beef liver. Three needles were inserted into the fresh beef liver sample using the apparatus, creating fiducial markers in the same manner as they are created in the prostate specimens. Parallel and approximately 20 mm from the needles, was inserted a pointed metal bar with a cross section as previously described (a pentagon formed from a symmetric hexagon, side length  $l = 4.62$  mm), creating a validation marker at the same position and orientation in each image. The needles and metal bar were left in place during the tissue fixation. The liver was then sectioned, embedded in paraffin and sliced to obtain whole mount histology slices using the same protocol as that used for a prostate specimen, described in Section 3.5. A sample beef liver histology slice is shown in Figure 4.13. The slices were digitised using the standardised method described in Section 3.6.

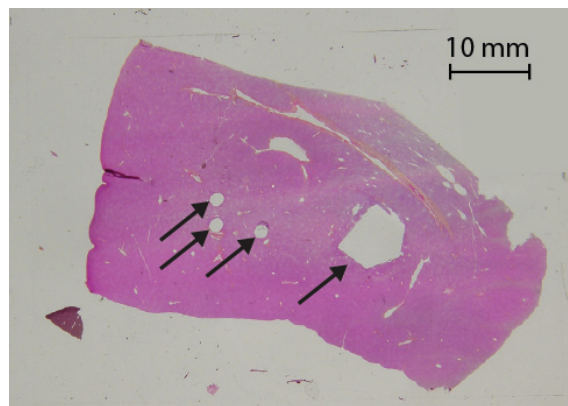


Figure 4.13: *Sample beef liver histology slice, the three fiducial markers and the validation marker are indicated by arrows.*

The fiducial markers were detected in each image and the ideal pentagonal cross-section was least-squares fitted to the validation marker detected in each image. The images were aligned and shear corrected using the method described in Section 4.6. The performance of the alignment was tested under three scenarios;

- (i) using 3 fiducial markers per image to align the dataset,
- (ii) using 2.71 markers per image to align the dataset (the average number visible and detected per image for a prostate specimen) and
- (iii) using 2.47 markers per image to align the dataset (the worst case number of markers visible and detected per image for a prostate specimen).

Note that for both (ii) and (iii), the fiducial markers to be eliminated were randomly selected, the random selection was carried out 30 times and the results reported are the average of the 30 iterations.

The accuracy of the alignment was quantified, for each of the three scenarios, at the fiducial markers by calculating the minimum, mean, maximum and standard deviation of the distances of each fiducial marker from its respective synthetic needle after alignment of the slices. The accuracy of the alignment was also quantified at the validation markers by calculating the minimum, mean, maximum and standard deviation of the distances from the centre of each validation marker to a 3D least-squares line passing through the centres of the validation markers after alignment of the slices.

For each of the three scenarios, the angular precision of the alignment was quantified by calculating the standard deviation of the orientations of the direction vectors of the validation markers after alignment of the images. The quality of the shear correction was measured by calculating the angular difference from the vertical of the 3D least-squares line passing through the centres of the validation markers after alignment and shear correction of the images.

### 4.8.3 Experimental Validation in 10 Prostate Specimens

Fiducial markers were created using the apparatus in 10 fresh prostate specimens. The histology slices were prepared following the protocol described in Section 3.5. The images were aligned and shear corrected using the method detailed in Section 4.6. The accuracy of the alignment was quantified at the fiducial markers by calculating the minimum, mean, maximum and standard deviation of the distances of each fiducial marker from its respective synthetic needle after alignment of the slices. The robustness of the algorithm was investigated. For three prostate datasets, the algorithm was iterated 5 times, from the pre-processing step (redefinition each iteration of the sample regions of the background and prostate) to the fine alignment and shear correction of each slice. For each dataset, the standard deviation of the alignment accuracy results of the 5 iterations was calculated.

## 4.9 Results

### 4.9.1 Results in Simulated Images

A dataset of simulated images was created for each prostate specimen studied. The parameters of the simulated images were set identical to those of the prostate dataset. After alignment and shear correction of the simulated images, the minimum, mean, maximum and standard deviation of the distances of the fiducial markers from their respective synthetic needles were limited only by the computing precision for each dataset studied.

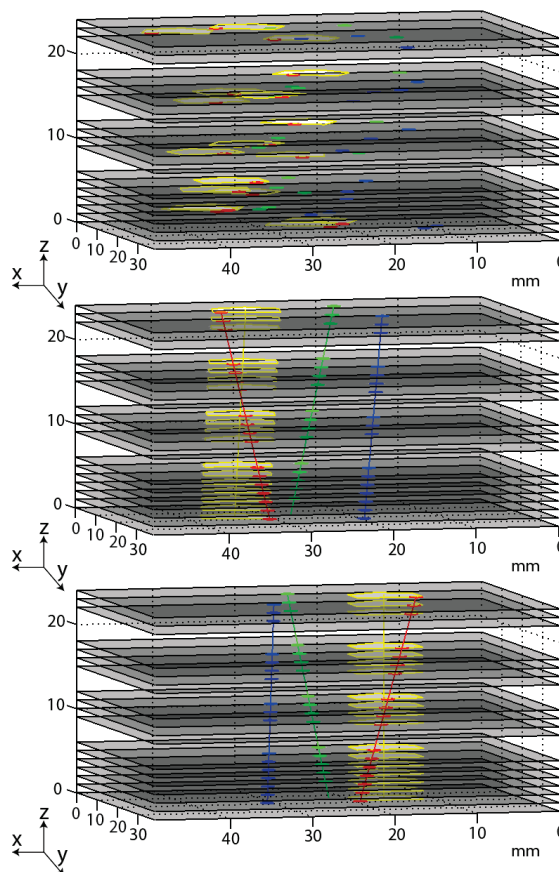
The accuracy of the alignment was also evaluated at the validation markers, positioned approximately 20 mm from the fiducial markers. After alignment and shear correction of the slices, a 3D least-squares line passing through the centres of the validation markers was calculated. The minimum, mean, maximum and standard deviation of the distances from the centre of each validation marker to the least-squares line was, for each dataset, limited only by the computing precision. Furthermore, the angular precision of the alignment,

defined as the standard deviation of the direction vector of the validation markers, was limited only by the computing precision.

The validation marker was located at the same position in each simulated image, therefore after alignment and shear correction of the slices, the 3D least-squares line passing through the centres of the validation markers should be exactly vertical. After alignment, but before shear correction, the average angle with respect to the vertical of the least-squares validation line was  $12.30^\circ \pm 4.36^\circ$  (minimum =  $7.58^\circ$ , maximum =  $19.88^\circ$ ). After shear correction, the angle with respect to the vertical of the least-squares validation line was on average  $0.06^\circ \pm 0.00^\circ$  (minimum =  $0.06^\circ$ , maximum =  $0.06^\circ$ ).

Figure 4.14 shows the stack of simulated images for a sample dataset, the fiducial markers and their respective synthetic needles are shown in red, green and blue, the validation marker and the 3D least-squares line passing through the centres of the validation markers are in yellow, (top) before alignment of the simulated images, (middle) after alignment of the images using the fiducial markers, the 3D least-squares line passing through the validation markers is at an angle of  $13.47^\circ$  to the vertical, (bottom) after shear correction of the simulated images, the validation markers line is now at an angle of  $0.06^\circ$  to the vertical. Note that the ensemble of slices have been flipped.

Figure 4.14: *A sample dataset of simulated images, the fiducial markers are shown in red, green and blue, the validation marker is outlined in yellow, (top) before alignment of the simulated images, (middle) after alignment of the images using the fiducial markers, red, green and blue lines indicate the synthetic needles and the least squares 3D line passing through the centres of the validation markers is in yellow, the line is at an angle of  $13.47^\circ$  to the vertical, (bottom) after shear correction of the simulated images, the least squares line passing through the validation markers is now at an angle of  $0.06^\circ$  to the vertical. Note that the ensemble of slices have been flipped.*



### 4.9.2 Results in Beef Liver

The beef liver dataset consisted of 20 images, on average 3 images per 6 mm section, see Figure 4.15 which shows the stack of beef liver images, (top) before alignment of the beef liver images, (middle) after alignment of the images using 2.71 fiducial markers per image, (bottom) after shear correction of the aligned images. The fiducial markers and their respective synthetic needles are shown in red, green and blue and the validation markers and the 3D least-squares line passing through the centres of the validation markers are shown in yellow.

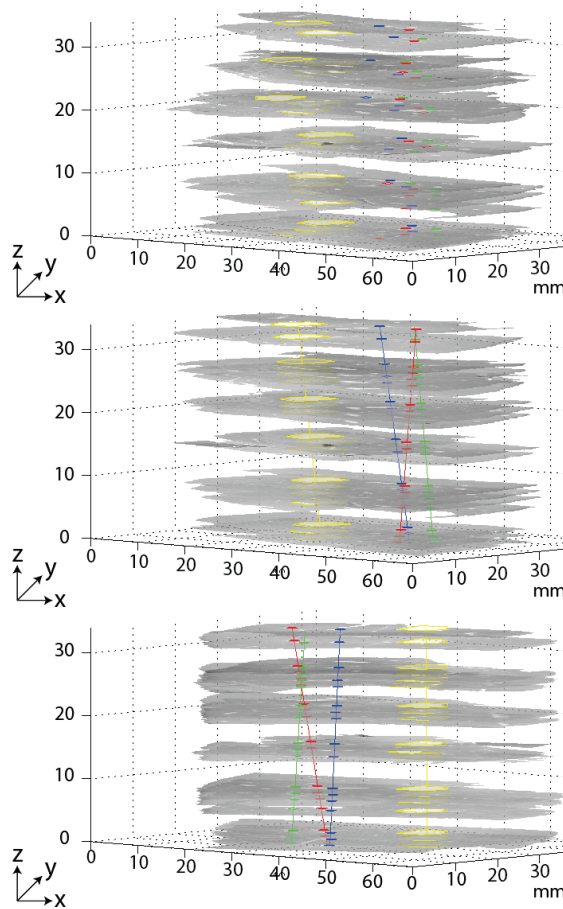


Figure 4.15: *The beef liver dataset consisted of 20 images, the fiducial markers and their respective synthetic needles are shown in red, green and blue and the validation markers and the 3D least-squares line passing through the centres of the validation markers is shown in yellow, (top) before alignment of the beef liver images, (middle) after alignment of the images using 2.71 fiducial markers per image, (bottom) after shear correction of the aligned images.*

The accuracy of the alignment, using 2.71 markers per image, was on average  $0.11 \pm 0.09$  mm at the fiducial markers (see Table 4.1) and  $0.58 \pm 0.43$  mm at the validation markers positioned approximately 20 mm from the fiducial markers (see Table 4.2). The angular precision, defined as the standard deviation of the orientations of the validation markers after alignment, using 2.71 markers per image, was on average  $2.67^\circ \pm 0.51^\circ$ , see Table 4.3. After alignment of the slices using 2.71 markers per image, but before shear correction, the average angle with respect to the vertical of the least-squares validation line was  $8.17^\circ \pm 1.45^\circ$ . After shear correction, the angle with respect to the vertical of the least-squares validation line was on average  $7.54^\circ \pm 1.46^\circ$ .

Nb. fiducial markers per image	min	mean	max	variance
3	0.01	0.12	0.45	0.09
2.71	0.01	0.11	0.41	0.09
2.47	0.01	0.11	0.36	0.08

Table 4.1: *Experimental validation in beef liver: performance of the alignment quantified (in mm) at the fiducial markers after alignment using 3, 2.71 and 2.47 fiducial markers per image.*

Nb. fiducial markers per image	min	mean	max	variance
3	0.14	0.52	1.34	0.35
2.71	0.10	0.58	1.65	0.43
2.47	0.12	0.66	1.79	0.46

Table 4.2: *Experimental validation in beef liver: performance of the alignment quantified (in mm) at the validation markers after alignment using 3, 2.71 and 2.47 fiducial markers per image.*

Nb. fiducial markers per image	min	mean	max	variance
3	-	2.35	-	-
2.71	1.89	2.67	4.04	0.51
2.47	1.81	2.92	4.14	0.69

Table 4.3: *Experimental validation in beef liver: angular precision of the alignment, quantified (in  $^{\circ}$ ) as the standard deviation of the orientation of the validation markers after alignment using 3, 2.71 and 2.47 fiducial markers per image. The results presented are the average of 30 iterations.*

Nb. fiducial markers per image	average angle before shear correction	average angle after shear correction
3	7.66	7.27
2.71	$8.17 \pm 1.45$	$7.54 \pm 1.46$
2.47	$7.58 \pm 2.11$	$6.96 \pm 2.20$

Table 4.4: *Experimental validation in beef liver: the quality of the shear correction was measured by calculating the angular difference from the vertical of the 3D least-squares line passing through the centres of the validation markers after alignment and before and after shear correction of the images. The results presented are the average of 30 iterations.*

### 4.9.3 Results in 10 Prostate Specimens

Fiducial markers were created in 10 fresh prostate specimens, resulting in an average of 19.2 histology slices digitised per specimen (minimum 17, maximum 22).

Values used in the algorithm were experimentally defined using a training dataset of 5 prostate specimens and were as follows: the weight coefficient in the geometric score,  $w = \frac{2}{3}$ , the classification of the detected objects according to their relative geometric score,  $S1$  contained the top  $3N$  scores and  $S2$  the next best  $N$  scores, the radius of the ROIs,  $r_{ROI} = 5$  mm, the error limit for each of the steps,  $L_1 = 0.3$  mm,  $L_2 = L_3 = L_4 = 0.5$  mm.

The segmentation of the prostate was achieved using a RGB threshold-based technique. This method was adequate as, irrespective of the slice dependent staining intensity, there was always a sharp gradient between the prostate tissue and the uniform intensity background for each R, G and B component of the image. Furthermore, the distinct difference between the tissue and background meant that a prior intensity normalisation of the images was unnecessary. Furthermore, we have verified that the proposed RGB threshold-based technique was more effective than a luminance-based thresholding of the monochrome image. The dashed line in Figure 4.2 and Figure 4.3 shows a sample segmentation result. This segmentation quality was achieved in each of the 192 images across the 10 prostate specimens, indicating that the RGB threshold-based segmentation technique was both adequate and robust.

Theoretically three fiducial markers are created in each histology slice, considering the digitised histology slices of the prostate specimen dataset, on average 93.7% of the markers created are visible to the eye (worst case 87.7%, best case 100%). Of those markers visible, on average 98.7% were returned as objects in the fiducial masks (worst case 96.2%, best case 100%).

By ordering the objects according to their relative geometric score, on average 88.4% of the objects included in  $S1$  and 9.2% of the objects included in  $S2$  are true markers. The overall result being that, on average, 99.0% (worst case 97.8%, best case 100%) of the true markers returned as objects in the masks had a geometric score sufficient to be considered, i.e. were included in  $S1$  or  $S2$ .

Of the objects included in ( $S1$ ,  $S2$ ), on average 98.5% were automatically correctly detected and identified (worst case 95.8%, best case 100%), excluding the three markers per dataset that are manually detected. This equates to, on average, the correct automatic detection and identification of 96.1% of the markers visible to the eye (worst case 93.6%, best case 100%). Overall, this results in an average of 2.71 markers per image to align the dataset (worst case 2.47, best case 2.89). Excluding the first image of each dataset, for which the three markers are manually detected, three markers were detected in 75.2% of the images and two markers were detected in 23.7% of the images. Images for which less than two markers were detected are discarded as the alignment cannot be calculated, less than two markers were detected in 1.1% of images.

Recall for processing step 2, Section 4.5 ‘True Fiducial Marker Detection and Identifi-

---

cation', that a minimum of two fiducial markers detected per needle is required to calculate the synthetic needles that define the ROIs. On average 11.6 markers (worst case 8, best case 15) are detected per needle by step 1.

There are two types of errors that can occur;

- type (i) an object that is not a true marker is determined to be a marker,
- type (ii) a marker is erroneously identified i.e. a marker created by needle 1 is identified as having been created by needle 2 or needle 3.

The error is first quantified as the distance between the erroneously detected object and the position of the marker it was determined as, referred to as the direct error measurement. However, as for a slice to be aligned, there must be at least 2 fiducial markers detected in the image, the effect of the error is reduced by the influence of the other markers detected. Thus the error is also quantified as the alignment accuracy of the image, i.e. the average distance after alignment of each of the detected fiducial markers from their respective synthetic needles. A total of 4 errors occurred, the details are as follows (format: patient, error type, direct error measurement, alignment accuracy of the image):

- patient 2, type (i), 2.54 mm, 0.04 mm;
- patient 6, type (i), 4.04 mm, 0.87 mm;
- patient 10, type (ii), 4.08 mm, 0.09 mm;
- patient 10, type (ii), 4.52 mm, 0.06 mm.

After fine alignment of each image, the distance of each detected fiducial marker from its respective synthetic needle is calculated for each prostate specimen. The mean distance (i.e. the mean accuracy) is  $0.18 \pm 0.13$  mm. Presented in Table 4.5 is the minimum, maximum, mean and standard deviation of the distances (in mm) for the worst case dataset (patient 3), the average of the 10 datasets, and the best case dataset (patient 5). In 98.6% of the cases, the distance of the detected fiducial marker from its respective synthetic needle is less than the radius of the needles used to create the markers.

	min	mean	max	variance
Worst case	0.01	0.30	0.97	0.23
Average	0.01	0.18	0.61	0.13
Best Case	0.01	0.10	0.30	0.07

Table 4.5: *Experimental validation in 10 prostate specimens: the accuracy of the alignment quantified (in mm) at the fiducial markers for the worst case dataset (patient 3), the average of the 10 datasets, and the best case dataset (patient 5).*

Figure 4.16 presents for a sample prostate specimen, (left) the stack of digitised histology slices with the relative inter-slice spacing respected along the z-axis, (right-upper row) the segmented and coarsely aligned prostate slices with the detected fiducial markers in red, green and blue, and (right-lower row) the segmented prostate slices after fine alignment, with the final synthetic needles.

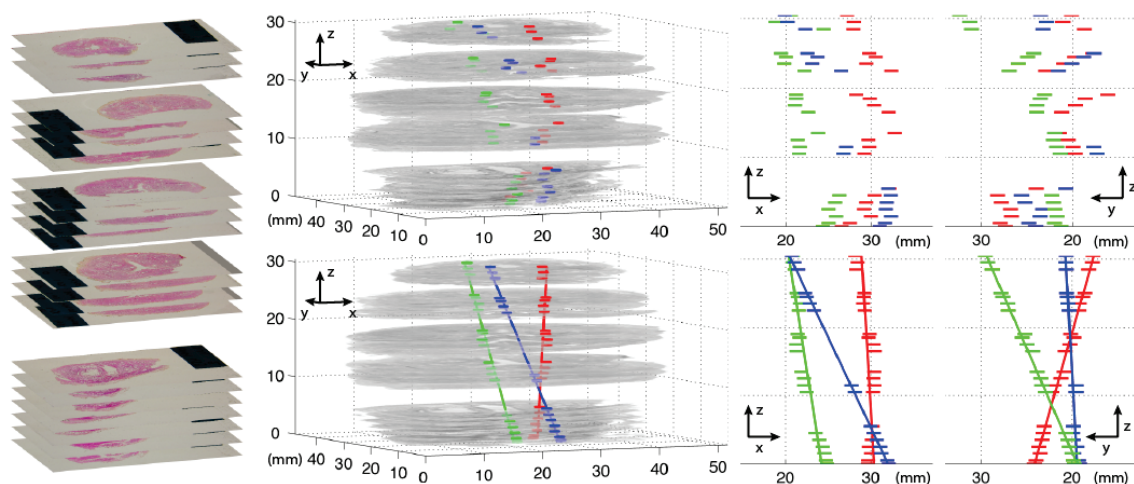


Figure 4.16: *Patient 1 (left) stack of digitised histology images (relative inter-slice spacing respected), (right-upper row) images segmented and coarsely aligned with the detected fiducial markers displayed in red (needle 1), green (needle 2), and blue (needle 3), 3D view, x-z view and y-z view, (right-lower row) as above after fine alignment of the slices.*

The robustness of the algorithm was investigated using the datasets of patient 3, patient 9 and patient 5 as they represented respectively the worst case, average case and best case in terms of alignment accuracy across the 10 patient datasets. For each dataset, the standard deviation of the alignment accuracy results (minimum, maximum and mean) of the 5 iterations was on average 0.01 mm (worst case 0.02 mm).

For an average of 19.2 images per prostate specimen, the algorithm takes approximately 5.5 minutes, with 30-60 s for the interactive initialisation.

## 4.10 Conclusion

The developed apparatus enables internal fiducial markers to be created in a rapid and standardised manner in fresh prostate specimens. The created fiducial markers are then automatically detected and identified enabling the alignment and shear correction of the stack of histology slices.

The quality of the alignment achieved using the proposed apparatus and method was first validated using simulated images which differed from the prostate datasets solely by the absence of tissue deformation. The accuracy of the alignment was limited only by the computing precision, both at the fiducial markers and at a point 20 mm away. Furthermore the angular precision of the alignment of each simulated dataset was limited only by the computing precision. This demonstrates that

- (i) there is no residual error associated with the algorithm for a situation where there is no deformation and
- (ii) a certain number of markers can be missed without affecting the performance of the alignment.

This indicates that the non-perfect alignment measured for each prostate dataset (average accuracy 0.18 mm) is thus due to the various tissue deformations and distortions previously discussed in Section 2.4.1. A limit of our method is that these deformations and distortions cannot be quantified. However, as a prostate cancer of volume  $< 0.5 \text{ cm}^3$  is classified as clinically insignificant [Stamey *et al.* (1993), Bastian *et al.* (2009)], we consider that the accuracy achieved justifies our choice to rigidly register the slices.

The algorithm was tested experimentally using a sample of beef liver. The slices were aligned using the fiducial markers, the average accuracy of the alignment was  $0.11 \pm 0.09$  mm at the fiducial markers, and  $0.58 \pm 0.43$  mm at the validation marker, using 2.71 fiducial markers per image. As the validation marker was positioned approximately 20 mm from the fiducial markers, it enabled an estimation of the quality of the alignment of a peripheral tumour. The angular precision, using 2.71 fiducial markers per image, was on average  $2.67^\circ \pm 0.51^\circ$ .

The protocol was tested on 10 prostate specimens, with 19.2 histology slices per specimen on average. The accuracy of the alignment at the fiducial markers was on average  $0.18 \pm 0.13$  mm.

The quality of the shear correction was evaluated first using simulated images. The average angle, with respect to the vertical, of the 3D least squares line passing through the validation markers after alignment of the simulated images but before shear correction was  $12.30^\circ \pm 4.36^\circ$  and after shear correction was  $0.06^\circ \pm 0.00^\circ$ . This result demonstrates firstly the necessity of including a shear correction calculation after alignment of the histology slices and secondly the quality of the proposed shear correction method.

The shear correction was also evaluated using the beef liver sample. After alignment of the slices using 2.71 markers per image, but before shear correction, the average angle with respect to the vertical of the least-squares validation line was  $8.17^\circ \pm 1.45^\circ$ . After shear correction, the angle with respect to the vertical of the least-squares validation line was on average  $7.54^\circ \pm 1.46^\circ$ .

The shear correction is achieved by comparing the dataset under test with the model geometry. The shear correction transformation is calculated such as to minimise the angular difference between the direction vectors of the respective synthetic needles in the model geometry and the dataset under test. The method assumes that the images of the dataset under test were cut along a plane parallel to the needle insertion guide of the apparatus. If the sectioning plane is at a tilt angle  $\theta$  to the needle insertion guide, the direction vectors of the synthetic needles in the dataset under test will not be the same as those in the model geometry. For the simulated images,  $\theta = 0^\circ$ . However, for the beef liver images, the tilt angle could not be ensured to be zero nor the difference from zero, if it existed, quantified. This is a partial explanation of the average shear correction result of  $7.54^\circ \pm 1.46^\circ$  in the beef liver sample.

Furthermore, the shear correction quality is measured as the angle, with respect to the vertical, of the 3D least squares line passing through the validation markers after alignment and shear correction of the slices. This assumes that the validation marker is vertical. As

before, this was assured for the simulated images but the angular difference, if it existed, was not measured for the beef liver sample. If an angular difference from the vertical existed, it would influence (improve or worsen) the accuracy of the reported quality of the shear correction in the beef liver sample. An interesting perspective, would thus be to repeat the beef liver validation experiment, creating the validation marker with an MR compatible material. A MR acquisition of the beef liver sample before sectioning would enable the exact angle with respect to the vertical of the validation marker to be measured thus rendering more accurate the shear correction quality reported. This perspective is further discussed in Chapter 6 ‘Perspectives and Conclusion’.

The tilt angle uncertainty equally exists for the prostate specimens. It is assumed that when the prostate is sliced into 6 mm sections, the plane along which the sections are cut is parallel to the needle insertion guide of the apparatus. The tilt angle is studied in detail in the next chapter, Chapter 5 ‘Histology - MR Registration’.

As previously discussed in Section 3.3.5, the angle geometry of the fiducial needles created in each prostate specimen is slightly different from the theoretical model geometry. Each inserted needle creates fiducial markers in straight 3D lines, however no assumption is made concerning the polar angle at which the line is positioned. The model geometry, that is the three theoretical polar angles with respect to the vertical axis at which the apparatus guides the insertion of the fiducial needles, is therefore not utilised in the developed algorithm. It remains advantageous however to insert the needles at an angle rather than vertically, for the reasons detailed in Section 3.3.4.

It could be imagined that the vertical position of each histology slice could be calculated from the model geometry, i.e. an optimisation of the fit of the three fiducial markers in each histology slice to the three fiducial needles. The vertical position of the histology slices was not calculated using this method because,

- (i) it had been noted that the fiducial marker angle geometry created in each prostate specimen is slightly different from the theoretical model geometry and
- (ii) the deformations due to the histology processing, in particular the shrinkage caused by the fixation, would have to be prior quantified and corrected for.

The vertical position of the histology slices, defined as the relative distance of each slice from the apex, was therefore calculated from the information written on the label attached to each histology slice by the anatomo-pathologists. The assumption was therefore made that the histology slices are parallel and that the information written on the label by the anatomo-pathologists is accurate. These assumptions are further discussed and examined in Section 6.3 of the final chapter, ‘Perspectives and Conclusion’.

As no optimum protocol yet exists to dissect prostatectomy specimens [Chen *et al.* (2010)], a perspective is the conception of an apparatus which would enable the position of the prostate specimen to be held rigid during the guided insertion of the fiducial needles and fixation. Slits at 6 mm intervals along the walls of the apparatus would ensure that the prostate is sectioned along planes parallel to the needle insertion guide of the apparatus.

Inspiration should be taken from the comprehensive overview of existing apparatus in [Chen *et al.* (2010)]. This perspective is further explored in Chapter 6 ‘Perspectives and Conclusion’.

The developed protocol has now been implemented as part of the standard clinical routine at our institution, less than 5 minutes is required for the creation of the fiducial markers. On average, 93.7% of the created fiducial markers are visible to the eye, those ‘lost’ are because the marker fell within for example the urethra or a portion of the slice was missing.

The algorithm presented for the detection and identification of the fiducial markers is, after an interactive initialisation (approximate duration 30-60 s), entirely automatic (average duration less than 6 minutes per dataset). On average, 96.1% of the visible markers are correctly detected and identified.

It was assumed that each fiducial needle created markers in a straight 3D line. In order to quantify this assumption, MR *ex vivo* images were acquired of 7 fresh prostate specimens after insertion of the fiducial needles. A point was placed at the location of each fiducial marker visible in the axial images, and 3D least-squares lines passing through the points were calculated. The average distance of each point from the line was  $0.15 \pm 0.11$  mm. As the radius of the fiducial needle is 0.82 mm, we consider our assumption justified.

The protocol and algorithm developed to achieve the alignment of the histology slices are ad hoc. The values used in the algorithm were experimentally defined using a training dataset in order to run this preliminary study. The results of the preliminary study are encouraging; the study has shown that it is feasible to create fiducial markers in the fresh prostate specimen, simply, quickly and in a standardised manner in order to integrate the protocol into the clinical routine. The study has also shown that the created fiducial markers are visible in the histology slices, and that they can be automatically detected and identified. Furthermore, the study has enabled a quantification of the alignment accuracy obtainable. Possible future work includes an automatic optimisation of the values used in the algorithm and an estimation of the influence of each parameter on the alignment precision achieved. A simpler, more structured algorithm, with fewer parameters could also be envisaged.



# 5

## HISTOLOGY - MR REGISTRATION

### CONTENTS

5.1	Introduction . . . . .	94
5.2	Features Description . . . . .	95
5.2.1	Ejaculatory Ducts . . . . .	95
5.2.2	Urethra . . . . .	97
5.3	3D Parametric Curve Fit . . . . .	98
5.4	Registration Parameters . . . . .	100
5.4.1	Shrinkage ( $s$ ) . . . . .	100
5.4.2	Shear ( $\alpha, \beta$ ) . . . . .	100
5.4.3	Tilt ( $\theta, \phi$ ) . . . . .	100
5.5	3D Histology - MR Registration Algorithm . . . . .	102
5.5.1	Algorithm Overview . . . . .	102
5.5.2	Preliminary Calculations . . . . .	103
5.5.3	Algorithm Pseudo-code . . . . .	104
5.5.4	Calculation of the Points of Rotation for Iteration $i$ . . . . .	105
5.5.5	Calculation of MR Vectors $\mathbf{v}_M(\theta, \phi)$ and Curve Coefficients $\mathbf{c}_M(\theta, \phi)$ . . . . .	107
5.5.6	Calculation of MR Initial Line and Curve Coordinates $\mathbf{p}_M(\mathbf{r}_{i,j}, \theta, \phi)$ . . . . .	108
5.5.7	Calculation of the Optimum Values of $\alpha, \beta$ and $s$ . . . . .	109
5.5.8	Calculation of the Optimum Rotation Point . . . . .	110
5.5.9	Convergence Definition . . . . .	111
5.5.10	Registration Evaluation . . . . .	112

5.6	Registration via Fiducial Needles . . . . .	112
5.6.1	Objectives and Details . . . . .	112
5.6.2	Results and Discussion . . . . .	113
5.7	Registration via Ejaculatory Ducts . . . . .	120
5.7.1	Objectives and Details . . . . .	120
5.7.2	Results and Discussion . . . . .	120
5.8	Conclusion . . . . .	122

## 5.1 Introduction

The previous chapter detailed the method developed to align a stack of 2D prostate histology slices. This chapter details the 3D registration of the aligned histology slices with the MR images. The 3D registration technique that has been developed is a feature-based technique, using the ejaculatory ducts to guide the registration.

The ejaculatory ducts are an anatomical landmark that are present in every prostate specimen and are visible in both histology slices and MR images acquired at standard clinical routine resolution. The anatomy and characteristics of the ejaculatory ducts are detailed and also the method by which they are identified in both MR and histology.

The ejaculatory ducts are curved structures, we represent the ducts using 3D 2<sup>nd</sup> order parametric curves, fitted to the identified coordinates in the images. The 3D histology - MR registration is thus reduced to the registration of two histology curves with two MR curves.

Three significant phenomena, described using five parameters, need to be taken into account in order to achieve the histology - MR registration. The first is the shrinkage of the prostate specimen caused by the fixation and histology processing. The second is the ‘shear effect’ previously discussed in Section 4.6. The final phenomenon we refer to as the ‘tilt’, it describes the angular difference between the histology sectioning plane and the MR imaging plane.

The registration algorithm designed to register the histology and MR data can be guided by either the ejaculatory ducts (i.e. curves) or the fiducial needles (i.e. lines). The overall algorithm and each step is fully detailed.

The developed algorithm has been tested with two different studies. First, the algorithm is used to register the histology and MR *ex vivo* data, with the registration guided by the fiducial needles. This first study enables an initial approximation of the previously mentioned phenomena (shrinkage, shear, tilt), as well as an estimation of the importance of including each of the parameters used to describe the phenomena in the algorithm. It is also an important feasibility study, evaluating the proposed idea of using the ejaculatory ducts to guide the registration.

The second application of the algorithm is to register the histology and MR *ex vivo* data, with the registration guided by the ejaculatory ducts. The registration accuracy

achieved can be objectively quantified using the fiducial needles, enabling an evaluation of the algorithm before application to MR *in vivo* images. The details and results of each of these studies are presented in Section 5.6 and Section 5.7 respectively.

## 5.2 Features Description

A feature-based technique has been developed to guide the 3D registration of the aligned histology slices with the MR images. It was initially intended to use both the ejaculatory ducts and urethra as features to guide the registration. Both are anatomical landmarks present in every prostate specimen and are visible in both histology slices and MR images acquired at standard clinical routine resolution. In this section, the anatomy, visual aspect and characteristics of the ejaculatory ducts and urethra are detailed.

### 5.2.1 Ejaculatory Ducts

#### Anatomy

The ejaculatory ducts are paired structures, referred to as the left and right ejaculatory duct, and are a direct continuation of the seminal vesicles. The ducts course superficially on the posterior surface of the prostate for 10 to 15 mm and then angle  $75^\circ$  anteriorly and penetrate the substance of the prostate for the final 5 to 8 mm of their length, see Figure 5.1. Within the prostate the ducts course obliquely towards each other as they progress from the proximal to distal region (regions labelled A and C respectively in Figure 5.1). The ejaculatory duct diameter varies along its course, and is larger proximally than distally; the average luminal diameter is  $1.7 \pm 0.3$  mm in the proximal region,  $0.6 \pm 0.1$  mm in the middle region and  $0.3 \pm 0.1$  mm in the distal region [Nguyen *et al.* (1996)]. The ejaculatory ducts terminate at the verumontanum, where they enter into the urethra.

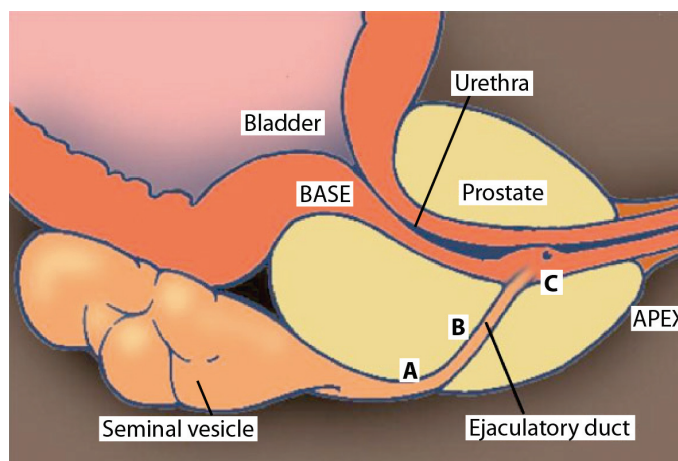


Figure 5.1: *The ejaculatory ducts are a direct continuation of the seminal vesicles. Within the prostate the ducts course obliquely towards each other as they progress from the proximal (A), through the middle (B) to the distal (C) region, at which point they enter into the urethra. Source: The Turek Clinic.*

From the study carried out by [Nguyen *et al.* (1996)], it would appear that ejaculatory duct dimensions are remarkably uniform among normal men. However it should be noted that the measurements were obtained from formalin fixed specimens and may therefore underestimate the dimensions *in vivo*. Furthermore, the specimens studied were derived from older patients (54 - 72 years old) and it is unknown whether patient age has an influence on ejaculatory duct dimensions.

## Identification

The ejaculatory ducts are an anatomical landmark present in every prostate and are visible in both histology slices and MR images acquired at standard clinical routine resolution.

In order to identify the ejaculatory ducts in the histology slices, the aligned histology images are visualised using MATLAB. The boundaries of the left and right ejaculatory ducts are outlined in the images in which they are visible. The centre of gravity of each outline is calculated and saved. The histology right and left ejaculatory ducts are thus each represented by a list of 3D coordinates, denoted respectively  $\mathbf{V}_{H,R}$  and  $\mathbf{V}_{H,L}$ , where  $\mathbf{V} = [\mathbf{V}_x, \mathbf{V}_y, \mathbf{V}_z]$ ,  $|\mathbf{V}| = N \times 3$ , with  $N$  the number of coordinates in the list, i.e. the number of images on which the duct was outlined. The ejaculatory ducts are visible in 7.6 histology slices on average (average of the five prostate specimens studied), (minimum 5, maximum 9). Figure 5.2 shows the subset of histology slices of a sample prostate specimen in which the ejaculatory ducts are visible, with the images ordered from the base to the apex. The position of the ejaculatory ducts is localised by a black-outlined rectangle in each image, a zoom of each rectangle (magnification  $\times 2$ ) can be found at the bottom right of each image. Pixel resolution 0.03 mm.

The ejaculatory ducts are identified in the MR *ex vivo* images by visualising the  $T_2$ -W axial images of the dataset using the OsiriX software (OsiriX Foundation, Switzerland). The ejaculatory ducts are characterised by a hypointense signal and a point is placed at the centre of each location that the left or right ejaculatory duct is visible. A list of 3D coordinates are exported and read into MATLAB. The MR *ex vivo* right and left ejaculatory ducts are denoted respectively  $\mathbf{V}_{M,R}$  and  $\mathbf{V}_{M,L}$ .

Five prostate specimens were studied, MR *ex vivo* images were acquired of four specimens at a pixel resolution of 0.31 mm, and one specimen at a pixel resolution of 0.16 mm. There were 15.6 axial images on average per prostate specimen (minimum 14, maximum 17). The ejaculatory ducts are visible in 4.2 MR *ex vivo* axial images on average, (minimum 4, maximum 5). Figure 5.3 shows the subset of MR *ex vivo* axial images of a sample prostate specimen (the same specimen as in Figure 5.2) in which the ejaculatory ducts are visible, with the images ordered from the base to the apex. The position of the ejaculatory ducts is localised by a white-outlined rectangle in each image, a zoom of each rectangle (magnification  $\times 2$ ) can be found at the bottom right of each image.

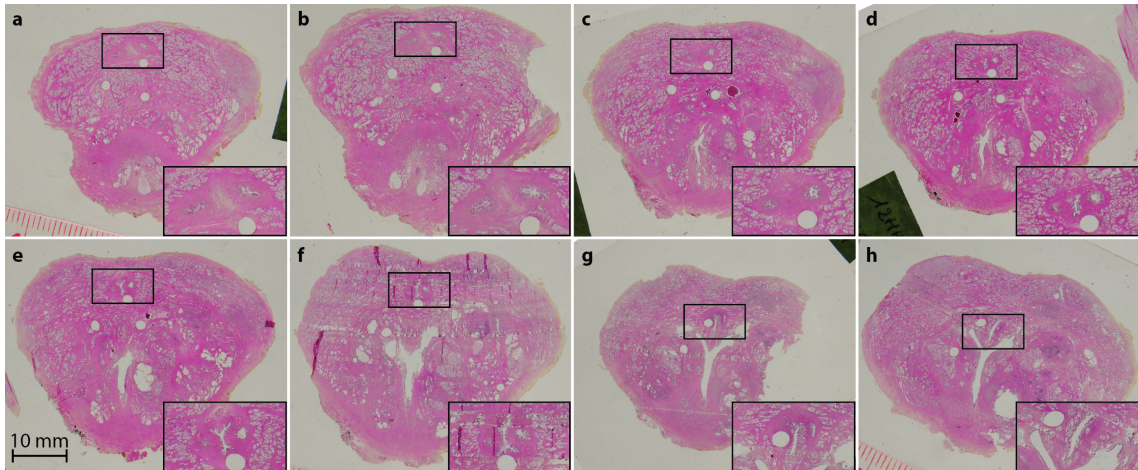


Figure 5.2: Subset of the histology slices of a prostate specimen in which the ejaculatory ducts are visible, ordered from the base to the apex. The ejaculatory ducts are located within the black-outlined rectangle in each image, the rectangle is zoomed (magnification  $\times 2$ ) in the bottom right of each image. Inter-slice spacing between images (a-b) 1 mm, (b-c) 5 mm, (c-d) 1 mm, (d-e) 1 mm, (e-f) 5 mm, (f-g) 3 mm, (g-h) 4 mm. Pixel resolution 0.03 mm. The scale in image (e) is the same for each of the images. See Figure 5.3 for the MR *ex vivo* images of the same prostate specimen.

### 5.2.2 Urethra

It was initially intended to use both the urethra and the ejaculatory ducts as features to guide the registration. Similarly to the ejaculatory ducts, the urethra is an anatomical feature present in every prostate specimen and is visible in both histology slices and MR images acquired at standard clinical routine resolution. As can be seen in Figure 5.1, the urethra enters the prostate at the base, passes through the prostate along a curved path and exits the gland at the apex.

The advantage of the urethra as an anatomical feature is therefore that it is present and visible in a far greater number of images of the prostate than the ejaculatory ducts. However, the axial length of the urethra is a significant disadvantage. Figure 5.4 shows a histology slice of a sample prostate specimen, with the approximately corresponding MR  $T_1$ -W *ex vivo* axial image. In order to improve the visualisation of the urethra in the MR *ex vivo* images, a flexible, hollow plastic tube, diameter 2 mm, was inserted into the urethra of the fresh prostate specimens before MR imaging. In Figure 5.4, the created fiducial markers are indicated with arrows in both the histology and MR image. In the MR image, the tube inserted into the urethra is visible as the slighter larger, hollow circle centred within the fiducial markers. For comparative purposes, the approximate position of the tube has been indicated in the histology slice. It can be seen that the axial length of the urethra, in this particular histology slice measures 18.5 mm. There is thus significant uncertainty as to the position of the 2 mm diameter flexible tube within the urethra. For this reason, the urethra is not considered to be an accurate feature to guide the 3D histology - MR registration and is no further considered.

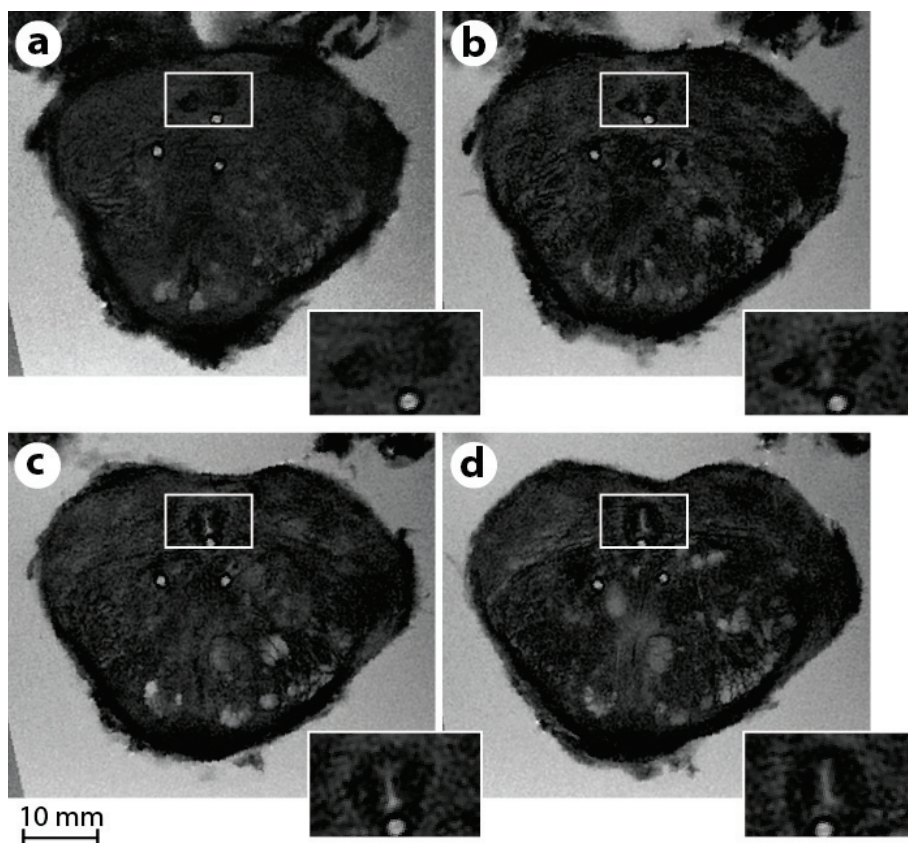


Figure 5.3: Subset of the MR *ex vivo* images of a prostate specimen in which the ejaculatory ducts are visible, ordered from the base to the apex. The ejaculatory ducts are located within the white-outlined rectangle in each image, the rectangle is zoomed (magnification  $\times 2$ ) in the bottom right of each image. Inter-slice spacing between images (a-b), (b-c) and (c-d) is 2 mm. Pixel resolution 0.16 mm. The scale is the same for each of the images. See Figure 5.2 for the histology images of the same prostate specimen.

### 5.3 3D Parametric Curve Fit

A 3D 2<sup>nd</sup> order parametric curve is least-squares fitted to the 3D coordinates of the centres of gravity of the manually identified ejaculatory ducts in the histology and MR images. The parametric curve  $\mathbf{f}(t)$  is given by

$$\mathbf{f}(t) = \begin{bmatrix} x(t) & y(t) & z(t) & 1 \end{bmatrix}, \quad 0 \leq t \leq 1$$

$$\text{where } \begin{cases} x(t) = c_{x,1}t^2 + c_{x,2}t + c_{x,3} \\ y(t) = c_{y,1}t^2 + c_{y,2}t + c_{y,3} \\ z(t) = c_{z,1}t^2 + c_{z,2}t + c_{z,3} \end{cases} \quad (5.1)$$

From the identification step, each ejaculatory duct has an associated  $N \times 3$  matrix, containing the 3D coordinates of the centres of gravity of the ejaculatory duct from each image in which it was identified. The general matrix is denoted  $\mathbf{V} = [\mathbf{V}_x, \mathbf{V}_y, \mathbf{V}_z]$ .

For each dimension  $d \in \{x, y, z\}$ , the polynomial coefficients  $(c_{d,1}, c_{d,2}, c_{d,3})$  are calcu-

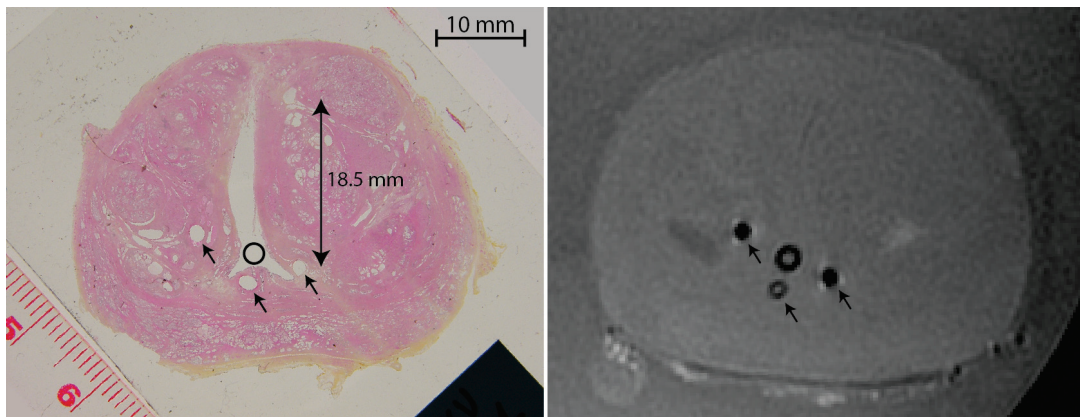


Figure 5.4: A histology slice of a sample prostate specimen (left), with the approximately corresponding MR  $T_1$ -W *ex vivo* axial image (right). The fiducial markers are indicated with arrows in both images. The flexible, hollow plastic tube inserted into the urethra of the fresh prostate before MR imaging can be seen in the MR image as the slightly larger, hollow circle centred within the fiducial markers. For comparative purposes, the approximate position of the tube has been indicated in the histology slice. Due to the significantly larger axial length of the urethra (18.5 mm) compared to the diameter of the inserted tube (2 mm), there is significant uncertainty as to the position of the tube within the urethra. Note that the scale is the same for both images.

lated as the least-squares solution of the system of equations

$$\begin{bmatrix} \mathbf{t}^2 & \mathbf{t}^1 & \mathbf{t}^0 \end{bmatrix} \begin{bmatrix} c_{d,1} \\ c_{d,2} \\ c_{d,3} \end{bmatrix} = \mathbf{V}_d \quad (5.2)$$

where  $\mathbf{t}^k$ ,  $k \in \{0, 1, 2\}$  is the  $N \times 1$  vector given by

$$\{\mathbf{t}^k\}_i = \left(\frac{i}{N-1}\right)^k, 0 \leq i \leq N-1 \quad (5.3)$$

and  $\mathbf{V}_d$  is the  $N \times 1$  matrix of coordinates of the identified duct in the dimension  $d \in \{x, y, z\}$ . The resulting  $4 \times 4$  polynomial coefficient matrix is denoted  $\mathbf{c}$

$$\mathbf{c} = \begin{bmatrix} c_{x,1} & c_{x,2} & c_{x,3} & 0 \\ c_{y,1} & c_{y,2} & c_{y,3} & 0 \\ c_{z,1} & c_{z,2} & c_{z,3} & 0 \\ 0 & 0 & 0 & 1 \end{bmatrix} \quad (5.4)$$

Using the polynomial coefficient matrix and Equation 5.1,  $\mathbf{f}(t)$  is evaluated for  $M$  points such that there is one point every  $\Delta$  distance along the curve (see Section 5.6 and Section 5.7 for the numerical values used). Each curve is thus represented by a  $M \times 4$  matrix of points denoted  $\mathbf{p}$  where  $\|p_i, p_{i+1}\| = \Delta$ .

## 5.4 Registration Parameters

Three significant phenomena, described using five parameters, need to be taken into account when calculating the transformation to register the histology and MR data, they are (i) shrinkage, (ii) shear and (iii) tilt. Each phenomenon and its associated parameter(s) is explained and detailed in this section.

### 5.4.1 Shrinkage ( $s$ )

The fixation and histology processing of the prostate specimen causes a shrinkage of the tissue. Published histology linear correction factors to compensate for tissue shrinkage vary considerably; 1.14 [Schned *et al.* (1996), Haider *et al.* (2007)], 1.22 [Bart *et al.* (2005), Egevad *et al.* (1998)], 1.33 [Egawa *et al.* (2000)], 1.5 [Noguchi *et al.* (2000)]. A single tissue shrinkage correction factor may not be applicable for all laboratories because of inter-laboratory variations in tissue processing procedures and differences in measuring shrinkage [Schned *et al.* (1996)]. Furthermore, to our knowledge, no study has yet examined whether the shrinkage is, as assumed, homogenous. We denote the histology linear correction factor as  $s$ , in theory  $s > 1$ .

### 5.4.2 Shear ( $\alpha, \beta$ )

The ‘shear effect’ has been previously discussed in Section 4.6. It arises due to the fact that the distance between any two points on a horizontal plane is unchanged by the application of a shear matrix,  $T_{\text{shear}}$ ,

$$T_{\text{shear}} = \begin{bmatrix} 1 & 0 & \alpha & 0 \\ 0 & 1 & \beta & 0 \\ 0 & 0 & 1 & 0 \\ 0 & 0 & 0 & 1 \end{bmatrix} \quad (5.5)$$

where  $\alpha$  and  $\beta$  are the shear parameters. The effect can be visually appreciated in Figure 5.5. In order to accurately register the aligned histology slices with the MR images, shear correction parameters,  $\alpha$  and  $\beta$ , must be included in the registration calculation.

### 5.4.3 Tilt ( $\theta, \phi$ )

The fiducial needles are inserted into the fresh prostate specimen using the developed apparatus, that holds horizontal and rigid the needle insertion guide, see Figure 3.1. It is then assumed that during histology processing, the prostate specimen is sectioned along a plane parallel to the needle insertion guide. The MR *ex vivo* axial imaging plane is oriented parallel to the polystyrene block, which is attached to the base of the prostate by the needle sheaths, see Figure 3.5. The MR *ex vivo* imaging plane is therefore parallel to the needle insertion guide. The MR *in vivo* axial imaging plane is oriented such as to be

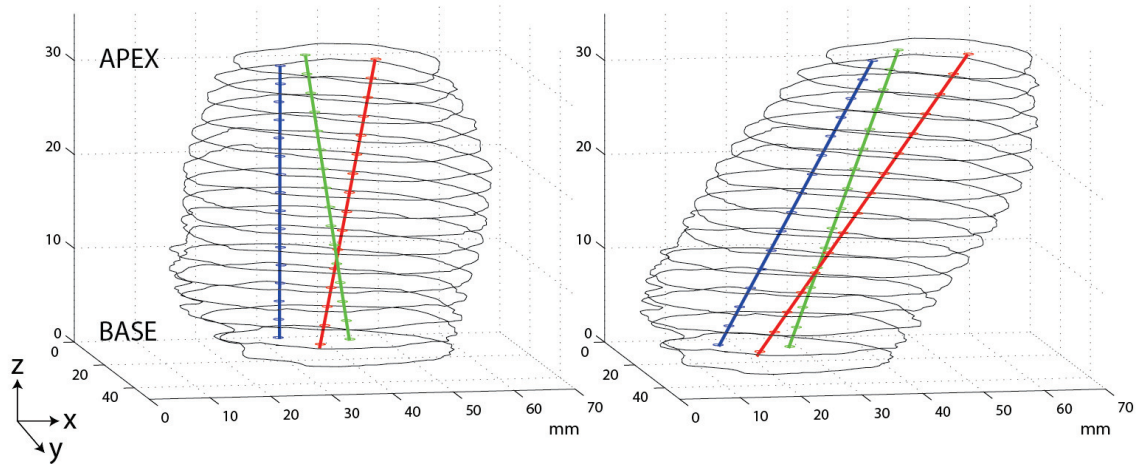


Figure 5.5: The ‘shear effect’ is due to the fact that the distance between any two points on a horizontal plane is unchanged by the application of a shear matrix,  $T_{shear}$ .

perpendicular to the rectal surface of the prostate, roughly parallel to the needle insertion guide.

The ‘tilt’ is defined as the angular difference between the histology sectioning plane and the MR (*in vivo* or *ex vivo*) imaging plane and is described using the elevation and azimuth angles of the polar coordinate system, denoted respectively as  $\theta$  and  $\phi$ , see Figure 5.6.

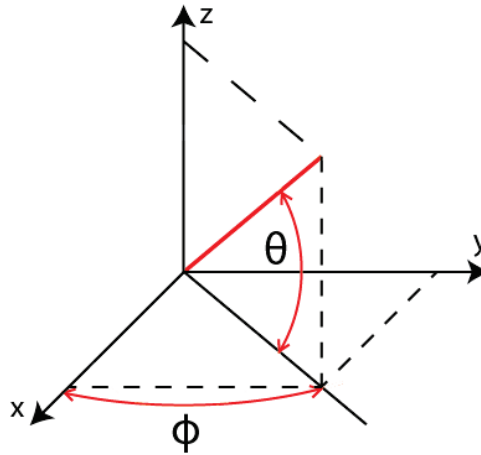


Figure 5.6: The ‘tilt’, defined as the angular difference between the histology sectioning plane and the MR imaging plane, is described using the elevation and azimuth angles of the polar coordinate system, denoted respectively as  $\theta$  and  $\phi$ . Note that usually  $\theta$  is measured with respect to the  $z$  axis, i.e.  $90^\circ - \theta$ , however for quantifying the tilt, it is more intuitive to measure  $\theta$  with respect to the  $x$ - $y$  plane.

The tilt causes significant deformation to the geometry of both lines and curves. A simplified 2D example is considered in Figure 5.7 which represents three lines, intersected by equally spaced planes. The planes are tilted at an angle  $\theta$  to the horizontal, Figure 5.7(a). The points of intersection of the lines and the planes are indicated by circles,

Figure 5.7(b). If it assumed that the images were acquired along horizontal planes and the imaging planes and points of intersection are therefore made horizontal, Figure 5.7(c), it can be seen that the vectors of the reconstructed lines passing through the points of intersection are different from those of the original three lines Figure 5.7(a).

In order to accurately register the aligned histology slices with the MR images, the tilt parameters,  $\theta$  and  $\phi$ , must be included in the registration calculation.

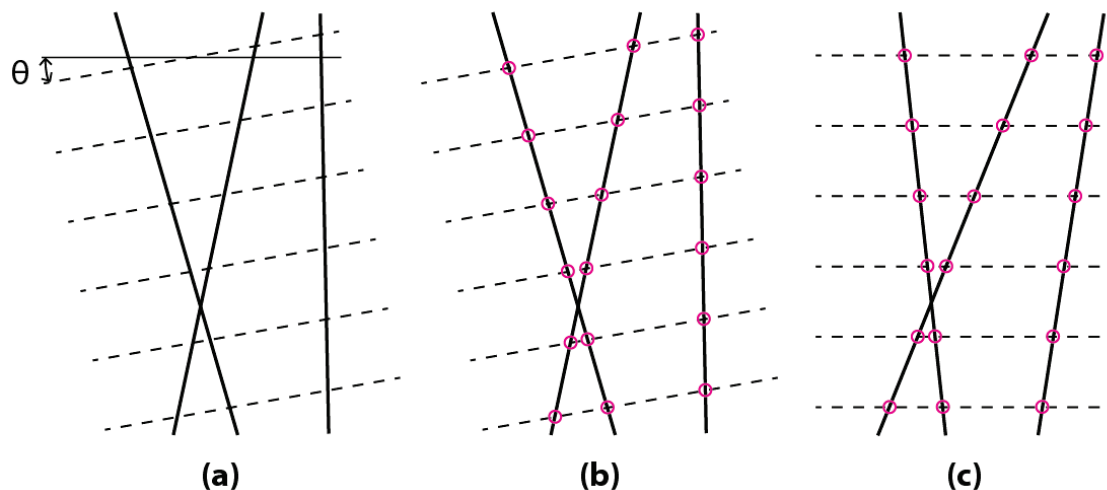


Figure 5.7: A simplified 2D example to demonstrate the effect of a tilt on the geometry of lines. Three lines are intersected by equally spaced planes, tilted at an angle  $\theta$  to the horizontal (a). The points of intersection of the lines and the planes are indicated by circles (b). If it assumed that the images were acquired along horizontal planes and the imaging planes and points of intersection are therefore made horizontal (c), it can be seen that the vectors of the reconstructed lines passing through the points of intersection are different from those of the original three lines (a).

## 5.5 3D Histology - MR Registration Algorithm

### 5.5.1 Algorithm Overview

The registration algorithm is designed to register the histology and MR (*in vivo* or *ex vivo*) data. The registration can be guided by either the ejaculatory ducts (i.e. curves) or the fiducial needles (i.e. lines). For either case, first one of the MR needles or ejaculatory ducts is chosen as a reference. For each iteration, the rotation points are defined along this reference line or curve and each rotation point is tested. Figure 5.8 illustrates an example, the rotation points (\*) are defined along the reference line, the rotation point being tested is denoted ( $\otimes$ ).

The rotation point defines the height at which the horizontal plane is positioned and is also the point of rotation about which the tilt is applied to the horizontal plane. The points of intersection of the tilted plane with the MR lines or curves define the starting points of the MR lines or curves. The starting points define the initial distances between

the lines or curves. Furthermore, the section of the MR line or curve to be included in the registration is measured from the starting points. Therefore the rotation point defines what section of each MR line or curve is to be registered to the histology line or curve.

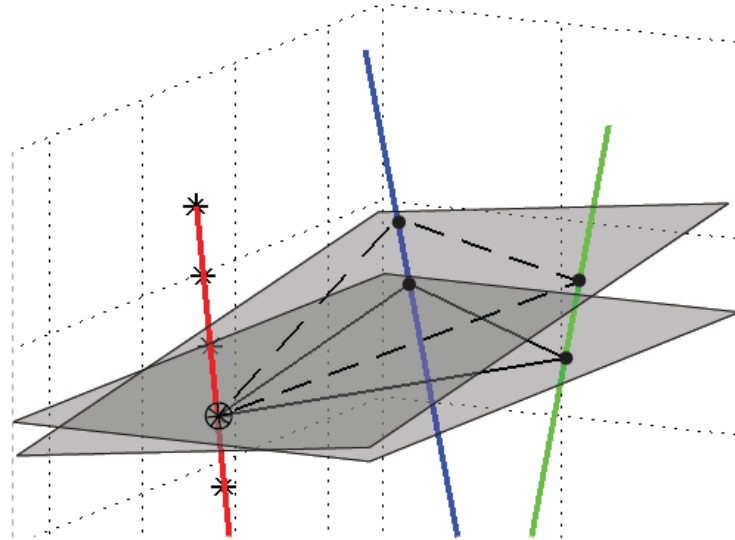


Figure 5.8: *Each iteration, rotation points (\*) are defined along a reference line or curve and each rotation point is then tested (⊗). The rotation point defines the height at which the horizontal plane is positioned and is the point of rotation about which the tilt is applied to the horizontal plane. The points of intersection of the tilted plane with the MR lines or curves define the starting points of the MR lines or curves. The starting points define the initial distances between the lines or curves and what section of the MR line or curve is to be included in the registration.*

For each rotation point tested, a range of tilt values are tested ( $0 \leq \theta \leq \theta_{max}$ ,  $0 \leq \phi \leq 359$ ). The tilt changes the MR line vectors or curve coefficients and also the starting points of the lines or curves. For each tilt value tested, the optimum values of the shrinkage correction coefficient and shear parameters are calculated such that the registration accuracy between the histology and MR is maximised, i.e. minimise the perpendicular distance between the respective histology and MR points. The algorithm is run until convergence.

### 5.5.2 Preliminary Calculations

If the registration is guided by the **ejaculatory ducts**, the following preliminary calculations are required,

- the curve coefficients of the left and right ejaculatory ducts in the histology data, denoted respectively  $\mathbf{c}_{H,L}$  and  $\mathbf{c}_{H,R}$ , or in general  $\mathbf{c}_H$ ,
- the curve coefficients of the left and right ejaculatory ducts in the MR data, denoted respectively  $\mathbf{c}_{M,L}$  and  $\mathbf{c}_{M,R}$ , or in general  $\mathbf{c}_M$ ,

- the initial coordinates of the left and right ejaculatory ducts in the histology data, i.e. the highest (with respect to the z-axis) coordinate, denoted respectively  $\mathbf{p}_{H,R}$  and  $\mathbf{p}_{H,L}$ , or in general  $\mathbf{p}_H$ ,
- the initial coordinates of the left and right ejaculatory ducts in the MR data, denoted respectively  $\mathbf{p}_{M,R}$  and  $\mathbf{p}_{M,L}$ , or in general  $\mathbf{p}_M$ .

If the registration is guided by the **fiducial needles** (only possible with the MR *ex vivo* data), the following preliminary calculations are required,

- the normalised vectors ( $\|\mathbf{v}\| = 1$ ), from the apex to the base, of the three fiducial needles in the histology data, denoted respectively  $\mathbf{v}_{H,1}$ ,  $\mathbf{v}_{H,2}$  and  $\mathbf{v}_{H,3}$ , or in general  $\mathbf{v}_H$ ,
- the normalised vectors ( $\|\mathbf{v}\| = 1$ ), from the apex to the base, of the three fiducial needles in the MR data, denoted respectively  $\mathbf{v}_{M,1}$ ,  $\mathbf{v}_{M,2}$  and  $\mathbf{v}_{M,3}$ , or in general  $\mathbf{v}_M$ ,
- the initial coordinates of the three fiducial needles in the histology data, denoted respectively  $\mathbf{p}_{H,1}$ ,  $\mathbf{p}_{H,2}$  and  $\mathbf{p}_{H,3}$ , or in general  $\mathbf{p}_H$ ,
- the initial coordinates of the three fiducial needles in the MR data, denoted respectively  $\mathbf{p}_{M,1}$ ,  $\mathbf{p}_{M,2}$  and  $\mathbf{p}_{M,3}$ , or in general  $\mathbf{p}_M$ .

### 5.5.3 Algorithm Pseudo-code

The pseudo-code of the registration algorithm is as follows. Each calculation step is detailed below.

---

 Algorithm 2: *3D Histology - MR Registration Algorithm.*


---

```

flag = 0 ;
iteration = 0 ;
define the initial rotation point spacing  $\Delta r_{initial}$  ;
while  $flag = 0$  do
  iteration = iteration + 1 ;
   $\Delta r_{iteration} = \frac{\Delta r_{initial}}{10^{iteration-1}}$  ;
  calculate the points of rotation ;
  for each rotation point calculated  $\mathbf{r}_{i,j}$  do
    for  $\theta = 0$  to  $\theta_{max}$  do
      for  $\phi = 0$  to 359 do
        calculate the tilted MR vectors  $\mathbf{v}_M(\theta, \phi)$  or curve coefficients
         $\mathbf{c}_M(\theta, \phi)$  ;
        calculate the tilted MR initial line or curve coordinates with respect
        to the rotation point  $\mathbf{p}_M(\mathbf{r}_{i,j}, \theta, \phi)$  ;
        calculate the optimum values of  $\alpha$ ,  $\beta$  and  $s$  ;
        calculate the error measure ;
      end
    end
  end
  calculate the optimum rotation point  $\mathbf{r}_{i,opt}$ ;
  test for convergence ;
  if  $convergence = 1$  then
    flag = 1 ;
  end
end

```

---

#### 5.5.4 Calculation of the Points of Rotation for Iteration $i$

**Iteration**  $i = 1$

We choose arbitrarily one of the **MR** needles or ejaculatory ducts as a reference to define the points of rotation. The first point of rotation is defined as the highest (along the z axis) coordinate of the chosen reference line or curve. For the first iteration ( $i = 1$ ), the remaining rotation points are then defined as equally spaced points from that initial rotation point along the reference line or curve, with the restriction that at least 50% of the reference line or curve is included from the rotation point to the end of the line or curve. For iteration 1, the spacing between the rotation points is defined as  $\Delta r_1 = \Delta r_{initial}$  mm. The rotation points are denoted  $\mathbf{r}_{i,j}$ , where  $i$  is the iteration and  $1 \leq j \leq$  the number of rotation points calculated for iteration  $i$ . Figure 5.9 shows the rotation points (indicated by an asterisk (\*) symbol) calculated for both a reference line and curve, the first rotation

point is differentiated by an encircled asterisk ( $\otimes$ ). The spacing between two successive rotation points is equal to  $\Delta r_1$  mm.

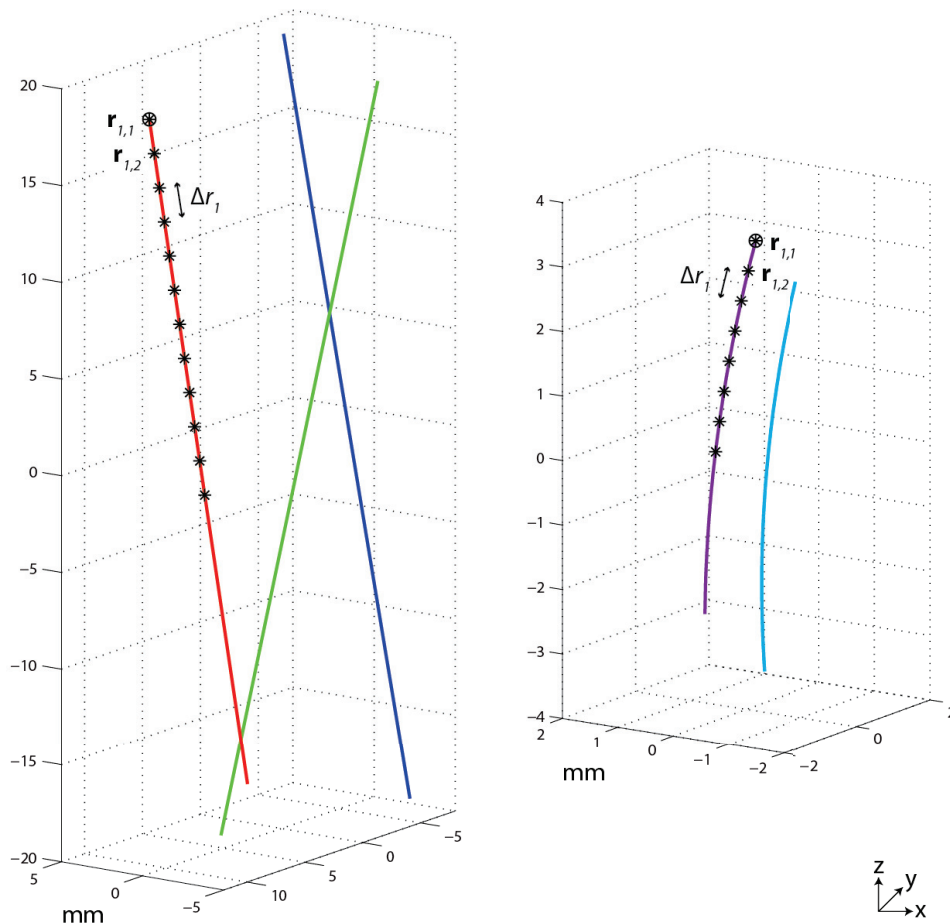


Figure 5.9: For the first iteration,  $i = 1$ , one of the MR needles (left) or ejaculatory ducts (right) is chosen arbitrarily as the reference. The first point of rotation is the highest coordinate of the chosen reference line or curve ( $\otimes$ ). The remaining rotation points ( $*$ ) are equally spaced points along the reference line or curve, with spacing  $\Delta r_1$  mm.

### Iteration $i > 1$

For each iteration  $i > 1$ , the rotation points are calculated with respect to the optimum rotation point calculated from the previous iteration  $i-1$ . If for an iteration  $i$  the optimum rotation point is denoted  $\mathbf{r}_{i,opt}$ , then the rotation points for an iteration  $i > 1$  are defined in the range

$$\mathbf{r}_{i-1,opt-1} : \mathbf{r}_{i-1,opt+1} \quad (5.6)$$

with the spacing between successive points  $\Delta r_i$  defined as

$$\Delta r_i = \frac{\Delta r_{initial}}{10^{i-1}} \quad (5.7)$$

Figure 5.10 shows on the left the rotation points tested for iteration  $i = 1$ , with spacing

$\Delta r_1$ . The optimum rotation point calculated at the conclusion of iteration  $i = 1$ ,  $\mathbf{r}_{1,opt}$  is indicated with a  $\otimes$  symbol. The area around this optimum point is zoomed on the right hand side of the image. For the next iteration,  $i = 2$ , the rotation points (denoted  $\bullet$ ) are calculated as equally spaced points in the range  $\mathbf{r}_{1,opt-1} : \mathbf{r}_{1,opt+1}$  with spacing  $\Delta r_2 = 0.1\Delta r_1$ .

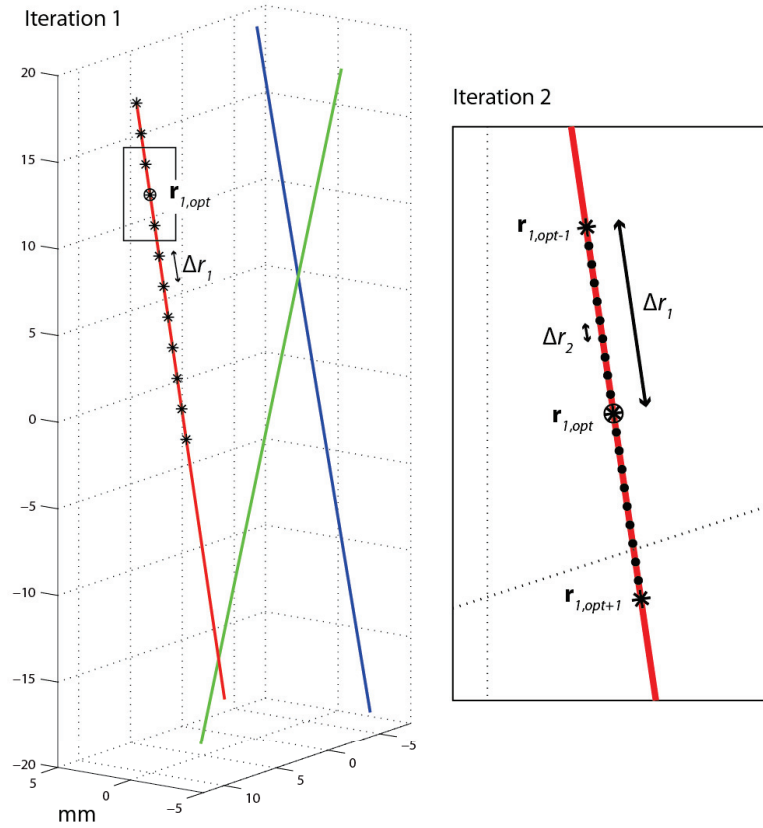


Figure 5.10: For each iteration  $i > 1$ , the rotation points are calculated with respect to the optimum rotation point calculated from the previous iteration,  $r_{i-1,opt}$  (denoted  $\otimes$ ). For iteration  $i$ , the rotation points are calculated in the range  $r_{i-1,opt-1} : r_{i-1,opt+1}$  with spacing between successive points  $\Delta r_i = 0.1\Delta r_{i-1}$ .

### 5.5.5 Calculation of MR Vectors $\mathbf{v}_M(\theta, \phi)$ and Curve Coefficients $c_M(\theta, \phi)$

For a given tilt, defined by the angles  $\theta$  and  $\phi$ , the corresponding matrices of rotation are

$$R(\theta) = \begin{bmatrix} 1 & 0 & 0 & 0 \\ 0 & \cos(\theta) & -\sin(\theta) & 0 \\ 0 & \sin(\theta) & \cos(\theta) & 0 \\ 0 & 0 & 0 & 1 \end{bmatrix} \quad (5.8)$$

and

$$R(\phi) = \begin{bmatrix} \cos(\phi) & -\sin(\phi) & 0 & 0 \\ \sin(\phi) & \cos(\phi) & 0 & 0 \\ 0 & 0 & 1 & 0 \\ 0 & 0 & 0 & 1 \end{bmatrix} \quad (5.9)$$

The effect of the tilt on the MR vectors is calculated according to

$$\mathbf{v}_M(\theta, \phi)^T = R(\phi)^T \times R(\theta)^T \times R(\phi) \times (\mathbf{v}_M)^T \quad (5.10)$$

where  $\mathbf{v}_M$  is the normalised ( $\|\mathbf{v}_M\| = 1$ ) MR vector  $\mathbf{v}_M = [v_x, v_y, v_z, 1]$ .

Similarly the effect of the tilt on the MR curves can be calculated from the polynomial coefficient matrix of the curve  $\mathbf{c}_M$ ,

$$\mathbf{c}_M(\theta, \phi)^T = R(\phi)^T \times R(\theta)^T \times R(\phi) \times \begin{bmatrix} c_{x,1} & c_{x,2} & c_{x,3} & 0 \\ c_{y,1} & c_{y,2} & c_{y,3} & 0 \\ c_{z,1} & c_{z,2} & c_{z,3} & 0 \\ 0 & 0 & 0 & 1 \end{bmatrix}^T \quad (5.11)$$

### 5.5.6 Calculation of MR Initial Line and Curve Coordinates $\mathbf{p}_M(\mathbf{r}_{i,j}, \theta, \phi)$

For a tilt, defined by the angles  $\theta$  and  $\phi$ , the normal of the tilted plane is defined by

$$\mathbf{n}_{tilt}^T = R(\phi)^T \times R(\theta) \times R(\phi) \times [0 \ 0 \ 1 \ 0]^T \quad (5.12)$$

The point of intersection,  $\mathbf{p}_{intersection}$ , of each MR line with the plane tilted about the rotation point  $\mathbf{r}_{i,j}$  is calculated by

$$\mathbf{p}_{intersection} = \mathbf{p}_l + \mathbf{v}_M \frac{(\mathbf{r}_{i,j} - \mathbf{p}_l) \cdot \mathbf{n}_{tilt}}{\mathbf{v}_M \cdot \mathbf{n}_{tilt}} \quad (5.13)$$

Where  $\mathbf{f} \cdot \mathbf{g}$  denotes the dot product of the two vectors  $\mathbf{f}$  and  $\mathbf{g}$ ,  $\mathbf{p}_l$  denotes a point on the MR line,  $\mathbf{v}_M$  the normalised ( $\|\mathbf{v}_M\| = 1$ ) MR line vector (from the apex to the base) and  $\mathbf{n}_{tilt}$  the normal of the tilted plane. The points of intersection then need to be inverse transformed (with respect to the tilted plane) such that they lie along a horizontal plane,

$$\mathbf{p}_M(\mathbf{r}_{i,j}, \theta, \phi)^T = R(\phi)^T \times R(\theta)^T \times R(\phi) \times (\mathbf{p}_{intersection})^T \quad (5.14)$$

These define the initial coordinates of the three MR lines after a tilt defined by  $\theta$  and  $\phi$ , applied about the rotation point  $\mathbf{r}_{i,j}$ .

Figure 5.11 illustrates this idea. The rotation points (\*) are defined along the reference line, the rotation point being studied is indicated ( $\otimes$ ). A horizontal plane, passing through the studied rotation point, is defined. The points of intersection of the three lines with the horizontal plane are indicated ( $\bullet$ ), solid lines between the points enable the distance

between the points of intersection to be appreciated. A tilt is applied to the plane ( $\theta = -10^\circ, \phi = 45^\circ$ ) about the point of rotation. The points of intersection of the three lines with the tilted plane are indicated ( $\bullet$ ), with dashed lines showing the distance (different from the solid line distances) between them.

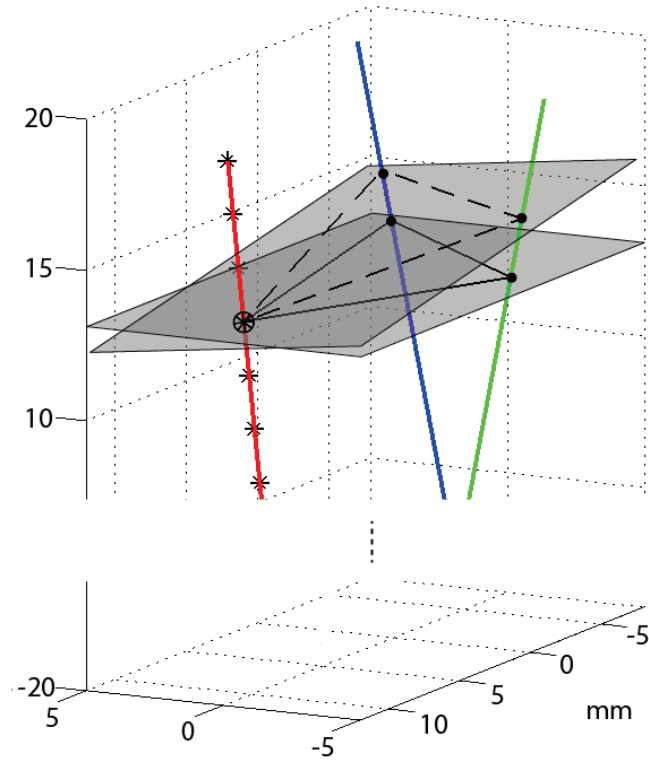


Figure 5.11: A horizontal plane is defined with respect to a rotation point ( $\otimes$ ). A tilt is applied to the plane ( $\theta = -10^\circ, \phi = 45^\circ$ ) about the point of rotation. The distances between the points of intersection ( $\bullet$ ) of the lines with the horizontal plane differs from the distances between the points of intersection of the lines with the tilted plane

### 5.5.7 Calculation of the Optimum Values of $\alpha$ , $\beta$ and $s$

For a tilt, defined by the angles  $\theta$  and  $\phi$  and applied about the point of rotation  $\mathbf{r}_{i,j}$ , the effect on the MR lines or curves has been calculated as respectively the vectors  $\mathbf{v}_M(\theta, \phi)$  or curve coefficients  $\mathbf{c}_M(\theta, \phi)$ , with initial line or curve coordinates  $\mathbf{p}_M(\mathbf{r}_{i,j}, \theta, \phi)$ .

An unconstrained nonlinear optimisation is used to determine the shrinkage and shear parameters ( $s$ ,  $\alpha$  and  $\beta$ ), using a quasi-Newton line-search method [Fletcher (1987), Al-Baali and Fletcher (1986)]. The aim is to determine the minimum of the multivariable function specified by

$$\min_{\mathbf{x}} f(\mathbf{x}) \quad (5.15)$$

where  $\mathbf{x}$  is the vector  $[s, \alpha, \beta]$  and  $f(\mathbf{x})$  is a function that returns a scalar. An initial estimate is supplied to define the starting point.

The shrinkage correction factor  $s$  is applied to the initial coordinates of the histology

data  $\mathbf{p}_H$ . The shear is applied to the tilted MR vectors  $\mathbf{v}_M(\theta, \phi)$  according to

$$\mathbf{v}_M(\theta, \phi, \alpha, \beta)^T = \begin{bmatrix} 1 & 0 & \alpha & 0 \\ 0 & 1 & \beta & 0 \\ 0 & 0 & 1 & 0 \\ 0 & 0 & 0 & 1 \end{bmatrix} \times \mathbf{v}_M(\theta, \phi)^T \quad (5.16)$$

The shear is similarly applied to the tilted MR curve coefficients  $\mathbf{c}_M(\theta, \phi)$  resulting in the coefficients  $\mathbf{c}_M(\theta, \phi, \alpha, \beta)$ .

The initial lengths of the histology lines or curves is known. Similarly the initial length of the MR lines or curves, from the starting points  $\mathbf{p}_M(\mathbf{r}_{i,j}, \theta, \phi)$ , is known. The length of each line or curve to be used, measured from the initial coordinates, is defined as the minimum of either the MR or histology lengths.

The histology shrink adjusted lines or curves are reconstructed using  $\mathbf{v}_H$  or  $\mathbf{c}_H$  and the initial coordinates  $\mathbf{p}_H(s)$ , with spacing between consecutive points along the line or curve defined as  $\Delta$  mm. Similarly, the MR tilted, sheared lines or curves are reconstructed using the vectors  $\mathbf{v}_M(\theta, \phi, \alpha, \beta)$  or curve coefficients  $\mathbf{c}_M(\theta, \phi, \alpha, \beta)$  and the starting coordinates  $\mathbf{p}_M(\theta, \phi)$ , with spacing between consecutive points along the line or curve defined as  $\Delta$  mm.

Therefore for each unique set of  $(\theta, \phi, s, \alpha, \beta)$  values to be tested, there are three MR lines to be registered with three histology lines or two MR curves to be registered with two histology curves. For both situations, the respective lines or curves are of equal length and defined with equally spaced points.

The registration is therefore reduced to the registration of two point clouds, with the association of the points between the two clouds known. The registration is achieved using Procrustes Analysis (see Appendix 1), which determines a linear transformation (translation, orthogonal rotation) of the points in one dataset to best conform them to the points in the second dataset. The error measure  $e$  is the average distance between the respective points in the two point clouds after the linear transformation has been applied.

This error measure is the returned scalar value of the function  $f(\mathbf{x})$  (Equation 5.15) that is being minimised, i.e.  $s$ ,  $\alpha$  and  $\beta$  are determined such that  $e$  is a minimum for a given  $\theta$  and  $\phi$ .

### 5.5.8 Calculation of the Optimum Rotation Point

For each iteration, each defined rotation point for that iteration is tested. For each rotation point, a range of tilt values are tested,  $0 \leq \theta \leq \theta_{max}$  and  $0 \leq \phi \leq 359$ . For each tilt value tested, the optimum values of  $s$ ,  $\alpha$  and  $\beta$  are determined, with an associated error measure  $e$ . Therefore for each rotation point, a result as in Figure 5.12 is obtained. That is, for each value of  $\theta$  and  $\phi$ , the parameters  $s$ ,  $\alpha$  and  $\beta$  are determined such that the error measure  $e$  is minimised. The minimum error of each rotation point is calculated.

The optimum rotation point for iteration  $i$ ,  $\mathbf{r}_{i,opt}$ , is defined as the rotation point with the minimum error.

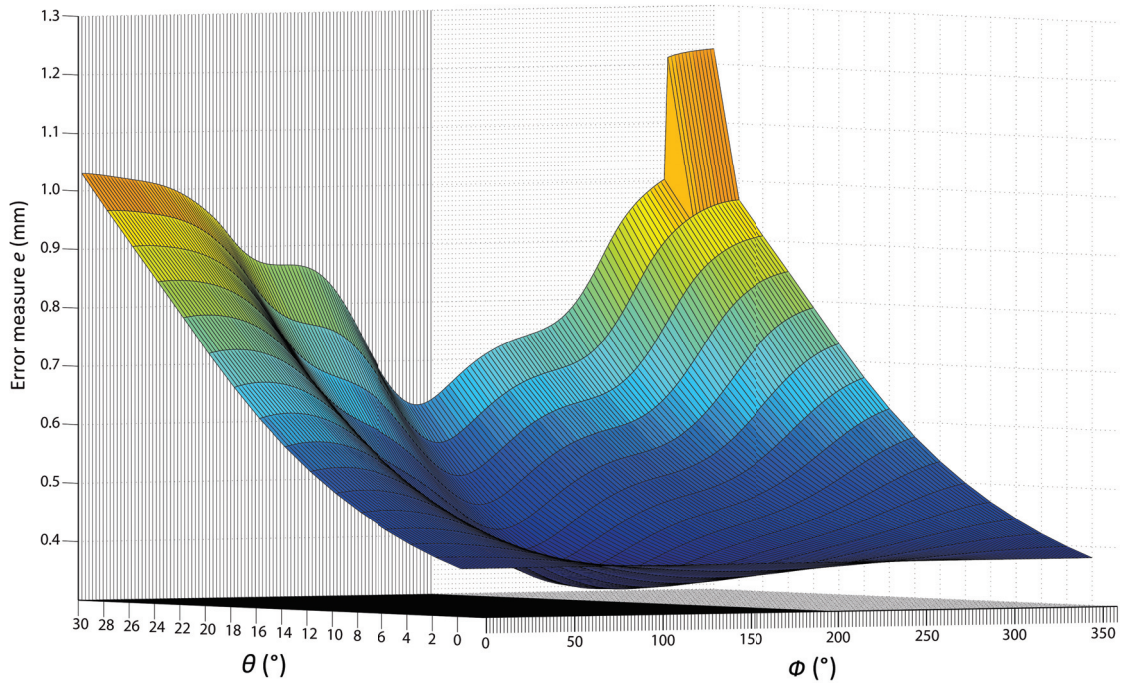


Figure 5.12: For each iteration, each defined rotation point for that iteration is tested. The figure shows a sample result for a rotation point being tested. That is, for each value of  $\theta$  and  $\phi$ ,  $s$ ,  $\alpha$  and  $\beta$  determined such that the error measure  $e$  is minimised.

### 5.5.9 Convergence Definition

At the end of each iteration  $i$ , the optimum rotation point has been calculated  $\mathbf{r}_{i,opt}$  with the associated optimum values  $\theta_{i,opt}$ ,  $\phi_{i,opt}$ ,  $\alpha_{i,opt}$ ,  $\beta_{i,opt}$ ,  $s_{i,opt}$  and the minimum error  $e_{i,opt}$ .

A convergence test is performed at the end of each iteration. The definition that convergence has been reached is that,

$$\Delta\theta < 0.5^\circ \ \& \ \Delta\phi < 0.5^\circ \ \& \ \Delta\alpha < 0.001 \ \& \ \Delta\beta < 0.001 \ \& \ \Delta s < 0.001 \ \& \ \Delta e < 0.001 \quad (5.17)$$

where

- $\Delta\theta = |\theta_{i,opt} - \theta_{i-1,opt}|$ ,
- $\Delta\phi = |\phi_{i,opt} - \phi_{i-1,opt}|$ ,
- $\Delta\alpha = |\alpha_{i,opt} - \alpha_{i-1,opt}|$ ,
- $\Delta\beta = |\beta_{i,opt} - \beta_{i-1,opt}|$ ,
- $\Delta s = |s_{i,opt} - s_{i-1,opt}|$  and
- $\Delta e = |e_{i,opt} - e_{i-1,opt}|$ .

### 5.5.10 Registration Evaluation

The accuracy of the developed 3D registration algorithm is quantified according to the metrics described by [Fitzpatrick (2010)]; in particular the fiducial registration error (FRE) and the target localisation error (TLE).

The registration algorithm is first applied to register the histology and MR *ex vivo* data, with the registration guided by the fiducial needles. For this first study, the FRE is therefore defined as the average perpendicular distance between the respective fiducial needles in the histology and MR data (measured in mm) after convergence of the algorithm. The TLE is defined as the average perpendicular distance between the respective ejaculatory ducts in the histology and MR data (measured in mm) after convergence of the algorithm.

The second application of the algorithm is to register the histology and MR *ex vivo* data, with the registration guided by the ejaculatory ducts. For the second study, the FRE is therefore defined as the average perpendicular distance between the respective ejaculatory ducts in the histology and MR data (measured in mm) after convergence of the algorithm. The TLE is defined as the average perpendicular distance between the respective fiducial needles in the histology and MR data (measured in mm) after convergence of the algorithm.

## 5.6 Registration via Fiducial Needles

### 5.6.1 Objectives and Details

The algorithm is first used to register the histology and MR *ex vivo* data, with the registration guided by the fiducial needles. This preliminary study is important for several reasons. Firstly, it enables an initial approximation of the parameters  $\theta$ ,  $\phi$ ,  $s$ ,  $\alpha$  and  $\beta$  to be achieved. Furthermore, it enables an estimation of the importance of including each of these parameters in the registration algorithm. Secondly, it enables the developed registration algorithm to be tested and moreover it enables the capabilities of the algorithm to be explored. Do further parameters need to be considered and integrated? Finally, the registration of the histology with the MR *ex vivo* data constitutes an important feasibility study. After registration of the two modalities using the fiducial needles, the average distance between the ejaculatory ducts will indicate the feasibility of using the ejaculatory ducts to register the MR and histology data.

Five prostate specimens were included in this preliminary study. The image acquisition parameters are detailed in Chapter 3. The histology slices were aligned as described in Chapter 4. Note that the shear correction of the histology slices was not included in the alignment protocol. The fiducial needles were identified in the MR images and the ejaculatory ducts were manually identified in both the histology and MR images (Section 5.2.1) and 3D parametric curves were fitted to each duct (Section 5.3).

The registration was achieved using the fiducial needles. For each prostate specimen, four different registration scenarios were tested,

- (i)  $f(s)$ : the registration was achieved taking the histology shrinkage correction factor into account as a variable parameter,
- (ii)  $f(s, \alpha, \beta)$ : the registration was achieved taking the histology shrinkage correction factor, as well as the shear parameters into account as variable parameters,
- (iii)  $f(s, \theta, \phi)$ : the registration was achieved taking the histology shrinkage correction factor, as well as the tilt parameters into account as variable parameters and finally,
- (iv)  $f(s, \alpha, \beta, \theta, \phi)$ : the registration was achieved taking the histology shrinkage correction factor, the shear parameters and the tilt parameters into account as variable parameters.

For this study,  $\theta$  was defined in the range  $0^\circ \leq \theta \leq 30^\circ$ ,  $\phi$  was defined in the range  $0^\circ \leq \phi \leq 359^\circ$ . The histology shrinkage correction factor  $s$  and the shear factors  $\alpha$  and  $\beta$  are unconstrained variables. The spacing between the points of the fiducial needles,  $\Delta = 1.0$  mm. The initial rotation point spacing along the reference fiducial needle is defined as  $\Delta r_{initial} = 2.0$  mm.

### 5.6.2 Results and Discussion

Table 5.1 to Table 5.5 detail, for each prostate specimen studied, the results of each registration scenario at the convergence of the algorithm. That is, the optimum values of the parameters included in the registration  $(s, \alpha, \beta, \theta, \phi)$ , the FRE - the average perpendicular distance between the respective fiducial needles in the histology and MR data (measured in mm) and the TLE - the average perpendicular distance between the respective ejaculatory ducts in the histology and MR data (measured in mm).

The first interest of this preliminary study was to enable an initial approximation of the parameters  $\theta$ ,  $\phi$ ,  $\alpha$ ,  $\beta$  and  $s$  to be achieved. From the five prostate specimens studied, the average value of  $\theta$  is  $13.6^\circ \pm 9.61^\circ$  (minimum  $3^\circ$ , maximum  $24^\circ$ ), measured from the most accurate registration  $f(s, \alpha, \beta, \theta, \phi)$ . Among the five prostate specimens studied, there is a significant variance in the values of  $\theta$  calculated. Furthermore, it is interesting to note that for two of the five prostate specimens,  $\theta > 20^\circ$ . As the MR *ex vivo* imaging plane was oriented parallel to the needle insertion guide of the apparatus,  $\theta$  corresponds to the angle at which the prostate specimen was sectioned during histology processing.  $\theta$  exhibits far greater variance and reaches a greater magnitude than had been expected. To our knowledge,  $\theta$  has not been previously estimated and thus a comparison with published values in the literature is not possible.

Considering the histology linear correction factor, from the five prostate specimens studied, the average value of  $s$  is  $1.07 \pm 0.03$  (minimum 1.03, maximum 1.11), measured from the most accurate registration  $f(s, \alpha, \beta, \theta, \phi)$ . This value is difficult to compare

to published values in the literature due to the significant variation of the published values, 1.14 [Schned *et al.* (1996), Haider *et al.* (2007)], 1.22 [Bart *et al.* (2005), Egevad *et al.* (1998)], 1.33 [Egawa *et al.* (2000)], 1.5 [Noguchi *et al.* (2000)]. Furthermore the assumption that this value is linear must be investigated.

The second interest of this preliminary study was to enable an estimation of the importance of including each of the parameters in the registration algorithm. The registration accuracy of the fiducial needles and ejaculatory ducts improves as more parameters are included in the algorithm. Considering first the registration  $f(s)$ , that is taking only the histology shrinkage correction factor into account as a variable parameter, the average perpendicular distance between the fiducial needles (FRE) is  $0.94 \pm 0.42$  mm, and between the ejaculatory ducts (TLE) is  $4.03 \pm 0.37$  mm, averaged over the five prostate specimens studied.

For the registration  $f(s, \alpha, \beta)$ , averaged over the five prostate specimens studied, the average perpendicular distance between the fiducial needles (FRE) is  $0.58 \pm 0.32$  mm, and between the ejaculatory ducts (TLE) is  $1.98 \pm 0.45$  mm.

For the registration  $f(s, \theta, \phi)$ , averaged over the five prostate specimens studied, the average perpendicular distance between the fiducial needles (FRE) is  $0.54 \pm 0.30$  mm, and between the ejaculatory ducts (TLE) is  $1.17 \pm 0.23$  mm.

These preliminary results indicate that a significant registration improvement is achieved by taking into account either the tilt or the shear, with the tilt appearing to have a greater influence on the accuracy of the registration. The registration accuracy is further improved by taking into account both the tilt and the shear. The results for the registration  $f(s, \alpha, \beta, \theta, \phi)$ , averaged over the five prostate specimens studied, are an average perpendicular distance between the fiducial needles (FRE) of  $0.45 \pm 0.25$  mm, and  $1.04 \pm 0.21$  mm between the ejaculatory ducts (TLE).

The preliminary study also enabled the developed registration algorithm to be tested and its capabilities to be explored. Considering the registration technique  $f(s, \alpha, \beta, \theta, \phi)$ , the average perpendicular distance between the fiducial needles (FRE) is  $< 0.45$  mm, averaged over the five prostate specimens studied. The average angular difference between the respective fiducial needles after convergence of the registration algorithm is  $3.15^\circ \pm 1.35^\circ$  (minimum  $0.25^\circ$ , maximum  $5.19^\circ$ ). The average perpendicular distance between the ejaculatory ducts (TLE) is approximately 1 mm.

Furthermore, for patients that a large tilt angle  $\theta$  was detected, there is a greater improvement in the registration accuracy by taking the tilt into account in the registration algorithm, than for patients for whom a small tilt angle was detected. For example, for patient 2, a tilt angle of  $24^\circ$  was detected. The average registration accuracy of the ejaculatory ducts (TLE) improved from  $9.88 \pm 0.10$  mm ( $f(s)$ ) to  $0.97 \pm 0.30$  mm ( $f(s, \alpha, \beta, \theta, \phi)$ ). Whereas for patient 3, for whom a tilt angle of only  $6^\circ$  was detected, the average registration accuracy of the ejaculatory ducts (TLE) changed far less significantly from  $0.62 \pm 0.25$  mm ( $f(s)$ ) to  $0.63 \pm 0.17$  mm ( $f(s, \alpha, \beta, \theta, \phi)$ ).

Lastly, this preliminary study was an important feasibility study as to whether the

histology and MR data could be registered using the ejaculatory ducts. After registration of the two modalities using the fiducial needles, the average perpendicular distance between the ejaculatory ducts (TLE) was  $1.04 \pm 0.21$  mm (worst case  $1.70 \pm 0.28$  mm, best case  $0.39 \pm 0.23$  mm). It would therefore appear that MR - histology registration via the ejaculatory ducts is worth considering.

Concerning the average number of iterations to convergence, the details for each registration technique are as follows;  $f(s)$  3.8 (minimum 3, maximum 4),  $f(s, \alpha, \beta)$  3.6 (minimum 3, maximum 4),  $f(s, \theta, \phi)$  3.6 (minimum 3, maximum 4),  $f(s, \alpha, \beta, \theta, \phi)$  4.2 (minimum 4, maximum 5).

The absolute variation of the parameters from one iteration to the next was small. The average values (excluding the last iteration before convergence) are,  $|\Delta s| = 0.01 \pm 0.01$  (minimum 0.00, maximum 0.03),  $|\Delta \alpha| = 0.01 \pm 0.01$  (minimum 0.00, maximum 0.04),  $|\Delta \beta| = 0.01 \pm 0.01$  (minimum 0.00, maximum 0.04),  $|\Delta \theta| = 0.55^\circ \pm 0.82^\circ$  (minimum  $0.00^\circ$ , maximum  $2.00^\circ$ ),  $|\Delta \phi| = 3.55^\circ \pm 5.75^\circ$  (minimum  $0.00^\circ$ , maximum  $20.00^\circ$ ), where  $|\Delta parameter| = |parameter_{i,opt} - parameter_{i-1,opt}|$ .

The average processing time to arrive at convergence for each registration technique was as follows;  $f(s)$  1.6 s (minimum 1.1 s, maximum 2.1 s),  $f(s, \alpha, \beta)$  3.5 s (minimum 2.6 s, maximum 4.7 s),  $f(s, \theta, \phi)$  1749 s (minimum 1602 s, maximum 1844 s),  $f(s, \alpha, \beta, \theta, \phi)$  3960 s (minimum 3444 s, maximum 4549 s).

The registration result for a sample prostate specimen is shown in Figure 5.13. The histology fiducial needles and ejaculatory duct curves are plotted in red, while the MR fiducial needles and ejaculatory duct curves are in blue. The registration is guided by the fiducial needles, using the registration technique  $f(s, \alpha, \beta, \theta, \phi)$ . The location of the manually identified ejaculatory ducts, in both histology and MR, are indicated by circles. Figure 5.14 shows for a sample patient, the shape of the error measure obtained at the optimum rotation point for each of the four iterations to convergence.

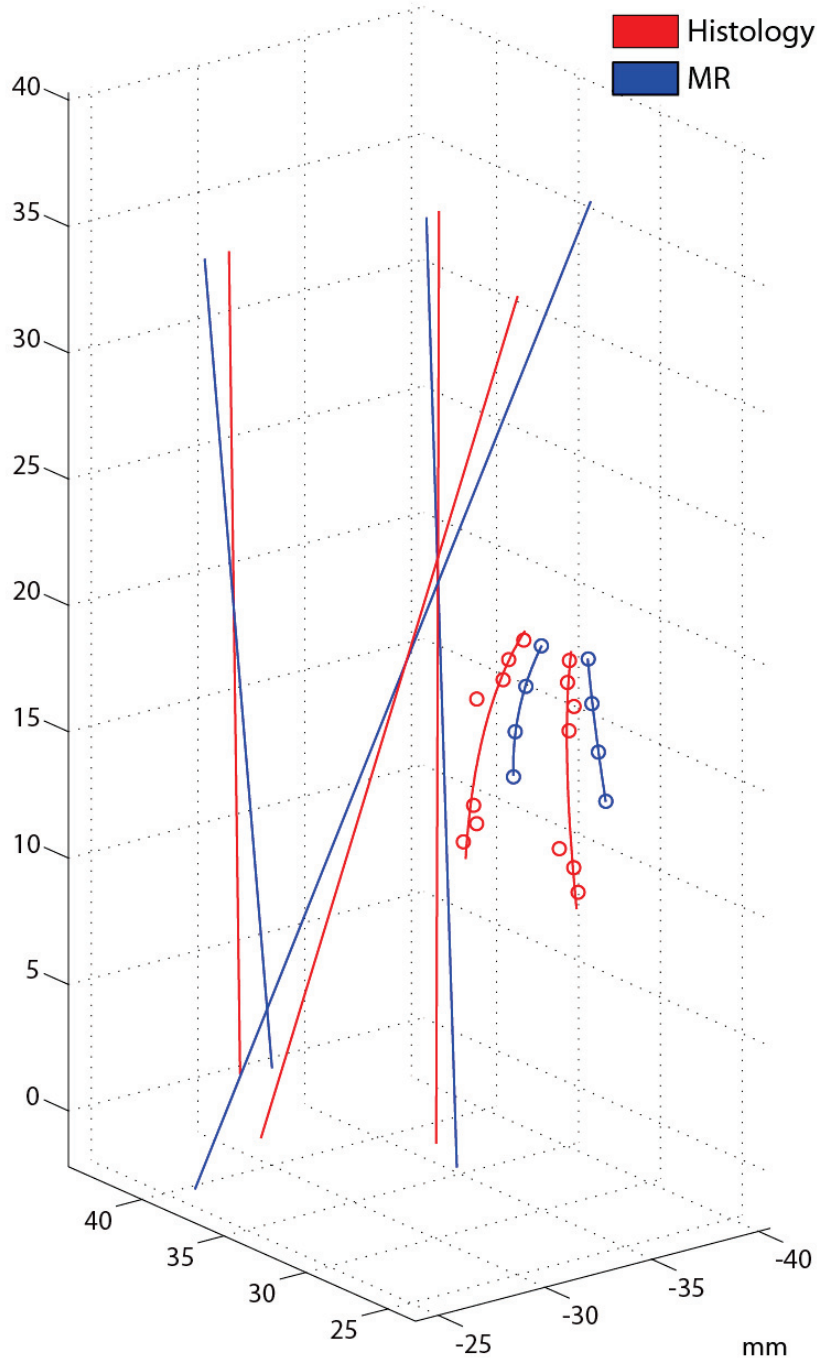


Figure 5.13: *Histology (red) and MR ex vivo (blue) fiducial needles and ejaculatory ducts showing the registration result for a sample prostate specimen. The registration is guided by the fiducial needles, using the registration technique  $f(s, \alpha, \beta, \theta, \phi)$ . The location of the manually identified ejaculatory ducts are indicated by circles.*

Registration technique	$s$	$\alpha$	$\beta$	$\theta$	$\phi$	Average perpendicular distance between histology and MR (mm)					
						needle 1	needle 2	needle 3	ejac. duct R	ejac. duct L	
$f(s)$	0.93	-	-	-	-	1.14 ± 0.53	0.35 ± 0.21	1.46 ± 0.75	2.01 ± 0.28	1.61 ± 0.35	
$f(s, \alpha, \beta)$	1.00	0.14	-0.41	-	-	0.35 ± 0.17	0.37 ± 0.24	0.43 ± 0.18	1.58 ± 0.04	0.65 ± 0.21	
$f(s, \theta, \phi)$	1.09	-	-	21°	159°	0.38 ± 0.22	0.45 ± 0.26	0.38 ± 0.23	1.14 ± 0.25	0.78 ± 0.22	
$f(s, \alpha, \beta, \theta, \phi)$	1.03	0.06	-0.19	12°	160°	0.27 ± 0.13	0.33 ± 0.20	0.37 ± 0.19	1.21 ± 0.15	0.63 ± 0.30	

Table 5.1: Prostate specimen 1: results at convergence for each registration technique tested.

Registration technique	$s$	$\alpha$	$\beta$	$\theta$	$\phi$	Average perpendicular distance between histology and MR (mm)					
						needle 1	needle 2	needle 3	ejac. duct R	ejac. duct L	
$f(s)$	0.80	-	-	-	-	1.02 ± 0.47	1.14 ± 0.02	1.25 ± 0.49	9.85 ± 0.16	9.90 ± 0.04	
$f(s, \alpha, \beta)$	1.09	-0.10	0.39	-	-	0.81 ± 0.46	0.77 ± 0.43	0.61 ± 0.37	4.47 ± 0.82	4.35 ± 0.45	
$f(s, \theta, \phi)$	1.09	-	-	21°	344°	0.48 ± 0.27	0.61 ± 0.35	0.46 ± 0.27	0.75 ± 0.32	1.04 ± 0.30	
$f(s, \alpha, \beta, \theta, \phi)$	1.09	0.08	-0.03	24°	335°	0.47 ± 0.27	0.60 ± 0.34	0.46 ± 0.28	1.11 ± 0.18	0.83 ± 0.43	

Table 5.2: Prostate specimen 2: results at convergence for each registration technique tested.

Registration technique	$s$	$\alpha$	$\beta$	$\theta$	$\phi$	Average perpendicular distance between histology and MR (mm)					
						needle 1	needle 2	needle 3	ejac. duct R	ejac. duct L	
$f(s)$	1.06	-	-	-	-	0.77 ± 0.30	0.23 ± 0.15	1.00 ± 0.56	0.42 ± 0.23	0.82 ± 0.28	
$f(s, \alpha, \beta)$	1.11	-0.25	-0.17	-	-	0.09 ± 0.04	0.22 ± 0.12	0.27 ± 0.16	0.51 ± 0.27	1.14 ± 0.16	
$f(s, \theta, \phi)$	1.13	-	-	15°	225°	0.21 ± 0.07	0.47 ± 0.23	0.34 ± 0.21	0.76 ± 0.30	1.60 ± 0.18	
$f(s, \alpha, \beta, \theta, \phi)$	1.11	-0.32	-0.25	6°	34°	0.06 ± 0.04	0.21 ± 0.12	0.27 ± 0.14	0.39 ± 0.23	0.87 ± 0.11	

Table 5.3: Prostate specimen 3: results at convergence for each registration technique tested.

Registration technique	$s$	$\alpha$	$\beta$	$\theta$	$\phi$	Average perpendicular distance between histology and MR (mm)					
						needle 1	needle 2	needle 3	ejac. duct R	ejac. duct L	
$f(s)$	0.99	-	-	-	-	1.04 ± 0.50	0.98 ± 0.45	0.97 ± 0.51	6.49 ± 1.32	7.38 ± 0.80	
$f(s, \alpha, \beta)$	1.09	-0.05	0.28	-	-	1.08 ± 0.63	0.93 ± 0.46	0.87 ± 0.51	1.56 ± 0.15	2.94 ± 2.09	
$f(s, \theta, \phi)$	1.06	-	-	15°	354°	0.76 ± 0.45	0.55 ± 0.32	0.61 ± 0.36	1.25 ± 0.20	1.56 ± 0.23	
$f(s, \alpha, \beta, \theta, \phi)$	1.06	0.08	-0.14	23°	346°	0.68 ± 0.40	0.52 ± 0.28	0.58 ± 0.33	1.20 ± 0.21	1.56 ± 0.21	

Table 5.4: Prostate specimen 4: results at convergence for each registration technique tested.

Registration technique	$s$	$\alpha$	$\beta$	$\theta$	$\phi$	Average perpendicular distance between histology and MR (mm)					
						needle 1	needle 2	needle 3	ejac. duct R	ejac. duct L	
$f(s)$	1.06	-	-	-	-	1.21 ± 0.72	0.49 ± 0.22	0.98 ± 0.41	1.36 ± 0.24	0.51 ± 0.03	
$f(s, \alpha, \beta)$	1.05	-0.19	0.17	-	-	0.68 ± 0.39	0.70 ± 0.35	0.55 ± 0.33	1.69 ± 0.29	0.86 ± 0.05	
$f(s, \theta, \phi)$	1.07	-	-	12°	323°	0.87 ± 0.46	0.91 ± 0.39	0.67 ± 0.42	1.96 ± 0.27	0.90 ± 0.03	
$f(s, \alpha, \beta, \theta, \phi)$	1.05	-0.25	0.18	3°	98°	0.68 ± 0.40	0.69 ± 0.36	0.53 ± 0.32	1.70 ± 0.28	0.88 ± 0.05	

Table 5.5: Prostate specimen 5: results at convergence for each registration technique tested.

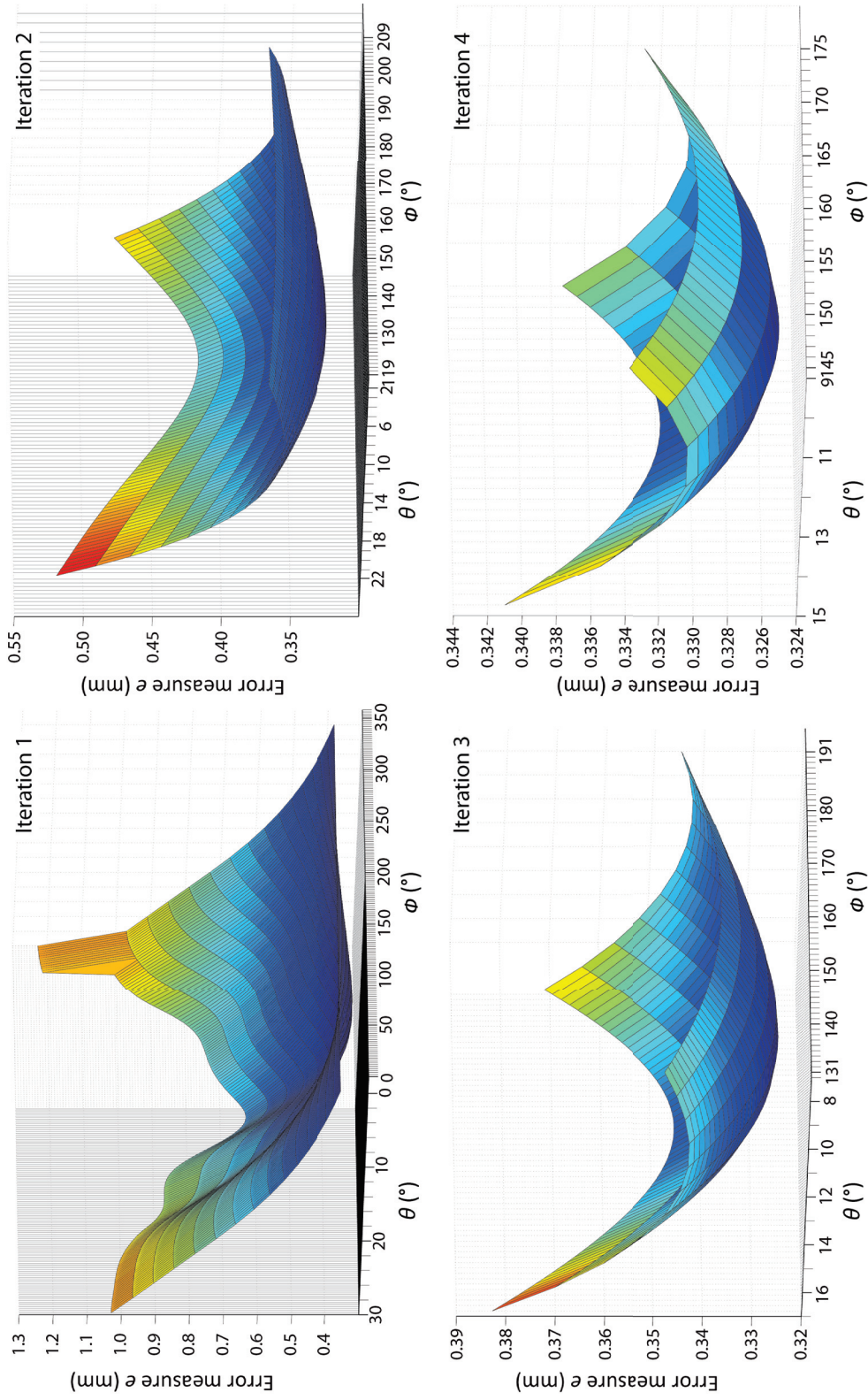


Figure 5.14: The shape of the error measure obtained at the optimum rotation point for each of the four iterations to convergence for a sample patient. The registration is guided by the fiducial needles, using the registration technique  $f(s, \alpha, \beta, \theta, \phi)$ .

## 5.7 Registration via Ejaculatory Ducts

### 5.7.1 Objectives and Details

The second application of the algorithm is to register the histology and MR *ex vivo* data, with the registration guided by the ejaculatory ducts. This study constitutes a second important feasibility study. The accuracy of the histology - MR *ex vivo* registration, achieved using the ejaculatory ducts, can be objectively quantified using the fiducial needles. This enables an evaluation of the MR - histology registration algorithm to be evaluated before application to MR *in vivo* images.

Four of the previous prostate specimens were included in this second study, patient 1, 3, 4 and 5. Patient 2 was excluded as the MR - histology registration, guided by the fiducial needles, showed that only a very small section of the identified histology and MR ejaculatory ducts overlapped.

As described in the previous section, the histology slices were aligned but not shear corrected, 3D parametric curves were fitted to each detected ejaculatory duct. The registration was guided by the ejaculatory ducts, using all possible variable parameters, that is  $f(s, \alpha, \beta, \theta, \phi)$ .

For this study,  $\theta$  was defined in the range  $0^\circ \leq \theta \leq 45^\circ$ ,  $\phi$  was defined as for the previous study, in the range  $0^\circ \leq \phi \leq 359^\circ$ . The histology shrinkage correction factor was constrained in the range  $1.00 \leq s \leq 1.11$ . The shear factors,  $\alpha$  and  $\beta$ , remain unconstrained variables as for the previous study. The spacing between the points of the curves,  $\Delta = 0.5$  mm. The initial rotation point spacing along the reference ejaculatory duct is defined as  $\Delta r_{initial} = 0.5$  mm.

### 5.7.2 Results and Discussion

Table 5.6 details, for each of the four prostate specimens studied, the results after one iteration of the algorithm - the optimum values of  $s$ ,  $\alpha$ ,  $\beta$ ,  $\theta$  and  $\phi$  as well as the FRE - the average perpendicular distance between the respective ejaculatory ducts in the histology and MR data (measured in mm) and the TLE - the average perpendicular distance between the respective fiducial needles in the histology and MR data (measured in mm).

Only one iteration was run for each prostate specimen for the following reasons,

- (i) considering the small absolute variation of the parameters from one iteration to the next measured from the previous study ( $|\Delta s|_{max} = 0.03$ ,  $|\Delta \alpha|_{max} = 0.04$ ,  $|\Delta \beta|_{max} = 0.04$ ,  $|\Delta \theta|_{max} = 2.00^\circ$ ,  $|\Delta \phi|_{max} = 20.00^\circ$ ), it was assumed that an approximation of the accuracy of the algorithm could be taken from the results obtained after the first iteration,
- (ii) the average processing time for one iteration of the algorithm is approximately 7-8 hrs,
- (iii) and finally, the results obtained after the first iteration were so poor that it was not judged to be time-worthy to continue the algorithm to convergence.

From the four prostate specimens studied, the average value of  $s$  is  $1.04 \pm 0.03$ ,  $\alpha$  is  $-0.05 \pm 0.56$ ,  $\beta$  is  $0.58 \pm 0.46$ ,  $\theta$  is  $40.0^\circ \pm 5.4^\circ$ ,  $\phi$  is  $161.5^\circ \pm 101.1^\circ$ . There is a very significant variation between the parameter values measured by the two studies, in particular with respect to  $\theta$  and  $\phi$ . The average absolute variations between the two studies for each parameter are,  $|\Delta s| = 0.04 \pm 0.03$  (minimum 0.00, maximum 0.08),  $|\Delta \alpha| = 0.49 \pm 0.44$  (minimum 0.01, maximum 0.08),  $|\Delta \beta| = 0.68 \pm 0.37$  (minimum 0.15, maximum 0.94),  $|\Delta \theta| = 29.0^\circ \pm 7.8^\circ$  (minimum  $19.0^\circ$ , maximum  $38.0^\circ$ ),  $|\Delta \phi| = 84.0^\circ \pm 58.7^\circ$  (minimum  $12.0^\circ$ , maximum  $152.0^\circ$ ), where  $|\Delta parameter| = | \text{average value of the parameter in study 1} - \text{average value of the parameter in study 2} |$ .

The average perpendicular distance between the ejaculatory ducts (FRE), averaged over the four studied prostates, is  $0.16 \pm 0.05$  mm (worst case  $0.22 \pm 0.22$  mm, best case  $0.11 \pm 0.05$  mm). This represents a significant improvement compared to the first study, where the average distance between the ejaculatory ducts was  $1.04 \pm 0.21$  mm.

However, the registration accuracy of the fiducial needles (TLE) is significantly poorer. The average perpendicular distance between the needles, averaged over the four studied prostates, is  $2.82 \pm 0.41$  mm (worst case  $5.25 \pm 1.08$  mm, best case  $1.55 \pm 0.93$  mm), compared to the average result obtained in the first study of  $0.45 \pm 0.25$  mm).

In conclusion, further work must be undertaken before the histology and MR data can be registered using the ejaculatory ducts. An investigation into possible problems that must be prior resolved is presented in the final chapter, ‘Conclusions and Perspectives’.

	Patient 1	Patient 3	Patient 4	Patient 5
$s$	1.07	1.03	1.06	1.00
$\alpha$	-0.79	0.56	0.07	-0.03
$\beta$	0.73	-0.10	0.80	0.88
$\theta$	$42^\circ$	$44^\circ$	$42^\circ$	$32^\circ$
$\phi$	$262^\circ$	$22^\circ$	$194^\circ$	$168^\circ$
needle 1 (mm)	$4.19 \pm 0.08$	$1.55 \pm 0.93$	$4.75 \pm 0.24$	$2.35 \pm 1.42$
needle 2 (mm)	$1.86 \pm 0.98$	$2.13 \pm 0.92$	$1.58 \pm 0.29$	$1.81 \pm 1.14$
needle 3 (mm)	$5.25 \pm 1.08$	$2.49 \pm 1.04$	$3.78 \pm 0.55$	$2.14 \pm 0.72$
ejac. duct R (mm)	$0.14 \pm 0.08$	$0.17 \pm 0.07$	$0.11 \pm 0.05$	$0.22 \pm 0.22$
ejac. duct L (mm)	$0.17 \pm 0.09$	$0.17 \pm 0.06$	$0.16 \pm 0.07$	$0.12 \pm 0.07$

Table 5.6: *Registration results after one iteration of the algorithm for the four prostate specimens studied. The registration is guided by the ejaculatory ducts, using the registration technique  $f(s, \alpha, \beta, \theta, \phi)$ . The results include the optimum values calculated for  $s$ ,  $\alpha$ ,  $\beta$ ,  $\theta$  and  $\phi$  as well as the average perpendicular distance (mm) between the fiducial needles (TLE) in the histology and MR data and the average perpendicular distance (mm) between the ejaculatory ducts (FLE) in the histology and MR data.*

## 5.8 Conclusion

The ejaculatory ducts are an anatomical landmark present in every prostate specimen and visible in both histology slices and MR images acquired at standard clinical routine resolution. They thus provide a means to guide the 3D histology - MR registration. The ejaculatory ducts are curved structures, therefore after manual identification of the ducts on the axial images and slices, a 3D 2<sup>nd</sup> order parametric curve can be least-squares fitted to the detected coordinates. The histology - MR registration is then simplified to the registration of two histology curves with two MR curves.

The algorithm developed was first tested by using the fiducial needles to guide the registration. This enabled a first approximation of the histology linear shrinkage correction factor and the tilt angle. The average value of  $s$  was  $1.07 \pm 0.03$  (minimum 1.03, maximum 1.11), which appears to be somewhat less than the published values in the literature which are in the range 1.14 - 1.5. The average value of  $\theta$  was  $13.6^\circ \pm 9.61^\circ$  (minimum  $3^\circ$ , maximum  $24^\circ$ ). Interesting to note was the significant variance in the values of  $\theta$  calculated. Furthermore, for this study,  $\theta$  corresponds to the angle at which the prostate specimen was sectioned during histology processing. The magnitude of the value was greater than had been expected. This value has, to our knowledge, not been previously estimated and thus a comparison is not possible.

The registration accuracy of the algorithm was tested with respect to the variable parameters included in the algorithm. The accuracy of the registration was improved by including either the shear or the tilt, and was further improved by including both the shear and the tilt. The average perpendicular distance between the fiducial needles (FRE) was  $0.45 \pm 0.25$  mm, and  $1.04 \pm 0.21$  mm between the ejaculatory ducts (TLE) for the registration technique  $f(s, \alpha, \beta, \theta, \phi)$ . It is therefore necessary to include each of the parameters, shrinkage, shear and tilt, in the registration algorithm.

Finally, the registration guided by the fiducial needles enabled an estimation of whether the histology and MR data could be registered using the ejaculatory ducts. The average perpendicular distance between the ejaculatory ducts (TLE) was  $1.04 \pm 0.21$  mm, indicating that the registration guided by the ejaculatory ducts is worth considering.

The second application of the algorithm was therefore to register the histology and MR *ex vivo* data, with the registration guided by the ejaculatory ducts. There was a significant variation in the values of the parameters calculated between the two studies. Though the average perpendicular distance between the ejaculatory ducts (FRE) was improved,  $0.16 \pm 0.05$  mm, the registration accuracy of the fiducial needles (TLE) was significantly reduced,  $2.82 \pm 0.41$  mm.

The algorithm developed to 3D register the aligned histology slices with the MR images of the prostate is ad hoc. The algorithm was developed as such in order to carry out two important feasibility studies. The first study - the registration of the histology and MR *ex vivo* data, with the registration guided by the fiducial needles - enabled an examination of the different phenomena that must be included in the algorithm as well as a first approx-

imation of the magnitude of the parameters used to describe the phenomena. The results of the first study are interesting. The shrinkage factor shows significant variance between prostate specimens and also appears to be consistently less than the values published in the literature. A detailed study of the shrinkage is required in order to determine if the phenomena is homogeneous within the specimen and constant between specimens. This perspective is further explored in Chapter 6 ‘Perspectives and Conclusion’. If a better understanding and quantification of the shrinkage factor could be achieved, it could be envisaged that the shrinkage factor is first applied to the histology data before registering the histology and MR images, therefore removing the shrinkage parameter from the variables to be optimised in the algorithm. The shear parameters could also be removed as variables to be optimised within the registration algorithm. A method to calculate the shear parameters within the histology alignment algorithm was presented in Chapter 4. However, as discussed in the Conclusion of that chapter, a more complete and accurate validation of the shear correction method must first be achieved. The removal of the shrinkage and shear parameters as variables of the registration algorithm would mean that the only variables to optimise in the registration algorithm are the tilt parameters. This would enable the developed algorithm to be simplified and the processing time reduced. It would also remove the requirement to evaluate whether the order in which the parameters ( $s, \alpha, \beta, \theta, \phi$ ) are optimised has an effect on the registration accuracy. When the algorithm has been simplified, it should be compared to, if not replaced by, more established existing algorithms, e.g. Iterative Closest Point (ICP) [Besl and McKay (1992)], Thin-Plate Spline (TPS) [Duchon (1977)], chamfer matching [Borgefors (1988)]. The first study was an important feasibility study to evaluate using the ejaculatory ducts to guide the registration. After registering the histology and MR data, using the fiducial needles to guide the registration, the average perpendicular distance between the ejaculatory ducts (TLE) was  $1.04 \pm 0.21$  mm. The results indicate that it is feasible to use the ejaculatory ducts as landmarks to guide the histology - MR registration.

The second study was therefore the registration of the histology and MR *ex vivo* data, with the registration guided by the ejaculatory ducts. The results of this second study - registration accuracy of the fiducial needles (TLE)  $2.82 \pm 0.41$  mm on average - showed that further work is required before the histology - MR registration can be achieved using the ejaculatory ducts. As previously mentioned, a detailed study of the shrinkage is required, as well as a more complete and accurate validation of the shear correction method. Furthermore, significant assumptions were made concerning the histology slices: that the inter-section spacing is 6 mm, that the sections are parallel, that the inter-slice spacing could be deduced from the slice labels and that the slices cut from a section are parallel. A comprehensive evaluation of these assumptions is required. This perspective is further explored in Chapter 6 ‘Perspectives and Conclusion’. The uncertainty associated with the inter-section and inter-slice spacing and the angular difference between the sections and slices could be reduced by the development of an apparatus which ensures the prostate is held rigid during the insertion of the fiducial needles and fixation. Slits incorporated

along the walls of the apparatus would ensure that the sections are parallel to each other and that the sections are parallel to the needle insertion guide. This perspective has been previously discussed in Chapter 4 and is further explored in Chapter 6.

The application of the developed registration algorithm to histology and MR *in vivo* data is direct. Though the MR *in vivo* resolution is lower than the MR *ex vivo* resolution, the ejaculatory ducts are visible *in vivo* due to the liquid present within the structures *in vivo*. The quality of the histology - MR *ex vivo* registration accuracy achieved can be accurately quantified using the fiducial needles, this is not possible for the histology - MR *in vivo* registration. The quality of the histology - MR *in vivo* registration can be estimated by manually identifying common landmarks visible in both modalities, e.g. cysts. However, the size of the detected landmarks as well as the uncertainty as to whether the same landmark has been identified in each modality, mean that the quantification of the quality of the histology - MR *in vivo* registration is less accurate. Therefore, as further work is required before the histology - MR registration can be achieved using the ejaculatory ducts and as the quality of the histology - MR *in vivo* registration can be less accurately quantified than the histology - MR *ex vivo* registration, the developed algorithm was not applied to MR *in vivo* data. Neither was a study carried out to quantify the registration quality achieved when using both the fiducial needles and the ejaculatory ducts to guide the registration. The overarching aim remains the 3D registration of histology slices and MR *in vivo* images, for which fiducial needles and ejaculatory ducts will never both be available to guide the registration.

# 6

## PERSPECTIVES AND CONCLUSION

### CONTENTS

6.1	Introduction . . . . .	125
6.2	Histology Shrinkage Correction Factor . . . . .	127
6.3	Distances and Angles between Histology Sections and Slices . . . . .	128
6.4	Complete Evaluation . . . . .	129
6.5	Registration Algorithm Extension . . . . .	131
6.6	Virtual Microscopy . . . . .	131
6.7	Conclusion . . . . .	132

### 6.1 Introduction

The aim of this thesis was to develop a method to 3D register the histology slices of radical prostatectomy specimens with MR *in vivo* images. The problem is two-fold, requiring first the alignment of the histology slices and then the 3D registration of the aligned histology slices with the MR images.

Considering first the histology slice alignment, an apparatus has been designed and fabricated that enables internal fiducial markers to be created in a rapid and standardised manner in fresh prostate specimens. An algorithm was then developed that automatically detects and identifies the created fiducial markers, enabling the alignment and shear correction of the stack of histology slices.

The developed protocol has been implemented as part of the standard clinical routine at our institution, less than 5 minutes is required for the creation of the fiducial markers. On average, 93.7% of the created fiducial markers are visible to the eye. The algorithm to detect and identify the fiducial markers is, after an interactive initialisation (approximate duration 30 - 60 s), entirely automatic (average duration less than 6 minutes per dataset). On average, 96.1% of the visible markers are correctly detected and identified.

The quality of the alignment achieved using the proposed apparatus and method was first validated using simulated images, whose sole difference from histology slices was the absence of tissue deformation. The resulting accuracy and angular precision of the alignment was limited only by the computing precision, demonstrating that there is no residual error associated with the algorithm for a situation where there is no deformation and that a certain number of markers can be missed without affecting the performance of the alignment.

The algorithm was tested experimentally using a sample of beef liver. The average accuracy of the alignment, using an average of 2.71 fiducial markers per image, was  $0.11 \pm 0.09$  mm at the fiducial markers, and  $0.58 \pm 0.43$  mm at a point 20 mm away from the fiducial markers, with an average angular precision of  $2.67^\circ \pm 0.51^\circ$ .

The protocol was tested on 10 prostate specimens, with 19.2 histology slices per specimen on average. The accuracy of the alignment at the fiducial markers was on average  $0.18 \pm 0.13$  mm.

The aligned histology slices require a shear correction. This shear correction can either be applied to the aligned histology slices, or included in the 3D histology - MR registration algorithm. If applied to the aligned histology slices, the quality of the shear correction was estimated as the angular difference from the vertical of the 3D least squares line passing through the validation markers. The average angular difference, evaluated first using the simulated images, was  $0.06^\circ \pm 0.00^\circ$  and using the beef liver sample was  $7.54^\circ \pm 1.46^\circ$ .

The second aspect of this thesis is the 3D registration of the aligned histology slices with the MR images. An algorithm was developed that guides the registration using the ejaculatory ducts, an anatomical landmark present in every prostate specimen and visible in both histology slices and MR images acquired at standard clinical routine resolution.

The algorithm developed was first tested by using the fiducial needles to guide the registration. This enabled a first approximation of the parameters that must be included in the registration algorithm, that is shrinkage ( $s$ ), shear ( $\alpha, \beta$ ) and tilt ( $\theta, \phi$ ). The average value of the histology linear shrinkage correction factor was  $1.07 \pm 0.03$  and the average value of the tilt angle was  $13.6^\circ \pm 9.61^\circ$ . There was significant variance in the values of the shrinkage and tilt calculated. Furthermore, for this study, the tilt angle corresponds to the angle at which the prostate specimen was sectioned during histology processing. The magnitude of the value was greater than had been expected.

The registration accuracy of the algorithm was tested with respect to the variable parameters included in the algorithm. The accuracy of the registration was improved by including either the shear or the tilt, and was further improved by including both the shear

and the tilt, indicating that it is necessary to include each of the parameters (shrinkage, shear and tilt) in the registration algorithm.

For the registration technique  $f(s, \alpha, \beta, \theta, \phi)$ , the average perpendicular distance between the fiducial needles was  $0.45 \pm 0.25$  mm, and  $1.04 \pm 0.21$  mm between the ejaculatory ducts. The registration accuracy of the ejaculatory ducts achieved indicated that the registration of the histology and MR data, guided by the ejaculatory ducts, is worth considering.

The second application of the algorithm was therefore to register the histology and MR *ex vivo* data, with the registration guided by the ejaculatory ducts. The accuracy of the registration was quantified using the fiducial needles, enabling an evaluation of the MR - histology registration algorithm to be evaluated before application to MR *in vivo* images. There was a significant variation in the values of the parameters calculated between the two studies. Though the average perpendicular distance between the ejaculatory ducts was improved,  $0.16 \pm 0.05$  mm, the registration accuracy of the fiducial needles was significantly reduced,  $2.82 \pm 0.41$  mm.

In order to improve the histology - MR registration, certain deformations and assumptions must be studied in detail, quantified and incorporated into the algorithm. The work to be done, the perspectives of this thesis, are detailed in the sections below.

## 6.2 Histology Shrinkage Correction Factor

The fixation and histology processing of the prostate specimen cause a shrinkage of the tissue. Published histology linear correction factors to compensate for tissue shrinkage vary considerably; 1.14 [Schned *et al.* (1996), Haider *et al.* (2007)], 1.22 [Bart *et al.* (2005), Egevad *et al.* (1998)], 1.33 [Egawa *et al.* (2000)], 1.5 [Noguchi *et al.* (2000)]. In order to proceed with the histology - MR registration, it is of absolute importance that the histology shrinkage is examined and quantified.

An apparatus has been designed and fabricated to enable the histology shrinkage study to be achieved. It is a plexi-glass guide, of dimension 50x50x20 mm, that can be attached to the previously made support in place of the needle insertion guide. Equally spaced holes, (spacing dx, dy) have been vertically drilled through the guide, see Figure 6.1.

The idea is to vertically insert approximately five of the previously used catheter needles into the tissue, using various holes such that there are needles inserted at the centre, middle region and extremity of the tissue. The needles are removed and the rigid plastic sheaths are left in place. Thread, which has been soaked in gadolinium and coloured dye, should be passed through the plastic sheaths and the sheaths can be removed. The gadolinium will ensure that the threads are visible in MR images and the dye will stain the tissue such that the position of the threads can be detected in the histology slices. An MR *ex vivo* acquisition will show the initial spacing between the threads. The tissue specimen is then fixed. The threads will not affect the shrinkage induced by the fixation. After re-soaking the threads in gadolinium, a second MR *ex vivo* acquisition of the specimen should be

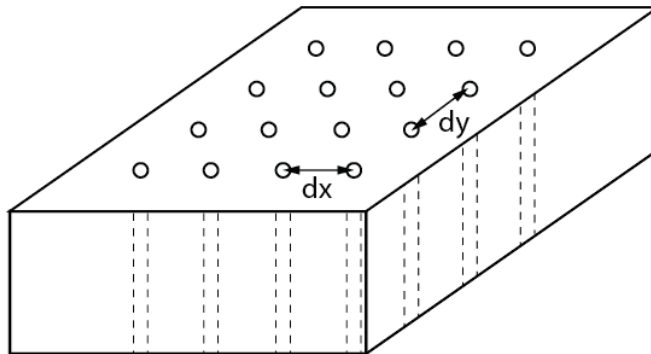


Figure 6.1: *The fixation and histology processing of the prostate causes a shrinkage of the tissue. The nature and magnitude of the shrinkage must be estimated. This plexi-glass guide, dimension 50x50x20 mm, can be attached to the previously made support and enables catheters to be vertically inserted into the tissue at definite distances from each other. Thread soaked in gadolinium and coloured dye can be passed through the catheters, enabling the shrinkage to be estimated after fixation and after histology processing.*

acquired. The shrinkage due to the fixation can thus be deduced. The threads can then be removed and the specimen histology processed. The dye will have stained the histology slices, enabling the slices to be aligned and the shrinkage and deformation associated with the histology processing routine to be estimated.

The experiment should first be tested on a beef liver sample to ensure the feasibility of the study, and then on 5 - 10 prostate specimens. The study protocol has been validated by the anatomico-pathologists at our institution. The study should enable the following questions to be answered,

- (i) Is the shrinkage homogeneous? If not, can it be modelled as a function of the distance from the centre of the prostate?
- (ii) Is the shrinkage factor constant between prostate specimens? If not, does it depend on the size of the prostate specimen, the fixation time, the formaldehyde concentration?

### 6.3 Distances and Angles between Histology Sections and Slices

During histology processing, the prostate specimen is first cut into 6 mm sections. These sections, ordered from the apex to the base, are labelled using roman numerals, e.g. X, XI, XII, etc. Each 6 mm section is embedded in paraffin and the paraffin-embedded tissue blocks are sliced using the microtome, approximately every 1 mm. The slices are then labelled with the roman numeral indicating which section it was cut from, and then a figure indicating the depth at which the slice is cut, i.e. for the section XII, the first slice from the section is labelled XII\_0, a slice 2 mm deeper is labelled XII\_2.

When aligning the histology slices, it was assumed that

- (i) the inter-section spacing is 6 mm,
- (ii) the sections are parallel,
- (iii) the inter-slice spacing could be deduced from the slice labels and
- (iv) the slices cut from a section are parallel.

These assumptions are difficult to quantify, however a first effort has been made using prostate specimen 1. The coordinates of the fiducial markers, for the subset of histology slices in which the three fiducial markers are visible (15 of the 21 slices), are saved for each slice. From the MR *ex vivo* acquisition of the prostate specimen, the coordinates of the three fiducial markers is calculated for horizontal planes spaced every 0.02 mm along the z-axis. For each histology slice, the optimum registration of the three histology markers with three MR markers is calculated. The optimum registration is defined as that which minimises the distance between the respective markers. The tilt is allowed to vary in the range,  $0^\circ \leq \theta \leq 30^\circ$ ,  $0^\circ \leq \phi \leq 359^\circ$ . Various linear histology shrinkage correction factors are first applied to the histology data,  $1.03 \leq s \leq 1.11$ .

The result is presented in Figure 6.2. It would appear that histology slices cut from the same section are approximately parallel. This was expected as the tissue is held rigid within the paraffin block and the paraffin block, once mounted, is held rigid by the microtome during slicing. The assumption that the sections are parallel should be further examined. However, it is in particular, the assumptions regarding the inter-section and inter-slice spacing that appears to be flawed.

A more accurate understanding of the shrinkage due to fixation and histology processing is first required. Then, a more complete study of the inter-section and inter-slice spacing should be carried out. The histology - MR registration cannot be considered before the histology slices are first accurately aligned.

A further perspective (previously mentioned in Chapter 4 ‘Histology Slice Alignment’) concerns the development of an apparatus that would enable the position of the prostate specimen to be held rigid during the guided insertion of the fiducial needles and fixation. If the apparatus could be designed such as to incorporate slits at 6 mm intervals along the walls of the apparatus, it would enable the prostate to be sectioned along planes parallel to the needle insertion guide of the apparatus. An advantage would be that the apparatus is MR compatible to enable the preliminary tests and trials to be carried out. Inspiration for such an apparatus should be taken from the comprehensive overview of existing apparatus in [Chen *et al.* (2010)].

## 6.4 Complete Evaluation

Once a detailed study of the shrinkage, inter-section spacing, inter-slice spacing, and the angles between the sections has been carried out and the results incorporated into the algorithm, a complete validation of the algorithm should be undertaken.

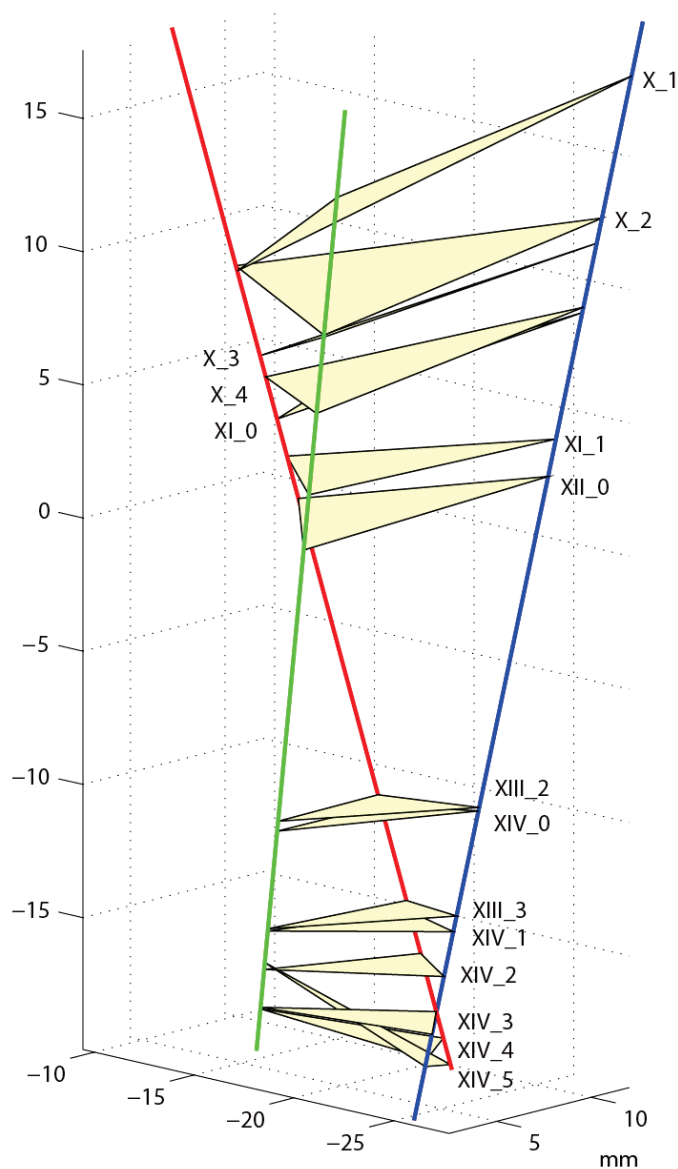


Figure 6.2: For prostate specimen 1, the coordinates of the histology fiducial markers (for histology slices in which three fiducial markers are visible) are registered to the MR *ex vivo* fiducial marker coordinates (data every 0.2 mm), varying the tilt in the range,  $0^\circ \leq \theta \leq 30^\circ$  and  $0^\circ \leq \phi \leq 359^\circ$ . The result shows that the assumptions regarding the inter-section and inter-slice spacing appear to be flawed. The assumption that the sections are parallel should also be further examined.

Similarly to the validation protocol for the alignment of the histology slices, a beef liver sample could be used. The fiducial markers should be inserted using the developed apparatus, as well as an MR compatible validation marker. Furthermore, curved needles could be used to insert thread, previously soaked in gadolinium and coloured dye, creating simulated ejaculatory ducts visible in MR and histology. An MR *ex vivo* acquisition of the fresh sample should be acquired. After fixation and histology processing, the histology slices can be aligned using the fiducial markers. The aligned histology slices can then be

3D registered to the MR images using the simulated ejaculatory ducts. The quality of the histology slice alignment can be quantified using the validation marker. The angle with respect to the vertical of the validation marker can be measured from the MR *ex vivo* images. As previously mentioned in Chapter 4 ‘Histology Slice Alignment’, this information was lacking from the previous validation study. The 3D histology - MR registration can be quantified using the fiducial needles.

## 6.5 Registration Algorithm Extension

The first requirement is a detailed study of the shrinkage, inter-section spacing, inter-slice spacing, and the angles between the sections. If the incorporation into the algorithm of the results of the study does not improve the registration accuracy, the addition of a cyst, visible in both the histology and MR data, to complement the ejaculatory ducts in guiding the registration could be tested.

## 6.6 Virtual Microscopy

This thesis was funded by the company Centre Compétence International en Télé-Image (CCITI). CCITI develop and sell scanners that enable histology slices to be digitised at very high resolution. The histology slices can be viewed at ten different levels. For each level, the image is composed of a number of JPEG tiles and an associated pixel resolution. For example, at level 9, the histology image is composed of one JPEG tile of dimension  $600 \times 600$  pixels, with a pixel resolution of  $863 \mu\text{m}$ . At level 0, the histology image is composed of 1554 JPEG tiles, each of dimension  $600 \times 600$  pixels, with a pixel resolution of  $1.7 \mu\text{m}$ . Figure 6.3 shows one JPEG tile ( $600 \times 600$  pixels) of a sample histology slice viewed at (a) level 5 (resolution  $53.9 \mu\text{m}$ ), (b) level 4 (resolution  $27.0 \mu\text{m}$ ), (c) level 3 (resolution  $13.5 \mu\text{m}$ ), (d) level 2 (resolution  $6.7 \mu\text{m}$ ), (e) level 1 (resolution  $3.4 \mu\text{m}$ ) and (f) level 0 (resolution  $1.7 \mu\text{m}$ ).

The process of high resolution histology slice digitisation is referred to as *virtual microscopy*. The advantages of virtual microscopy are numerous; the access, archiving, annotation and sharing of the slices is simplified. The inherent risk of damaging or breaking the glass histology slices is eliminated. An unlimited number of users can examine the slices at the same time, independent of access time or location. This renders the slices available to a broader audience, meaning that a second opinion can be more easily obtained. Multiple slides can be opened, analysed and compared at the same time and on the same screen. Furthermore the use of virtual microscopes can transform traditional teaching methods by removing the reliance on physical space, equipment and specimens to a model that is solely dependent upon computer-internet access.

Virtual microscopy enables the integration of image processing algorithms into the standard anatomo-pathology routine, for example, automatic identification of malignant regions, calculation of the area and volume of detected malignant regions, identification

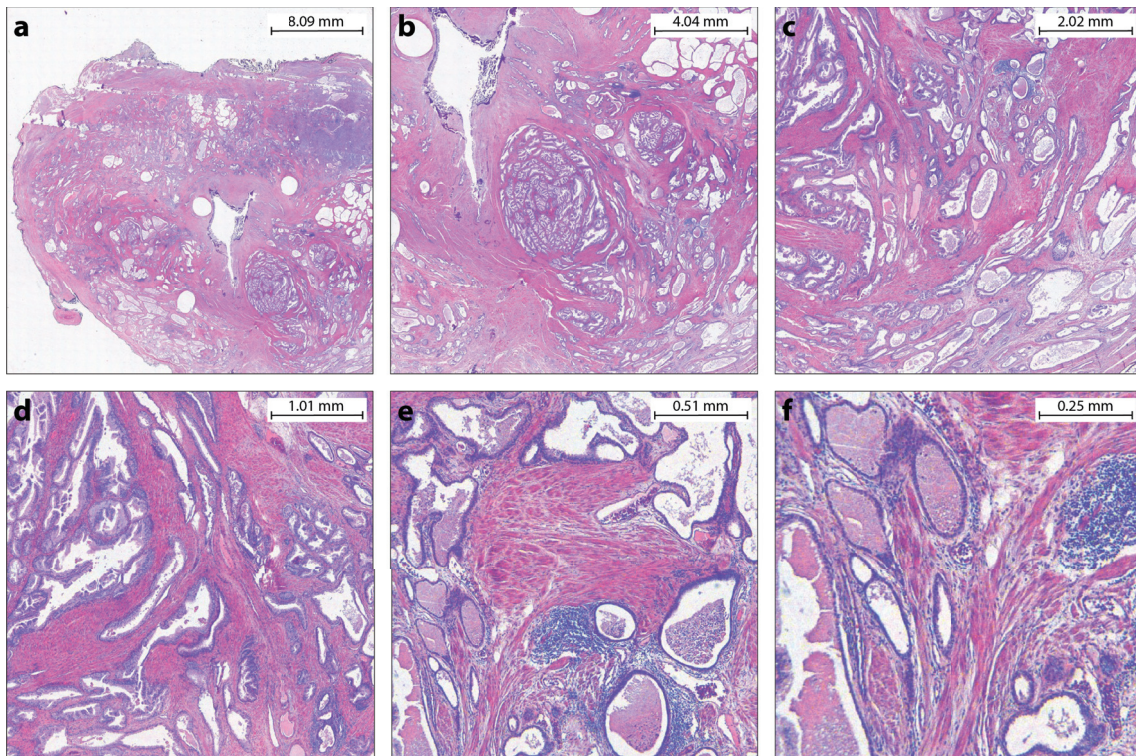


Figure 6.3: *Virtual microscopy refers to the high resolution digitisation of histology slices. One JPEG tile ( $600 \times 600$  pixels) of a sample prostate histology slice viewed at (a) level 5, resolution  $53.9 \mu\text{m}$ , total number of tiles = 4, (b) level 4, resolution  $27.0 \mu\text{m}$ , total number of tiles = 9, (c) level 3, resolution  $13.5 \mu\text{m}$ , total number of tiles = 30, (d) level 2, resolution  $6.7 \mu\text{m}$ , total number of tiles = 110 (e) level 1, resolution  $3.4 \mu\text{m}$ , total number of tiles = 399 and (f) level 0, resolution  $1.7 \mu\text{m}$ , total number of tiles = 1554. The scale of each image is indicated in the top right hand corner. The histology slice was digitised using a CCITI scanner and viewed using CCITI developed software.*

of the Gleason grade of a designated area. Furthermore the positive surgical margins can be delineated and incorporated into the reconstructed prostate histology volume, enabling an accurate evaluation and visual appreciation of the surgery performed.

## 6.7 Conclusion

In conclusion, an apparatus has been designed and tested that enables internal fiducial markers to be created in a rapid and standardised manner in fresh prostate specimens and an algorithm has been developed and tested that automatically detects and identifies the created fiducial markers, enabling the alignment and shear correction of a stack of histology slices. Though the alignment accuracy was quantified using simulated images, a beef liver sample and 10 prostate specimens, further issues must be studied before it can be confidently asserted that the histology slices are accurately aligned. In particular, the histology inter-slice spacing and the angle between the slices must be further examined.

A second algorithm has been developed that 3D registers the aligned histology slices

with the MR images, using the ejaculatory ducts to guide the registration. Three significant phenomena, described using five parameters, that need to be included in the registration algorithm have been identified and studied. However, in particular, the shrinkage that the histology undergoes due to the fixation and histology processing must be better understood and quantified before the histology and MR data can be registered.





# APPENDIX

## A.1 Procrustes Analysis

Procrustes analysis [Kendall (1989), Bookstein (1991), Seber (1984)] determines the linear transformation (translation  $T$  and orthogonal rotation  $R$ ) of the points in matrix  $B$  to best register them to the points in matrix  $A$ . The goodness-of-fit criterion is the average distance between the respective points after the transformation has been applied.

$A$  and  $B$  are  $n \times m$  matrices, that is they both have the same number of 3D points. Procrustes analysis matches  $B(i)$  to  $A(i)$ .

### Centre at the origin

The two matrices of coordinates are first centred at the origin;

$$A_0 = A - \bar{A} \tag{A.1}$$

$$B_0 = B - \bar{B} \tag{A.2}$$

where  $\bar{A}$  and  $\bar{B}$  represent the mean of matrix  $A$  and  $B$  respectively.

### Centred Frobenius norm

The centred Frobenius norm is calculated for each matrix as;

$$\|A_F\| = \sqrt{\sum_{i=1}^n \sum_{j=1}^m |a_{i,j}|^2} \tag{A.3}$$

$$\|B_F\| = \sqrt{\sum_{i=1}^n \sum_{j=1}^m |b_{i,j}|^2} \quad (\text{A.4})$$

### Scale

The matrices are scaled to the same unit norm,

$$A_{0,1} = \frac{A_0}{\|A_F\|} \quad (\text{A.5})$$

$$B_{0,1} = \frac{B_0}{\|B_F\|} \quad (\text{A.6})$$

### Calculation $R$

The matrix  $H$  is calculated,

$$H = A_{0,1}^T \times B_{0,1} \quad (\text{A.7})$$

The singular value decomposition (SVD) of this matrix,

$$H = U \times S \times V^T \quad (\text{A.8})$$

enables the matrix  $X$  to be calculated

$$X = V \times U^T \quad (\text{A.9})$$

$R$  is defined depending on the value of the determinant of  $X$ ;

- if  $\det(X) = 1$ , then  $R = X$ ,
- if  $\det(X) = -1$ , then  $R^T = V^T \times U^T$  [Arun *et al.* (1987)].

### Calculation $T$

The translation component is calculated as,

$$T = \bar{A} - (\bar{B} \times R) \quad (\text{A.10})$$

### Error measure

The normalised error measure, the goodness-of-fit criterion, is calculated as

$$e = \frac{1}{n} \sum_{i=1}^n \|(b_i \times R) + T - x_i\| \quad (\text{A.11})$$

# BIBLIOGRAPHY

- [Aarnink *et al.* (1998)] Aarnink, R., Beerlage, H., De La Rosette, J., Debruyne, F., and Wijkstra, H. (1998). Transrectal ultrasound of the prostate: innovations and future applications. *The Journal of urology*, 159:1568–1579.
- [Akin *et al.* (2006)] Akin, O., Sala, E., Moskowitz, C. S., Kuroiwa, K., Ishill, N. M., Pucar, D., Scardino, P. T., and Hricak, H. (2006). Transition zone prostate cancers: Features, detection, localization, and staging at endorectal mr imaging. *Radiology*, 239:784–792.
- [Al-Baali and Fletcher (1986)] Al-Baali, M. and Fletcher, R. (1986). An efficient line search for nonlinear least squares. *Journal of Optimization Theory and Applications*, 48:359–377.
- [Andriole *et al.* (2009)] Andriole, G., Crawford, E., Grubb III, R., Buys, S., Chia, D., Church, T., Fouad, M., Gelmann, E., Kvale, P., Reding, D., *et al.* (2009). Mortality results from a randomized prostate-cancer screening trial. *New England Journal of Medicine*, 360:1310–1319.
- [Arun *et al.* (1987)] Arun, K. S., Huang, T. S., and Blostein, S. D. (1987). Least-squares fitting of two 3-d point sets. *IEEE Transactions on Pattern Analysis and Machine Intelligence*, PAMI-9(5):698–700.
- [Asha *et al.* (2005)] Asha, D., Al-Qaisiehb, B., Bottomleya, D., Careya, B., and Josepha, J. (2005). The impact of hormone therapy on post-implant dosimetry and outcome following iodine-125 implant monotherapy for localised prostate cancer. *Radiotherapy and Oncology*, 75:303–306.
- [Aus *et al.* (2005)] Aus, G., Abbou, C., Bolla, M., Heidenreich, A., Schmid, H., Van Poppel, H., Wolff, J., and Zattoni, F. (2005). Eau guidelines on prostate cancer. *European urology*, 48:546–551.
- [Bahn *et al.* (2002)] Bahn, D., Lee, F., Badalament, R., Kumar, A., Greski, J., and Chernenick, M. (2002). Targeted cryoablation of the prostate: 7-year outcomes in the primary treatment of prostate cancer. *Urology*, 60:3–11.
- [Bangma *et al.* (2007)] Bangma, C. H., Roemeling, S., and Schroder, F. H. (2007). Overdiagnosis and overtreatment of early detected prostate cancer. *World journal of urology*, 25:3–9.

- [Bardinet *et al.* (2002)] Bardinet, E., Ourselin, S., Dormont, D., Malandain, G., Tande, D., Parain, K., Ayache, N., and Yelnik, J. (2002). Co-registration of histological, optical and mr data of the human brain. In *MICCAI 2002*, pages 548–555.
- [Barry (2001)] Barry, M. (2001). Prostate-specific-antigen testing for early diagnosis of prostate cancer. *New England Journal of Medicine*, 344:1373–1377.
- [Bart *et al.* (2005)] Bart, S., Mozer, P., Hemar, P., Lenaour, G., Comperat, E., Renard-Penna, R., Chartier-Kastler, E., and Troccaz, J. (2005). MRI-histology registration in prostate cancer. In *Proceedings of Surgetica'2005*, pages 361–367.
- [Bastian *et al.* (2009)] Bastian, P. J., Carter, B. H., Bjartell, A., Seitz, M., Stanislaus, P., Montorsi, F., Stief, C. G., and Schroder, F. (2009). Insignificant prostate cancer and active surveillance: from definition to clinical implications. *European urology*, 55(6):1321–1332.
- [Bauer *et al.* (1999)] Bauer, J., Zeng, J., Weir, J., Zhang, W., Sesterhenn, I., Connelly, R., Mun, S., and Moul, J. (1999). Three-dimensional computer-simulated prostate models: lateral prostate biopsies increase the detection rate of prostate cancer. *Urology*, 53:961–967.
- [Beheshti *et al.* (2008)] Beheshti, M., Vali, R., Waldenberger, P., Fitz, F., Nader, M., Loidl, W., Broinger, G., Stoiber, F., Foglman, I., and Langsteger, W. (2008). Detection of bone metastases in patients with prostate cancer by 18 f fluorocholine and 18 f fluoride pet-ct: a comparative study. *European journal of nuclear medicine and molecular imaging*, 35:1766–1774.
- [Berry *et al.* (1984)] Berry, S., Coffey, D. S., Walsh, P. C., and Ewing, L. L. (1984). The development of human benign prostatic hyperplasia with age. *The Journal of Urology*, 132:474–479.
- [Besl and McKay (1992)] Besl, P. J. and McKay, N. D. (1992). Method for registration of 3-d shapes. In *Robotics-DL tentative*, pages 586–606. International Society for Optics and Photonics.
- [Bill-Axelsson *et al.* (2005)] Bill-Axelsson, A., Holmberg, L., Ruutu, M., Häggman, M., Andersson, S., Bratell, S., Spångberg, A., Busch, C., Nordling, S., Garmo, H., *et al.* (2005). Radical prostatectomy versus watchful waiting in early prostate cancer. *New England Journal of Medicine*, 352:1977–1984.
- [Björndahl (2010)] Björndahl, L. (2010). Semen analysis: Essentials for the clinician. *Reproductive Endocrinology and Infertility*, pages 379–388.
- [Blana *et al.* (2006)] Blana, A., Rogenhofer, S., Ganzer, R., Wild, P., Wieland, W., and Walter, B. (2006). Morbidity associated with repeated transrectal high-intensity focused ultrasound treatment of localized prostate cancer. *World journal of urology*, 24:585–590.

- [Blana *et al.* (2008)] Blana, A., Murat, F., Walter, B., Thuroff, S., Wieland, W., Chaussy, C., and Gelet, A. (2008). First analysis of the long-term results with transrectal hifu in patients with localised prostate cancer. *European urology*, 53:1194–1203.
- [Bookstein (1991)] Bookstein, F. L. (1991). *Morphometric Tools for Landmark Data*. Cambridge University Press.
- [Borboroglu *et al.* (2000)] Borboroglu, P. G., Comer, S. W., Riffenburgh, R. H., and Am-ling, C. L. (2000). Extensive repeat transrectal ultrasound guided prostate biopsy in patients with previous benign sextant biopsies. *The Journal of urology*, 163:158–162.
- [Borgefors (1988)] Borgefors, G. (1988). Hierarchical chamfer matching: A parametric edge matching algorithm. *Pattern Analysis and Machine Intelligence, IEEE Transactions on*, 10(6):849–865.
- [Bostwick and Cheng (2008)] Bostwick, B. and Cheng, L. (2008). *Urologic Surgical Pathology*. Mosby Elsevier, 2 edition.
- [Bouchelouche *et al.* (2010)] Bouchelouche, K., Turkbey, B., Choyke, P., and Capala, J. (2010). Imaging prostate cancer: an update on positron emission tomography and magnetic resonance imaging. *Current urology reports*, 11:180–190.
- [Bouchelouche and Oehr (2008)] Bouchelouche, K. and Oehr, P. (2008). Positron emission tomography and positron emission tomography/computerized tomography of urological malignancies: an update review. *The Journal of urology*, 179:34.
- [Bozzini *et al.* (2012)] Bozzini, G., Colin, P., Nevoux, P., Villers, A., Mordon, S., and Betrouni, N. (2012). Focal therapy of prostate cancer: energies and procedures. In *Urologic Oncology: Seminars and Original Investigations*. Elsevier.
- [Breen *et al.* (2003)] Breen, M. S., Lancaster, T. L., Lazebnik, R. S., Nour, S. G., Lewin, J. S., and Wilson, D. L. (2003). Three-dimensional method for comparing *in vivo* interventional MR images of thermally ablated tissue with tissue response. *J Magn Reson Imaging*, 18(1):90–102.
- [Breen *et al.* (2005)] Breen, M. S., Lazebnik, R. S., and Wilson, D. L. (2005). Three-dimensional registration of magnetic resonance image data to histological sections with model-based evaluation. *Ann Biomed Eng*, 33(8):1100–1112.
- [Calabrò and Sternberg (2007)] Calabrò, F. and Sternberg, C. (2007). Current indications for chemotherapy in prostate cancer patients. *European urology*, 51:17–26.
- [Chappelow *et al.* (2007)] Chappelow, J., Madabhushi, A., Rosen, M., Tomaszewski, J., and Feldman, M. (2007). Multimodal image registration of ex vivo 4 tesla mri with whole mount histology for prostate cancer detection. In *SPIE Medical Imaging: Image Processing*, volume 6512, page 65.

- [Chen *et al.* (2010)] Chen, L. H., Ho, H., Lazaro, R., Thng, C. H., Yuen, J., Ng, W. S., and Cheng, C. (2010). Optimum slicing of radical prostatectomy specimens for correlation between histopathology and medical images. *Int J Comput Assist Radiol Surg*, 5(5):471–487.
- [Cifor *et al.* (2011)] Cifor, A., Bai, L., and Pitiot, A. (2011). Smoothness-guided 3-D reconstruction of 2-D histological images. *Neuroimage*, 56(1):197–211.
- [Cohen *et al.* (1998)] Cohen, F., Yang, Z., Huang, Z., and Nianov, J. (1998). Automatic matching of homologous histological sections. *Biomedical Engineering, IEEE Transactions on*, 45:642–649.
- [Crouzet *et al.* (2010)] Crouzet, S., Rebillard, X., Chevallier, D., Rischmann, P., Pasticier, G., Garcia, G., Rouviere, O., Chapelon, J.-Y., and Gelet, A. (2010). Multicentric oncologic outcomes of high-intensity focused ultrasound for localized prostate cancer in 803 patients. *European urology*, 58:559–566.
- [Dall’Era *et al.* (2012)] Dall’Era, M., Albertsen, P., Bangma, C., Carroll, P., Carter, H., Cooperberg, M., Freedland, S., Klotz, L., Parker, C., and Soloway, M. (2012). Active surveillance for prostate cancer: a systematic review of the literature. *European Urology*, 62:976–983.
- [Dauguet *et al.* (2007)] Dauguet, J., Delzescaux, T., Conde, F., Mangin, J.-F., Ayache, N., Hantraye, P., and Frouin, V. (2007). Three-dimensional reconstruction of stained histological slices and 3d non-linear registration with *in-vivo* MRI for whole baboon brain. *J Neurosci Methods*, 164(1):191–204.
- [Delongchamps *et al.* (2011)] Delongchamps, N. B., Rouanne, M., Flam, T., Beuvon, F., Liberatore, M., Zerbib, M., and Cornud, F. (2011). Multiparametric magnetic resonance imaging for the detection and localization of prostate cancer: combination of t2-weighted, dynamic contrast-enhanced and diffusion-weighted imaging. *BJU international*, 107:1411–1418.
- [Djulgovic *et al.* (2010)] Djulgovic, M., Beyth, R., Neuberger, M., Stoffs, T., Vieweg, J., Djulgovic, B., Dahm, P., *et al.* (2010). Screening for prostate cancer: systematic review and meta-analysis of randomised controlled trials. *British Medical Journal*, 341:c4543.
- [Doi (2007)] Doi, K. (2007). Computer-aided diagnosis in medical imaging: historical review, current status and future potential. *Computerized medical imaging and graphics*, 31:198–211.
- [Draisma *et al.* (2003)] Draisma, G., Boer, R., Otto, S., Van Der Crujisen, I., Damhuis, R., Schröder, F., and De Koning, H. (2003). Lead times and overdetection due to prostate-specific antigen screening: estimates from the european randomized study of screening for prostate cancer. *Journal of the National Cancer Institute*, 95:868–878.

- [Draisma *et al.* (2009)] Draisma, G., Etzioni, R., Tsodikov, A., Mariotto, A., Wever, E., Gulati, R., Feuer, E., and de Koning, H. (2009). Lead time and overdiagnosis in prostate-specific antigen screening: Importance of methods and context. *Journal of National Cancer Institute*, 101:374–383.
- [Drew *et al.* (2010)] Drew, B., Jones, E., Reinsberg, S., Yung, A., Goldenberg, S., and Kozlowski, P. (2010). Device for sectioning prostatectomy specimens to facilitate comparison between histology and in vivo mri. *Journal of Magnetic Resonance Imaging*, 32:992–996.
- [Duchon (1977)] Duchon, J. (1977). Splines minimizing rotation-invariant semi-norms in sobolev spaces. In *Constructive theory of functions of several variables*, pages 85–100. Springer.
- [Eastham *et al.* (2003)] Eastham, J., Kattan, M., Riedel, E., Begg, C., Wheeler, T., Gerigk, C., Gonen, M., Reuter, V., and Scardino, P. (2003). Variations among individual surgeons in the rate of positive surgical margins in radical prostatectomy specimens. *Journal of Urology*, 170:2292–2295.
- [Edge *et al.* (2010)] Edge, S. B., Byrd, D. R., Compton, C. C., Fritz, A. G., Greene, F. L., and Trotti, A. (2010). *Ajcc cancer staging manual* (7th ed). Springer, New York, pages 113–120.
- [Egawa *et al.* (2000)] Egawa, S., Takashima, R., Matsumoto, K., Mizoguchi, H., Kuwao, S., and Baba, S. (2000). Infrequent involvement of the anterior base in low-risk patients with clinically localized prostate cancer and its possible significance in definitive radiation therapy. *Japanese Journal of Clinical Oncology*, 30:126–130.
- [Egevad *et al.* (1998)] Egevad, L., Engstrom, K., and Busch, C. (1998). A new method for handling radical prostatectomies enabling fresh tissue harvesting, whole mount sections, and landmarks for alignment of sections. *Journal of Urologic Pathology*, 9:17–28.
- [Eichler *et al.* (2006)] Eichler, K., Hempel, S., Wilby, J., Myers, L., Bachmann, L., and Kleijnen, J. (2006). Diagnostic value of systematic biopsy methods in the investigation of prostate cancer: a systematic review. *The Journal of urology*, 175:1605–1612.
- [Etzioni *et al.* (2002)] Etzioni, R., Penson, D. F., Legler, J. M., di Tommaso, D., Boer, R., Gann, P. H., and Feuer, E. J. (2002). Overdiagnosis due to prostate-specific antigen screening: Lessons from u.s. prostate cancer incidence trends. *Journal of the National Cancer Institute*, 94:981–990.
- [Fan *et al.* (2011)] Fan, X., Haney, C., Agrawal, G., Pelizzari, C., Antic, T., Eggenner, S., Sethi, I., River, J., Zamora, M., Karczmar, G., *et al.* (2011). High-resolution mri of excised human prostate specimens acquired with 9.4 t in detection and identification of cancers: Validation of a technique. *Journal of Magnetic Resonance Imaging*, 34:956–961.

- [Ferlay *et al.* (2010)a] Ferlay, J., Parkin, D. M., and Steliarova-Foucher, E. (2010a). Estimates of cancer incidence and mortality in europe in 2008. *Eur J Cancer*, 46(4):765–781.
- [Ferlay *et al.* (2010)b] Ferlay, J., Shin, H. R., Bray, F., Forman, D., Mathers, C., and Parkin, D. M. (2010b). Estimates of worldwide burden of cancer in 2008: Globocan 2008. *Int J Cancer*, 127:2893–917.
- [Fitzgibbon *et al.* (1996)] Fitzgibbon, A. W., Pilu, M., and Fisher, R. B. (1996). Direct least squares fitting of ellipses. In *Proceedings of the 13th International Conference on Pattern Recognition, 1996*, volume 1, pages 253 – 257.
- [Fitzpatrick (2010)] Fitzpatrick, J. M. (2010). The role of registration in accurate surgical guidance. *Proceedings of the Institution of Mechanical Engineers, Part H: Journal of Engineering in Medicine*, 224:607–622.
- [Flanigan *et al.* (1994)] Flanigan, R., Catalona, W., Richie, J., Ahmann, F., Hudson, M., Scardino, P., DeKernion, J., Ratliff, T., Kavoussi, L., Dalkin, B., *et al.* (1994). Accuracy of digital rectal examination and transrectal ultrasonography in localizing prostate cancer. *The Journal of urology*, 152:1506.
- [Fletcher (1987)] Fletcher, R. (1987). *Practical Methods of Optimization, 2nd Edition*. John Wiley & Sons.
- [Frank *et al.* (2007)] Frank, S., Pisters, L., Davis, J., Lee, A., Bassett, R., and Kuban, D. (2007). An assessment of quality of life following radical prostatectomy, high dose external beam radiation therapy and brachytherapy iodine implantation as monotherapies for localized prostate cancer. *The Journal of urology*, 177:2151–2156.
- [Franks (1954)] Franks, L. M. (1954). Atrophy and hyperplasia in the prostate proper. *The Journal of pathology and bacteriology*, 68:617–622.
- [Gibb *et al.* (2012)] Gibb, M., Burton, R., Bollensdorff, C., Afonso, C., Mansoori, T., Schotten, U., Gavaghan, D., Rodriguez, B., Schneider, J., Kohl, P., *et al.* (2012). Resolving the three-dimensional histology of the heart. In *Computational Methods in Systems Biology*, pages 2–16.
- [Gibson *et al.* (2012)a] Gibson, E., Crukley, C., Gaed, M., Gómez, J., Moussa, M., Chin, J., Bauman, G., Fenster, A., and Ward, A. (2012a). Registration of prostate histology images to ex vivo mr images via strand-shaped fiducials. *Journal of Magnetic Resonance Imaging*, 36:1402–1412.
- [Gibson *et al.* (2012)b] Gibson, E., Gómez, J., Moussa, M., Crukley, C., Bauman, G., Fenster, A., and Ward, A. (2012b). 3d reconstruction of prostate histology based on quantified tissue cutting and deformation parameters. In *Society of Photo-Optical Instrumentation Engineers (SPIE) Conference Series*, volume 8317, page 22.

- [Girouin *et al.* (2007)] Girouin, N., Mège-Lechevallier, F., Tonina Senes, A., Bissery, A., Rabilloud, M., Maréchal, J.-M., Colombel, M., Lyonnet, D., and Rouvière, O. (2007). Prostate dynamic contrast-enhanced mri with simple visual diagnostic criteria: is it reasonable? *European radiology*, 17:1498–1509.
- [Gleason (1981)] Gleason, D. F. (1981). Histologic grading and staging of prostatic carcinoma. *The American Journal of Surgical Pathology*, 5:193.
- [Goubran *et al.* (2012)] Goubran, M., Khan, A., Crukley, C., Buchanan, S., Santyr, B., Peters, T., *et al.* (2012). Robust registration of sparsely sectioned histology to ex-vivo mri of temporal lobe resections. In *SPIE Medical Imaging*, page 83141V.
- [Greene *et al.* (1991)] Greene, D. R., Wheeler, T. M., Egawa, S., Dunn, J. K., and Scardino, P. T. (1991). A comparison of the morphological features of cancer arising in the transition zone and in the peripheral zone of the prostate. *The Journal of Urology*, 146:1069–1076.
- [Guest *et al.* (2001)] Guest, E., Berry, E., Baldock, R., Fidrich, M., and Smith, M. (2001). Robust point correspondence applied to two-and three-dimensional image registration. *Pattern Analysis and Machine Intelligence, IEEE Transactions on*, 23:165–179.
- [Guichard *et al.* (2007)] Guichard, G., Larré, S., Gallina, A., Lazar, A., Faucon, H., Chemamaa, S., Allory, Y., Patard, J. J., Vordos, D., Hoznek, A., Yiou, R., Salomon, L., Abbou, C., and de la Taille, A. (2007). Extended 21-sample needle biopsy protocol for diagnosis of prostate cancer in 1000 consecutive patients. *European Urology*, 52:430–435.
- [Haas *et al.* (2007)] Haas, G., Delongchamps, N., Jones, R., Chandan, V., Serio, A., Vickers, A., Jumbelic, M., Threatte, G., Korets, R., and Lilja, H. (2007). Needle biopsies on autopsy prostates: sensitivity of cancer detection based on true prevalence. *Journal of the National Cancer Institute*, 99:1484–1489.
- [Haider *et al.* (2007)] Haider, M., van der Kwast, T., Tanguay, J., Evans, A., Hashmi, A., Lockwood, G., and Trachtenberg, J. (2007). Combined t2-weighted and diffusion-weighted mri for localization of prostate cancer. *American Journal of Roentgenology*, 189:323–328.
- [Halpern (2006)] Halpern, E. (2006). Contrast-enhanced ultrasound imaging of prostate cancer. *Reviews in urology*, 8:S29.
- [Hara *et al.* (2008)] Hara, R., Jo, Y., Fujii, T., Kondo, N., Yokoyama, T., Miyaji, Y., and Nagai, A. (2008). Optimal approach for prostate cancer detection as initial biopsy: prospective randomized study comparing transperineal versus transrectal systematic 12-core biopsy. *Urology*, 71:191–195.
- [Heidenreich *et al.* (2008)] Heidenreich, A., Aus, G., Bolla, M., Joniau, S., Matveev, V., Schmid, H., and Zattoni, F. (2008). Eau guidelines on prostate cancer. 53:68–80.

- [Heidenreich *et al.* (2011)] Heidenreich, A., Bellmunt, J., Bolla, M., Joniau, S., Mason, M., Matveev, V., Mottet, N., Schmid, H., van der Kwast, T., Wiegel, T., *et al.* (2011). Eau guidelines on prostate cancer. part 1: screening, diagnosis, and treatment of clinically localised disease. *European urology*, 59:61–71.
- [Heijmink *et al.* (2009)] Heijmink, S., Scheenen, T., van Lin, E., Visser, A., Kiemeny, L., Witjes, J., and Barentsz, J. (2009). Changes in prostate shape and volume and their implications for radiotherapy after introduction of endorectal balloon as determined by mri at 3t. *International Journal of Radiation Oncology Biology Physics*, 73:1446–1453.
- [Hellerstedt and Pienta (2008)] Hellerstedt, B. and Pienta, K. (2008). The current state of hormonal therapy for prostate cancer. *CA: a cancer journal for clinicians*, 52:154–179.
- [Humm *et al.* (2003)] Humm, J., Ballon, D., Hu, Y., Ruan, S., Chui, C., Tulipano, P., Erdi, A., Koutcher, J., Zakian, K., Urano, M., *et al.* (2003). A stereotactic method for the three-dimensional registration of multi-modality biologic images in animals: Nmr, pet, histology, and autoradiography. *Medical physics*, 30:2303.
- [Iremashvili *et al.* (2012)] Iremashvili, V., Pelaez, L., Manoharan, M., Jorda, M., Rosenberg, D., and Soloway, M. (2012). Pathologic prostate cancer characteristics in patients eligible for active surveillance: A head-to-head comparison of contemporary protocols. *European urology*, 62:462–468.
- [Jhavar *et al.* (2005)] Jhavar, S., Fisher, C., Jackson, A., Reinsberg, S., Dennis, N., Falconer, A., Dearnaley, D., Edwards, S., Edwards, S., Leach, M., *et al.* (2005). Processing of radical prostatectomy specimens for correlation of data from histopathological, molecular biological, and radiological studies: a new whole organ technique. *Journal of clinical pathology*, 58:504–508.
- [Johns and Houlston (2003)] Johns, L. E. and Houlston, R. S. (2003). A systematic review and meta-analysis of familial prostate cancer risk. *BJU international*, 91:789–794.
- [Kamoi *et al.* (2008)] Kamoi, K., Okihara, K., Ochiai, A., Ukimura, O., Mizutani, Y., Kawauchi, A., and Miki, T. (2008). The utility of transrectal real-time elastography in the diagnosis of prostate cancer. *Ultrasound in medicine & biology*, 34:1025–1032.
- [Kaplan *et al.* (2002)] Kaplan, I., Oldenburg, N. E., Meskell, P., Blake, M., Church, P., and Holupka, E. J. (2002). Real time mri-ultrasound image guided stereotactic prostate biopsy. *Magnetic resonance imaging*, 20:295–299.
- [Kay *et al.* (1998)] Kay, P., Robb, R., and Bostwick, D. (1998). Prostate cancer microvessels: a novel method for three-dimensional reconstruction and analysis. *The Prostate*, 37:270–277.
- [Kendall (1989)] Kendall, D. G. (1989). A survey of the statistical theory of shape. *Statistical Science*, 4:87–99.

- [Kiessling *et al.* (2005)] Kiessling, F., Le-Huu, M., Kunert, T., Thorn, M., Vosseler, S., Schmidt, K., Hoffend, J., Meinzer, H., Fusenig, N., and Semmler, W. (2005). Improved correlation of histological data with dce mri parameter maps by 3d reconstruction, reslicing and parameterization of the histological images. *European radiology*, 15:1079–1086.
- [Kim *et al.* (1995)] Kim, B., Frey, K. A., Mukhopadhyay, S., Ross, B. D., and Meyer, C. R. (1995). Co-registration of MRI and autoradiography of rat brain in three-dimensions following automatic reconstruction of 2D data set. In *Proceedings of the First International Conference on Computer Vision, Virtual Reality and Robotics in Medicine*, pages 262–266.
- [Kimm *et al.* (2012)] Kimm, S., Tarin, T., Lee, J., Hu, B., Jensen, K., Nishimura, D., and Brooks, J. (2012). Methods for registration of magnetic resonance images of ex vivo prostate specimens with histology. *Journal of Magnetic Resonance Imaging*, 36:206–212.
- [Kozlowski *et al.* (2006)] Kozlowski, P., Chang, S., Jones, E., Berean, K., Chen, H., and Goldenberg, S. (2006). Combined diffusion-weighted and dynamic contrast-enhanced mri for prostate cancer diagnosis—correlation with biopsy and histopathology. *Journal of Magnetic Resonance Imaging*, 24:108–113.
- [Kuligowska *et al.* (2001)] Kuligowska, E., Barish, M., Fenlon, H., and Blake, M. (2001). Predictors of prostate carcinoma: Accuracy of gray-scale and color doppler us and serum markers. *Radiology*, 220:757–764.
- [Kupelian *et al.* (2002)] Kupelian, P., Elshaikh, M., Reddy, C., Zippe, C., and Klein, E. (2002). Comparison of the efficacy of local therapies for localized prostate cancer in the prostate-specific antigen era: a large single-institution experience with radical prostatectomy and external-beam radiotherapy. *Journal of clinical oncology*, 20:3376–3385.
- [Kurhanewicz *et al.* (2008)] Kurhanewicz, J., Vigneron, D., Carroll, P., and Coakley, F. (2008). Multiparametric magnetic resonance imaging in prostate cancer: present and future. *Current opinion in urology*, 18:71.
- [Langer *et al.* (2009)] Langer, D., van der Kwast, T., Evans, A., Trachtenberg, J., Wilson, B., and Haider, M. (2009). Prostate cancer detection with multi-parametric mri: Logistic regression analysis of quantitative t2, diffusion-weighted imaging, and dynamic contrast-enhanced mri. *Journal of Magnetic Resonance Imaging*, 30:327–334.
- [Lazebnik *et al.* (2003)] Lazebnik, R. S., Lancaster, T. L., Breen, M. S., Lewin, J. S., and Wilson, D. L. (2003). Volume registration using needle paths and point landmarks for evaluation of interventional MRI treatments. *IEEE Trans Med Imaging*, 22(5):653–660.
- [Loughlin *et al.* (1998)] Loughlin, M., Carlbom, I., Busch, C., Douglas, T., Egevad, L., Frimmel, H., Norberg, M., Sesterhenn, I., and Frogge, J. (1998). Three-dimensional

- modeling of biopsy protocols for localized prostate cancer. *Computerized medical imaging and graphics*, 22:229–238.
- [Lowsley (1912)] Lowsley, O. S. (1912). The development of the human prostate gland with reference to the development of other structures at the neck of the urinary bladder. *American Journal of Anatomy*, 13:299–349.
- [Madabhushi *et al.* (2005)] Madabhushi, A., Feldman, M., Metaxas, D., Tomaszewski, J., and Chute, D. (2005). Automated detection of prostatic adenocarcinoma from high-resolution ex vivo mri. *Medical Imaging, IEEE Transactions on*, 24:1611–1625.
- [Makni (2010)] Makni, N. (2010). Méthodes d’identification, d’aide au diagnostic et de planification utilisant de l’imagerie multi-modalité pour les thérapies focales du cancer de la prostate. Master’s thesis.
- [Malandain *et al.* (2004)] Malandain, G., Bardinnet, E., Nelissen, K., and Vanduffel, W. (2004). Fusion of autoradiographs with an MR volume using 2-D and 3-D linear transformations. *Neuroimage*, 23(1):111–127.
- [Mansoori *et al.* (2007)] Mansoori, T., Plank, G., Burton, R., Schneider, J., Kohl, P., Gavaghan, D., and Grau, V. (2007). An iterative method for registration of high-resolution cardiac histoanatomical and mri images. In *Biomedical Imaging: From Nano to Macro, 2007. ISBI 2007. 4th IEEE International Symposium on*, pages 572–575.
- [Mathew *et al.* (2012)] Mathew, L., Alabousi, M., Wheatley, A., Aladl, U., Slipetz, D., Hogg, J., Fenster, A., and Parraga, G. (2012). Development and proof-of-concept of three-dimensional lung histology volumes. In *Society of Photo-Optical Instrumentation Engineers (SPIE) Conference Series*, volume 8317, page 55.
- [Mazaheri *et al.* (2010)] Mazaheri, Y., Bokacheva, L., Kroon, D., Akin, O., Hricak, H., Chamudot, D., Fine, S., and Koutcher, J. (2010). Semi-automatic deformable registration of prostate mr images to pathological slices. *Journal of Magnetic Resonance Imaging*, 32:1149–1157.
- [McNeal (1981)] McNeal, J. (1981). The zonal anatomy of the prostate. *The Prostate*, 2:35–49.
- [Merrick *et al.* (2007)] Merrick, G. S., Gutman, S., Andreini, H., Taubenslag, W., Lindert, D. L., Curtis, R., Adamovich, E., Anderson, R., Allen, Z., Butler, W., and Wallner, K. (2007). Prostate cancer distribution in patients diagnosed by transperineal template-guided saturation biopsy. *European urology*, 52:715–724.
- [Moore *et al.* (2013)] Moore, C. M., Robertson, N. L., Arsanious, N., Middleton, T., Villers, A., Klotz, L., Taneja, S. S., and Emberton, M. (2013). Image-guided prostate biopsy using magnetic resonance imaging-derived targets: a systematic review. *European urology*, 63:125–140.

- [Moradi *et al.* (2012)] Moradi, M., Salcudean, S., Chang, S., Jones, E., Buchan, N., Casey, R., Goldenberg, S., and Kozlowski, P. (2012). Multiparametric mri maps for detection and grading of dominant prostate tumors. *Journal of Magnetic Resonance Imaging*, 35:1403–1413.
- [Murphy *et al.* (2011)] Murphy, R., Kawashima, A., and Peller, P. (2011). The utility of 11c-choline pet/ct for imaging prostate cancer: a pictorial guide. *American Journal of Roentgenology*, 196:1390–1398.
- [Naughton *et al.* (1998)] Naughton, C. K., Smith, D. S., Humphrey, P. A., Catalona, W. J., Keetch, D. W., *et al.* (1998). Clinical and pathologic tumor characteristics of prostate cancer as a function of the number of biopsy cores: a retrospective study. *Urology*, 52:808–813.
- [Nguyen *et al.* (1996)] Nguyen, H., Ezzell, J., and Turek, P. (1996). Normal human ejaculatory duct anatomy: a study of cadaveric and surgical specimens. *The Journal of urology*, 155:1639–1642.
- [Nicolau *et al.* (2010)] Nicolau, C., Izquierdo, L., and Alcaraz, A. (2010). Imaging techniques in prostate cancer. *European Urological Review*, 5:15–21.
- [Noguchi *et al.* (2000)] Noguchi, M., Stamey, T., McNeal, J., and Yemoto, C. (2000). Assessment of morphometric measurements of prostate carcinoma volume. *Cancer*, 89:1056–1064.
- [Ou *et al.* (2009)] Ou, Y., Shen, D., Feldman, M., Tomaszewski, J., and Davatzikos, C. (2009). Non-rigid registration between histological and mr images of the prostate: a joint segmentation and registration framework. In *Computer Vision and Pattern Recognition Workshops, 2009. CVPR Workshops 2009. IEEE Computer Society Conference on*, pages 125–132.
- [Ourselin *et al.* (2001)a] Ourselin, S., Bardin, E., Dormont, D., Malandain, G., Roche, A., Ayache, N., Tande, D., Parain, K., and Yelnik, J. (2001a). Fusion of histological sections and MR images: Towards the construction of an atlas of the human basal ganglia. In *Proceedings MICCAI*, pages 743–751.
- [Ourselin *et al.* (2001)b] Ourselin, S., Roche, A., Subsol, G., Pennec, X., and Ayache, N. (2001b). Reconstructing a 3d structure from serial histological sections. *Image and vision computing*, 19:25–31.
- [Owen and Katz (2005)] Owen, D. and Katz, D. (2005). A review of the physical and chemical properties of human semen and the formulation of a semen simulant. *Journal of andrology*, 26:459.

- [Park *et al.* (2008)] Park, H., Piert, M. R., Khan, A., Shah, R., Hussain, H., Siddiqui, J., Chenevert, T. L., and Meyer, C. R. (2008). Registration methodology for histological sections and *in vivo* imaging of human prostate. *Acad Radiol*, 15(8):1027–1039.
- [Patel *et al.* (2011)] Patel, P., Chappelow, J., Tomaszewski, J., Feldman, M., Rosen, M., Shih, N., and Madabhushi, A. (2011). Spatially weighted mutual information (swmi) for registration of digitally reconstructed ex vivo whole mount histology and in vivo prostate mri. In *Engineering in Medicine and Biology Society, EMBC, 2011 Annual International Conference of the IEEE*, pages 6269–6272.
- [Pinto *et al.* (2011)] Pinto, P. A., Chung, P. H., Rastinehad, A. R., Baccala, A. A., Kruecker, J., Benjamin, C. J., Xu, S., Yan, P., Kadoury, S., Chua, C., *et al.* (2011). Magnetic resonance imaging/ultrasound fusion guided prostate biopsy improves cancer detection following transrectal ultrasound biopsy and correlates with multiparametric magnetic resonance imaging. *The Journal of urology*, 186:1281–1285.
- [Plank *et al.* (2009)] Plank, G., Burton, R., Hales, P., Bishop, M., Mansoori, T., Bernabeu, M., Garny, A., Prassl, A., Bollensdorff, C., Mason, F., *et al.* (2009). Generation of histo-anatomically representative models of the individual heart: tools and application. *Philosophical Transactions of the Royal Society A: Mathematical, Physical and Engineering Sciences*, 367:2257–2292.
- [Porter *et al.* (2001)] Porter, B., Rubens, D., Strang, J., Smith, J., Totterman, S., and Parker, K. (2001). Three-dimensional registration and fusion of ultrasound and mri using major vessels as fiducial markers. *Medical Imaging, IEEE Transactions on*, 20:354–359.
- [Postma and Schröder (2005)] Postma, R. and Schröder, F. (2005). Screening for prostate cancer. *European journal of cancer*, 41:825–833.
- [Puech *et al.* (2009)] Puech, P., Betrouni, N., Makni, N., Dewalle, A.-S., Villers, A., and Lemaitre, L. (2009). Computer-assisted diagnosis of prostate cancer using dce-mri data: design, implementation and preliminary results. *International journal of computer assisted radiology and surgery*, 4:1–10.
- [Reynier *et al.* (2004)] Reynier, C., Troccaz, J., Fourneret, P., Dusserre, A., Gay-Jeune, C., Descotes, J., Bolla, M., and Giraud, J. (2004). Mri/trus data fusion for prostate brachytherapy. preliminary results. *Medical Physics*, 31:1568–1575.
- [Richie *et al.* (1993)] Richie, J., Catalona, W., Ahmann, F., Hudson, M., Scardino, P., Flanigan, R., Dekernion, J., Ratliff, T., Kavoussi, L., Dalkin, B., *et al.* (1993). Effect of patient age on early detection of prostate cancer with serum prostate-specific antigen and digital rectal examination. *Urology*, 42:365–374.
- [Roobol *et al.* (2012)] Roobol, M. J., van Vugt, H. A., Loeb, S., Zhu, X., Bul, M., Bangma, C. H., van Leenders, A. G., Steyerberg, E. W., and Schröder, F. H. (2012). Prediction

of prostate cancer risk: The role of prostate volume and digital rectal examination in the erspc risk calculators. *European Urology*, 61:577 – 583.

- [Rouviere *et al.* (2006)] Rouviere, O., Reynolds, C., Hulshizer, T., Rossman, P., Le, Y., Felmlee, J., and Ehman, R. (2006). Mr histological correlation: a method for cutting specimens along the imaging plane in animal or ex vivo experiments. *Journal of Magnetic Resonance Imaging*, 23:60–69.
- [Rouvière *et al.* (2003)] Rouvière, O., Raudrant, A., Ecochard, R., Colin-Pangaud, C., Pasquiou, C., Bouvier, R., Maréchal, J., and Lyonnet, D. (2003). Characterization of time-enhancement curves of benign and malignant prostate tissue at dynamic mr imaging. *European radiology*, 13:931–942.
- [Roy *et al.* (2003)] Roy, C., Buy, X., Lang, H., Saussine, C., and Jacqmin, D. (2003). Contrast enhances color doppler endorectal sonography of prostate: Efficiency for detecting peripheral zone tumors and role for biopsy procedure. *The Journal of urology*, 170:69–72.
- [Samavati *et al.* (2011)] Samavati, N., McGrath, D., Lee, J., van Kwast, T., Jewett, M., Ménard, C., and Brock, K. (2011). Biomechanical model-based deformable registration of mri and histopathology for clinical prostatectomy. *Journal of Pathology Informatics*, 2.
- [Scheidler *et al.* (1999)] Scheidler, J., Hricak, H., Vigneron, D., Yu, K., Sokolov, D., Huang, L., Zaloudek, C., Nelson, S., Carroll, P., and Kurhanewicz, J. (1999). Prostate cancer: localization with three-dimensional proton mr spectroscopic imaging-clinicopathologic study. *Radiology*, 213:473–480.
- [Schned *et al.* (1996)] Schned, A., Wheeler, K., Hodorowski, C., Heaney, J., Ernstoff, M., Amdur, R., and Harris, R. (1996). Tissue-shrinkage correction factor in the calculation of prostate cancer volume. *The American journal of surgical pathology*, 20:1501–1506.
- [Schröder *et al.* (2012)] Schröder, F., Hugosson, J., Roobol, M., Tammela, T., Ciatto, S., Nelen, V., Kwiatkowski, M., Lujan, M., Lilja, H., Zappa, M., *et al.* (2012). Prostate-cancer mortality at 11 years of follow-up. *New England Journal of Medicine*, 366:981–990.
- [Seber (1984)] Seber, G. A. F. (1984). *Multivariate Observations*. John Wiley & Sons.
- [Seise *et al.* (2011)] Seise, M., Alhonnoro, T., and Kolesnik, M. (2011). Interactive registration of 2d histology and 3d ct data for assessment of radiofrequency ablation treatment. *Journal of Pathology Informatics*, 2.
- [Shah *et al.* (2009)] Shah, V., Pohida, T., Turkbey, B., Mani, H., Merino, M., Pinto, P., Choyke, P., and Bernardo, M. (2009). A method for correlating in vivo prostate magnetic

- resonance imaging and histopathology using individualized magnetic resonance-based molds. *Review of Scientific Instruments*, 80:104301–104301.
- [Shipley *et al.* (1999)] Shipley, W., Thames, H., Sandler, H., Hanks, G., Zietman, A., Perez, C., Kuban, D., Hancock, S., and Smith, C. (1999). Radiation therapy for clinically localized prostate cancer. *Journal of the American Medical Association*, 281:1598–1604.
- [Shojaii *et al.* (2011)] Shojaii, R., Karavardanyan, T., Yaffe, M., and Martel, A. (2011). Validation of histology image registration. In *SPIE Medical Imaging*, page 79621E.
- [Singh *et al.* (2008)] Singh, A. K., Kruecker, J., Xu, S., Glossop, N., Guion, P., Ullman, K., Choyke, P. L., and Wood, B. J. (2008). Initial clinical experience with real-time transrectal ultrasonography-magnetic resonance imaging fusion-guided prostate biopsy. *BJU international*, 101:841–845.
- [Soloway *et al.* (2002)] Soloway, M., Pareek, K., Sharifi, R., Wajzman, Z., McLEOD, D., Wood Jr, D., Puras-Baez, A., *et al.* (2002). Neoadjuvant androgen ablation before radical prostatectomy in ct2bnxmo prostate cancer: 5-year results. *The Journal of urology*, 167:112.
- [Stamey *et al.* (1993)] Stamey, T. A., Freiha, F. S., McNeal, J. E., Redwine, E. A., Whittemore, A. S., and Schmid, H. P. (1993). Localized prostate cancer. *Cancer*, 71(S3):933–38.
- [Stanford *et al.* (2000)] Stanford, J., Feng, Z., Hamilton, A., Gilliland, F., Stephenson, R., Eley, J., Albertsen, P., Harlan, L., and Potosky, A. (2000). Urinary and sexual function after radical prostatectomy for clinically localized prostate cancer. *Journal of the American Medical Association*, 283:354–360.
- [Stock *et al.* (2006)] Stock, R., Cesaretti, J., and Stone, N. (2006). Disease-specific survival following the brachytherapy management of prostate cancer. *International Journal of Radiation Oncology Biology Physics*, 64:810–816.
- [Taira *et al.* (2009)] Taira, A. V., Merrick, G. S., Galbreath, R. W., Andreini, H., Taubenslag, W., Curtis, R., Butler, W. M., Adamovich, E., and Wallner, K. E. (2009). Performance of transperineal template-guided mapping biopsy in detecting prostate cancer in the initial and repeat biopsy setting. *Prostate cancer and prostatic diseases*, 13:71–77.
- [Tang (2011)] Tang, M. (2011). Automatic registration and fast volume reconstruction from serial histology sections. *Computer Vision and Image Understanding*, 115:1112–1120.
- [Tanimoto *et al.* (2006)] Tanimoto, A., Nakashima, J., Kohno, H., Shinmoto, H., and Kuribayashi, S. (2006). Prostate cancer screening: The clinical value of diffusion-

- weighted imaging and dynamic mr imaging in combination with t2-weighted imaging. *Journal of Magnetic Resonance Imaging*, 25:146–152.
- [Tannock *et al.* (2004)] Tannock, I., de Wit, R., Berry, W., Horti, J., Pluzanska, A., Chi, K., Oudard, S., Théodore, C., James, N., Turesson, I., *et al.* (2004). Docetaxel plus prednisone or mitoxantrone plus prednisone for advanced prostate cancer. *New England Journal of Medicine*, 351:1502–1512.
- [Taylor *et al.* (2004)] Taylor, L. S., Porter, B. C., Nadasdy, G., di Sant’Agnese, P. A., Pasternack, D., Wu, Z., Baggs, R. B., Rubens, D. J., and Parker, K. J. (2004). Three-dimensional registration of prostate images from histology and ultrasound. *Ultrasound Med Biol*, 30(2):161–168.
- [Tessler *et al.* (2012)] Tessler, L., Sultan, R., Ramakrishnan, V., Weiss, R., Goldfeder, R., Wu, W., Mitra, R., and Kibel, A. (2012). The diagnostic value of digital rectal examination for prostate cancer: an analysis of over 50,000 biopsies. In *Prostate Cancer: Detection and Screening I*.
- [Trivedi *et al.* (2012)] Trivedi, H., Turkbey, B., Rastinehad, A., Benjamin, C., Bernardo, M., Pohida, T., Shah, V., Merino, M., Wood, B., Linehan, W., *et al.* (2012). Use of patient-specific mri-based prostate mold for validation of multiparametric mri in localization of prostate cancer. *Urology*, 79:233–239.
- [Turkbey *et al.* (2009)] Turkbey, B., Pinto, P., and Choyke, P. (2009). Imaging techniques for prostate cancer: implications for focal therapy. *Nature Reviews Urology*, 6:191–203.
- [Turkbey *et al.* (2011)] Turkbey, B., Shah, V., Pang, Y., Bernardo, M., Xu, S., Kruecker, J., Locklin, J., Baccala, A., Rastinehad, A., Merino, M., *et al.* (2011). Is apparent diffusion coefficient associated with clinical risk scores for prostate cancers that are visible on 3-t mr images? *Radiology*, 258:488–495.
- [Vargas *et al.* (2012)] Vargas, H. A., Akin, O., Shukla-Dave, A., Zhang, J., Zakian, K. L., Zheng, J., Kanao, K., Goldman, D. A., Moskowitz, C. S., Reuter, V. E., *et al.* (2012). Performance characteristics of mr imaging in the evaluation of clinically low-risk prostate cancer: A prospective study. *Radiology*, 265:478–487.
- [Varghese *et al.* (2003)] Varghese, T., Techavipoo, U., Liu, W., Zagzebski, J., Chen, Q., Frank, G., and Lee Jr, F. (2003). Elastographic measurement of the area and volume of thermal lesions resulting from radiofrequency ablation: pathologic correlation. *American Journal of Roentgenology*, 181:701–707.
- [Verma and Rajesh (2011)] Verma, S. and Rajesh, A. (2011). A clinically relevant approach to imaging prostate cancer: review. *American Journal of Roentgenology*, 196:S1–S10.

- [Vieillefond *et al.* (2004)] Vieillefond, A., Sibony, M., Molinié, V., and Camparo, P. (2004). *Pathologie tumorale de la prostate*. Elsevier.
- [Ward *et al.* (2010)] Ward, A., Crukley, C., McKenzie, C., Montreuil, J., Gibson, E., Gomez, J., Moussa, M., Bauman, G., and Fenster, A. (2010). Registration of *in vivo* prostate magnetic resonance images to digital histopathology images. In *Prostate Cancer Imaging. Computer-Aided Diagnosis, Prognosis, and Intervention*, volume 6367, pages 66–76.
- [Ward *et al.* (2012)] Ward, A., Crukley, C., McKenzie, C., Montreuil, J., Gibson, E., Romagnoli, C., Gomez, J., Moussa, M., Chin, J., Bauman, G., *et al.* (2012). Prostate: Registration of digital histopathologic images to *in vivo* mr images acquired by using endorectal receive coil. *Radiology*, 263:856–864.
- [Weinreb *et al.* (2009)] Weinreb, J. C., Blume, J. D., Coakley, F. V., Wheeler, T. M., Cormack, J. B., Sotito, C. K., Cho, H., Kawashima, A., Tempany-Afdhal, C. M., Macura, K. J., *et al.* (2009). Prostate cancer: Sextant localization at mr imaging and mr spectroscopic imaging before prostatectomy - results of acrin prospective multi-institutional clinicopathologic study. *Radiology*, 251:122–133.
- [Welch and Black (2010)] Welch, H. G. and Black, W. C. (2010). Overdiagnosis in cancer. *Journal of National Cancer Institute*, 102:605–613.
- [Xiao *et al.* (2011)] Xiao, G., Bloch, B. N., Chappelow, J., Genega, E. M., Rofsky, N. M., Lenkinski, R. E., Tomaszewski, J., Feldman, M. D., Rosen, M., and Madabhushi, A. (2011). Determining histology-MRI slice correspondences for defining MRI-based disease signatures of prostate cancer. *Comput Med Imaging Graph*, 35(7-8):568–578.
- [Xu *et al.* (2008)] Xu, S., Kruecker, J., Turkbey, B., Glossop, N., Singh, A. K., Choyke, P., Pinto, P., and Wood, B. J. (2008). Real-time mri-trus fusion for guidance of targeted prostate biopsies. *Computer Aided Surgery*, 13:255–264.
- [Yossepowitch *et al.* (2009)] Yossepowitch, O., Bjartell, A., Eastham, J., Graefen, M., Guillonneau, B., Karakiewicz, P., Montironi, R., and Montorsi, F. (2009). Positive surgical margins in radical prostatectomy: outlining the problem and its long-term consequences. *European urology*, 55:87–99.
- [Yushkevich *et al.* (2006)] Yushkevich, P., Avants, B., Ng, L., Hawrylycz, M., Burstein, P., Zhang, H., and Gee, J. (2006). 3D mouse brain reconstruction from histology using a coarse-to-fine approach. In *Biomedical Image Registration*, volume 4057, pages 230–237.
- [Zagoria (2004)] Zagoria, R. (2004). *Genitourinary radiology: the requisites*. Mosby Incorporated.
- [Zakian *et al.* (2005)] Zakian, K., Sircar, K., Hricak, H., Chen, H., Shukla-Dave, A., Eberhardt, S., Muruganandham, M., Ebor, L., Kattan, M., Reuter, E., Scardino, P., and

- Koutcher, J. A. (2005). Correlation of proton mr spectroscopic imaging with gleason score based on step-section pathologic analysis after radical prostatectomy. *Radiology*, 234:804–814.
- [Zhan *et al.* (2007)] Zhan, Y., Ou, Y., Feldman, M., Tomaszewski, J., Davatzikos, C., and Shen, D. (2007). Registering histological and mr images of prostate for image-based cancer detection. *Academic radiology*, 14:1367.
- [Zhao *et al.* (1993)] Zhao, W., Young, T., and Ginsberg, M. (1993). Registration and three-dimensional reconstruction of autoradiographic images by the disparity analysis method. *Medical Imaging, IEEE Transactions on*, 12:782–791.
- [van Engelen *et al.* (2011)] van Engelen, A., Niessen, W., Klein, S., Groen, H., Verhagen, H., Wentzel, J., van der Lugt, A., and de Bruijne, M. (2011). Multi-feature-based plaque characterization in ex vivo mri trained by registration to 3d histology. *Physics in Medicine and Biology*, 57:241.



# PUBLICATIONS

## INTERNATIONAL PEER-REVIEWED JOURNAL

- i **C. Hughes**, O. Rouvière, F. Mege-Lechevallier, R. Souchon and R. Prost. Robust Alignment of Prostate Histology Slices With Quantified Accuracy. *IEEE Transactions on Biomedical Engineering*, 60(2): 281 - 291, Feb. 2013.

## INTERNATIONAL PEER-REVIEWED CONFERENCE PROCEEDINGS

- i **C. Hughes**, O. Rouvière, F. Mege-Lechevallier, R. Souchon and R. Prost. A Novel Method for 3D Prostate MR-Histology Registration using Anatomical Landmarks. *20th European Signal Processing Conference (EUSIPCO)*, 2591 - 2595, Bucharest, Romania, 2012.
- ii **C. Hughes**, O. Rouvière, F. Mege-Lechevallier, R. Souchon and R. Prost. Robust Alignment of Prostate Histology Slices With Quantified Accuracy. *Proc. of SPIE, Vol. 8314, Medical Imaging 2012: Image Processing*, 83141N-1 - 83141N-10, San Diego, USA, 2012.

## NATIONAL PEER-REVIEWED CONFERENCE

- i **C. Hughes**, O. Rouvière, F. Mege-Lechevallier and R. Prost. 3D MR - Histology Registration : examining the effects of shear, tilt and shrinkage. *Journées scientifiques, Nouvelles méthodologies en imagerie du vivant*, Lyon, 2012.
- ii **C. Hughes**, O. Rouvière, F. Mege-Lechevallier, R. Souchon and R. Prost. Méthode de recalage 3D des images IRM avec les coupes histologiques de la prostate. *Journées Françaises de radiologie (JFR) 2012*, Paris, 2012.



# ABBREVIATIONS

ADC	Apparent diffusion coefficient
ADT	Androgen deprivation therapy
AFMS	Anterior fibromuscular stroma
AS	Active surveillance
BPH	Benign prostatic hyperplasia
CT	Computed tomography
CZ	Central zone
DCE	Dynamic contrast-enhanced
DRE	Digital rectal examination
DWI	Diffusion-weighted imaging
ERBT	External beam radiation therapy
HIFU	High intensity focused ultrasound
HRPC	Hormone refractory prostate cancer
HT	Hormonal therapy
MRI	Magnetic resonance imaging
MRS	Magnetic resonance spectroscopy
PCa	Prostate cancer
PET	Positron emission tomography
PSA	Prostate specific antigen
PSM	Positive surgical margin
PZ	Peripheral zone
RP	Radical prostatectomy
T	Tesla
TRUS	Transrectal ultrasound
TZ	Transition zone
$T_1$ -W	$T_1$ -weighted
$T_2$ -W	$T_2$ -weighted
US	Ultrasonography

---

**Titre** Méthode de mise en correspondance tridimensionnelle entre des coupes IRM de la prostate et les coupes histologiques des pièces de prostatectomie

**Résumé** Le cancer de la prostate est le cancer le plus fréquent chez l'homme en Europe, néanmoins il n'existe actuellement pas de technique d'imagerie permettant de détecter avec précision les tumeurs dans la glande. Sachant que les coupes histologiques contiennent la réalité de terrain concernant le diagnostic, il est nécessaire de recalibrer les images de chaque technique d'imagerie aux coupes histologiques afin de pouvoir les évaluer. De plus, comme il n'existe pas de méthode permettant de contrôler précisément le plan de coupe histologique, le recalage doit être considéré comme un problème 3D. Un dispositif permettant de réaliser, de manière rapide et standardisée, des marqueurs internes dans les coupes histologiques a été développé, de même qu'un algorithme permettant de détecter automatiquement ces marqueurs, de les identifier et d'aligner les coupes histologiques. La méthode a été testée sur 10 prostates, avec en moyenne 19.2 coupes par prostate, et a permis d'obtenir une précision de recalage moyenne de  $0.18 \pm 0.13$  mm au niveau des marqueurs. Un deuxième algorithme a été développé pour recalibrer les coupes histologiques, une fois alignées, avec les images IRM. Ce recalage a été conçu pour être guidé par les canaux éjaculateurs, un repère anatomique présent dans chaque prostate et visible à la fois en histologie et dans les images IRM cliniques, acquises avec une résolution standard. L'algorithme a d'abord été testé en s'appuyant sur les marqueurs artificiels. La précision obtenue pour le recalage était en moyenne de  $0.45 \pm 0.25$  mm au niveau des marqueurs et de  $1.04 \pm 0.21$  mm au niveau des canaux éjaculateurs. L'algorithme a enfin été testé en guidant le recalage à l'aide de la position des canaux éjaculateurs. La précision moyenne obtenue était alors de  $0.16 \pm 0.05$  mm au niveau des canaux éjaculateurs et de  $2.82 \pm 0.41$  mm au niveau des marqueurs. Ces résultats suggèrent une valeur du facteur de rétrécissement de l'ordre de  $1.07 \pm 0.03$  et une inclinaison vis à vis du plan de coupe histologique de l'ordre de  $13.6^\circ \pm 9.61^\circ$ , avec une variance importante pour ces deux paramètres.

**Mots-clés** Alignement, marqueurs, histologie, IRM, cancer de la prostate, recalage 3D

---

**Title** 3D registration of prostate histology slices with MR images

**Abstract** Prostate cancer is the most frequently diagnosed cancer of men in Europe, yet no current imaging technique is capable of detecting with precision tumours in the prostate. The histology slices are the gold standard for the diagnosis. Therefore, in order to evaluate each imaging technique, the histology slices must be precisely registered to the imaged data. As it cannot be assumed that the histology slices are cut along the same plane as the imaged data is acquired, the registration must be considered as a 3D problem. An apparatus has been developed that enables internal fiducial markers to be created in the histology slices in a rapid and standardised manner. An algorithm has been developed that automatically detects and identifies these markers, enabling the alignment of the histology slices. The method has been tested on 10 prostate specimens, with 19.2 slices on average per specimen. The accuracy of the alignment at the fiducial markers was on average  $0.18 \pm 0.13$  mm. A second algorithm was developed to 3D register the aligned histology slices with the MR images. The registration is designed to be guided by the ejaculatory ducts, an anatomical landmark present in every prostate and visible in both histology and MR images acquired at standard clinical resolution. The algorithm was first tested by using the fiducial needles to guide the registration. The average registration accuracy was  $0.45 \pm 0.25$  mm at the fiducial needles and  $1.04 \pm 0.21$  mm at the ejaculatory ducts. The algorithm was then tested by using the ejaculatory ducts to guide the registration. The average registration accuracy was  $0.16 \pm 0.05$  mm at the ejaculatory ducts and  $2.82 \pm 0.41$  mm at the fiducial needles. The results suggest that the histology shrinkage factor is of the order  $1.07 \pm 0.03$  and the tilt of the histology slicing plane is  $13.6^\circ \pm 9.61^\circ$ , with both parameters showing significant variance.

**Keywords** Alignment, fiducial markers, histology, MRI, prostate cancer, 3D registration

---

**Laboratoires** LabTau, INSERM U1032, 151 cours Albert Thomas, 69424 Lyon Cedex 03.

Université de Lyon, CREATIS; CNRS UMR5220; Inserm U1044; INSA-Lyon; Université Lyon 1, 7 Av. Jean Capelle, 69621 Villeurbanne, France.

---

